Universiteit Antwerpen

Faculteit Wetenschappen
Departement Fysica

VRIJE UNIVERSITEIT BRUSSEL

Faculteit Wetenschappen en
Bio-ingenieurswetenschappen
Vakgroep Fysica

Commissioning of the SoLid experiment for the observation of electron antineutrinos at the BR2 reactor

Simon Vercaemer

November 2018

Promotoren:
Prof. Dr. Nick van Remortel
Prof. Dr. Petra Van Mulders

Proefschrift ingediend met het oog op het behalen van
de academische graad Doctor in de Wetenschappen

Doctoral exam commission:

Prof. Dr.	Nick van Eijndhoven (Vrije Universiteit Brussel)	*chair*
Prof. Dr.	Stijn Buitink (Vrije Universiteit Brussel)	*secretary*
Prof. Dr.	Petra Van Mulders (Vrije Universiteit Brussel)	*promotor*
Prof. Dr.	Nick van Remortel (Universiteit Antwerpen)	*promotor*
Prof. Dr.	Wim De Malsche (Vrije Universiteit Brussel)	
Prof. Dr.	Ioana C. Mariş (Université Libre de Bruxelles)	
Dr.	Mathieu Bongrand (Université Paris Sud)	

Cover kindly designed by Isis Van Parijs
Front cover image: top view of the BR2 core,
picture provided by SCK•CEN
Back cover image: inside view of the Phase 1 container

ISBN: 9789493079021
NUR CODE: 910, 926

Printed by:
Crazy Copy Center Productions,
VUB Pleinlaan 2,
1050 Brussel

+32 2 629 33 44
crazycopy@vub.ac.be
www.crazycopy.be

Contents

Introduction

Nuclear reactors are great. They provide us with carbon free energy at a very low cost in (human) lives[1]. They also provide a great opportunity to do physics. Wolfgang Pauli postulated the existence of the neutrino in 1930 in order to explain the electron energy spectrum in beta decays. He is quoted saying "I have done a terrible thing, I have postulated a particle that cannot be detected.". Twenty six years later, Frederick Reines and Clyde Cowan discovered the electron antineutrino at the Savannah River nuclear power plant (Aiken, South Carolina, USA). Another five years later, muon neutrinos were discovered.

Neutrinos are the only elementary particles that do not fit perfectly within the Standard Model, this is the theoretical framework that describes the elementary particles and their interactions. While neutrinos are massless according to the Standard Model, measurements with a variety of neutrino sources between the late 1960's and the early 2000's definitively proved neutrinos have a non-zero mass. As a result of this non-zero mass, a neutrino created in one flavour can be observed as having a different flavour. This process is known as neutrino oscillations. The parameters governing the oscillations between flavours are two mass differences and three mixing angles. These five parameters have all been measured over the last decades. Despite the progress, several anomalies remain to be understood.

One of these anomalies is the so-called reactor antineutrino anomaly. This is the mismatch between predictions from reactor models and observations from reactor neutrino experiments, the calculations predict about three percent more neutrinos than observed. This deficit is observed consistently across experiments located at different reactors and using different detector techniques and operated completely independently. Another deficit, the so-called Gallium anomaly, was observed during the calibration of solar neutrino detectors using a radioactive source. Unlike the reactor anomaly, the Gallium anomaly concerns neutrinos. While one deficit can be due to a wrong prediction, two deficits observed with different particles is a sign of possible underlying new physics. These two anomalies led to the theoretical prediction of the 'sterile neutrino', a new neutrino outside of the Standard Model that, unlike other neutrinos, does not interact with matter.

The SoLid experiment, 'Search for Oscillation with a Lithium 6 detector' in full, is a reactor neutrino experiment located at the BR2 reactor at SCK•CEN in Mol, Belgium. Its goal is to resolve the reactor antineutrino anomaly by observing the signature of the sterile neutrino. The large predicted mass difference between the sterile neutrino and the other neutrinos requires close proximity to the reactor core. With its point of closest approach of 6.2 m, the SoLid detector is the neutrino experiment placed closest to a nuclear reactor in the world.

This thesis gives an overview of my research during the past four years. It starts

[1] These were all the politically charged statements in this thesis.

by introducing the sterile neutrino in Chapter 1 and the two SoLid detectors I worked on as well as the BR2 facility in Chapter 2. Chapters 3 and 4 provide detail on the commissioning of these two detectors: respectively for the SM1 prototype detector and the full scale Phase 1 detector. These two chapters have a focus on neutron detection, key to the reconstruction of antineutrino events, as this is a subject I worked on a lot. Chapter 5 provides a thorough overview of the dominant correlated backgrounds to the Phase 1 detector as well as the first observation of a reactor on excess consistent with antineutrino signals. Finally, Chapter 6 gives an outlook on what is possible with the SoLid detector when improvements are made to the analysis and more data is collected.

Chapter 1

Neutrinos in the Standard Model and beyond

1.1 Neutrinos in the Standard Model

1.1.1 Introduction to the Standard Model

At the smallest scale of things, the world is described by the Standard Model (SM) of particle physics. The SM makes predictions using quantum field theory (QFT) that can then be compared to measurements made at various particle physics experiments world wide. These predictions for the fundamental particles and forces are of such precision that the theory is typically written with capital letters.

An overview of the SM particles and their interactions is given in Figure 1.1. In the left figure, the twelve fermions, i.e. spin 1/2 particles, can be vertically split into three successively heavier generations. Except for the mass of the particles, all generations are identical: two strongly interacting quarks (u, d; c, s; t, b), an electrically charged lepton (e; μ; τ) and an electrically neutral lepton (neutrino, ν_e; ν_μ; ν_τ). The first generation particles are stable. Quarks interact via all fundamental forces, charged leptons via the electromagnetic and the weak force, neutrinos interact only via the weak force. These interactions are shown on the right hand side of Figure 1.1. The spin-1 bosons mediate the fundamental forces. Gluons (g) mediate the strong nuclear force, the $W\&Z$ bosons the weak interaction and photons (γ) the electromagnetic interaction. The Brout-Englert-Higgs (H) boson, a scalar boson, generates the mass of most of the fundamental particles.

1.1.2 Massless neutrinos

As mentioned, neutrinos only interact through the weak nuclear force. In the late 1960's, the weak nuclear force has been unified with the electromagnetic force by Weinberg, Salam and Glashow to form the electroweak theory. For this achievement, they shared the 1979 Physics Nobel Prize [1]. The next paragraphs will delve a bit deeper into the (electro)weak force and SM neutrino masses.

Properties of the weak nuclear force

There are two types of weak interaction: charged current (CC) and neutral current (NC). In CC interactions, one unit of electrical charge and one unit of weak isospin is exchanged apart from energy and momentum, e.g. for the decay of a muon: $\mu^- \rightarrow$

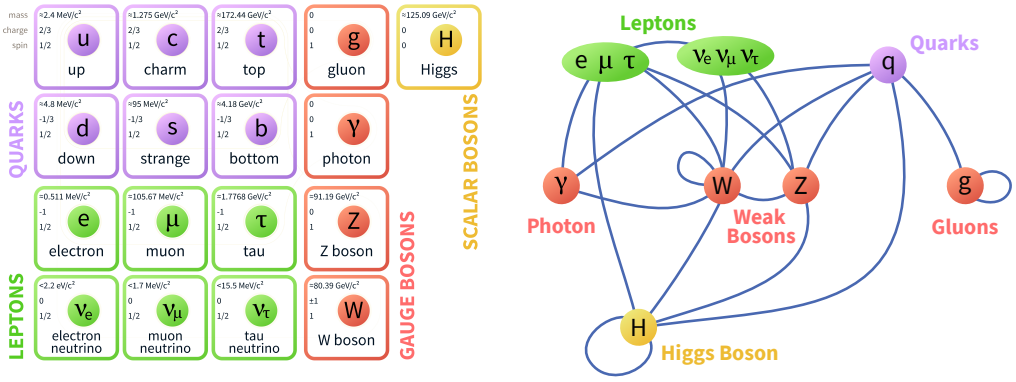

Figure 1.1: Schematic overview of all known particles (left) and interactions (right) included in the Standard Model.

$e^- + \nu_\mu + \bar{\nu}_e$. NC interactions only transfer energy and momentum, leading to e.g. elastic scattering of neutrinos on nuclei. CC interactions are mediated by the charged W boson, NC interactions by the neutral Z boson [2].

CC interactions only couple to left handed (LH) particles, neutral current interactions couple to both chiralities, but stronger to LH than right handed (RH) particles. For antiparticles, this is reversed: CC couples only to RH antiparticles and NC couples stronger to RH than LH antiparticles. This is encoded into the electroweak theory by placing LH particles in weak isospin doublets and RH particles in singlets. The lepton singlets and doublets are listed in Equation 1.1.

$$\begin{pmatrix} \nu_e \\ e^- \end{pmatrix}_L, \quad \begin{pmatrix} \nu_\mu \\ \mu^- \end{pmatrix}_L, \quad \begin{pmatrix} \nu_\tau \\ \tau^- \end{pmatrix}_L \quad , \quad e^-_R, \quad \mu^-_R, \quad \tau^-_R \tag{1.1}$$

As can be seen from Equation 1.1, RH neutrinos are not included in the SM [2].

Standard Model neutrino mass

Particle masses are generated in various ways in the SM. For the massive gauge bosons (i.e. $W^\pm$ and Z), this is done via the Brout-Englert-Higgs mechanism (for which Francois Englert and Peter Higgs received the Physics Nobel Prize in 2013 [3], Robert Brout died in 2011). Fermions receive masses in the SM by adding a term of the form

$$m\bar{\psi}\psi = m\left(\bar{\psi}_L\psi_R + \bar{\psi}_R\psi_L\right) \tag{1.2}$$

in the Lagrangian. In Equation 1.2, m is the fermion mass and ψ is the fermion field with its RH and LH components. An implicit requirement for adding a mass term in the Lagrangian is the existence of both right and left handed particles. It is clear that this equation will always return zero if either of the two spinor components is not included. Since RH neutrinos and LH antineutrinos are not included in the SM, neutrinos are massless in this framework.

1.2 Neutrinos beyond the Standard Model

1.2.1 Neutrino oscillations

In the 1960's Raymond Davis came up with an experiment to study the inner workings of the sun, the Homestake Experiment. A big tank with chlorine was placed deep in the

Homestake gold mine (Lead, South Dakota, USA) to observe neutrinos coming from the fusion processes that power the sun. With a neutrino detection threshold of 814 keV, detection of the 862 keV neutrinos from ^{7}Be cycle was possible. From other observations, it was well known how much neutrinos were expected. The experiment however only measured roughly one third that number [4, 5]. As a follow up on the Homestake experiment, several gallium based detectors were built (GNO, GALLEX, SAGE). These detectors had a lower energy threshold than the Homestake experiment (233 keV, giving access to pp-cycle neutrinos) and had the advantage that they could be calibrated with a radioactive source. The three mentioned experiments consistently measured slightly more than half the expected rate [5]. In 1987, KamiokaNDE (initially Kamioka nucleon decay experiment, later Kamioka neutrino detection experiment) started measuring the more energetic solar neutrinos using a water Cherenkov detector (with a $\sim$7 MeV detection threshold) in the Mozumi Zinc mine (Kamioka, Japan). They too measured a deficit, measuring roughly half the predicted value [4, 5].

All these experiments were working with the same model of the sun, the differences in the observed deficits suggested the solar model was not to blame. Since the Cherenkov effect was well understood, the detection principles were not to blame either. What was missing was an understanding of the physics of the messenger, neutrinos. In 1998, the SuperK collaboration (an upgraded version of KamiokaNDE) provided first evidence for neutrino oscillations using neutrinos produced in cosmic ray interactions with the atmosphere all over the world. Four years later, the SNO collaboration irrefutably proved the existence of neutrino oscillations, explaining the deficit of all previous experiments by measuring solar neutrinos in three channels at the same time: through CC interactions (only sensitive to ν_e), through NC interactions (equally sensitive to all flavours) and through elastic scattering (sensitive to all flavours, but more to ν_e than ν_μ and ν_τ). Combination of these channels allows determination of the total ν flux (ϕ_{NC}) and the fraction of electron neutrinos that remains (ϕ_{CC}/ϕ_{NC}) [6]. Neutrino oscillations are only possible when neutrinos have a non-zero mass, providing evidence for 'beyond the SM' physics[1]. Therefore, the observation by SNO led to the Physics Nobel Prizes in 2002 (Davis and Koshiba, the driving force behind KamiokaNDE) and 2015 (Kajita, Koshiba's successor at KamiokaNDE, and McDonald, the mind behind SNO) [7, 8].

Neutrino oscillations require both mass and a difference between the flavour and mass eigenstates. The flavour eigenstates are those listed in Figure 1.1: ν_e, ν_μ and ν_τ (collectively ν_α), neutrinos interact through the flavour eigenstates. When propagating through space-time, neutrinos are in their mass eigenstate: ν_1, ν_2 and ν_3, collectively denoted as ν_i. Transformation between the two different eigenstates happens via the PMNS[2] matrix:

$$\begin{pmatrix}\nu_e\\ \nu_\mu\\ \nu_\tau\end{pmatrix} = \begin{pmatrix}U_{e1} & U_{e2} & U_{e3}\\ U_{\mu1} & U_{\mu2} & U_{\mu3}\\ U_{\tau1} & U_{\tau2} & U_{\tau3}\end{pmatrix}\begin{pmatrix}\nu_1\\ \nu_2\\ \nu_3\end{pmatrix} \tag{1.3}$$

The superposition of the various flavour eigenstates that make up the mass eigenstates can be generated by inverting this relation [5].

In Equation 1.3, the mass eigenstate neutrinos ν_i are listed according to their ν_e content where ν_1 has most and ν_3 has least ν_e contribution. This implies that $|U_{e1}| > |U_{e2}| > |U_{e3}|$, but not that $m_1 > m_2 > m_3$. This ordering of the mass eigenstates has

[1] "Up to now, this is the only proven 'beyond the Standard Model' physics known to humanity" – A. de Gouvêa, 7/08/2017

[2] Pontecorvo, Maki, Nakagawa and Sakata

no implications on the relative masses of each of the ν_is, it leaves six possible orderings of m_1, m_2 and m_3.

Two neutrino approximation

In a two neutrino system (with flavour eigenstates ν_α and ν_β and mass eigenstates ν_1 and ν_2), Equation 1.3 simplifies to

$$\begin{pmatrix}\nu_\alpha\\ \nu_\beta\end{pmatrix} = \begin{pmatrix}U_{\alpha 1} & U_{\alpha 2}\\ U_{\beta 1} & U_{\beta 2}\end{pmatrix}\begin{pmatrix}\nu_1\\ \nu_2\end{pmatrix} \tag{1.4}$$

and, for the $SU(2)$ group, can be rewritten as

$$\begin{pmatrix}\nu_\alpha\\ \nu_\beta\end{pmatrix} = \begin{pmatrix}cos\theta & sin\theta\\ -sin\theta & cos\theta\end{pmatrix}\begin{pmatrix}\nu_1\\ \nu_2\end{pmatrix}. \tag{1.5}$$

The superposition then becomes

$$|\nu_\alpha\rangle = cos\theta\,|\nu_1\rangle + sin\theta\,|\nu_2\rangle \tag{1.6}$$
$$|\nu_\beta\rangle = -sin\theta\,|\nu_1\rangle + cos\theta\,|\nu_2\rangle \tag{1.7}$$

The propagation of a particle, in this case a neutrino, is described by $|\nu_i(t)\rangle = e^{-iE_it}\,|\nu_i(0)\rangle$, where E_i is the energy of ν_i. When applying this to one of the flavour eigenstates, this becomes

$$|\nu_\alpha(t)\rangle = cos\theta\, e^{-iE_1t}\,|\nu_1(0)\rangle + sin\theta\, e^{-iE_2t}\,|\nu_2(0)\rangle \tag{1.8}$$

The probability of finding a different flavour, a so-called appearance, after a time t is given by

$$P_{\nu_\alpha\to\nu_\beta}(t) = |\langle\nu_\beta(t)|\nu_\alpha(0)\rangle|^2 = sin^2(2\theta)\,sin^2\left(\frac{E_2-E_1}{2}t\right) \tag{1.9}$$

Neutrino oscillations are typically not measured in terms of time since their creation but rather as the distance, L, they travelled. Since neutrinos are very light, even the lowest energies make them relativistic. Einstein's mass energy equivalence [9] extended with momentum p can be approximated as $E_i = p_i + m_i^2/2E_i$. Due to the relativistic speed, velocity v can be approximated as the speed of light c and $t = c/L$ can applied. Assuming $p_i = p_j$, the above formula transforms to

$$P_{\nu_\alpha\to\nu_\beta}(E[\mathrm{GeV}], L[\mathrm{km}]) = sin^2(2\theta)\,sin^2\left(1.27\frac{\Delta m_{21}^2 L}{E}\right) \tag{1.10}$$

where $\Delta m_{21}^2 = m_2^2 - m_1^2$ is the squared mass difference. For disappearance, the probability a neutrino keeps the same flavour, the above formula simply becomes

$$P_{\nu_\alpha\to\nu_\alpha}(E[\mathrm{GeV}], L[\mathrm{km}]) = 1 - sin^2(2\theta)\,sin^2\left(1.27\frac{\Delta m_{21}^2 L}{E}\right) \tag{1.11}$$

in the case of a two neutrino system.

Three neutrino oscillation

Doing a similar exercise leads to the following expression for the oscillation probability of an (anti)neutrino of flavour α to flavour β:

$$P\left(\overset{(-)}{\nu}_\alpha \rightarrow \overset{(-)}{\nu}_\beta\right) = \sum_j \left|U_{\beta j}\right|^2 \left|U_{\alpha j}\right|^2 + 2\sum_{j>k} \left|U_{\beta j}U^*_{\alpha j}U_{\alpha k}U^*_{\beta k}\right| cos\left(\frac{\Delta m^2_{jk}}{2E}L \mp \phi_{\beta\alpha;jk}\right) \quad (1.12)$$

with $\phi_{\beta\alpha;jk} = arg\left(U_{\beta j}U^*_{\alpha j}U_{\alpha k}U^*_{\beta k}\right)$. In case of antineutrinos, the argument in the cosine is $+\phi$; for neutrinos, one has to use $-\phi$ [5].

Notice that the absolute masses of the neutrinos do not come into play in the oscillation formulae, only the squared mass differences Δm^2_{jk} do. On top of that, the squared mass splitting is within a sine squared function for the two neutrino approach, so oscillation experiments are only sensitive to the absolute value of the mass splitting. The neutrino mass hierarchy is therefore hidden to first order.

1.2.2 Results from oscillation experiments

For three neutrinos with different mass, there are three squared mass differences. From resonance effects in the sun, it was found that m_1 and m_2 are close together and that $m_1 < m_2$. Oscillations of atmospheric neutrinos indicated the mass difference between m_3 and the other masses was rather large. As a result, $\left|\Delta m^2_{21}\right|$ is so small compared to $\left|\Delta m^2_{31}\right|$ and $\left|\Delta m^2_{32}\right|$ that these last two are taken as equal. Two mass hierarchies remain: normal ($m_1 < m_2 < m_3$) and inverted ($m_3 < m_1 < m_2$). Due to the large difference in squared mass splittings, there is relatively little interference between oscillations caused by the large squared mass differences and oscillations caused by the small squared mass difference. The matrix in Equation 1.3 is therefore often parametrized as three submatrices, each describing a two neutrino oscillation system, i.e.

$$U_{PMNS} = \underbrace{\begin{pmatrix} 1 & 0 & 0 \\ 0 & c_{23} & s_{23} \\ 0 & -s_{23} & c_{23} \end{pmatrix}}_{\text{Athmospheric}} \overbrace{\underbrace{\begin{pmatrix} c_{13} & 0 & s_{13}e^{-i\delta_{CP}} \\ 0 & 1 & 0 \\ -s_{13}e^{-i\delta_{CP}} & 0 & c_{13} \end{pmatrix}}_{\text{Reactor}}}^{\text{Accelerator}} \underbrace{\begin{pmatrix} c_{12} & s_{12} & 0 \\ -s_{12} & c_{12} & 0 \\ 0 & 0 & 1 \end{pmatrix}}_{\text{Solar}} \quad (1.13)$$

The notation s_{ij} and c_{ij} indicate respectively the sine and cosine of mixing angle θ_{ij} between state i and j. Also made explicit is the Dirac CP-violating phase δ_{CP}.

Neutrino oscillation experiments can be classified in four categories: accelerator, reactor, atmospheric and solar neutrino experiments. Each of these types has a specific region of L/E and a specific set of reactions they can probe. As shown in Equation 1.13, the L/E ratio defines the oscillation an experiment is sensitive to.

Solar neutrino experiments have an enormous baseline (150 million km) and relatively low energy, resulting in an L/E of $\sim 2.8 \cdot 10^{10}$ km/GeV. It is not this extreme value which allows solar experiments to probe Δm^2_{21} and θ_{21}, the sensitivity to these parameters comes from resonance effects within the sun due to its high density. The solar neutrino energy is well below the muon and tau production threshold, allowing only detection of ν_e disappearance in the CC channel and $\nu_e \rightarrow \nu_\alpha$ appearance via NC.

The first values were published by the SNO collaboration in 2001. Earlier experiments could not determine these values since they had no handle on the energy (radiochemical) or had no access to NC interactions (Super-KamiokaNDE). Contemporary solar neutrino experiments (kamLAND, Borexino, Super-KamiokaNDE) were able to refine the values measured by SNO.

Reactor neutrino experiments have a relatively small neutrino energy window up to ~ 10 MeV for $\bar{\nu}_e$ coming from isotopes undergoing fission in the core of a nuclear reactor, again allowing only $\bar{\nu}_e \to \bar{\nu}_e$ disappearance through CC interactions and $\bar{\nu}_e \to \bar{\nu}_\alpha$ appearance via NC interactions. So far, there are no known ways to detect NC interactions from reactor antineutrinos, the only realistic way is via the CC inverse beta decay process (IBD):

$$\bar{\nu}_e + p \to n + e^+ \tag{1.14}$$

Since the particles on the right hand side of this reaction are more massive than the left hand side, the neutrino detection energy window is reduced to between 1.8 and 10 MeV. Picking the correct position for the detector allows fixing the L/E window to a particular value that an experiment can probe. This allows measurement of θ_{13} and put constraints on δ_{CP} when combined with data from accelerator experiments. A more in depth analysis of nuclear reactors and the neutrino production process will be given in Section 1.3.3.

Atmospheric neutrino experiments have an enormous L/E range, caused by both the range in baseline and energy. This allows atmospheric neutrino experiments to measure $\left|\Delta m^2_{31}\right|$ and θ_{23}. These parameters can also be measured with **accelerator neutrino experiments**, they have a fixed baseline and a very well understood and narrow energy spectrum; the L/E range for a single accelerator experiment is limited but carefully chosen. Both atmospheric and accelerator experiments can probe a wide range of oscillations and have access to a multitude of detection techniques. Accelerator experiments have a better handle on the pre-oscillation flavour, which allows for better constraining $\left|\Delta m^2_{31}\right|$ and θ_{23} than with atmospheric experiments. Accelerator experiments can determine a convolution of δ_{CP} and θ_{13} to great accuracy. Using input from (future) reactor experiments, δ_{CP} can be heavily constrained. They can also resolve the hierarchy problem.

All data from these experiments is combined in a **global best fit** [10]. When all mixing parameters (three angles, two squared mass splittings and δ_{CP}) are left free to explain all appearance and disappearance results of all flavours at all available energies and distances as good as possible, the values listed in Table 1.1 are found. Since the mass hierarchy is not yet known, two values are presented for each parameter.

1.3 Anomalies and open questions

There are a number of open questions on neutrinos, these are summarized in this section. First, the unknown fundamental properties of neutrinos will be discussed. Next, a number of anomalies in the measurements will be presented.

1.3.1 Fundamental neutrino properties

Dirac or Majorana

The oscillation experiments have proven that at least two of the three neutrinos are massive while the SM assumes neutrinos to be massless. The SM has to be modified to

Parameter	best fit ($\pm 1\sigma$)	
	normal hierarchy	inverted hierarchy
Δm^2_{21} $\left[10^{-5}\text{eV}^2\right]$	$7.40^{+0.21}_{-0.20}$	$7.40^{+0.21}_{-0.20}$
Δm^2 $\left[10^{-3}\text{eV}^2\right]$	$+2.494^{+0.33}_{-0.031}$	$-2.465^{+0.32}_{-0.031}$
$sin^2\theta_{12}$	$0.307^{+0.013}_{-0.012}$	$0.307^{+0.013}_{-0.012}$
$sin^2\theta_{23}$	$0.538^{+0.033}_{-0.069}$	$0.554^{+0.023}_{-0.033}$
$sin^2\theta_{13}$	$0.02206^{+0.00075}_{-0.00075}$	$0.02227^{+0.00074}_{-0.00074}$
δ_{CP}/π	$2.04^{+0.38}_{-0.27}$	$2.42^{+0.18}_{-0.17}$

Table 1.1: Neutrino mixing parameters according to the global best fit. Δm^2 is defined as Δm^2_{31} in the normal hierarchy and Δm^2_{32} for the inverted hierarchy [10].

accommodate these masses and there are two dominant proposals to do so. Neutrinos are Dirac particles, like all other fermions, or, neutrinos are Majorana particles, being their own antiparticles. A combination of both is theoretically also possible.

In the Dirac case, RH neutrinos, ν_R, are added to the SM and a mass term is introduced as for all other fermions. When filling in Equation 1.2 with neutrino fields, this becomes

$$m_d \bar{\nu}_d \nu_d = m_d \left(\bar{\nu}_L \nu_R + \bar{\nu}_R \nu_L\right) \tag{1.15}$$

where the subscript d indicates coupling of the neutrinos to a Higgs doublet. The mass m_d can be generated via coupling to vacuum expectation value of a Higgs doublet. Coupling to the weak scale, 246 GeV, requires the coupling to be very small, e.g. 10^{-14} for $m_\nu = 1$ meV, which is disfavoured by theoretical physicists [11]. It should be noted that since RH neutrinos do not interact via the weak force in the SM, ν_R is considered 'sterile' in this model.

In the Majorana case, no new particles are added, it is assumed that neutrinos and their charge conjugate are identical: $\nu_R = \nu_R^C$. This is not possible for the charged leptons and quarks, but is not excluded for the chargeless neutrinos. Adding mass in the Majorana case is similar to the Dirac case, but two cases arise: one for the 'active' flavours ($\mathcal{L}_t$) that interact in the SM and one for the 'sterile' flavours ($\mathcal{L}_s$) that do not.

$$-\mathcal{L}_t = \frac{m_L}{2}\left(\bar{\nu}_L \nu_R^C + \bar{\nu}_R^C \nu_L\right) = \frac{m_L}{2}\left(\bar{\nu}_L C \bar{\nu}_L^T + \nu_L^T C \nu_L\right) = \frac{m_L}{2}\bar{\nu}_M \nu_M \tag{1.16}$$

$$-\mathcal{L}_s = \frac{M_R}{2}\left(\bar{\nu}_L^C \nu_R + \bar{\nu}_R \nu_L^C\right) = \frac{M_R}{2}\left(\bar{\nu}_L C \bar{\nu}_L^T + \nu_L^T C \nu_L\right) = \frac{M_R}{2}\bar{\nu}_{M_s} \nu_{M_s} \tag{1.17}$$

m_L can be generated by a coupling to a Higgs triplet (hence the subscript t), either with a small coupling or a small vacuum expectation value of the Higgs triplet. The generation of M_R depends on the theory. Equations 1.16 and 1.17 are both creation and annihilation terms, violating lepton number by two units [5, 11].

Probing the Dirac or Majorana nature of neutrinos is done using the creation-annihilation property in neutrinoless double beta decay experiments. A limited number of isotopes undergo double beta decay, emitting two electrons and two neutrinos. If neutrinos are Majorana particles and therefore their own antiparticle, the two neutrinos can annihilate inside the nucleus. This would leave only the electrons to carry away all the energy, resulting in a peak in the spectrum at the Q-value of the decay.

Mass hierarchy

As mentioned in Section 1.2.2, there are two allowed 'neutrino mass hierarchies': the normal and the inverted hierarchy. In theory, oscillation experiments are sensitive to the sign of Δm^2_{32} through the interference terms in the three neutrino oscillation model. In practice, a very good energy resolution and high statistics are required in order to resolve the effect this interference causes. Several experiments plan to resolve the hierarchy problem using a variety of sources and detection techniques. Examples are the JUNO (reactor), T2K (accelerator), NOνA (accelerator), DUNE (accelerator and atmospheric), PINGU (atmospheric), ORCA (atmospheric), Hyper-K (atmospheric) experiments [12].

Absolute neutrino mass

Even when the mass hierarchy is resolved, the absolute values of the neutrino masses remain hidden. To perform a neutrino mass measurement, a different type of experiment is needed. One option is to determine the neutrino mass by observing a deflection at the end of the electron energy spectrum in beta decay. This is the aim of experiments looking at tritium decay (KATRIN, Project 8) or electron capture on holmium 163 (ECHo, HOLMES, NuMECS). Also neutrinoless double beta decay experiments (kamLAND-ZEN, SNO+, CUORE, PandaX, EXO200) are sensitive to the deflection in the electron energy spectrum [13, 14].

1.3.2 Anomalies in neutrino data

There are a number of anomalies observed in the measurements performed by neutrino experiments. The most prominent ones are the LSND/MiniBooNE anomaly, the Gallium anomaly and the reactor antineutrino anomaly. The Gallium and LSND/MiniBooNE anomalies will be briefly introduced here, the reactor antineutrino anomaly will be discussed in more detail in the next section. Another anomaly in the data of reactor experiments is the observation of an excess in the visible positron energy spectrum at 5 MeV. This will also be discussed in the next section.

The LSND/MiniBooNE anomaly

The LSND experiment was designed in 1989 to detect neutrino oscillations from $\bar{\nu}_\mu$ to $\bar{\nu}_e$. The mineral oil (CH_2) detector was placed 30 m from the neutrino production site, a beamdump at the Los Alamos National Laboratory (Los Alamos, New Mexico, USA). The beam consists of 95% $\bar{\nu}_\mu$ from decay at rest (DaR) μ^+ particles created in π^+ decay and 5% ν_μ from π^+ decaying in flight (DiF)[3]. DaR antineutrinos have a well known energy spectrum up to 52.8 MeV, the 'Michel' electron energy spectrum from muon decay. Due to the low number of events and the large systematic uncertainties, DiF neutrinos were used as a cross check for the DaR analysis. $\bar{\nu}_\mu \to \bar{\nu}_e$ oscillations were detected via the $\bar{\nu}_e + p \to e^+ + n$ and $\bar{\nu}_e + {}^{12}\mathrm{C} \to e^+ + X$ interactions, while $\nu_\mu \to \nu_e$ oscillation were detected via $\nu_e + {}^{12}\mathrm{C} \to e^- + X$. The LSND collaboration observed an excess of $51.8^{+18.7}_{-16.9} \pm 8.0$ $\bar{\nu}_e$ events and $18.1 \pm 6.6 \pm 4.0$ ν_e events. A competing experiment, KARMEN, performed a similar measurement at a shorter baseline and did not find an excess [11, 16, 17].

[3] No kaons were produced since the 800 MeV proton beam is well below the 3.2 GeV center of mass energy required for kaon production [15].

The MiniBooNE experiment was designed to investigate the LSND excess. It performed measurements at the same L/E ratio of $\sim$ 1m/MeV using a neutrino beam with ten times the LSND $\bar{\nu}$ energy and with the detector placed ten times further from the source. For these higher neutrino energies, DiF of pions and kaons is required. To focus the (anti)neutrino beam, a focussing horn is placed downstream from the proton target. It focusses the pions and kaons into the decay tunnel where the neutrinos are created with a forward boost. Such a horn can only focus either positively or negatively charged particles, diffusing the other sign particles; this allows the MiniBooNE experiment to operate in either neutrino or antineutrino mode. Initially, the MiniBooNE experiment confirmed the LSND excesses only below 475 MeV in neutrino mode and over the entire energy range (200 to 1250 MeV) in antineutrino mode [11]. After collecting more data, an excess consistent with the LSND result was observed over the entire energy range in both neutrino and antineutrino mode. The combined significance of the LSND (3.8σ) and MiniBooNE (4.8σ) excess is 6.1σ [18].

The Gallium anomaly

The solar experiments mentioned earlier in Section 1.2.1 used intense ^{51}Cr and ^{37}Ar sources for calibration. Both sources predominantly decay via electron capture with neutrino energies less than 1 MeV (90% 0.75 MeV, 10% 0.43 MeV for ^{51}Cr and 100% 0.81 MeV for ^{37}Ar), making them ideal sources to calibrate a gallium solar neutrino detector. Calibration was performed by placing a source inside the detector and reading out the detector after some time. Due to the half life of the sources, a shorter run time was used in the calibration campaign than in data taking mode, which was the only difference between calibration and physics data taking. The calibration result is obtained by comparing the measured and expected number of neutrinos, where the expected number can be calculated from the known source activity. The combined calibration result yielded 0.86 ± 0.05, a 2.8σ deviation from unity and a 14% deficit [19–21].

1.3.3 The reactor antineutrino anomaly

Nuclear reactors 'burn' fissile isotopes such as ^{235}U or ^{239}Pu. Both ^{235}U and ^{239}Pu naturally decay via alpha decay, they have half lives of respectively $70.4 \cdot 10^6$ and $24.1 \cdot 10^3$ years. In a nuclear reactor, the fuel is bombarded with neutrons, causing it to undergo fission. In the fission process, the mother isotope breaks up into two daughters and a number of neutrons, on average 2.4 neutrons for ^{235}U and 2.9 for ^{239}Pu [22]. It is crucial to balance the number of neutrons emitted and absorbed by fissile isotopes. When on average more than 1 neutron is captured per fission, the number of atoms undergoing fission will grow exponentially, turning the reactor into a nuclear bomb.

Neutrinos are not produced directly in the fission process, they are the result of beta emissions in the decay chains of the unstable daughter isotopes. On average, there are 1.92 neutrinos produced above the IBD threshold per fission for ^{235}U and 1.45 for ^{239}Pu [23]. There are thousands of possible beta decays for every fissile isotope, the emitted neutrino energy spectrum is a combination of all the energy spectra of these decays. Predicting this spectrum is typically done via either *ab initio* calculations or *electron conversion* [24]. The electron spectrum conversion method consists of taking a measured electron energy spectrum from a thin foil of fissile material exposed to a thermal neutron flux and connecting it to a neutrino energy spectrum. In the ab initio method, the spectrum is obtained by making the sum of all beta decay spectra. This requires adding all possible decay chains of all fission daughters, weighted according to

their branching fractions and the fuel composition. All information that goes into this calculation comes out of nuclear databases. The ab initio method allows for creation of both the neutrino and electron spectrum for a fissile isotope. The quality of the generated neutrino spectrum can thus be checked by comparing the generated electron spectrum to a measured spectrum, i.e. the spectra used for the electron conversion method.

Due to the great difficulty of performing an ab initio calculation and the existence of only one qualitative set of electron spectra (measured in 1982 by Schreckenbach *et al.* in the ILL research reactor in Grenoble, France), there are only very few calculations of the reactor neutrino energy spectrum. Until 2011, the most often used spectra were electron conversion spectra calculated by Schreckenbach *et al.* in 1985 (^{235}U) and 1989 (^{241}Pu and ^{230}Pu) based on the 1982 electron spectrum[4] [25–27]. In 2011, Mueller *et al.* published a new set of calculations, based on the ab initio approach and verified against the 1982 data [24]. While the shape of the two predicted neutrino energy spectra is the same, there is a three percent increase in the normalization of the neutrino flux. As a result of this renormalization of the predicted flux, the expected to observed $\bar{\nu}_e$ ratio moved from 0.976 ± 0.024 to 0.934 ± 0.024 for experiments with a baseline of less than 1000 m, a 2.7σ deficit. This deficit, shown in Figure 1.2 for the various experiments at different distances from the reactor, is known as the reactor antineutrino anomaly (RAA) [28–30]. An analysis of the antineutrino rate as a function of the fissile isotope by Daya Bay indicates the deficit is due to ^{235}U [31].

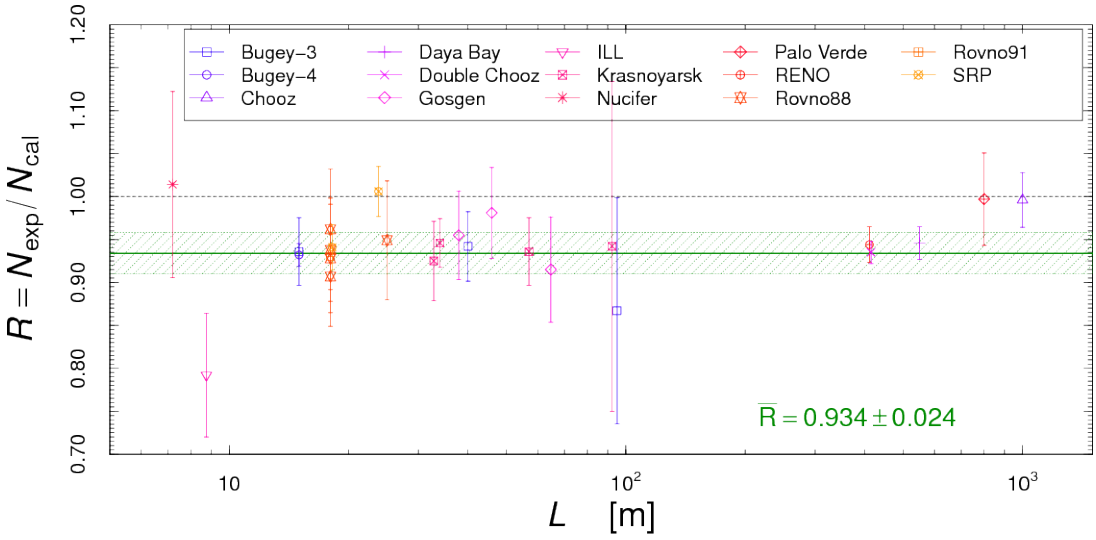

Figure 1.2: The ratio of the measured to the predicted number of reactor neutrinos as a function of the distance (baseline) from the reactor. Results are given for all short (< 1 km) baseline experiments [29].

The 5 MeV bump

When measuring θ_{13}, reactor experiments avoided most of the uncertainties coming from the neutrino flux by using identical near and far detectors and studying the ratio of the observed neutrinos in the near and far detectors. However, analysis of the absolute energy spectra revealed an excess in antineutrino events with a visible energy of roughly 5 MeV. The result is shown for three current reactor experiments in Figure 1.3. Moreover, the size of the excess has been shown to scale with the reactor power [32].

[4]Since there was no ^{238}U measurement, no spectrum was calculated for ^{238}U.

Oddly, the older Bugey3 experiment did not measure an excess over the predicted spectrum at this energy [33].

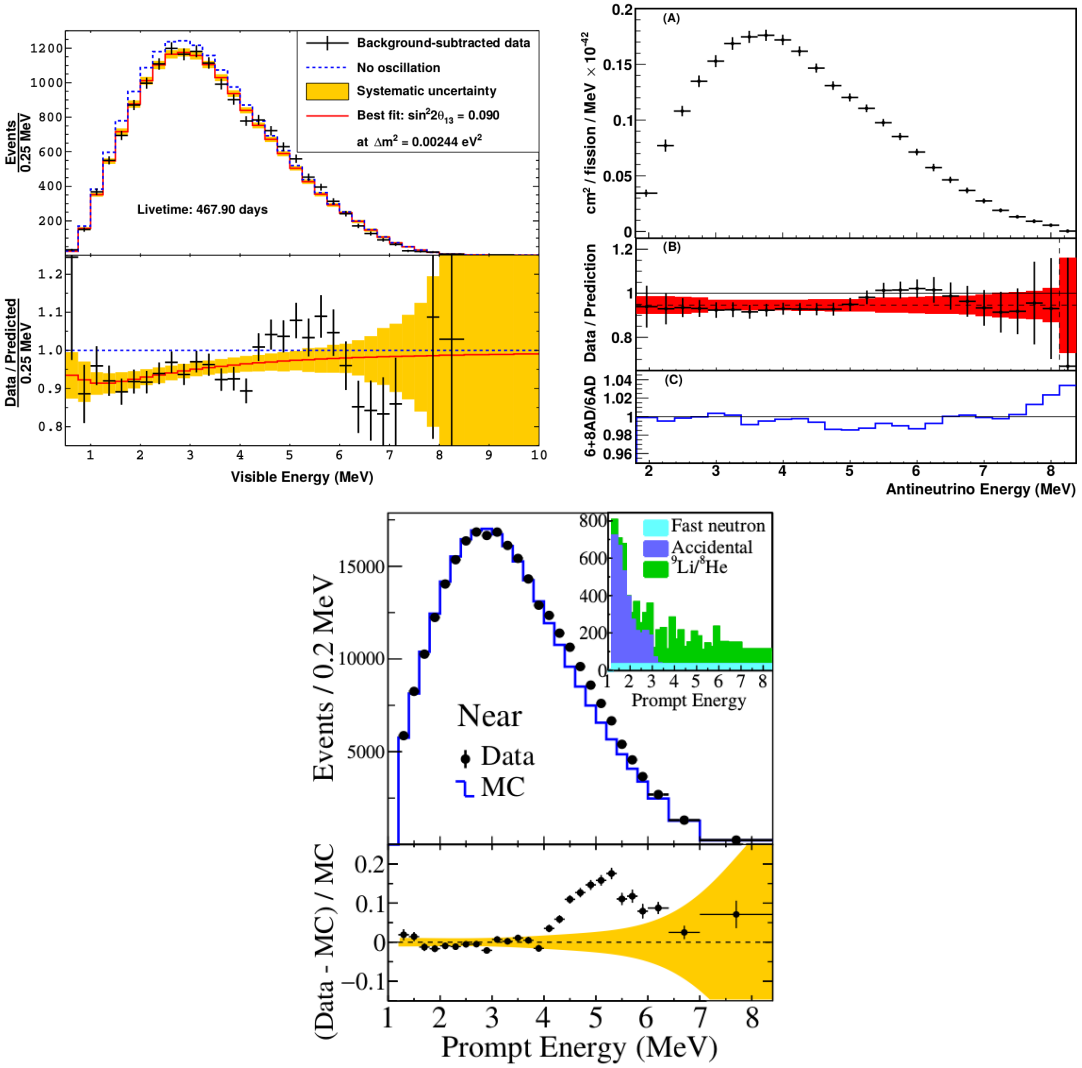

Figure 1.3: Comparison of the observed and expected IBD positron or antineutrino energy spectra by Double Chooz (top left) [34], Daya Bay (top right) [35] and RENO (bottom) [32]. For all experiments, the deviation from the expectation is larger than the uncertainty (shaded bands).

1.4 The sterile neutrino hypothesis

The anomalies presented in the previous sections are either caused by problems in the predictions or measurements or by the presence of new physics. An example of new physics is the introduction of a new neutrino flavour which would lead to additional oscillations, explaining the deficits and excesses of the anomalies discussed in Section 1.3. However, measurements at the LEP collider in the 1990's showed that there are exactly three active light neutrinos, as can be seen in Figure 1.4. Hence, adding another active light neutrino would clearly contradict this measurement. Adding a new neutrino is possible if it does not interact via any of the forces in the SM, making it 'sterile' (ν_s). Introduction of such a sterile neutrino adds a new massive neutrino ν_4 and makes

the PMNS matrix a 4×4 matrix, introducing eight new parameters to the oscillation system. The four matrix elements related to the mixing of ν_s (U_{s1}, U_{s2}, U_{s3}, U_{s4}) can not be probed by experiments, leaving four new parameters: U_{e4}, $U_{\mu 4}$, $U_{\tau 4}$ and m_{ν_4}. Measuring the new oscillation parameters could provide insight or the solution to the reactor, Gallium and LSND/MiniBooNE anomalies.

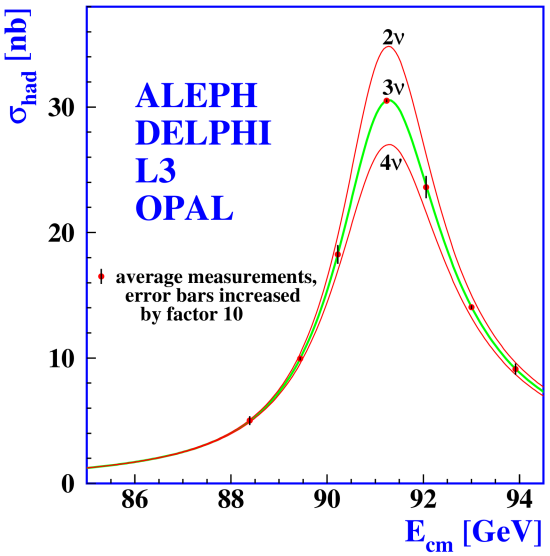

Figure 1.4: Measurement to the invisible cross section of the Z boson. Shown are the predictions for 2, 3 and 4 active neutrinos and the measured cross section allowing for neutrinos with a mass up to 40.19 GeV. The best fit to the data is at 2.9840 ± 0.0082 active neutrinos lighter than 40.19 GeV [36].

For the reactor and Gallium anomalies, i.e. disappearance of $\bar{\nu}_e$ and ν_e, only two new parameters are relevant, m_{ν_4} and U_{e4}. In a two neutrino approximation, these parameters are directly related to Δm^2_{14} and $sin^2\left(2\theta_{ee}\right)$ (Equation 1.18). A fit to all globally available data, indicating what combination of parameter values has been scanned an excluded by the various experiments and what combinations are still allowed, results in a best fit of $\Delta m^2_{41} = 1.7$ eV^2 and $sin^2\left(2\theta_{ee}\right) = 0.066$ or $\Delta m^2_{41} = 1.29$ eV^2 and $sin^2\left(2\theta_{ee}\right) = 0.0089$, depending on the experimental results included in the analysis. This is shown in Figure 1.5, both publications use methods very similar to those discussed in Sections 2.3.1 and 2.3.2. Constraints to the allowed regions come from various experiments sensitive to ν_e and $\bar{\nu}_e$ disappearance which did not observe the reactor and gallium anomaly deficits [29, 37].

To explain the LSND and MiniBooNE anomalies (i.e. appearance of ν_e and $\bar{\nu}_e$ in ν_μ and $\bar{\nu}_\mu$ beams) with a sterile neutrino, two of the new matrix elements are involved: U_{e4} and $U_{\mu 4}$. To resolve these appearance anomalies, constraints on the matrix elements have to be taken into account: U_{e4} is constrained by the values found in the reactor and Gallium anomalies, $U_{\mu 4}$ by the lack of a ν_μ or $\bar{\nu}_\mu$ disappearance anomaly. In order to determine the best values for all four new mixing parameters, including $U_{\tau 4}$, another global fit is performed to all available data, including experiments that did not see any anomalous behaviour ('Glo17' [5]). From the matrix elements relevant to the

[5]Results from the following experiments are included in the 'Glo17' dataset: Reactor experiments: Bugey-3, Bugey-4, Chooz, Daya Bay, Double Chooz, Gosgen, ILL, Krasnoyarsk87, Krasnoyarsk94, Krasnoyarsk99, NEOS, Nucifer, Palo Verde, RENO, Rovno88, Rovno91, SRP. Other experiments: BNL-E776, CDHSW, ICARUS, IceCube, KARMEN, LSND, MiniBooNE, MINOS, NOMAD, OPERA, SciBooNE-MiniBooNE

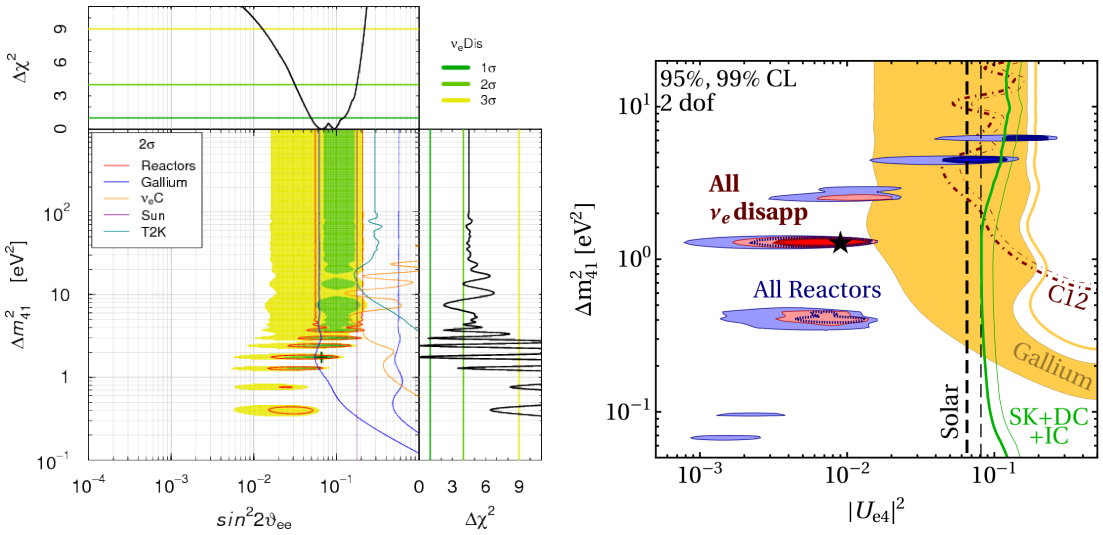

Figure 1.5: Allowed regions in the $sin^2(2\theta_{ee}) - \Delta m^2_{41}$ plane from global ν_e and $\bar{\nu}_e$ disappearance data for a global analysis by Giunti *et al.* (left) [29] and Kopp *et al.* (right) [37]. The best-fit points are indicated as a '+' (left) and a '⋆' (right). Differences between the two figures are related to differences in the available datasets at the time of publication.

LSND/MiniBooNE anomaly, three mixing angles can be obtained:

$$\begin{aligned} sin^2(2\theta_{e\mu}) &= 4\,|U_{e4}|^2\,|U_{\mu 4}|^2 \\ sin^2(2\theta_{ee}) &= 4\,|U_{e4}|^2\left(1-|U_{e4}|^2\right) \\ sin^2(2\theta_{\mu\mu}) &= 4\,|U_{\mu 4}|^2\left(1-|U_{\mu 4}|^2\right) \end{aligned} \tag{1.18}$$

Figure 1.6 shows the allowed regions of the global fit for the squared mass splitting as a function of each of these mixing angles. Also shown are the 3σ allowed regions of the individual appearance ('App') and disappearance ('ν_α Dis') and combined disappearance ('Dis') anomalies in the global fit. The global best fit values relevant for RAA, shown in the middle panel of Figure 1.6, correspond to $\Delta m^2_{41} = 1.7$ eV^2 and $sin^2(2\theta_{ee}) = 0.080$ [29]. It is clear that there is great tension between appearance data from LSND and MiniBooNE and all other data, suggesting the sterile neutrino hypothesis might be false.

Additionally, the oscillation probability of a neutrino only depends on its energy and on the distance travelled before it is detected. It does not depend on the source. The fact that Daya Bay observes a fission fraction dependence in the amplitude of the deficit, a larger ^{235}U fission fraction results in a larger deficit, further suggests the sterile neutrino hypothesis might be false [31].

It is worth noting that other extensions to the SM are possible as well, these extensions include more than one sterile neutrino, e.g. 3+2 or 3+3 scenarios. These scenarios however do not significantly decrease the tension present in the 'standard' 3+1 model [11, 38].

1.5 Probing the sterile neutrino hypothesis

Several experiments probe the phase space of the sterile neutrino hypothesis mentioned in the previous section in the electron or muon channel. The experiments probing the

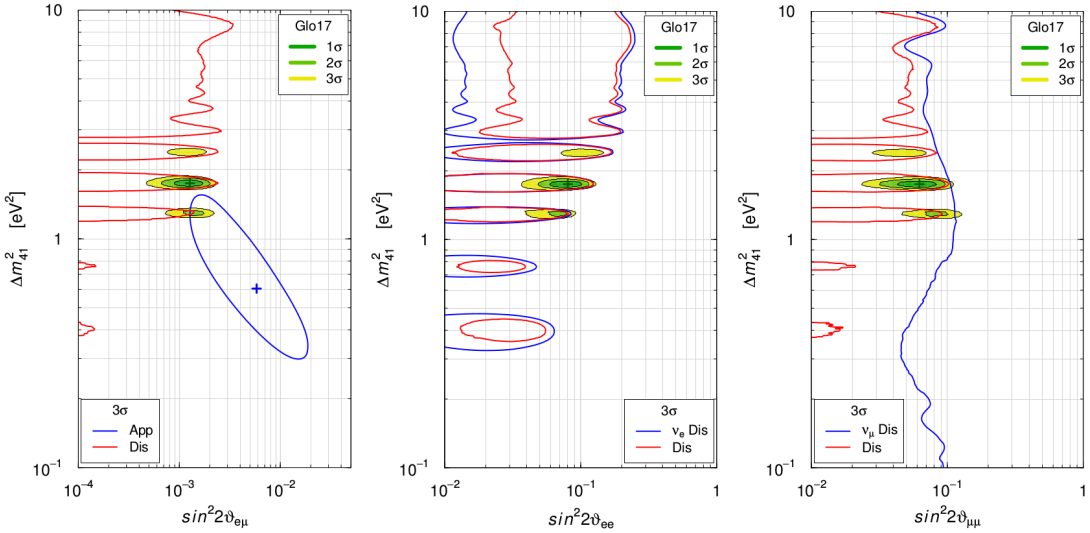

Figure 1.6: Allowed regions in the $sin^2(2\theta_{\alpha\beta}) - \Delta m^2_{14}$ planes obtained in the 3+1 global fit 'Glo17' of all short baseline (SBL) data. There is a comparison with the 3σ allowed regions obtained from SBL appearance data (App, the LSND/MiniBooNE anomaly) and the 3σ constraints obtained from (anti)electron neutrino disappearance (ν_e Dis, the Gallium and reactor anomalies). The lack of disappearance data for ν_μ and $\bar{\nu}_\mu$ is made clear with the 'ν_μ Dis' limit in the third figure. The combined ν_e and ν_μ constraints are grouped in 'Dis', shown on all three plots. Best fits are indicated with crosses [29].

electron channel are built to be maximally sensitivity to sterile neutrinos with parameters consistent with or close to the value mentioned in Section 1.4. Experiments using the muon are typically large multipurpose experiments which perform also searches for sterile neutrinos such as IceCube, T2K and NoVA. The electron channel experiments are located at very short distance from nuclear reactors[6]. The main experiments are:

DANSS, short for 'detector of the reactor antineutrino based on solid scintillator', is located underneath the fourth reactor core of the Kalinin nuclear power plant, (Udomly, Russia). The detector consists of $100 \times 4 \times 1$ cm^3 gadolinium coated plastic scintilator bars placed in orthogonal layers. The light produced in the bars is read out via wavelength shifting fibres and a combination of silicon photomultipliers (SiPM) and photomultiplier tubes (PMT). The neutrons produced in IBD interations are captured on ^{157}Gd (0.26 Mb thermal neuton capture cross section) releasing a 7.9 MeV gamma, providing neutron identification. The positron produced in the IBD interaction scintillates in the polystyrene bars, providing the energy and location via the orthogonally placed bars. The 1 m^3 detector is shielded by the reactor core and building, providing 50 m.w.e. of shielding to cosmic radiation. The detector is mounted on a crane and can be moved up and down, providing a range in baselines between 10 and 12 m [41].

NEOS, an acronym of 'neutrino experiment for oscillation at short baseline', is located 24 m away from the fifth reactor core of the Hanbit Nuclear Power Complex (Yeonggwang, South Korea). The detector consists of a 1 m^3 cylindrical tank filled with liquid scintillator doped with ^{157}Gd. The light produced in the tank is detected from both ends with 19 8" PMTs on either side. The location of the IBD interaction is determined from the arrival time and amplitude of the signal seen by each PMT [42].

PROSPECT, the 'precision oscillation and spectrum experiment', is located be-

[6] A notable exception is the SOX experiment. This experiment proposed to measure neutrinos from a 3.7 PBq ^{144}Ce source using the BoreXino detector [39]. This experiment was unfortunately cancelled due to technical problems in the production of the source [40].

tween 7 and 12 m from the HFIR research reactor at ORNL (Oak Ridge, Tennessee, USA). The detector consists of a single volume of ^{6}Li doped liquid scintillor segmented into 120 optical cells by highly reflective barriers. The optical cells, each measuring $14.4 \times 14.4 \times 120$ cm^3, are read out by a 5" PMT on either side. The detector can be moved over a range of 3 m [43].

STEREO, is an experiment located 10 m from the core of the ILL research reactor (Grenoble, France). The detector consists of six vertical cells $\left(40 \times 40 \times 90 \text{ cm}^3\right)$ filled with ^{157}Gd doped liquid scintillator and read out by four 8" PMTs mounted on top of each cell [44].

Neutrino4 is an experiment at the SM3 experimental reactor (Dimitrovgrad, Russia). The detector consists of fifty $22.5 \times 22.5 \times 85$ cm^3 tanks filled up to 70 cm with ^{157}Gd doped liquid scintillator. The detector sits on a trolley that can be moved between 6 m and 12 m from the reactor core. Each tank is being read out from the top by a single PMT [45].

The five experiments mentioned above all released preliminary results with limited statistics, shown in Figure 1.7. Using 235 days of data split over three crane positions, the DANSS collaboration excludes the Mention *et al.* [28] best fit point of $\left(\Delta m^2_{14},\ sin^2 2\theta_{14}\right) = \left(2.3 \text{ eV}^2,\ 0.14\right)$ at more than 5σ. The sterile neutrino oscillation fit to the DANSS data prefers $\left(1.4 \text{ eV}^2,\ 0.05\right)$ [46]. The NEOS collaboration fits eight months of reactor on data to the extrapolated reactor antineutrino spectrum measured by the Daya Bay experiment. The Mention *et al.* best fit point is excluded at more than 90% CL. Two optimal fit points are found: $\left(1.73 \text{ eV}^2,\ 0.05\right)$ and $\left(1.30 \text{ eV}^2,\ 0.04\right)$ [42]. Relying on 33 days of reactor on data, PROSPECT is able to exclude the Mention *et al.* best fit at 2.3σ CL. They do not provide the best fit point for a sterile neutrino [47]. Similarly, the STEREO collaboration excludes the Mention *et al.* best fit at 97.5% CL using 66 of reactor on data [48]. Using 480 days of reactor on data and 278 days of reactor off data, Neutrino4 excluded the combined reactor and gallium allowed region below $\Delta m^2_{14} \approx 4$ eV^2 at 99.7%. They do however observe an oscillation pattern at $\Delta m^2_{14} = 7.22$ eV^2 and $sin^2 2\theta_{14} = 0.35$ with a 3 σ significance [45].

Nucifer is located 7.2 m from the core of the Osiris reactor (Saclay, France), the experiment name is an underwordly pun on the reactor name. Even though Nucifer was originally designed to provide a non-invasive reactor monitoring tool for non-proliferation, the design and location proved to be suitable for detection of short baseline oscillations. The detector consists of an 850 l tank filled with ^{157}Gd doped liquid scintillator from which light is detected using 18 PMTs with 8" diameter [49].

SoLid, short for 'search for oscillations with a lithium-6 detector', is located at 6.2 m from the core of BR2 research reactor (Mol, Belgium). Both the detector and the reactor will be discussed to great extent in Chapter 2. The currently operating SoLid experiment will be combined with the **CHANDLER** (Carbon Hydrogen AntiNeutrino Detector with a Lithium Enhanced ROL) technology, probably from late 2019 onwards. The detector consists of plastic scintillating cubes made into a Raghavan Optical Lattice (ROL). A ROL is created by separating the cubes with an air gap. Light produced in a cube will mostly remain in the rows touching the faces of the initial cube via internal reflection. Reading out all outer faces thus provides the location and energy of the interaction. In between the horizontal layers, ^{6}Li:ZnS(Ag) screens are sandwiched to provide neutron identification. This reduces the amount of PMTs required by one dimension [50]. The neutron produced in the IBD reaction is captured on ^{6}Li, creating an α and a tritium particle which share 4.78 MeV. The alpha and tritium particles scintillate in the Zns(Ag), producing scintillation light with a different characteristic

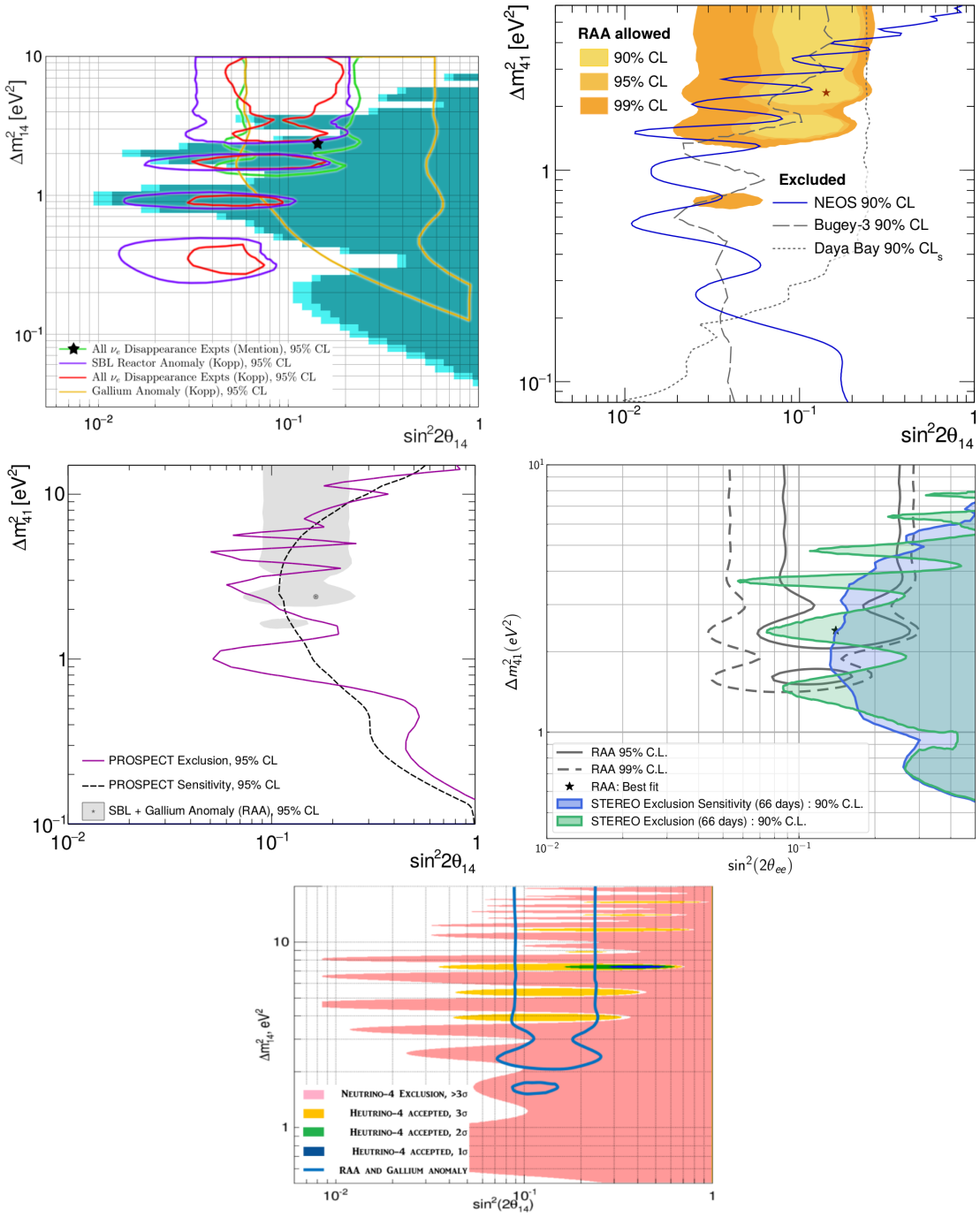

Figure 1.7: First results by DANSS [46] (top left), NEOS [42] (top right), PROSPECT [47] (center left), STEREO [48] (center right) and Neutrino4 [45] (bottom) probing the oscillation parameter phase space for a sterile neutrino.

decay time. The neutron is then identified via pulse pulse shape discrimination, this is the same process as used for the SoLid detector. It will be discussed thoroughly in Chapters 2, 3 and 4. A mini-CHANDLER prototype is currently being tested at the North Anna nuclear power plant (Mineral, Virginia, USA).

NuLat, an abreviation of 'neutrino lattice', is located near the NIST research reactor (Gaithersburg, Maryland, USA). The collaboration also explores the possibility to take data next to a nuclear reactor powering an aircraft carrier. The detector technology consists of ^{6}Li doped plastic scintillator 2.5" cubes stacked into one large cube making up a ROL [51].

Chapter 2

The SoLid Experiment at the BR2 reactor

The SoLid collaboration aims to resolve the RAA within a few years of taking data. The SoLid detector has been installed at the Belgian Research Reactor 2 (BR2 reactor) on the SCK•CEN site in Mol, Belgium. In this chapter, BR2 (Section 2.1) and the SoLid detector concept (Section 2.2) will be introduced along with various predecessors of the detector that finally resulted in the current full scale detector. Finally, in Section 2.3, the sensitivity of the SoLid experiment to sterile neutrinos will be shown.

2.1 The BR2 reactor at SCK•CEN

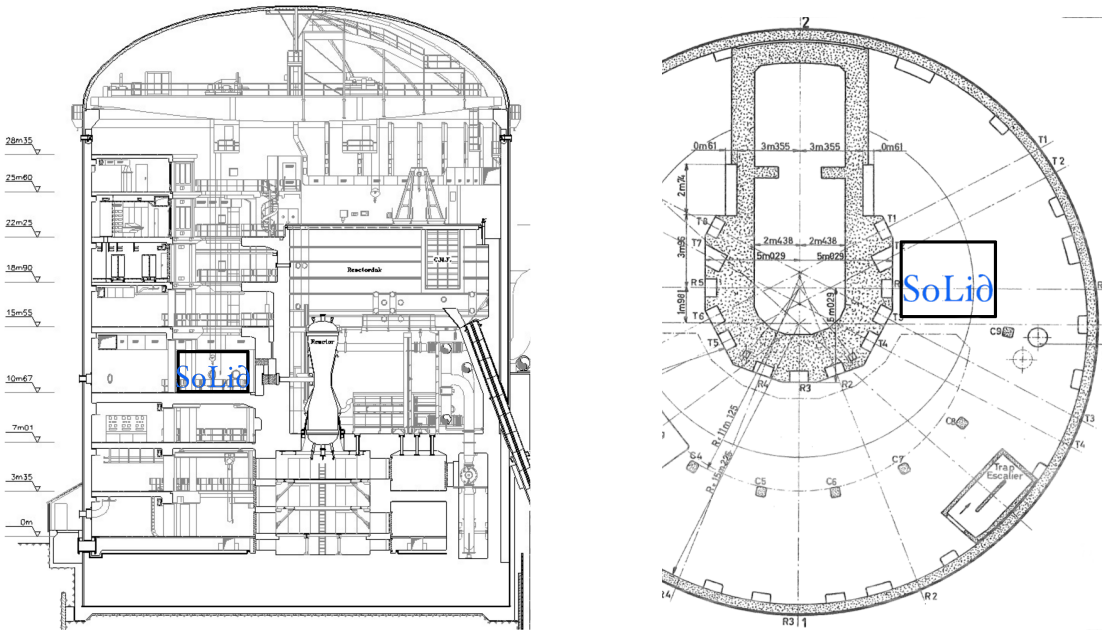

Figure 2.1: Schematics of the BR2 reactor building with the SoLid logo superimposed at the detector location in a box that corresponds with the shielding. Left, a vertical cut through of the reactor building and right the map of the third floor where the SoLid detector is located.

The BR2 reactor is a research reactor, giving it vastly different design and operational characteristics than a typical reactor found in a nuclear power plant. These

different characteristics make the BR2 reactor highly suitable for a sterile neutrino search [52, 53]:

- Compact core: The BR2 core consists of a conical beryllium matrix that guides the fuel rods into a space as small as 1 m^3, reducing the effective core diameter to less than 1 m. The conical shape of the reactor core can be seen in Figure 2.1 (left). The small core limits the smearing of the short baseline oscillations under investigation.

- Close approach: Due to the small core, the reactor pool, the surrounding reactor vessel and the vessel wall are relatively close to the reactor core. The outer side of the concrete wall surrounding the pool is only 5 m away from the center of the reactor core, as can be seen on the floor plan in Figure 2.1 (right).

- Favourable environment: During the data collection periods, no interfering experiments were taking place in the environment of the SoLid detector. All beam ports to the experimental hall have been closed, resulting in a low rate of reactor neutrons and gammas compared not only to detectors at nuclear power plants (DANSS, NEOS) but also at other research reactors such as ILL (STEREO), HFIR (PROSPECT), SM3 (Neutrino4) and Osiris (Nucifer).

- Fuel composition: The BR2 fuel is highly enriched uranium ($\sim$ 93.5% ^{235}U), limiting the effective number of fissile isotopes to one. This facilitates reactor calculations, allows for a measurement of the ^{235}U spectrum and probing the aforementioned 5 MeV bump.

- Short reactor cycles: The main activity of BR2 is the irradiation of materials, e.g. silicon, and the production of medical isotopes. The optimal operation scheme for these purposes are short cycles of three to four weeks with a month long rest period in between two cycles. These reactor off periods allow for a precise determination of the background.

2.2 The SoLid detectors

Antineutrinos produced in the reactor core are detected via the IBD process mentioned in Section 1.2.2 (Equation 1.14):

$$\bar{\nu}_e + {}^1_1p \rightarrow e^+ + {}^1_0n \ \ (E_{\bar{\nu}_e} > 1.806 \text{ MeV}) \tag{2.1}$$

In order to reduce the probability of misidentifying various types of background, the SoLid experiment requires identification of the positron and the neutron within a small distance and time window. Backgrounds to the experiment include:

- Reactor gammas and neutrons: As mentioned in Section 2.1, BR2 has a low reactor background compared to other research reactors and nuclear powerplants. These backgrounds scale with the reactor power and contribute to the so-called accidental background, i.e. the background arising from the random coincidence of a gamma and an uncorrelated neutron.

- Cosmic radiation: The muon component of cosmic ray interactions in the atmosphere is highly penetrating and interacts in the detector orders of magnitude more often than the expected neutrino signal. The neutron component of cosmic

ray showers (both produced in the primary interaction and in muon spallation reactions) contribute to the correlated background when a high energy neutron enters the detector, thermalizes and is captured.

- Natural radioactivity: Radioactive isotopes naturally present in any environment are also present in the detector materials and in the BR2 containment building. Certain decay chains can mimic a neutrino interaction, creating a correlated background.

The SoLid detectors are designed to efficiently select the IBD events, reject the background and provide the spatial and energy resolution required to resolve the RAA [54]. An in depth discussion of these backgrounds is given in Sections 4.6.3 (reactor gammas) and 5.2 (cosmic radiation and natural radioactivity).

2.2.1 The SoLid detector concept

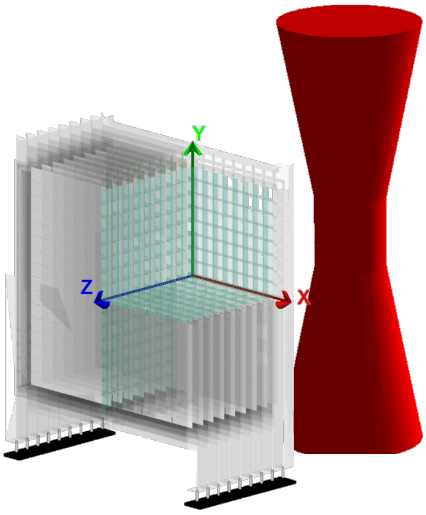

Figure 2.2: Coordinate system used for the SoLid SM1 prototype (illustrated here) and full scale detector. The Z axis points away from the reactor core (shown in red).

The detector is composed of optically isolated detection cells from which scintillation light is evacuated using wavelength shifting (WLS) fibres in the two dimensions (X and Y) perpendicular to the direction pointing away from the reactor core (Z) as is indicated in Figure 2.2. Each fibre accepts light from multiple cubes, the coincidence of X and Y fibres allows localization of the cube from which the light originated. Each WLS fibre has a silicon photomultiplier (SiPM) on one end and a mirror on the other end. A detection cell consists of a plastic scintillator cube of roughly $5 \times 5 \times 5$ cm^3 made from polyvinyltoluene (PVT). Each PVT cube is lined with one or more ^{6}LiF:ZnS(Ag) scintillator sheets, as shown in the left panel of Figure 2.3. Also shown are grooves milled out of the sides of the cube for the WLS fibres and the reflective wrapping used for optical isolation of the cubes.

The positron produced by a neutrino interacting in a PVT cube will result in a prompt scintillation in this PVT cube. The neutron first thermalizes and is then captured on a ^{6}Li nucleus in a ^{6}LiF:ZnS(Ag) sheet. The subsequent scintillation signal of ZnS(Ag) can be distinguished from the PVT scintillation signal because of its significantly longer decay time [55, 56]. The thermalization and capture of the neutron

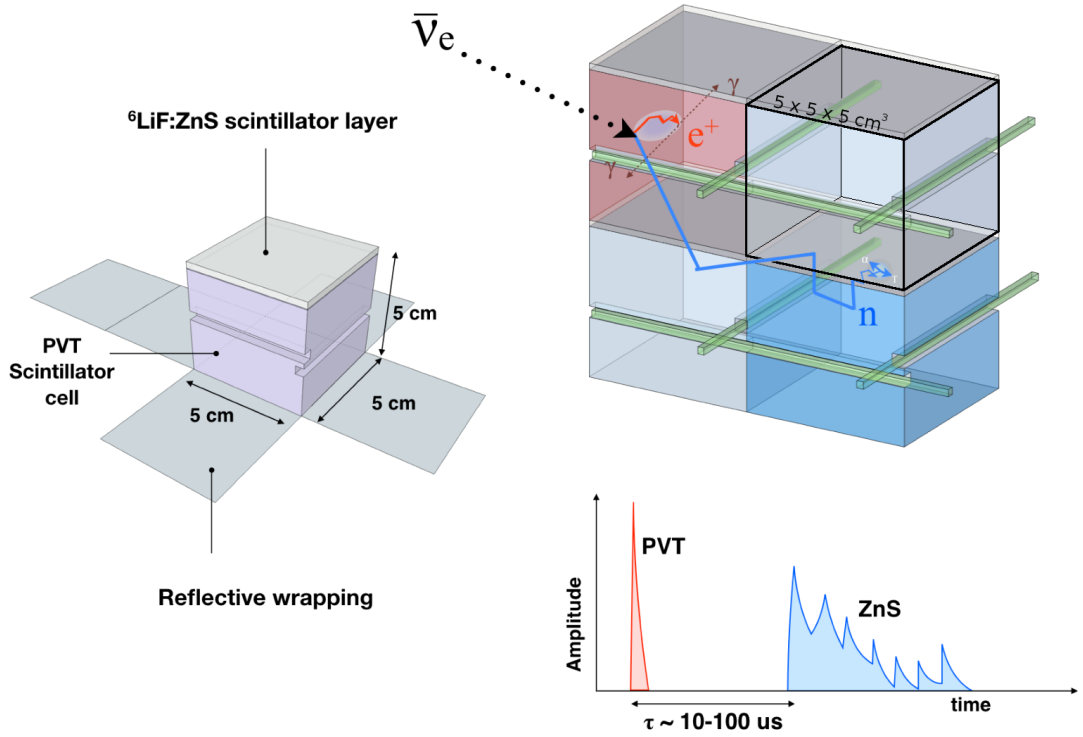

Figure 2.3: Illustration of the detection principle of the SoLid experiment. Left, a detection cell is shown with the grooved cube, the ^{6}LiF:ZnS(Ag) sheet and the unfolded Tyvek wrapping. The fibres are omitted here but shown on the upper right panel. Right, an illustration of an antineutrino interaction (IBD event). In the top panel, the particles and their interactions are shown, the bottom panel shows the resulting waveforms [54].

happens within a characteristic time and distance, resulting in a neutron signal that is delayed with respect to the prompt positron signal but located in close proximity to the cube with the prompt signal. A neutrino interaction and a sketch of the expected waveforms are depicted on the right hand side of Figure 2.3 [54].

The materials used in the detection cells are discussed in more detail in the following paragraphs.

PVT cubes

The PVT cubes (Eljen EJ200 [55]) play several crucial roles in the neutrino detection process for the SoLid experiment:

1. Neutrino target: The PVT cubes provide the protons required for the IBD reaction to take place. The PVT that is used contains $5.2 \cdot 10^{22}$ protons per cm^3 [55].

2. Prompt signal: The positron produced in the IBD reaction produces scintillation light in the same cube as in which the neutrino interacted, allowing determination of the neutrino interaction point up to 5 cm. Due to conservation of momentum, the positron is created with nearly all of the available kinetic energy. The amount of scintillation light produced by the positron is thus a measure of the neutrino energy and the relatively high light yield of PVT allows accurate determination of the positron energy [57].

3. Neutron thermalization: Although the neutron receives only a small fraction of the available kinetic energy (0.05 MeV on average [24,58]), this is far higher than the kinetic energy of thermal neutrons (25 meV). The neutron quickly loses energy through elastic collisions with nuclei in the PVT until it reaches thermal energies. At this point, the neutron capture cross section on a ^{6}Li nucleus dominates.

4. Light collection: The light produced in the ^{6}LiF:ZnS(Ag) sheet upon neutron capture reaches the WLS fibres via the PVT cube. PVT and ZnS(Ag) both have their emission peak at about 420 nm, guaranteeing the required optical transparency [54]. The cubes also hold the lithium screens in place.

Moreover, PVT is relatively inexpensive and easy to machine into cubes.

Lithium screens

The ^{6}LiF:ZnS(Ag) sheets (also called lithium screens) are an emulsion of 95% ^{6}Li enriched LiF and ZnS(Ag) microcrystals suspended in epoxy [56, 59]. At thermal neutron energies, the cross section for neutron capture on ^{6}Li is very high (936 b, compared to 0.3 b for hydrogen and 0.5 mb for carbon [60]), ensuring that most neutrons will be captured on lithium. The exact fraction of neutrons captured on lithium depends on the number and configuration of lithium screens placed on each cube, ranging from ∼50% (one lithium screen) to ∼80% (three lithium screens) for the investigated configurations [61]. Also the neutron capture time depends on the number and configuration of the screens, ranging from ∼40 μs (three lithium screens) to ∼100 μs (one lithium screen) [61]. Upon neutron capture, the ^{6}Li atom breaks up in an alpha and a tritium nucleus with 4.78 MeV of kinetic energy shared between them: $n + {}^6\mathrm{Li} \rightarrow \alpha + {}^3_1\mathrm{T} + 4.78$ MeV. Since both these particles are highly ionizing, they deposit all their energy in the lithium screen, exciting the scintillating ZnS(Ag) microcrystals.

Wavelength shifting fibres

The light produced in the PVT cubes and the lithium screens has to be transported to the SiPMs to be read out. This transport is done by 3×3 mm^2 WLS fibres placed in 5×5 mm^2 grooves in the sides of the PVT cubes. The fibres shift the blue light from the PVT and ZnS(Ag) scintillation (425 and 450 nm emission peaks respectively [55,56]) to green light (500 nm emission peak) by absorbing the light and emitting it isotropically at longer wavelengths. The WLS fibres enhance the light detection efficiency since the SiPMs are more efficient at this wavelength. Coating with a low refractive index reduces the probability for the light to escape from the fibre [53]. All SoLid detector phases use WLS fibres produced by Saint-Gobain [62].

Silicon photomultipliers

The SiPMs are soldered on one end of a small rectangular printed circuit board (PCB). On the other end of the PCB, the connection to the readout electronics is made via coax or twisted pair cables. This connection also provides the voltage required to operate the SiPM. The SiPMs and WLS fibres are mechanically connected by clamping the PCB in a 3D printed housing. The optical connection between the fibre and the SiPM is achieved using optical grease.

Hamamatsu SiPMs are used in all SoLid detectors [63]. These consists of many avalanche photo diodes (APD) connected in parallel. When biased above the breakdown voltage, the APDs are in geiger mode, amplifying the single photo electron liberated by an incoming photon to an avalanche of electrons, creating a detectable voltage difference. The amplitude of this signal, a so-called pixel avalanche (PA), is steered by the overvoltage applied to the SiPM. Other characteristics that depend on the applied overvoltage are the photon detection efficiency (the probability that an incoming photon creates an avalanche), the crosstalk probability (the probability for an avalanche in one APD to trigger an avalanche in a neighbouring APD) and the dark count rate (DCR, the rate of avalanches due to thermal excitations). The operating voltage therefore has to be chosen high enough to have a high detection efficiency and low enough to avoid too much crosstalk and a too high DCR.

Optical isolation

The PVT cubes and lithium screens are wrapped in white DuPont Tyvek wrappers for optical isolation from the neighbouring cubes [64]. At the appropriate places, 5×5 mm^2 holes are made in the wrappers for the WLS fibres. Apart from optically isolating the detection cells, the wrapping also reflects photons back into the PVT cube, thereby increasing the light collection efficiency.

2.2.2 Proof of concept: NEMENIX

The NEMENIX detector (short for 'neutrino measurement non income experiment', a term coined by Edgar Koonen[1]), shown in the left image of Figure 2.4, was operational from 2013 to 2015 to demonstrate the possibility of neutron discrimination against γ, $e^{\pm}$ and μ using the segmented hybrid scintillator technology. It consisted of $4 \times 4 \times 4$ cubes housed in an aluminium box and read out by one WLS fibre (BCF-91) for each row of cubes in the X and Y direction, resulting in 32 readout channels. The SiPMs

[1]Former BR2 project manager, deputy BR2 reactor manager and enthusiastic supporter of the SoLid experiment. Edgar sadly passed away in October 2017.

(S10931-050P) were coupled to four CAEN 1724 digitisation and readout modules. The aluminium box was placed in 20 cm thick high density polyethylene (HDPE) box acting as shielding to reduce the amount of reactor gammas interacting in the detector. Another CAEN 1724 module was used to operate four muon veto panels. Two large panels were placed horizontally outside the shielding, one above and one below the detector. Two smaller panels were placed vertically inside the shielding, left and right of the NEMENIX detector.

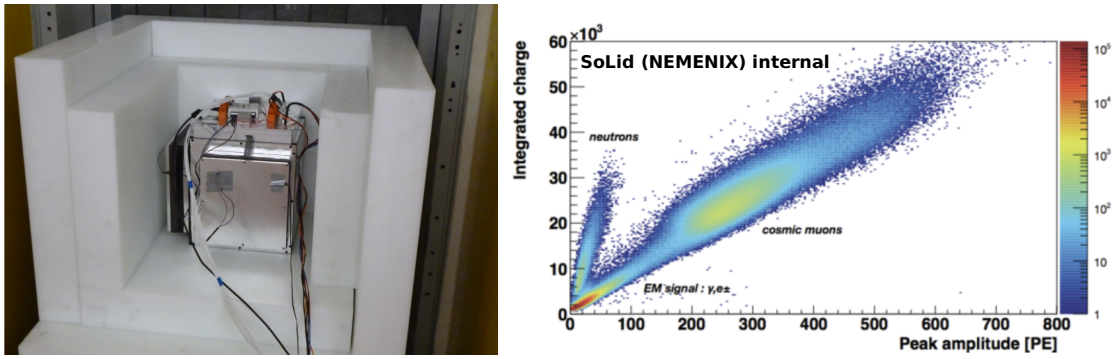

Figure 2.4: The NEMENIX detector. Left, a picture with open shielding at BR2 prior to the installation of the muon veto panels. Right, particle discrimination using the integrated charge and maximal peak amplitude of the waveforms. Both the integrated charge and peak amplitude are expressed in PA.

The right panel of Figure 2.4 shows the integrated charge of a signal as a function of its maximal amplitude. Three regions can be identified. At high integrated charge and amplitude, cosmic ray muons crossing the detector can be seen. A muon traversing PVT deposits roughly 2 MeV/cm. The broad distribution is due to different path lengths when muons travel through the cubes. At lower amplitudes but at the same integral to amplitude ratio, a population of lower energy scintillations in the PVT cube can be seen, these are caused by γ and $e^{\pm}$ interactions. This ratio is typical for the short decay time of PVT scintillation. The higher integral to amplitude ratio population labelled 'neutrons' in Figure 2.4 is due to the longer decay time of the ZnS(Ag) scintillator in the lithium screens. This clear separation of particle types proved the capability of the SoLid detector technology.

2.2.3 A SoLid prototype: SoLid Module 1

The aim of the SoLid Module 1 prototype (SM1, pictured in Figure 2.5) was to show the scalability of the detector concept, increasing the scale from $4 \times 4 \times 4$ cubes to 9 detection planes of 16×16 cubes each. The cubes were held in place with 2 cm thick black HDPE bars at the edges of each plane. The HDPE helped to improve the reflection and moderation of neutrons created at the edges of the plane. The front and back faces of each plane were capped with a 2 mm thick black HDPE sheet. The cubes and HDPE moderators were housed in a hollow aluminium frame in which the SiPMs and mirrors were placed. The entire module was placed in 9 cm thick HDPE walls (shown in beige (left) and green (right) in Figure 2.5) which provided passive shielding against neutrons and gammas coming from the reactor. Like NEMENIX, SM1 was operated at room temperature ($\sim 25\ ^{\circ}$C). Additionally, eight muon veto planes were installed. Three planes were placed on top of the shielding, three planes below the shielding and two inside the shielding. The muon veto planes inside the shielding were placed perpendicular to the planes outside the shielding, one plane on top and one plane

below the detector (shown in pink and black in the GEANT4[2] schematic in Figure 2.5).

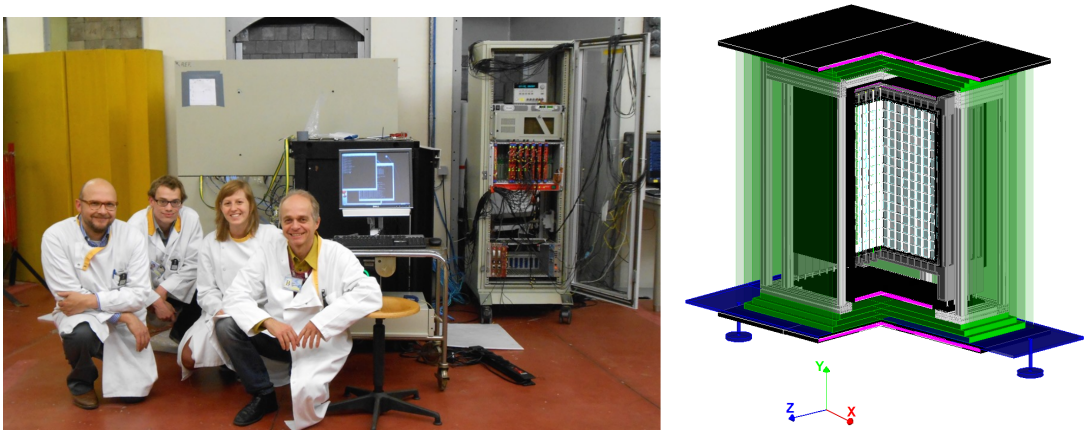

Figure 2.5: The SM1 detector after installation (left) and in a GEANT4 schematic (right). The electronics rack on the right of SM1 belongs to NEMENIX which was still taking data at that point.

Single cladded WLS fibres (BCF-91) were used with a single fibre through each row of cubes in the X and Y direction, resulting in 32 readout channels per plane. More recent SiPMs with reduced cross talk (S12572-050P) compared to NEMENIX were positioned alternating on the left or right end of the fibre to guarantee a more homogeneous readout of the entire plane. The SiPMs were amplified and digitized (62.5 MS/s) with front end electronics built for this purpose. The front end fed its output to FPGAs where the trigger logic was implemented. When a trigger occurred, 256 samples (16 ns each) of all triggering channels were written to disk. The SM1 detector came online during the last days of a reactor cycle in February 2015 and was operational until August 2015. Only 51 hours of reactor on data could be collected since the BR2 reactor was shut down when the reactor cycle in February 2015 ended for a period of 1.5 years for the planned decennial replacement of the beryllium core. During the remaining time, reactor off background data and source calibration data were collected.

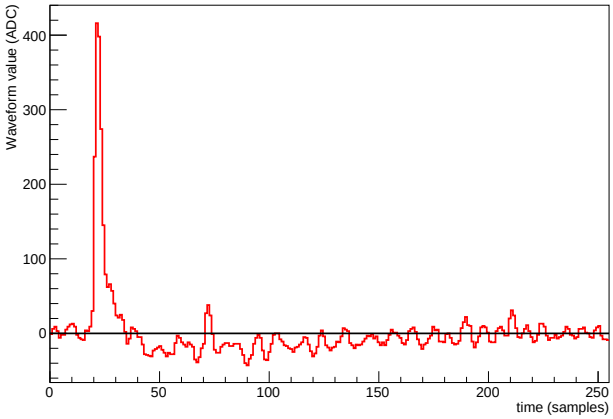

Figure 2.6: Example of an SM1 waveform showing the oscillatory noise and the undershoot. Undershoot is the waveform dipping below the baseline (black line) after the peak, the noise can be observed as oscillations superimposed on the waveform.

[2]GEANT4 is a toolkit for simulating the passage of particles through matter [65]. It is used to simulate the interaction of particles with the various detector materials.

Due to time pressure to collect data during the last reactor cycle, the development and integration time for the readout electronics of the SM1 prototype was very limited, resulting in a number of flaws that affected the data quality and trigger rates. There was a significant amount of oscillatory noise in the waveforms, with up to three PA ($\sim$ 75 ADC) in amplitude on the worst channels, as well as 'undershoot' following peaks. Both of these issues are shown in Figure 2.6. The oscillatory noise prevented the implementation of zero suppression (ZS), necessitating implementation of an $X-Y$ coincidence trigger with a fairly high threshold (170 ADC $\approx$ 6.5 PA $\approx$ 500 keV) in order to keep the data rate manageable. Additionally, a random trigger was taking unbiased data at a regular rate [53]. The performance of the SM1 detector in terms of neutron detection as well as the impact of the aforementioned issues is discussed in Chapter 3.

2.2.4 The full scale SoLid detector: Phase 1

The Phase 1 full scale detector is larger than the SM1 prototype. The number of 16×16 cube detection planes was extended to 50 planes, split in 5 modules of 10 planes each. Based on the performance of the SM1 detector [53], the SoLid detector design was further optimized. Most of the design changes aim to increase the efficiency to detect neutrino interactions by increasing the light yield and by improving the neutron capture and detection efficiency. A list of the design changes and their impact is given in the following section and is summarized in Table 2.1.

Phase 1 design optimizations

Apart from increasing the number of planes from 9 to 50, which increases the sensitivity to sterile neutrinos (see Section 2.3), the particle detection efficiency of each plane has been significantly improved as well. The light yield was studied in detail on a dedicated test bench [66]. The main results of this study are summarized here.

- To increase the light yield, two fibres are used for each row of cubes in both the X and Y direction. Each of the two fibres in the same direction is read out at opposite ends, resulting in a much more homogeneous light yield over all cubes in a plane. The double readout increases the amount of light extracted from each cube by 40%.

- The use of double cladded WLS fibres (BCF-91A) increases the capture efficiency of light in the fibre (+15%) and increases the attenuation length of the fibre (+5%). The decreased attenuation effectively increases the light yield of the cubes furthest away from the SiPMs to a value closer to the effective light yield of a nearby cube. Due to four fibres reading out the cubes, the effect of using double instead of single cladded fibres results in an increase in light yield of 60% for every single cube before taking decreased attenuation into account.

- At the non-SiPM side of each fibre, an improved mirror made from aluminised mylar increases the light yield with another 40% compared to the SM1 mirror.

- The light yield is further enhanced by increasing the reflection of light into the cubes. The use of thicker Tyvek wrappers (105 g/m^2 instead of 75 g/m^2) increases the light yield by 30%.

The combined effect of all aforementioned modifications can be seen in Figure 2.7. The 43% difference in light yield between the two cubes with the highest and the lowest light yield values in the SM1 detector is reduced to 6% in the Phase 1 detector [66].

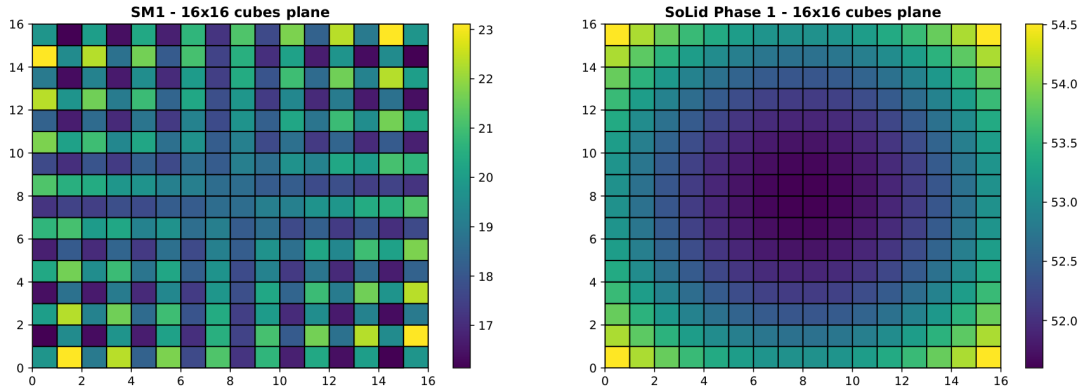

Figure 2.7: Light yield maps for the SM1 (left) and Phase 1 (right) detector extrapolated from dedicated light yield measurements [66]. The average light yields are respectively 18.9 and 52.3 PA/MeV for the SM1 and Phase 1 detector. The maximal difference in light yield between any two cubes is 6% for the Phase 1 detector compared to 43% for the SM1 detector.

The black HDPE frame lining used in SM1 severely distorted the measured attenuation pattern [53]. These were therefore replaced with white HDPE, which reflects the light more effectively. Similarly, the 2 mm thick black HDPE plane caps were replaced by 105 g/m^2 white Tyvek sheets. This not only increases the light yield but also reduces the number of protons and hence the number of IBD reactions in 'dead' material. In the SM1 detector there was 2.5 kg of plane cap for 32 kg of active material while in the Phase 1 detector, this is only 130 g.

To improve the neutron capture efficiency, and therefore the neutrino detection efficiency, an additional lithium screen was placed on every cube. Geant4 simulations show this improves the capture efficiency on ^{6}Li from 52% to 66% [61]. Unfortunately, for every added lithium screen, the light yield drops by 10% since the lithium screens are less reflective than the Tyvek wrapping [66].

Other updates to the detector are aimed at reducing the amount of background. The shielding was increased from 9 cm on all sides to 50 cm on the sides and on top of the detector. The detector roof is constructed from 20 layers of 2.5 cm thick HDPE plates placed on top of one another. The walls are built out of 0.5 m thick polyethylene bricks filled with water. Underneath, on top and in front, 2 mm thick cadmium (2 kb thermal neutron capture cross section) sheets have been incorporated in the container walls to limit the flux of thermal neutrons reaching the detector. In the roof and floor of the container, only the region directly above and below the detector are covered. In the side facing the reactor wall, the entire wall of the container is covered with cadmium. Last, the DCR of the SiPMs is reduced by a factor three by placing the detector in a thermally insulated shipping container cooled to 10 °C [67].

All these changes result in a much larger detector that looks very different compared to the SM1 detector (Figure 2.5). A picture from the inside of the container during construction and a Geant4 schematic, including the shielding, are shown in Figure 2.8.

Detector component	SM1	Phase 1	Improved parameter
WLS fibres	1 per direction (X and Y) single cladded	2 per direction (X and Y) double cladded	increased light collection, increased homogeneity reduced attenuation. increased light collection
Fibre mirror	aluminium	aluminised mylar	increased light collection
Tyvek wrappers	75 g/m^2	105 g/m^2	increased reflectivity
Frame lining	black HDPE	white HDPE	increased reflectivity
Plane caps	black 2 mm HDPE plate	white 105 g/m^2 Tyvek	increased reflectivity reduced proton contamination from 'dead' material
Lithium screens	1 per cube no reflective backing	2 per cube reflective backing	increased capture probability, reduced capture time increased neutron light yield
Shielding	9 cm HDPE	50 cm water walls, 50 cm HDPE roof, Cd sheets underneath	reduced background
Operating temperature	room temperature ($\sim$ 25 °C)	cooled ($\sim$ 10 °C)	reduced DCR
Trigger	coincidence threshold trigger (amplitude)	neutron trigger (number of peaks)	increased neutron detection efficiency

Table 2.1: Overview of design improvements between the SM1 and Phase 1 detectors.

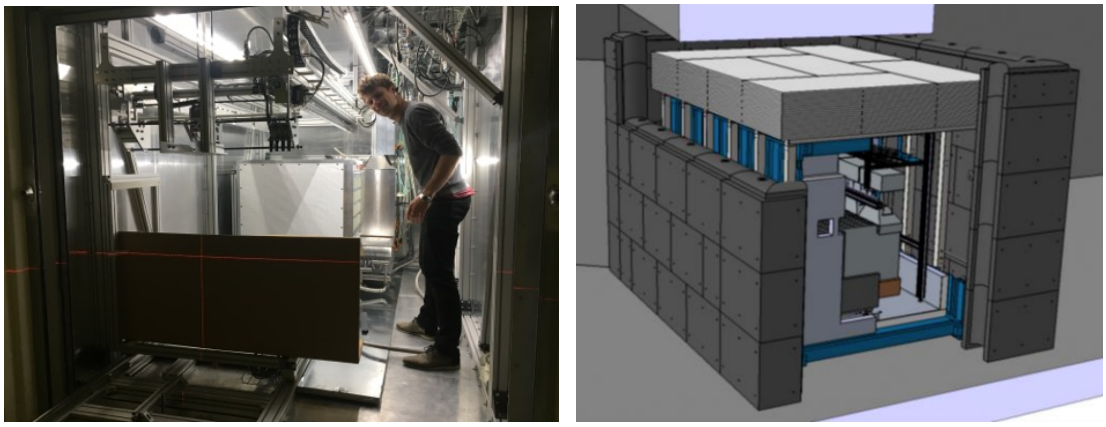

Figure 2.8: The inside of the Phase 1 container with part of the detector in place (left, collaborator for scale) and a Geant4 schematic of the detector, container, water wall and HDPE roof.

Phase 1 triggers

The detection efficiency of IBD positrons and neutrons is improved using new readout electronics. The new electronics does not suffer from the issues observed in SM1 (Section 2.2.3). Undershoot is now only visible after the largest peaks, essentially only affecting cosmic ray muons. Noise is limited to 10% of a PA in the worst channels. A ZS scheme, which significantly reduces the data rate, was implemented. A simple peak finding algorithm is used for the online neutron trigger. Both of these are implemented in the Artix7 FPGAs. Each FPGA processes the information of one plane. The digitisation rate has been lowered from 62.5 MS/s (16 ns samples) to 40 MS/s (25 ns samples), relaxing the system requirements and reducing the data rate without compromising the detector capabilities.

The online neutron trigger counts the number of peaks over a threshold (PoT) in a rolling time window and triggers when this number reaches a local maximum and exceeds a specified threshold. Both the time window, the number of peaks and the peak threshold are subject to optimization. To facilitate the reconstruction of IBD candidate events, a neutron trigger activates the reading out of an IBD buffer kept in the memory of the FPGA. This buffer consists of all ZS data for a number of planes surrounding the plane providing the trigger, within a time window before the trigger took place. The time window is several factors larger than the typical neutron capture time. The number of planes read out and the length of the buffer are again open for optimization, balancing the data rate against the neutrino detection efficiency.

Apart from the neutron trigger, also a threshold and periodic trigger have been developed. The periodic trigger, which periodically reads out all channels of the detector regardless of the content of this data, is typically not active during data taking. The threshold trigger is set at a higher amplitude than what was used for the SM1 detector since it now primarily serves to detect cosmic ray muons in an unbiased way. The data being read out following a threshold trigger is different for the Phase 1 detector compared to the SM1 detector. When a threshold trigger occurred in the SM1 detector, only those channels that triggered in coincidence were being read out during 4.1 μs (256 samples of 16 ns). For the Phase 1 detector, there is no coincidence requirement and all ZS data in the plane where the trigger occurred is read out during 6.4 μs (256 samples of 25 ns).

The trigger and its efficiency are discussed in Chapter 4.

Phase 1 construction

The design and construction of the Phase 1 detector took well over a year. A cooled container and two calibration robots were designed and built, all new electronics was developed, tested and produced, more than 12800 cubes were washed, wrapped and assembled in 50 planes. All details on the cube and plane assembly were inserted in a database. A picture of the cube assembly room is shown in Figure 2.9. The wrapping procedure is explained in the caption.

Figure 2.9: Cube wrapping setup in Ghent, Belgium. In the top right of the picture is the computer with connection to the database. Attached to the computer is a scale to weigh the bare cube and the bare lithium screens and a barcode reader to keep track of the cube number, PVT batch number and lithium screen batch number. When all these values are introduced in the database, the parts are brought to the table in the front of the picture where the cube is wrapped. The cube is oriented using the metal tool on the table, placed in the Tyvek wrapper with the aligned neutron screens and closed with tape. The metal tool also serves as a check on the cube size, cubes that are too large to fit in the extrusions are rejected. The wrapped cube, i.e. an assembled detection cell, is then returned to the first table so it can be weighted again and stored until it is placed in a frame.

The mass of the bare PVT cubes is shown in the left plot of Figure 2.10. It is clear that all cubes are machined to high precision resulting in a small spread in mass ($m = 119.67 \pm 0.12$ g). The two populations that are observed are due to a reduced thickness in a number of PVT slabs from which the cubes are machined. Even with this distortion, the standard deviation on the bare PVT cube mass is only 0.1% of the mean value.

The lithium screens used for the Phase 1 detector have a reflective backing to increase the neutron light yield (see Table 2.1). This is only true for the 196 'inner' cubes in a plane, the 'outer' 60 cubes have lithium screens without reflective backing. The impact of the different mass of these lithium screens can be seen in the right panel of Figure 2.10 showing the total mass of the assembled cubes averaged over all planes. A difference of 1.57 ± 0.19 g is observed between the inner and outer detection cells due to the backing of the lithium screens.

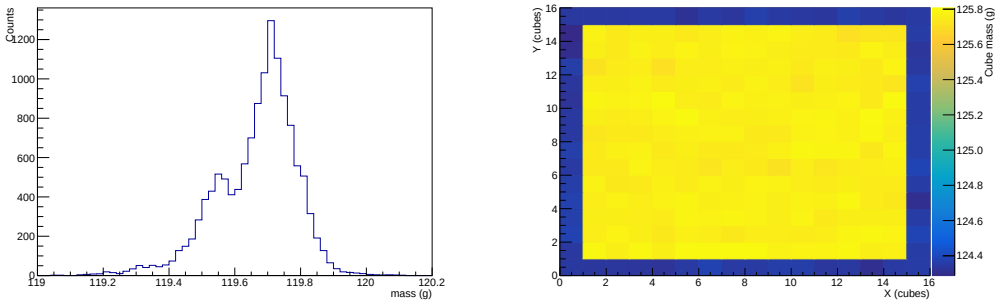

Figure 2.10: Distribution of the mass of the bare PVT cube (left) and the mass of the wrapped cubes averaged over 50 planes as a function of the cube position in the plane (right).

Phase 1 calibration

As mentioned in the previous section, two calibration robots were built for the Phase 1 detector. The first robot, CaliPSo (Calibration Plane for SoLid), was created to assess the quality of the planes after construction and to provide an initial calibration. The second robot, CROSS (CalibRation On Site SoLid), was installed inside the container, suspended over the planes, and is used to calibrate the detector over the life time of the experiment. Both robots have a 3D movable head that can bring a radioactive source to the desired location. Neutron sources (^{252}Cf, AmBe) and gamma sources (^{22}Na, ^{137}Cs, ^{54}Mn, ^{65}Zn, ^{207}Bi, AmBe) can be attached to both robots to perform a neutron efficiency measurement or an energy calibration, respectively. Additionally, CaliPSo can be equipped with a triggerhead for the ^{22}Na source to provide an external trigger on the two annihilation gammas emitted in coincidence.

The initial calibration and data quality assurance campaign was done at the University of Ghent, where the SM1 and Phase 1 detectors were assembled, using the CaliPSo robot. A frame was loaded onto the robot, the ^{22}Na triggerhead was attached and all cubes were scanned. This allowed for a determination of the light yield of every single cube when exposed to the 1.27 MeV gammas in a virtually background free environment. The result of this scan is shown in Figure 2.11. It can be seen that the light yield is very uniform over the entire detector (87.3 ± 7.2 PA/MeV) with a spread of less than 10%.

The larger value than predicted by [66] (Figure 2.7, 52.3 ± 2.0 PA/MeV) can be attributed to a variety of factors. First of all, the CaliPSo measurement does not take crosstalk in the SiPMs into account, whereas the light yield test bench study applies a correction for this effect. The size of this effect is $17.7 \pm 1.0\%$ at 1.5 V over voltage in the test bench study [66]. Undoing this correction increases the test bench prediction to 63.5 ± 2.5 PA/MeV. Additionally, the value presented in the light yield study does not take the effect of neighbouring cubes into account. While a test using a single row of cubes determined the light yield increases by 12% compared to a single cube, no test with neighbouring cubes on four (CaliPSo) or six (Phase 1) faces was performed. Assuming the light yield increases by 6% for every face that has a neighbouring cube, the extrapolated light yield for a cube with four neighbours is 78.7 ± 3.1 PA/MeV, a 1.1σ difference between the test bench prediction and the observation.

While the two figures are now almost consistent within one sigma, the assumption to extrapolate the effect of two touching cubes to respectively one and four touching cubes is speculative. Additionally, the effect of the Tyvek plane covers present in CaliPSo but not in the test bench has not been taken into account. However, qualitative differences

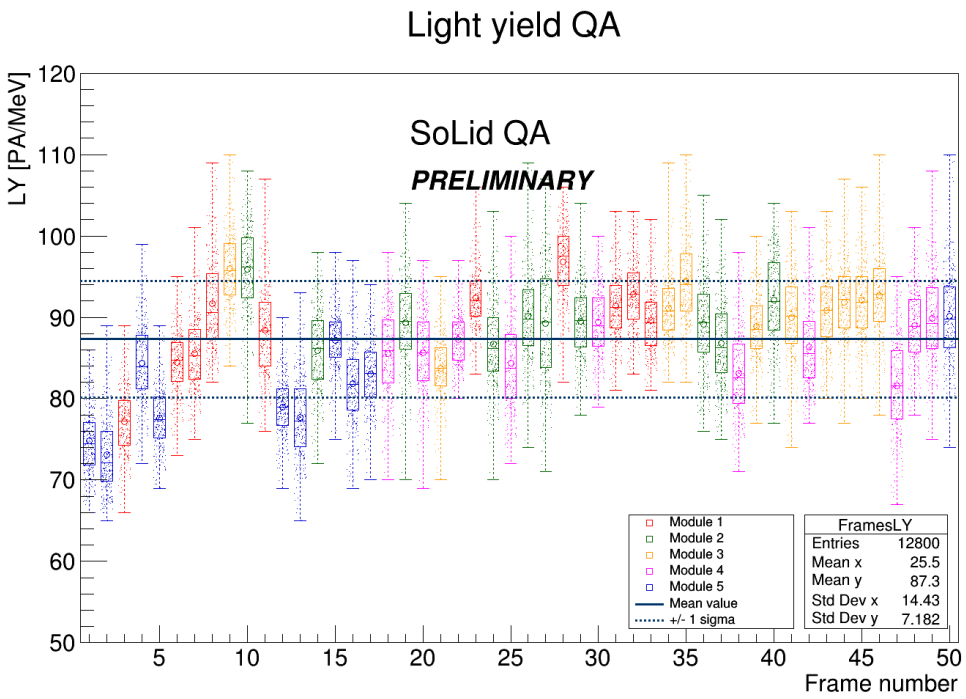

Figure 2.11: The ^{22}Na light yield measurements of all planes using the CaliPSo robot. The full range (whiskers), central two quarters (box), average (circle) and median (central line) are shown for each plane as well as the global mean and standard deviation.

between the two tests benches exist, further explaining possible discrepancies. Even though the CaliPSo calibration triggerhead was inspired on the one used in the light yield test bench, completely different electronics with a different voltage supply, sampling rate and signal amplification were used. Moreover, the two sets of measurements were performed in distinct environments with possibly very different origins of noise.

Using the CaliPSo robot, a neutron source (^{252}Cf) was positioned at specific places to preliminary determine the neutron identification efficiency of each cube. The results of this neutron scan are shown Figure 2.12. In this figure, both the absolute identification efficiency compared to a Geant4 simulation (left axis) and the relative efficiency of all cubes compared to the cubes in the same position on other planes (right axis) are shown. The Geant4 model used for the absolute identification efficiency includes the capture efficiency (see Section 3.3). Thus, the numbers reported here, $60.5 \pm 3.3\%$, correspond to the identification efficiency. This value however does not reflect the true capability of the Phase 1 detector for neutron identification. The CaliPSo robot operated at room temperature with stricter settings than those used in physics mode, i.e. the neutron trigger was set at 11 PoT in the CaliPSo runs while the 2017 data was collected using 9 PoT. Also the offline neutron identification criteria were not optimized for the CaliPSo calibration campaign.

It is worth noting that a number of planes do not have a relative efficiency determination in Figure 2.12. For these planes, the sources were not placed at the same position as for the other planes or an AmBe source was used instead of the ^{252}Cf source. These planes were omitted from this comparison to avoid a bias. The uniformity of the detector in terms of neutron identification is very good, with less than 10% variation across the planes. A more detailed in-situ calibration using the CROSS robot is discussed in Section 4.5.

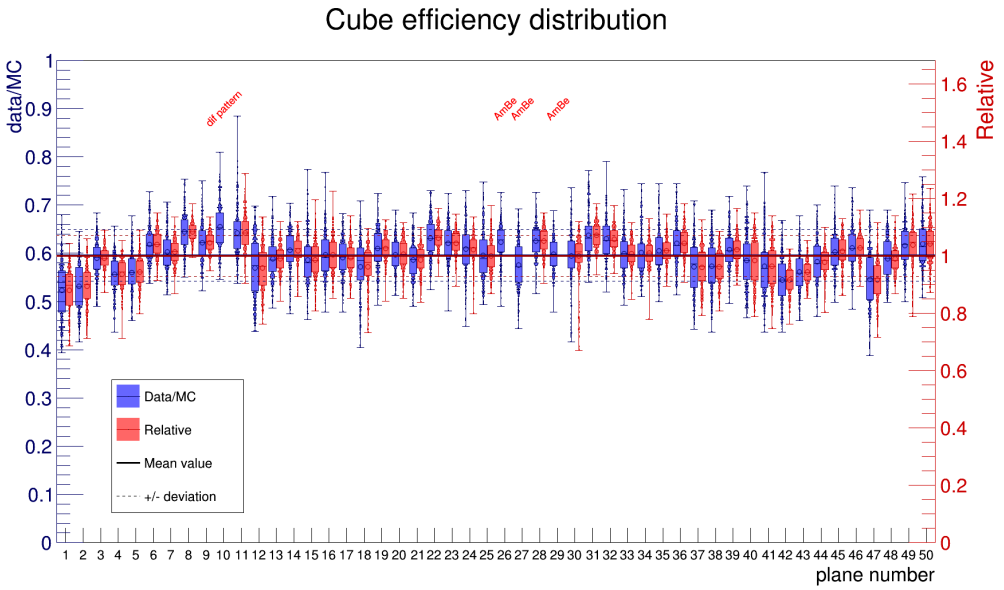

Figure 2.12: The ^{252}Cf neutron efficiency measurements of all planes using the CaliPSo robot.

The CROSS robot exploits the modular structure of the Phase 1 detector, the modules are placed on a rail and are attached to actuators so that each module can move roughly 5 cm. A radioactive source can be placed on the CROSS calibration head via an opening in the water wall and a hatch in the container. The calibration head can subsequently be lowered into the gap created between any two modules, thus allowing for a calibration of the fully assembled detector in its experimental environment. The head however can not serve all positions on the plane, as is shown in Figure 2.13. In particular, the bottom and the sides of the plane can not be reached due to size constraints in the container. This limitation combined with calibration positions only being available at the edge of every module imposes statistical limitations to the calibration of the bottom of the planes in the middle of a module. The amount of time each source is allowed at each position has to be optimized to combine the best light yield calibration with the best neutron capture efficiency determination using the limited time budget available for each calibration.

2.3 Sensitivity to sterile neutrinos

The performance or sensitivity of the SoLid experiment is expressed in the amount of phase space allowed for sterile neutrinos that can be scanned in a reasonable amount of time. This is visualised in plots like those in Figure 1.5. In this section, the influence of various parameters on the sensitivity of the detector is shown.

The sensitivity of the experiment to the oscillation parameters is obtained by comparing the observed number of events in each bin of visible energy (E_{vis}) and distance (L) to the predicted number of events in this bin. Figure 2.14 shows the predicted number of IBD events in case of no oscillations and in case of $sin^2(2\theta_{ee}) = 0.5$ and $\Delta m^2_{41} = 1.78$ eV^2. A χ^2 method can be used to find the oscillation parameters that best describe the data. These parameters are found by minimizing the expression

$$\chi^2 = \sum_{i,j} \frac{(S_{ij} - (T_{ij} + B_{ij}))^2}{S_{ij}}, \tag{2.2}$$

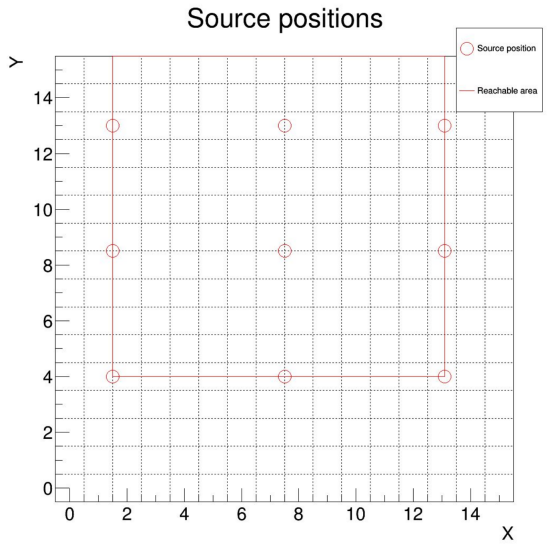

Figure 2.13: CROSS calibration positions used for the neutron detection efficiency determination (Section 4.5). Also indicated are the regions on a plane that are inaccessible to the CROSS calibration head [68].

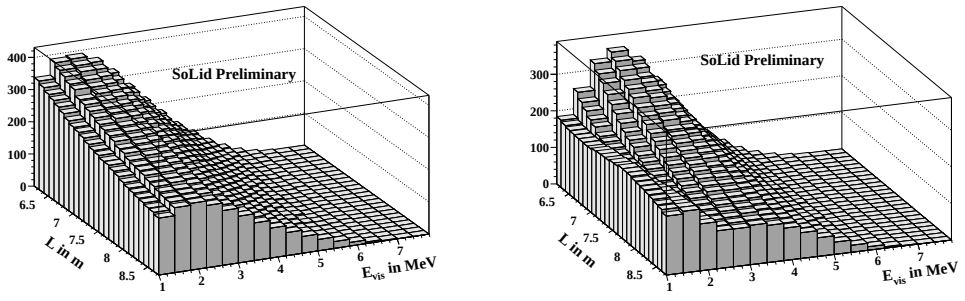

Figure 2.14: Number of detected IBD events as a function of visible energy (E_{vis}) and travel distance (L) in case of no oscillations (left) and in case of $sin^2(2\theta_{ee}) = 0.5$ and $\Delta m^2_{41} = 1.78$ eV^2 (right).

where S_{ij}, T_{ij} and B_{ij} are respectively the observed number of events, the predicted number of IBD events and the expected number of background events in each distance bin i and energy bin j. While B_{ij} is independent of different oscillation parameters, T_{ij} depends on the values of $sin^2(2\theta_{ee})$ and Δm^2_{41}, e.g. in the two neutrino approximation (Equation 1.11):

$$T_{ij} \propto P_{\bar{\nu}_e \to \bar{\nu}_e}(L_i, E_j) = 1 - sin^2(2\theta_{ee})\, sin^2\left(1.27\frac{L_i \Delta m^2_{41}}{E_j}\right). \tag{2.3}$$

2.3.1 Pull terms based χ^2

In Equation 2.2, only the statistical uncertainty on the measurement is taken into account. Bin to bin uncorrelated uncertainties (σ_{b2b}) have to be added to both the prediction T_{ij} and the background B_{ij}, representing potential uncertainties in respectively the detector response and the background prediction. When these bin to bin uncertainties are added, Equation 2.2 becomes:

$$\chi^2 = \sum_{i,j} \frac{(S_{ij} - (T_{ij} + B_{ij}))^2}{S_{ij} + (\sigma_{b2b} T_{ij})^2 + (\sigma_{b2b} B_{ij})^2}. \tag{2.4}$$

Uncertainties that are correlated between bins can not be introduced in the same way as σ_{b2b} in Equation 2.4. These are taken into account by so-called 'pull terms' [69]. The uncertainty on the normalization of the prediction T_{ij} is correlated across all bins. A nuisance parameter α_t is introduced, allowing the normalization of the prediction to float. The nuisance parameter α_t has a correlated uncertainty σ_t. Similarly α_b and σ_b are introduced to take into account the correlated uncertainty of the background prediction. With these two pull terms, Equation 2.4 becomes

$$\chi^2 = \sum_{i,j} \frac{(S_{ij} - ((1+\alpha_t)T_{ij} + (1+\alpha_b)B_{ij}))^2}{S_{ij} + (\sigma_{b2b} T_{ij})^2 + (\sigma_{b2b} B_{ij})^2} + \left(\frac{\alpha_t}{\sigma_t}\right)^2 + \left(\frac{\alpha_b}{\sigma_b}\right)^2. \tag{2.5}$$

Evaluation of Equation 2.5 now requires optimization over α_t and α_b.

Similarly, systematic uncertainties for the visible energy and distance reconstruction are introduced with a pull term for each energy bin j and distance bin i:

$$\begin{aligned}\chi^2 = &\sum_{i,j} \frac{\left(S_{ij} - \left((1 + \alpha_t + \alpha^{(j)}_{E_{vis}} + \alpha^{(i)}_L)T_{ij} + (1+\alpha_b)B_{ij}\right)\right)^2}{S_{ij} + (\sigma_{b2b} T_{ij})^2 + (\sigma_{b2b} B_{ij})^2} \\ &+ \left(\frac{\alpha_t}{\sigma_t}\right)^2 + \left(\frac{\alpha_b}{\sigma_b}\right)^2 + \sum_j \left(\frac{\alpha^{(j)}_{E_{vis}}}{\sigma^{(j)}_{E_{vis}}}\right)^2 + \sum_i \left(\frac{\alpha^{(i)}_L}{\sigma^{(i)}_L}\right)^2\end{aligned} \tag{2.6}$$

Each χ^2 evaluation requires minimization of all introduced nuisance parameters α, resulting in values of the nuisance parameters that best describe the data. In Figure 2.14, 17 bins in energy and 25 bins in distance are used, resulting in 44 nuisance parameters that have to be simultaneously minimized.

2.3.2 Covariance matrix based χ^2

A different way to take correlated uncertainties into account is achieved by using covariance matrices. In this case, Equation 2.6 simplifies to

$$\chi^2 = D^T M^{-1} D \tag{2.7}$$

In this expression, the data matrices D are a serialised version of the 2D histograms shown in Figure 2.14. First all energy values for the first distance bin are listed, then all energy values for the second distance bin, continuing until all distance bins have been included resulting in an $N \times 1$ matrix. For the binning scheme used in Figure 2.14, $N = 425$. D is the difference between this $N \times 1$ matrix for the observation and the sum of the background and the prediction, respectively indicated by S_{ij}, B_{ij} and T_{ij} in Section 2.3.1.

The matrix M in Equation 2.7 contains all uncertainties present in Equation 2.6 and can be decomposed into the sum of several uncertainty matrices, i.e. $M = M_{stat} + M_{b2b} + M_L + M_E + M_t + M_b$. These M matrices follow the same serialisation scheme as the D matrix, resulting in a $N \times N$ matrix. The uncorrelated uncertainties are diagonal matrices while the correlated uncertainties result in matrices with off-diagonal elements. In order to calculate the χ^2 in Equation 2.7, a CPU costly $N \times N$ matrix inversion has to be performed. The computing time required for this inversion when using 17 energy bins and 25 distance bins (resulting in a 425×425 matrix) is similar to minimizing the function in Equation 2.6 in a 44 dimensional space. The matrix inversion has the advantage of being deterministic and being independent from any initial guess and allows easy input of previously calculated matrices, e.g. the signal prediction matrix making use of complicated reactor calculations.

2.3.3 Impact of experimental parameters on the sensitivity

The impact of various experimental parameters on the sensitivity of the SoLid Phase 1 experiment are presented in this section using simulated samples. The results of studies like the one presented here motivated the design choices. An overview of the experimental parameters and their design values is given in Table 2.2. When investigating the effect of an experimental parameter, all other parameters are kept constant at their default value. The 'fissile isotopes' and 'spectrum' parameters are not numerical and can therefore not be varied easily. The highly enriched nature of the BR2 fuel warrants the choice of using only ^{235}U. Reactor calculations show that at most 0.41% of fissions come from other isotopes [70]. When the Phase 1 detector design was being optimized, the background model obtained from studies with the SM1 detector was the only background model available.

The IBD efficiency is the product of three individual efficiencies: the ^{6}Li capture efficiency, the ZnS(Ag) detection efficiency and the signal reconstruction efficiency. The ^{6}Li capture efficiency has been fixed to 66% by the choice for two neutron screens in the XZ configuration. Neutron detection efficiency measurements indicate a ZnS(Ag) detection efficiency of 79.4% (see Section 4.5). This value is the result of a long optimization process and is therefore relatively stable. In order to achieve the design IBD detection efficiency of 30%, the signal reconstruction efficiency has to reach 57%.

Number of modules / Active mass

Since the Phase 1 detector is composed of modules consisting of ten planes each, the effect of the detector length on the sensitivity is studied as a function of the number of modules. Effectively, this sudy also provides the impact of increasing or decreasing the active mass, since the active mass changes by 306 kg per module that is added or removed. This effect is shown in Figure 2.15. It is clear that the sensitivity at the best fit mass improves with an increasing number of modules. At least four modules

Parameter	Value
Reactor	
Thermal power (P_{th})	60 MW
Fissile isotopes	^{235}U only
Duty cycle	150 days/year
Baseline	
Point of closest approach	6.2 m
Detector	
Proton density	$5.17 \cdot 10^{22}$ cm^{-3}
Number of modules	5
Dimensions	$0.8 \times 0.8 \times 2.5$ m^3
Active mass	1.6 tons
Data taking time	3 years
IBD efficiency (ε)	30%
Energy resolution	$14\%/\sqrt{E_{vis}}$
Background	
S:B	3
Spectrum	From SM1 data

Table 2.2: Summary of the experimental parameters and the default values used for sensitivity studies.

are needed to cover the phase space allowed in the best fit from Kopp *et al.* [30] when operating the detector for three years.

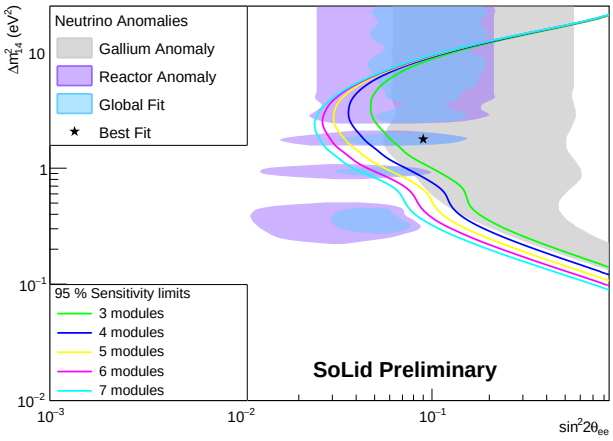

Figure 2.15: Sensitivity of the SoLid experiment to sterile neutrinos as a function of the number of detector modules.

Increasing the detector length hardly moves the sensitivity at high values of Δm^2_{41} while it improves significantly at low values of Δm^2_{41}. This can be understood from Equation 2.3. A more massive sterile neutrino will have a shorter oscillation length when keeping the energy constant. For the highest Δm^2_{41} values, even a short detector contains an entire oscillation length. For the lowest Δm^2_{41} values, a longer detector accommodates a larger fraction of the oscillation length, boosting the sensitivity at low Δm^2_{41} values. The increased sensitivity to $sin^2\,(\theta_{ee})$ is due to the increased number of antineutrinos detected that comes with a larger detector. The effect of increased statistics is discussed in the 'Data taking time' paragraph.

The SoLid experiment collected reactor on data with four modules ($0.8\times0.8\times2.0$ m^3, 1280 kg) during November - December 2017. In January 2018, a fifth module was installed in the container ($0.8 \times 0.8 \times 2.5$ m^3, 1600 kg). From February 2018, all collected data has five modules. Additional space is left in the container for a sixth module ($0.8\times0.8\times3.0$ m^3, 1920 kg), although there are currently no plans to construct a sixth module.

Energy resolution

As mentioned in Section 2.2.4, one of the main problems of SM1 was insufficient light yield, a proxy for the energy resolution. SM1 had an energy resolution of 20% for 1 MeV deposited by electrons or positrons in a single cube, corresponding to approximately 25 detected photons (pixel avalanches or PA) per MeV of deposited energy. In Figure 2.16, the impact of the energy resolution is clearly visible. An improved energy resolution reduces the amount of IBD candidates reconstructed in the 'wrong' energy bin. As a result, the smearing between bins is reduced, which results in a gain in sensitivity. In particular, the sensitivity for large Δm^2_{41} values is improved. At these values, a small change in energy has a significant impact since Δm^2_{41} and energy are inversely proportional (Equation 2.3).

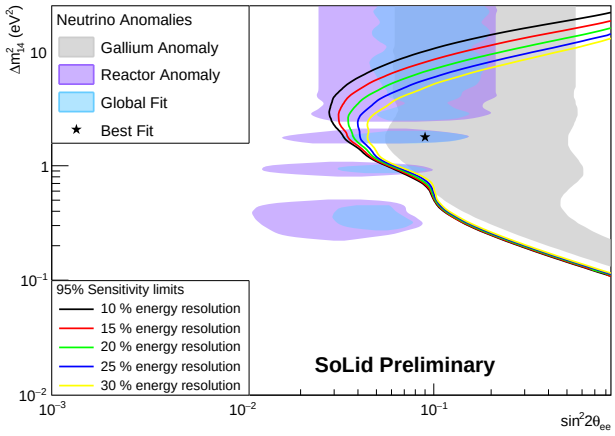

Figure 2.16: Sensitivity of the SoLid experiment to sterile neutrinos as a function of energy resolution.

The updates to the detector design listed in Table 2.1 are mostly geared towards a superior light yield for the Phase I detector. Together, these changes result in an improvement of over 300% on the test bench [66]. CaliPSo measurements indicate the Phase I detector will detect roughly 72 PA per MeV deposited by electrons or positrons, resulting in an energy resolution of $\sim$ 11% for 1 MeV if all the energy is deposited in a single cube.

Point of closest approach

The point of closest approach is limited by the position of the reactor wall, 5 m from the reactor core. Beyond that, the detector can be placed at any distance within the containment building. Due to the shielding, a water gutter and the insulating container, the effective point of closest approach is at 6.2 m. The left plot of Figure 2.17 shows the effect when moving the detector up to one meter towards and away from the reactor core.

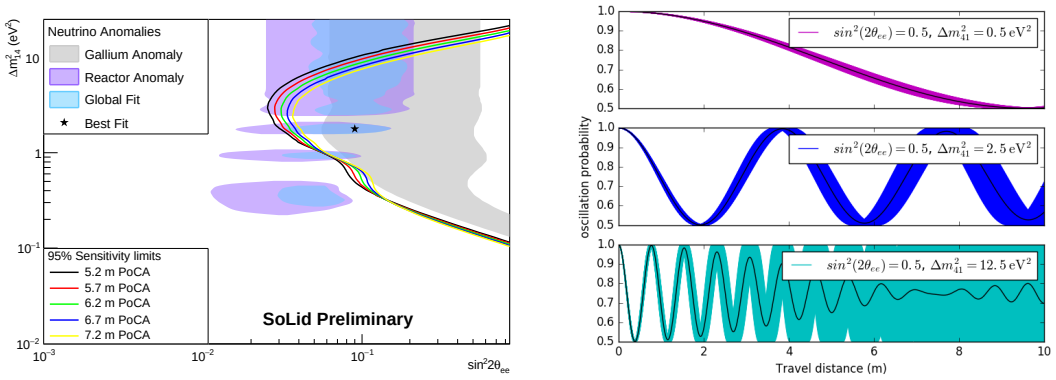

Figure 2.17: Left, the sensitivity of the SoLid experiment to sterile neutrinos at various distances from the reactor core. Right, the impact of the distance on the oscillation smearing due to finite E_{vis} bins for multiple Δm^2_{41} values. For each Δm^2_{41} value, the coloured band represent energies between 3.7 and 4.1 MeV, the most populated energy bin in the simulation. The black line shows the average value.

The impact on the exclusion region for large Δm^2_{41} values can again be explained by the shorter oscillation length. Due to the finite bin size, the oscillation pattern is smeared after a number of oscillation lengths. This smearing due to the energy binning is shown in the right panel of Figure 2.17. There is also smearing due to the distance bins which is not shown here. When moving the detector towards or away from the reactor, the change in number of oscillation lengths is much larger for high values of Δm^2_{41} than it is for low values. Moving the detector backwards, away from the reactor core, exposes high Δm^2_{41} values to significantly more smearing, reducing the sensitivity. Likewise, the increase in sensitivity is larger for high Δm^2_{41} values when bringing the detector closer to the reactor. The increased sensitivity in $sin^2\left(\theta_{ee}\right)$ due to a shorter baseline is an effect of the increased statistics due to the inverse square law. This is discussed in the next paragraph.

Data taking time / Thermal reactor power / IBD efficiency / Proton density / Duty cycle

The effect of increasing the data taking time of the experiment is reducing the relative statistical uncertainty. Extending the data taking time of the experiment indefinitely will not allow probing the entire phase space down to the lowest mixing angles since at a certain point, the total uncertainty will be dominated by systematic uncertainties. Due to the square root behaviour of the statistical uncertainty, added data taking time will have diminishing effects, as can be seen in the left panel of Figure 2.18. Unlike variations examined earlier, additional events do not change the L/E ratio probed by the detector. Therefore, a longer data taking time does not influence the exclusion limit in the direction of Δm^2_{41} at either high or low values. The effect from more events results in an improved sensitivity towards low $sin^2(2\theta_{ee})$ values. This effect does not depend on the origin of the additional detected neutrinos, be it a longer life time, a more powerful reactor with a higher duty cycle, a higher IBD detection efficiency or more interactions due to more available protons or being closer to the source.

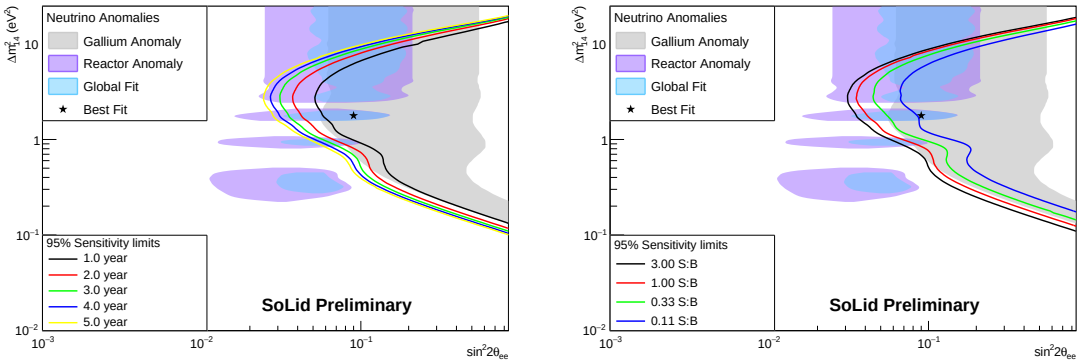

Figure 2.18: Sensitivity of the SoLid experiment to sterile neutrinos for various years of operation (left) and at various S:B ratios. The minimal planned data taking time of the Phase 1 detector is three year, a S:B ratio of three is assumed in all calculations.

Signal to background ratio

The signal to background ratio (S:B) is effectively the average T_{ij}/B_{ij} ratio over all bins. It is obvious that a higher S:B will increase the sensitivity of the experiment. The impact of various assumptions for the S:B ratio is shown in right panel of Figure 2.18. It can be seen that the impact of reducing the background is similar to collecting more data at the same S:B ratio as can be seen by comparing the two panels of Figure 2.18. This can be explained from the relative statistical uncertainty. Each point in these exclusion plots corresponds to different values for T_{ij} as a function of Δm^2_{41} and $sin^2(2\theta_{ee})$ while B_{ij} remains constant. The total statistical uncertainty is calculated from $S_{ij} \approx T_{ij} + B_{ij}$ with only the T_{ij} part providing discrimination power. Increasing the S:B ratio increases the functional part of the data, in effect reducing the relative statistical uncertainty. Hence increasing the data taking time of the experiment and increasing the S:B ratio both result in a smaller statistical uncertainty.

Chapter 3

Neutron identification with SM1

As mentioned in Chapter 2, SM1 was operational from February 2015 until August 2015. During the operational period, data was taken when the reactor was on and off. In addition, data with radioactive sources was collected for energy calibration and neutron efficiency determination.

3.1 SM1 commissioning

The commissioning of SM1 happened from November 2014 until February 2015. Due to the issues mentioned in Chapter 2 and the small dataset collected when the reactor was on in February 2015, no neutrinos were observed. Hence, no oscillation analysis was performed. Both the low light collection efficiency and readout electronics are part of the explanation. The light collection efficiency problems and solutions have been explained in Chapter 2. In this section, the SM1 readout electronics is discussed.

The 32 channels of each of the nine SM1 planes were read out by a purpose built analogue electronics board. This board provides the connection between the SiPMs and the FPGAs where the trigger logic is implemented. The analogue boards thus provide the high voltage to the SiPMs and collect, amplify and digitise the voltage differences from the breakdown of the APDs in the SiPMs. It is this digitised signal which is fed to the FPGAs in the GLIB [71], the digital electronic boards. Two analogue boards are connected to a single GLIB, leaving half the capacity available on the last GLIB to operate the muon veto panels. Despite two planes being read out by the same GLIB, planes did not communicate, essentially making the SM1 detector nine single plane detectors operated in parallel.

3.1.1 Analogue electronics

The analogue electronic boards developed within the SoLid collaboration were the main cause for the issues briefly mentioned in Chapter 2. The boards are therefore discussed in more detail in this section. Most of the issues summarized in this section were only found out during the three month long commissioning period.

The signal flows from left to right in Figure 3.1, beginning with two rows of connectors for the mini-coax cables to the SiPM PCBs mounted in the frames. Two cabled analogue boards are shown in the right panel. The left bank was used to read out vertical fibres, the right bank for the horizontal fibres. Each four channels share an amplifier (labelled ‘quad amplifier’, LMH6626), the output of which is piped to the corresponding analogue to digital converter (labelled ‘16 CH. ADC’, AD9249). The

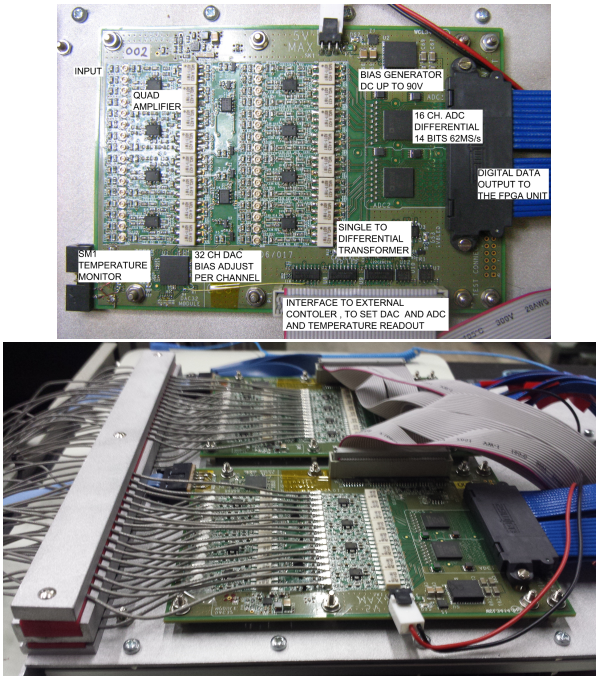

Figure 3.1: SM1 analogue electronic boards, left the bare board with indications of the function of several components [53], right two cabled boards mounted in the cassette that also houses the shared GLIB (not in the picture).

resulting digital signal is then sent to the GLIB via the blue ribbon cable on the right of the board.

It is suspected that during the production of the boards, a reel of passive components, either resistors or capacitors, providing the connection between the mini-coax connectors and the quad amplifiers ran out. This reel was probably replaced by a new reel of passive components with slightly different specifications, giving rise to a different pulse shape in the channels with components from the new reel.

The DC/DC converter that provides the bias voltage to the SiPMs (labelled '32 CH DAC', LT3482) has a switching frequency of 650 kHz. This switching is picked up by the channels located closest to the converter, resulting in oscillatory noise with the same frequency. As a result, 2% of the detector channels had to be masked since the amplitude of the noise was close to the trigger threshold. Channels further away were not masked but also experienced oscillations at 650 kHz. Another cause of oscillations were the amplifier circuits, inducing oscillations between 6 and 8 MHz on all channels. In the channels that were affected most, these oscillations had an amplitude up to 3 PA. The oscillations and the undershoot caused by capacitances in the amplification circuit are shown in Figure 2.6, but another example is presented in Figure 3.3.

During the analysis of the data produced by the SM1 detector, both undershoot and noise corrections were developed. The former based on deconvolving the signal from the stray capacitance that caused the undershoot in the first place, the second was an empirical method using a fast fourier transform so the dominant oscillating frequencies could be subtracted. Neither of these methods were deployed by default in the data analysis. For both corrections, the additional uncertainty from an extra processing step was not cost effective, e.g. the undershoot correction introduced a slope in the pedestal for some waveforms. Additionally, the noise subtraction was very CPU expensive, preventing a swift progression of the analysis.

3.1.2 Gain determination

To guarantee a homogeneous detector response, all channels had to be equalized. This is achieved by equalizing the gain, i.e. the amplitude of a single PA, expressed in ADC/PA, of all channels. The gain is a feature of the digitisation electronics and depends on the used hardware, the applied voltage and indirectly on the SiPM temperature. Since the hardware is invariant over the duration of the experiment and the temperature effect is known [67], only the variation as a function of voltage had to be determined. For SM1, the voltages were chosen such that the gain is the same on all channels.

The gain is determined from dark count spectra such as those shown in Figure 3.2. Thermal excitations in the SiPM create a free electron, which triggers an avalanche in that APD, causing a 1 PA peak in the data. Higher amplitude peaks in the dark count spectra are caused by cross talk between APDs. The amplitude of all SiPM peaks have an intrinsic distribution due to poissonian nature of the electron avalanche that makes up the signal. The Hamamatsu S12572-050P SiPMs convert a single detected photon typically in $1.25 \cdot 10^6$ electrons when operated at 25 °C and with a voltage of 2.6 V over the breakdown voltage, resulting in a relative uncertainty of 0.1% on the amplitude of the signal [63]. Due to the oscillatory noise, the amplitude of a peak depends on the phase of the oscillation. In SM1, the uncertainty due to the oscillation phase is over 30%, making the gain determination much more challenging.

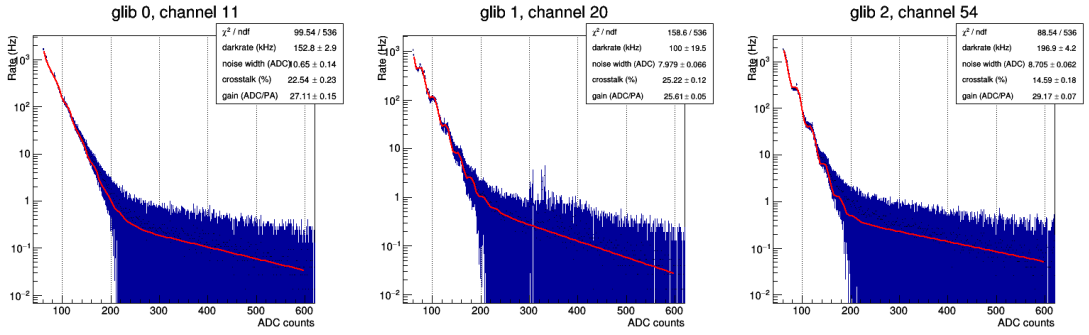

Figure 3.2: Gain determination during a calibration run for three channels selected to show the range of noise present in the SM1 detector.

In order to determine the gain of a channel at a given voltage, a pedestal subtracted dark count spectrum is created using data collected with the random trigger. Due to the undershoot, the average value of all samples provides the pedestal level. The dark count spectrum is created from the pedestal subtracted value of all local maxima of the waveforms in the random trigger dataset. Without a threshold, most of the entries in this spectrum would be the oscillation maxima. In order to avoid these entries, a threshold is set above the oscillation amplitude of most channels.

The resulting spectrum is then fitted with the following function:

$$f(x) = A \sum_{i=1}^{n} B^{(1-i)} e^{(x-iC)^2/(2D^2)} + Ee^{-Fx} \tag{3.1}$$

In this equation, A is the rate of single PA peaks, B is the cross talk probability, C is the gain and D is the amplitude of the oscillations. Additionally, an exponential function is added to describe the tail of the spectrum. The function in Equation 3.1 was designed to determine the gain, all other SiPM parameters returned by this fit were not used.

Performing the fit at several voltages allows determining the gain - voltage slope for every channel. This slope is required to determine the voltage needed to set all SiPMs such that their gain is 25 ADC/PA. Using this method, the gains were equalized to a precision of 20%. After the commissioning, crossing muons allowed an equalisation to 2% [53].

3.2 Neutron identification

Based on the different decay times of the PVT and ZnS(Ag) scintillators, a neutron identification algorithm was developed. In particular, the long decay time of the ZnS(Ag) scintillator results in an initial peak followed by a number of peaks of decreasing amplitude. In contrast, the scintillation light from PVT consists of a single sharp peak. Example waveforms for each scintillator are shown in Figure 3.3.
In this thesis, signal originating from ZnS(Ag) is called nuclear scintillation (NS) since it is signal from alpha and tritium particles. PVT signal are predominantly cause by electrons, positrons, muons and photons, it is therefore dubbed electromagnetic scintillation (ES). Particle identification (PId) relies on the integral over amplitude ratio $\mu = I/A$ of the signal. The two waveforms in Figure 3.3 were selected to have similar amplitudes, clearly showing μ is much larger for NS signal than for ES, allowing discrimination between the two.

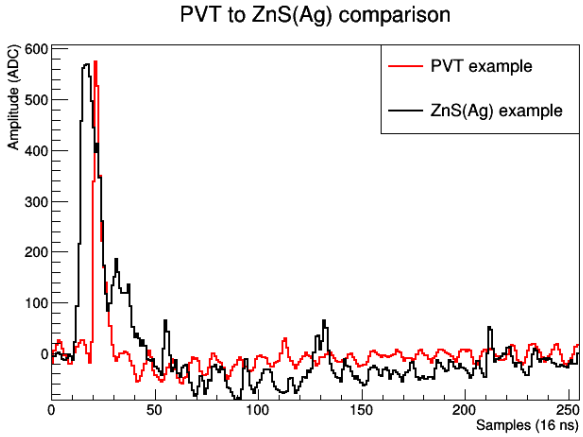

Figure 3.3: Comparison of an ES signal (red) and NS (black) signal candidate. These candidates were selected to have a similar amplitude.

The coincidence requirement of the SM1 trigger guarantees there is always at least one X signal for every Y signal and *vice versa*. In order to improve the separation between NS and ES signals, μ_x and μ_y are combined. Due to the new reel, a staggering effect between even and odd channels i can be seen in the average μ_i values $\langle\mu_i\rangle$. This is shown in the left panel of Figure 3.4 for one of the planes of the SM1 detector. In order to avoid the reel effect, a correction is applied to μ_i before combining the μ_x and μ_y signal information. The channel correction cc_i aims to bring all $\langle\mu_i\rangle$ to the same value:

$$cc_i = \frac{\frac{1}{n}\sum_{j}^{n}\langle\mu_j\rangle}{\langle\mu_i\rangle}. \tag{3.2}$$

The correction is applied by multiplying cc_i with μ_i, centring all $\langle\mu_i\rangle$ on the same value. The right panel of Figure 3.4 shows $\mu_i \times cc_i$ for the same channels and data as shown

in the left panel.

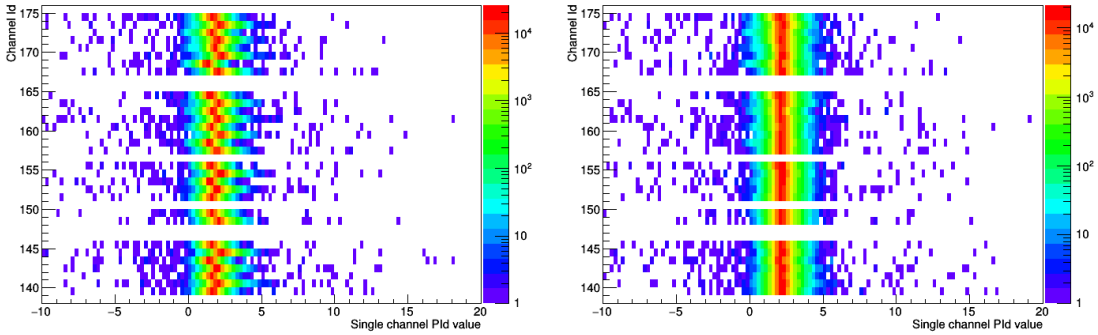

Figure 3.4: The effect of the reel change on the average integral over amplitude ratio $\langle \mu_i \rangle$ for different channels in reactor off data (a neutron poor dataset). μ_i is shown before (left) and after (right) the correction. Channels 138 and 150 are masked due to the high noise amplitude, the remaining 'empty' channels are unused. Each bunch of eight channels correspond to sensors on a different side of the plane.

Figure 3.5 graphically shows the determination of the per channel particle identification (PId, $PId_i = \mu_i \times cc_i$) discussed in the previous paragraphs. This is shown for the x and y channels of an ES and an NS scintillation signal, clearly showing the higher values of the integral for the NS signal.

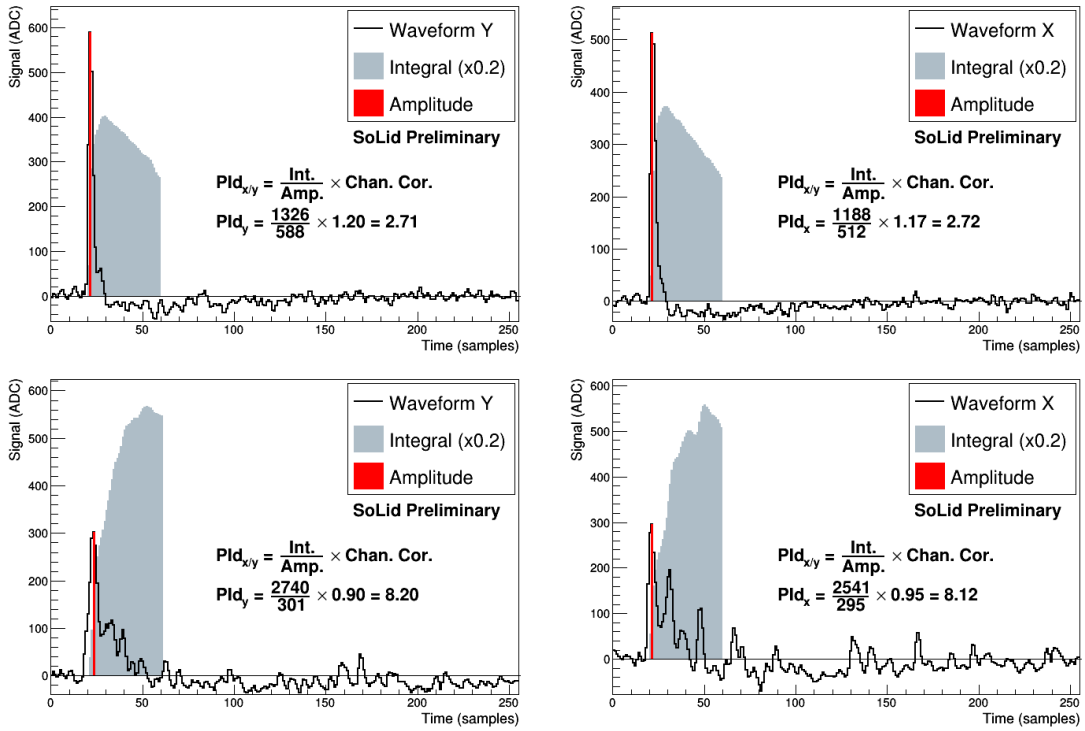

Figure 3.5: Infographic explaining the neutron identification process for an ES signal (top) and an NS signal (bottom) for X (right) and corresponding Y (left). The final PId value is obtained by combining the X and Y PId values.

The information of the X and Y channel corresponding to the same signal is combined by adding the two corrected μ_i values. Hence the combined neutron discrimination parameter PId is given by

$$\text{PId} = \mu_x \times cc_x + \mu_y \times cc_y. \tag{3.3}$$

Signals with a large PId value are more likely to correspond to an NS scintillation and therefore a neutron signal. Signals with a small PId on the other hand correspond to a ES scintillation signal.

Instead of the sum of the two values, multiplication was also considered. However, this did not result in an improved separation between ES and NS scintillation signals, as can be seen in the right panel of Figure 3.6. The two PId distributions look similar, but when multiplying the corrected μ_i values, the tail of the distribution is much broader. Also the description of the neutron population would be made more complex, moving from a roughly Gaussian distribution for the sum of the two channel signals to the convolution of two roughly Gaussian distributions in case of multiplication.

Despite the poor detector performance, the neutron identification is capable of reliably identifying an NS signal out of 10^5 ES scintillations. This can be seen in the left panel of Figure 3.7. Assuming a Gaussian distribution for the NS PId values and a PId threshold value of 10, which was used in most analyses, results in a neutron selection efficiency of 98.3%. Reducing the PId value will increase the selection efficiency but reduce the sample purity. Also shown in the left panel of Figure 3.7 are PId distributions for datasets where a radioactive source was introduced near the detector for calibration purposes. The positions of these sources are indicated in the right panel of Figure 3.7.

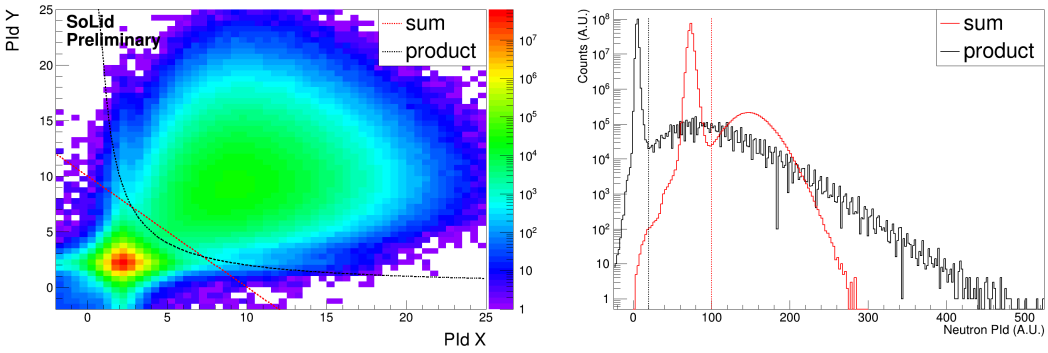

Figure 3.6: Neutron identification parameters of single channel pairs in a neutron rich dataset (left). The bottom left population are ES signals, the top right are NS. The two lines depict possible PId thresholds in different combination schemes. On the right, the 1D representation of the left histogram with sum and product combinations. The proposed PId thresholds shown on the left plot are drawn here as well. The sum combination has been scaled by a factor 5 and shifted by 50 for visibility.

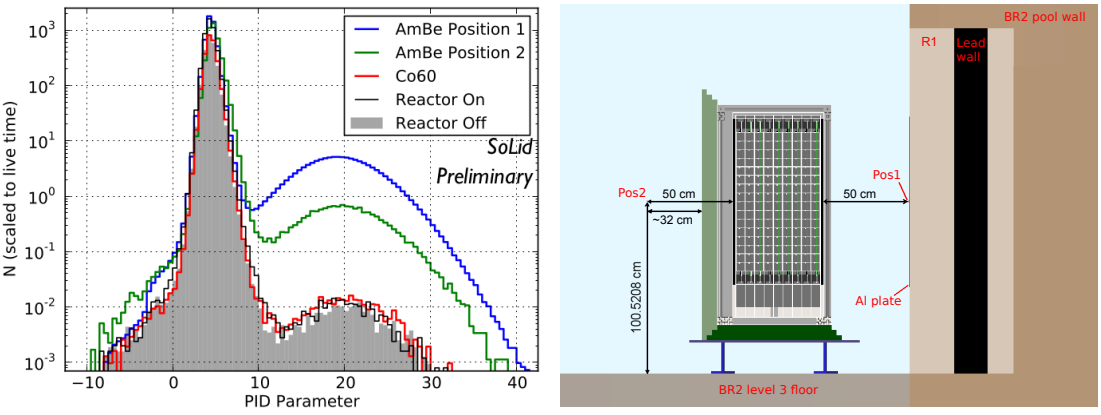

Figure 3.7: Neutron identification for various datasets (left) and the source positions and shielding situation for the source runs (right). The excess due to the AmBe neutron source is clearly visible, as well as the effect of the shielding when comparing the two AmBe positions. No excess is detected with the ^{60}Co gamma source (located at position 1) with respect to the reactor off dataset.

Determination of the integration range

A free parameter in the neutron identification algorithm is the integration range when calculating the integral of the waveform. As mentioned in the Section 3.1.2, the integral of an entire waveform is zero due to the undershoot. Therefore, the integration range should be optimized such that enough of the secondary pulses of the NS waveform are included in the integral without reducing the integral of an ES waveform to zero. Additionally, to minimize the exposure to oscillatory noise, the integral range is chosen to be an integer multiple of the oscillation period, which is eight samples.

To optimize the integration range, the following figure of merit (FoM) is defined:

$$\text{FoM} = \frac{\alpha_{NS} - \alpha_{ES}}{\beta_{NS} + \beta_{ES}}. \tag{3.4}$$

Where α_x and β_x are the mean and width of the respective populations in the distribution of PId values. It is assumed that the populations of ES (low α) and NS (high α) signals are described by a Gaussian. A high FoM indicates a better separation between the two populations. A scan over possible integration ranges is shown in Figure 3.8. For each integration range in the scan, an integral over amplitude histogram was filled for each cube. The two channels were combined by adding their μ values after subtracting $\langle \mu_i \rangle$.

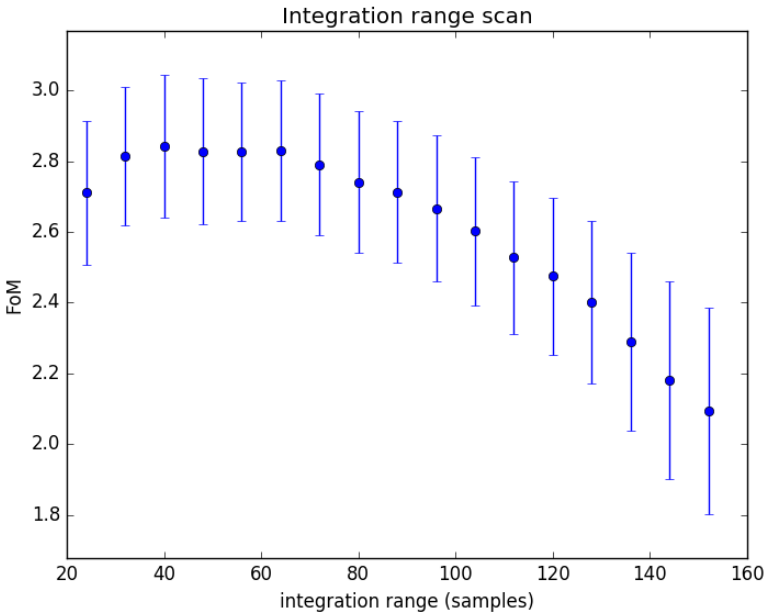

Figure 3.8: Scan over the integration range to find the optimal range for maximal separation between ES and NS signals.

Two Gaussians were fitted to each of the PId distributions obtained with different integration ranges. Using the fitted means and widths, the FoM was determined for each integration range and for every cube. The average and standard deviation of the FoM for each integration range was calculated from the per cube FoM values. These are displayed in Figure 3.8. An integration range of 40 samples was chosen since it had the best FoM by a small margin and the detector equalisation using muons (Section 3.1.2) was performed using 40 samples as integration length.

3.3 Neutron detection efficiency

The detection efficiency of a free neutron in the SM1 detector (ε_n) is the product of two individual efficiencies: the probability for it to be captured on ^{6}Li (ε_{Li}) and the efficiency for reading out and identifying the resulting NS scintillation signal as a neutron (ε_{NS}):

$$\varepsilon_n = \varepsilon_{Li} \times \varepsilon_{NS}. \tag{3.5}$$

The following sections discuss how these efficiencies were determined.

3.3.1 Neutron capture efficiency

The capture efficiency ε_{Li} depends on the neutron source, since different sources have different neutron energies, resulting in a different thermalization process which leads to a different escape probability. Also the initial position and direction of the neutron play a role, since these determine when the neutron will first encounter a lithium screen. For this study, IBD events were simulated using GEANT4. Both the cube of the neutrino interaction and the location inside the cube are randomly chosen, resulting in a number of IBD neutrons originating from cube i, nIBD(i). Similarly, nCap(i) is the number of neutrons originating from cube i that are captured on any ^{6}LiF:ZnS(Ag) screen in the detector. If a neutron is not captured on ^{6}Li, it either escapes the detector or is captured on other nuclei present in the detector. The capture efficiency of each cube i is then determined as:

$$\varepsilon_{Li}(i) = \frac{\text{nCap}(i)}{\text{nIBD}(i)}. \tag{3.6}$$

The neutron capture efficiency of the entire detector can then be calculated as the average of all cubes:

$$\varepsilon_{Li} = 52.0 \pm 0.5(\text{stat}) \pm 3.1(\text{syst})\% \tag{3.7}$$

The systematic uncertainty was determined by varying the thickness of the lithium screens by 14% and the total number of ^{6}Li atoms by 10% according to measurements performed during the SM1 construction process and from specifications provided by the manufacturer [56, 59]. The average detector efficiency hides the large variation for the first and last planes compared to the other planes, as is shown in Figure 3.9. In the IBD reaction, the neutron is emitted mainly in the direction of travel of the neutrino [58]. In the SM1 detector, the lithium screen is placed on the side of the cube facing the reactor. With this configuration, a lot of IBD neutrons created in the last plane are able to escape, explaining the relatively low capture efficiency in that plane [72].

3.3.2 NS signal detection efficiency

The detector efficiency is determined from a comparison between data collected with an AmBe neutron source and GEANT4 simulation of the neutron source. Two source positions were used, as visualised in the right panel of Figure 3.7. The predicted rates per plane are shown in Figure 3.10 for both positions. The large difference in neutron rate between the two positions is caused by the presence of shielding during data taking in position 2.

For an individual cube i, the NS efficiency is given by

$$\varepsilon_{NS}(i) = \frac{R_{data}(i)}{R_{MC}(i)} \tag{3.8}$$

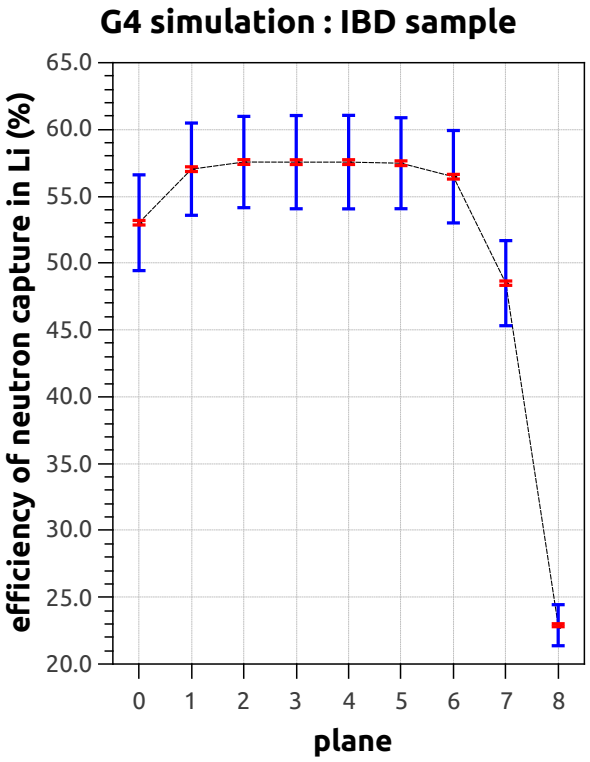

Figure 3.9: Capture probability per plane of IBD neutrons with statistical (red) and systematic (blue) uncertainties [72].

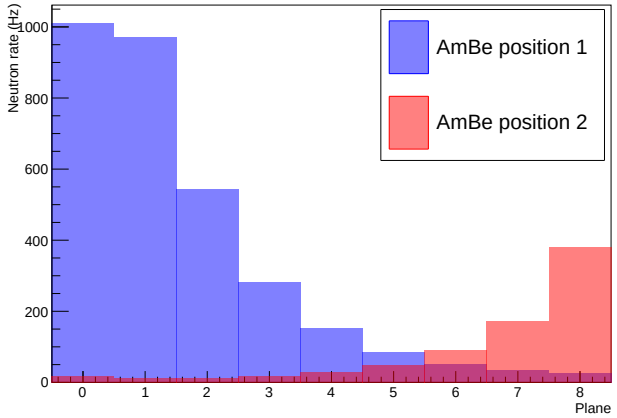

Figure 3.10: GEANT4 predicted neutron rates per plane for source position 1 (blue) and 2 (red) [72].

where $R_{data}(i)$ and $R_{MC}(i)$ are the measured and simulated neutron rate in cube i respectively. The NS efficiency of the entire detector is calculated as the average of the detector efficiencies of the individual cubes.

$$\varepsilon_{NS} = \frac{1}{n}\sum_{i}^{n}\frac{R_{data}(i)}{R_{MC}(i)} \tag{3.9}$$

where n is a subset of all cubes selected as follows: Only those cubes where the observed rate with the neutron source is at least ten times the neutron rate observed without a neutron source in a reactor off sample are considered. Additionally, the relative statistical uncertainty on the cube rate was required to be less than 40%. In order for a cube to be considered, these conditions must be met for both source positions. The first two planes were excluded from the analysis due to a significant amount of dead time for the data collected with the AmBe source in position 1. This increase in dead time is caused by the γ activity of the AmBe source.

These criteria result in a subset of 1325 cubes (57.5%) and an average NS efficiency of

$$\varepsilon_{NS} = 5.46 \pm 0.02(\text{stat}) \pm 1.20(\text{syst})\% \tag{3.10}$$

for position 1 and

$$\varepsilon_{NS} = 5.65 \pm 0.04(\text{stat}) \pm 1.24(\text{syst})\% \tag{3.11}$$

for position 2. The systematic uncertainty is due to uncertainties in the dead time calculation of the readout electronics, which was varied by 20% and the source activity, varied by 10%.

The correlation between the efficiencies of individual cubes found at two source positions is shown in Figure 3.11. Combining the two measurements, the SM1 neutron detector efficiency is

$$\varepsilon_{NS} = 5.51 \pm 0.02(\text{stat}) \pm 1.21(\text{syst})\% \tag{3.12}$$

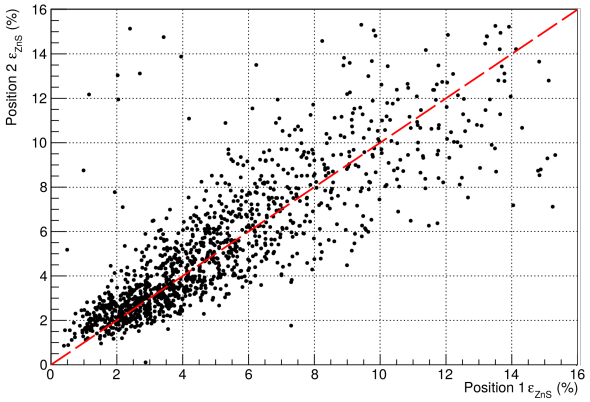

Figure 3.11: Correlation of ε_{NS} (labelled as 'ε_{ZnS}') of cubes that satisfy the selection criteria in both positions [72].

3.3.3 Causes of the low neutron detection efficiency

Since detecting neutrinos relies on detecting the coincidence of a positron and a neutron, the neutron detection efficiency plays a crucial role in the antineutrino detection efficiency for the SoLid detector. With the very low neutron detection efficiency of the SM1 detector, in particular the NS detection efficiency, ε_{NS}, it is impossible to have a competitive detector[1] (see Sections 1.5 and 2.3.3). In order to improve the neutron detection efficiency, the causes for the low efficiency were investigated. This section will elaborate on the two main causes of the low detection efficiency.

Amplitude of the nuclear scintillation signal

Figure 3.11 showed a wide spread for the NS efficiency, ranging from 0.5% to 14% and correlated between the two positions of the AmBe neutron source. This wide range can be explained by attenuation in the WLS fibres. This attenuation effect is shown in Figure 3.12 for cubes for which the distance from the cube to the SiPM is similar in both directions. A factor two in efficiency is observed between the cubes nearest and furthest away from both SiPMs. The attenuation constant of the fibres was measured to be 1.3 ± 0.1 m^{-1} using cosmic ray muons [53]. The fibres in the detector have a length of only 80 cm. Due to attenuation, the high trigger threshold on both the X and Y fibres forming a coincidence results in a low efficiency for cubes that are far away from the SiPM in either the X or Y direction (or both). The loss of half the NS signals after travelling less than one attenuation length in the WLS fibres indicates the trigger threshold is located in the falling side on the NS amplitude spectrum, prompting the hypothesis of a low NS amplitude population which peaks below 6.5 PA

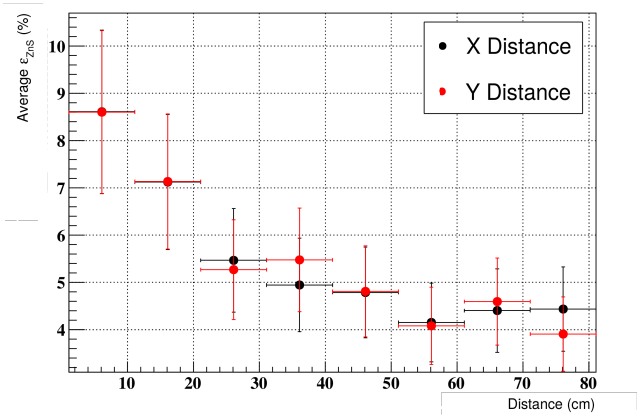

Figure 3.12: NS efficiency (labelled as 'ε_{ZnS}') as a function of the distance between the cube and the SiPM.

A dedicated setup was designed to measure the amplitude spectrum of the NS signals and the impact of the trigger threshold on the NS efficiency. A single cube with one lithium screen was wrapped with Tyvek and placed in a light tight box together with a moderated AmBe source. Two short WLS fibres (65 mm) were placed in the grooves and had a SiPM on one side and a mirror on the other side. Additionally, a

[1]DANSS boasts a 70% IBD detection efficiency, this includes neutron capture and identification and reconstruction of the positron-neutron coincidence [73]. They however provide no evidence for this claim. Like SoLid, PORSPECT aims for an IBD detection efficiency of 30% [74]. This requires a neutron detection efficiency well over 50%.

1 cm diameter PMT was placed against the cube on the face opposite to the lithium screen, reading out the light through a hole cut in the Tyvek. The high light collection efficiency of the PMT allows an NS signal selection which is both more pure and more efficient than what could be achieved by the SiPMs. NS signals were identified with the PMT by requiring the waveform to remain over a relatively low threshold for 4.4 μs, exploiting the long decay time of the ZnS(Ag) scintillator. The PMT neutron trigger was used as an external trigger to read out the SiPMs.

The amplitudes measured by the SiPMs upon a neutron trigger of the PMT is shown in Figure 3.13. Implementation of the SM1 trigger requirements (a 6.5 PA threshold and a narrow coincidence requirement, labelled 'SiPM 0/1 triggering' in Figure 3.13) on the neutron amplitude sample reduces the neutron sample by 75%, resulting in a maximal NS efficiency of 25%, assuming the PMT neutron trigger is 100% efficient. This is much larger that the NS efficiency reported in Equation 3.12 or even with the highest values shown in Figure 3.11. However, the single cube setup is expected to have a better NS efficiency than even the best cubes in SM1 due to better readout electronics and reduced attenuation. The noise and undershoot in the SM1 detector signals further reduce the maximum value for the NS efficiency. The spectrum shown in Figure 3.13 therefore confirms the low neutron amplitude hypothesis. Gains in light yield, which would result in higher NS amplitudes, and a reduction of the trigger threshold would thus increase the NS efficiency.

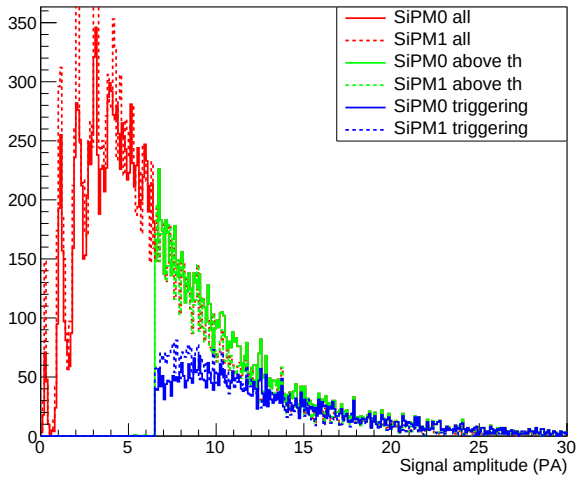

Figure 3.13: Maximum amplitude of a neutron signal measured by two SiPMs on a short WLS fibre ('all', red). The SM1 trigger threshold ('above th', green) and coincidence requirement ('triggering', blue) are implemented offline to show the effect of the readout logic on the efficiency [72].

Coincidence trigger requirement

The XY time coincidence window of the trigger was kept as tight as possible in order to limit the data rate. Enlarging the time window increases the probability of a random coincidence of a dark count of a SiPM in an X and Y channel. The trigger required an X and a Y signal to take place within 48 ns (3 samples). This requirement was based on the coincidence time for ES signals studied using random trigger data. Indeed, in random trigger data where the coincidence requirement is not applied, a three sample coincidence is a valid choice for ES signals, selecting roughly 99.9% of signals. However

for NS signals, the distribution is much wider, resulting in selection of at most 94% of signals. This is shown in Figure 3.14. Both distributions are limited on either side due to the cube reconstruction algorithm in the processing software. Matching X and Y fibres into a signal cube was done within a 6.1 sample (97.6 ns) window to allow for the wider distribution of NS signal. It can be seen in Figure 3.14 that the tail of the ES signal distribution is negligible compared to the peak, while for NS signals, the tails are much more prominent.

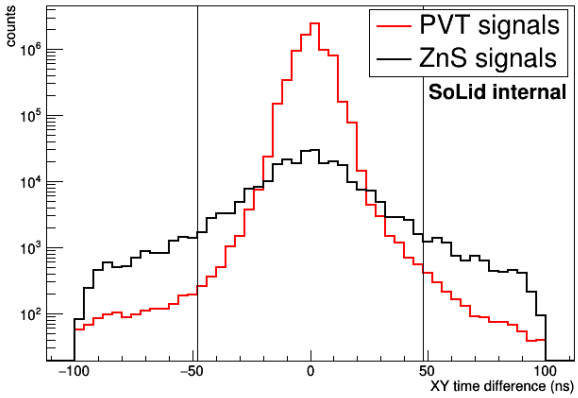

Figure 3.14: Coincidence timing between ES signals (red, labelled 'PVT') and NS signals (black, labelled 'ZnS') using random trigger data. The vertical lines indicate the window used for the online coincidence trigger. Offline, the full range of the plot is used.

The much wider distribution in NS can be understood from the characteristics of the scintillator and the way the neutron time is determined in the SM1 detector. An NS signal has an exponential decay in brightness [75]. Hence in an individual scintillation signal, this will result in a collection of successive peaks of decreasing amplitude. Due to the low light yield of the SM1 detector, statistical effects may result in a secondary peak with a higher amplitude than the first peak. Additionally, the oscillatory noise has an important effect on the low amplitude NS signals. The combined effect of these features significantly broadens the ΔT distribution for NS signals compared to ES signals.

The NS time is determined as the time at which the waveform first crosses the 170 ADC threshold. For the low amplitude NS signals, this happens typically at the coincidence of the initial peaks on the X and Y channels. It may happen that the first peak reaches the threshold on one channel but not in the other channel and that due to a statistical fluctuation a secondary peak makes the coincidence, resulting in a wrong NS time. This effect also broadens the ΔT distribution of NS signals shown in Figure 3.14.

3.4 Conclusion

As discussed in the previous sections, the low neutron detection efficiency obtained for the SM1 detector is due to the trigger. In particular, the coincidence requirement and the high threshold strongly reduce the efficiency. The trigger was implemented in this way to reduce the data rate to an acceptable level. The SM1 detector consisted of only nine planes. Therefore, design changes had to be made in order to keep the data rate of the Phase 1 detector at an acceptable level while creating a competitive experiment. From Figures 3.12, 3.13 and 3.14, it is clear that a decrease in trigger threshold is

essential for a higher neutron detection efficiency, while increasing or getting rid of the coincidence requirement is less crucial. A higher neutron detection efficiency can be achieved by either increasing the light yield, reducing the trigger threshold, or a combination of both. Table 2.1 shows that most of the design changes aim to increase the light yield. A dedicated neutron trigger was developed for the Phase 1 detector. This trigger, mentioned in Table 2.1, works on a single channel, thus eliminating the coincidence requirement. The threshold set in this trigger is the ZS threshold, which is set at values between 0.5 and 1.5 PA. The neutron trigger developed for the Phase 1 detector is discussed more extensively in Chapter 4.

Chapter 4

Commissioning of the Phase 1 detector

As discussed in Chapter 3, the performance of the SM1 detector was below expectations due to several reasons, among others the low light yield and the low neutron detection efficiency. A number of measures were taken to improve both, as is discussed in Section 2.2.4. After completion of the construction, the Phase 1 detector was installed next to the BR2 reactor and commissioned in order to collect data of sufficient quality to perform a sterile neutrino oscillation search. This chapter provides details on this effort, focused mainly on the commissioning of the NS objects. However, the first section will be devoted to the reconstruction and energy determination of ES signals.

4.1 ES object reconstruction

Reconstruction of ES objects in the Phase 1 detector is done in multiple steps. First, the ES signals are reconstructed into cubes giving the location. Second, the energy of each cube is determined.

4.1.1 Cube reconstruction

The orthogonal fibre readout at the end of each row or column of cubes provides only the row or column information. In order to reconstruct a cube, information of the rows and columns has to be combined. In the first step, all possible cubes are formed. In case of multiple signals in one plane or a signal combined with a dark count, too many cubes are reconstructed, as is illustrated in Figure 4.1. An additional problem of this reconstruction is the determination of the energy. By simply combining the values of X and Y channels, some combinations can be assigned an incorrect and too large energy value.

In order to reduce the number of wrongly reconstructed cubes, the asymmetry AS is introduced,

$$AS = \left| \frac{A_H - A_V}{A_H + A_V} \right| \tag{4.1}$$

where A_H and A_V are respectively the summed amplitudes of the peaks on the horizontal and vertical fibres contributing to the reconstructed cube. Cases where the reconstructed cube corresponds to a real signal, such as the cube indicated with '1-1' in Figure 4.1, are expected to have a very low asymmetry since the light acceptance of all fibres is the same. Any asymmetry in these cases is induced by the statistical

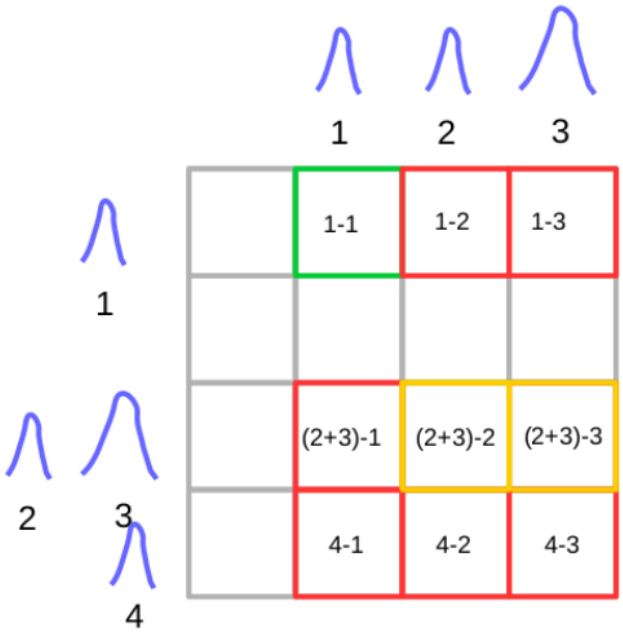

Figure 4.1: Sketch of the reconstruction of ambiguous SiPM signals in the same plane. The detected waveforms are indicated on the side of the 4x4 grid with a corresponding identification, signal four is a dark count and has no match. Cubes that are correctly reconstructed with the correct energy indicated in green, correct cubes with a wrong energy reading are indicated in orange, wrongly reconstructed cubed are indicated in red [76].

nature of counting a small number of photons. Signal from a real object matched with a dark count (cubes '4-1', '4-2' and '4-3') have a very high asymmetry due to the very low amplitude of SiPM dark count signals and the fact that there is typically only a signal in one of the two SiPMs facing a row or column for a dark count. The cases with ambiguity due to the mixing of true signals ('1-2', '1-3', '(2+3)-1', '(2+3)-2' and '(2+3)-3') will have an intermediate asymmetry value [76].

4.1.2 Cube energy determination

Determination of the energy of a cube with a reconstructed ES object is performed in three steps. First, the ADC value per channel is converted to the corresponding number of PAs using the gain. The per channel values are then combined to get the total number of detected photons in that cube. Finally, the PA value of that cube is converted to energy using the light yield per cube. The light yield per cube has been determined from calibration runs with a ^{22}Na source. Ambiguities such as those described in Figure 4.1 are avoided by applying an isolation criterion. This restriction can not be applied in an antineutrino analysis since a significant fraction of positrons cross a Tyvek wrapper and deposit light in multiple cubes. As a workaround, the cube with the highest energy is chosen as the interaction cube. This selection also reduces the sensitivity to wrongly reconstructed cubes.

In this thesis, data collected over two periods will be used: December 2017 and May 2018. The trigger settings between these two periods were different (see Section 4.6). Relevant for the energy determination is the increase in over voltage applied to the SiPMs. Increasing the over voltage increases not only the gain and the quantum efficiency of the SiPM, thus increasing the light yield, but also the crosstalk and the

DCR. At the time of writing, no light yield values are available for the over voltage applied in May 2018, only values for December 2017 are available. From tracking the energy deposition of crossing muons, it was determined the increase in over voltage from the December 2017 to May 2018 leads to a ten percent increase in light yield. When using May 2018 data, a correction factor of 1.1 is therefore applied on light yield values determined for December 2017 settings [77].

4.2 The Phase 1 detector neutron trigger

As mentioned in Chapter 2 and 3, the main trigger of the experiment moved from a threshold trigger for the SM1 detector to a neutron trigger for the Phase 1 detector. This section will reiterate on the workings of the neutron trigger and provide more detail to the design choices involved. In order to explain the neutron trigger logic, the data flow of the Phase 1 detector has to be outlined. Next, the trigger logic and the determination of the trigger parameters will be discussed.

4.2.1 The Phase 1 data structure

Time is split in 256 sample trigger blocks by the FPGAs that handle the trigger logic, the SiPMs are sampled every 25 ns. The trigger blocks, 6.4 μs each, are stored in the FPGA memory until they are either written to disk upon request of a trigger or discarded when no trigger occurred. A trigger block is discarded when the FPGA buffer memory is full and a new trigger block has to be stored in the buffer. Dead time occurs when a trigger requires a block to be written to disk while it has been overwritten by a different trigger already, e.g. the Phase 1 neutron trigger writes 60 trigger blocks before the trigger took place to disk, both for the plane in which the trigger was initiated and for a number of planes surrounding that plane. Dead time is monitored during the operation of the detector since it leads to data loss and is shown in Figure 4.2.

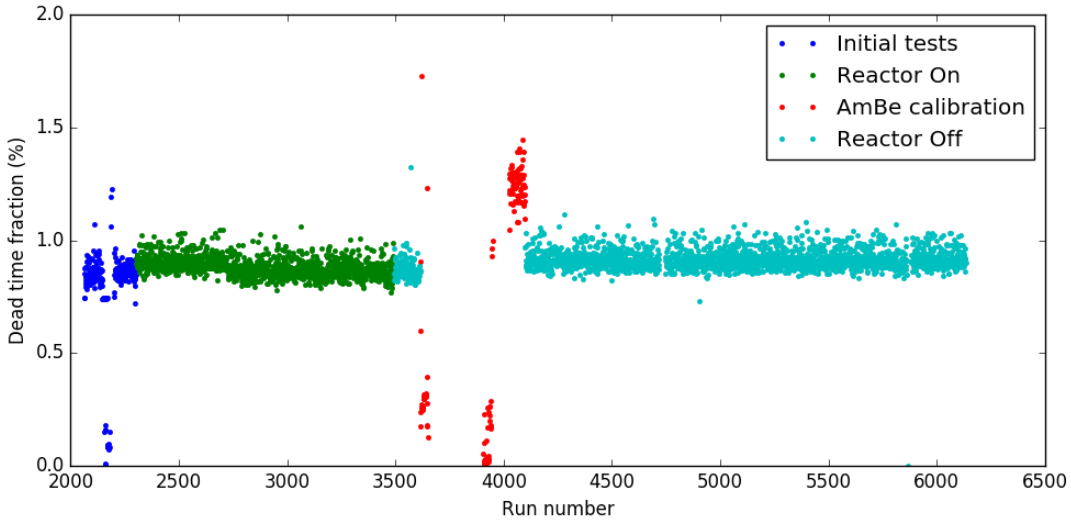

Figure 4.2: Average detector dead time during December 2017. It can be seen that during data taking, the dead time is stable around 1%.

The content of a trigger block consists of zero suppressed (ZS) waveforms. Only those sections of the waveform that exceed the ZS threshold (1.5 PA) are stored in the

buffer. Additionally, a number of samples before and after the crossing of the ZS level are stored as well. Therefore, a block does not have a fixed size, but could contain anything from a few dark counts to a real scintillation signal of a neutron captured on ^{6}Li.

4.2.2 Neutron trigger logic

The Phase 1 detector online neutron identification relies on a peak counting algorithm. When the number of peaks over the neutron buffer ZS threshold in a 256 sample rolling window exceeds nine, the trigger is activated. The window keeps rolling until a local maximum in PoT is reached. Only when this local maximum is reached, the trigger fires. The block in which the trigger takes place is then decisive to determine what data is written to disk. Next to the block in which the trigger took place, also the 60 preceding and four following blocks are written to disk, respectively referred to as the IBD buffer and the post-trigger buffer. These 65 blocks (416 μs) are written to disk for both the plane in which the trigger occurred as well as three planes on either side. This last parameter, the number of planes on either side being read out next to the triggering plane, is named 'planehop'.

The six parameters mentioned in the previous paragraphs, listed in Table 4.1 with typical values, are set in the firmware controlling the FPGAs. The values used in the previous paragraphs are the initial settings used to collect data in December 2017. These settings were then optimized for data collection during later reactor cycles. The optimization aims to improve the trigger purity, thus limiting the data volume, while also keeping the efficiency as high as possible. These optimized values, used from April 2018 onwards, are also shown in Table 4.1. The maximum allowed false positive neutron trigger (FPNT) rate is constrained more by the long term data storage capabilities of the collaboration than the rising dead time accompanying a high FPNT rate. Indeed, the dead time during operation is typically around 1%, as can be seen in Figure 4.2.

	December 2017	April 2018
planehop	3	3
general ZS level	1.5 PA	1.5 PA
neutron trigger ZS level	1.5 PA	0.6 PA
PoT threshold	9	17
IBD buffer	60 blocks	60 blocks
post-trigger buffer	4 blocks	4 blocks

Table 4.1: Neutron trigger parameters with the values used for data collection in December 2017 and from April 2018 onwards. The general ZS level is technically not part of the neutron trigger.

4.3 Neutron trigger parameters

Of the parameters listed in Table 4.1, only 'planehop' and 'IBD buffer' determine the capabilities of the detector to reconstruct antineutrinos from the neutrons captured in lithium screens. They are also the main drivers for the data consumption of the neutron trigger. Both have to be sufficiently large so that in case of an IBD reaction, the positron accompanying the captured neutron takes place in one of the planes within planehop and during the period covered by the IBD buffer. The value of these parameters

is driven by physics arguments and can therefore not be reduced further without a significant reduction in the performance of the detector.

In Figure 4.3, the time difference and plane distance (ΔZ) between the positron and neutron in simulated IBD events is shown. The IBD buffer parameter value determines the fraction of the ΔT distribution, shown left, that is stored. With a value of 60 blocks (384 μs), the positron signal is within the buffer for $99.72 \pm 0.15\%$ of the simulated IBD events. The planehop parameter determines at what ΔZ value the distribution is cut. With a planehop parameter value of 3, $99.76 \pm 0.15\%$ of the positrons are kept.

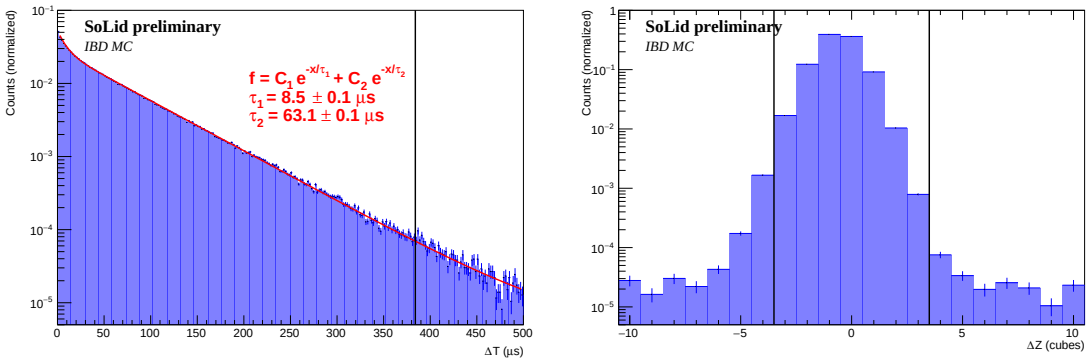

Figure 4.3: ΔT (left) and ΔZ (right) distributions between the positron and neutron signal of simulated IBD events in the five module Phase 1 detector [78]. The regions selected by the neutron trigger settings used in December 2017 are indicated with vertical lines.

The PoT and neutron ZS threshold levels determine the trigger rate and thus the purity and efficiency. Increasing the PoT level will result in a sample with higher purity but will reject NS signals that have a limited number of peaks. Reducing the ZS level will increase the number of SiPM dark counts in the PoT value. Figure 4.4 shows the neutron trigger rate for a number of PoT values for two different ZS thresholds both when the container was hot and cold. Low PoT points have a high trigger rate and a high efficiency but a low purity. The sample purity is determined from the fraction of triggers that pass the offline NS identification criterion (see next paragraph), it is about 15% for the settings used in December 2017 and 47% for the May 2018 settings. The relative NS detection efficiency on the Y-axis of both panels of Figure 4.4 is determined from comparison to the rate passing the offline trigger in the December 2017 settings [79].

The lack of difference between the two temperatures indicates the main driver of the FPNT rate is not temperature dependent, excluding dark counts as the main background to the neutron trigger. It can also be seen that reducing the ZS threshold to 0.5 and at the same time increasing the PoT threshold to 17 will increase the purity of the triggered sample while keeping the efficiency constant. This implies a reduction of the data volume collected by the trigger, which allows expansion of the IBD buffer, the post-trigger buffer and/or the planehop values.

The post trigger buffer influences neither the neutron trigger efficiency or purity nor the antineutrino reconstruction probability; no physical events are expected to take place after a neutron is captured. The data in this time window is stored with exactly the same read out settings as the IBD buffer window, allowing the data in this window to be used for accidental background studies. This topic will be touched upon later in this chapter.

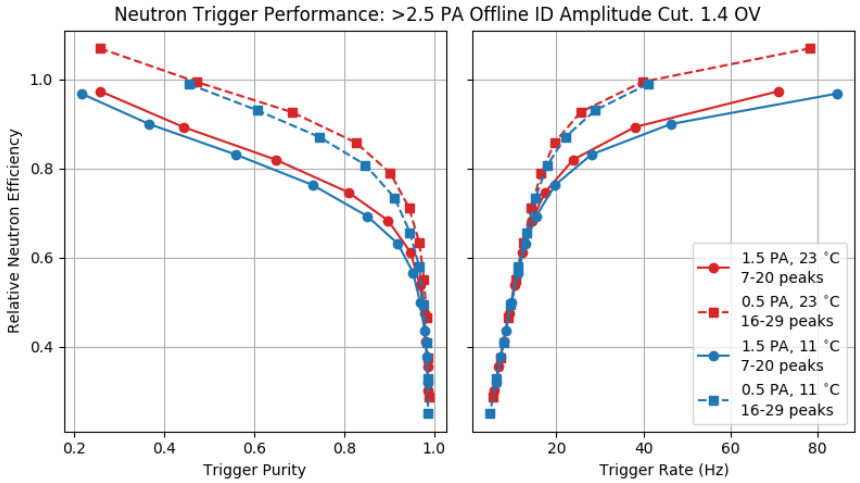

Figure 4.4: The relative efficiency of the neutron trigger as a function of purity (left) and trigger rate (right) for a variety of PoT and two ZS threshold values [79].

4.3.1 Offline NS identification

Since the neutron trigger is based on a single channel, offline algorithms are required to determine the cube in which the ZnS(Ag) scintillation took place. Additionally, this step allows pruning the neutron triggers to reject the FPNT background mentioned in the previous section. In the offline trigger, four fibre coincidences are made based on the PoT of two by two orthogonal channels, as is illustrated in the right panel of Figure 4.6. The online trigger provides the channel and the time in which the trigger took place. This channel is combined with the channel at the other end of the row or column. For the orthogonal channels, a scan is performed over all 16 columns or rows to find the channel pair with the highest combined PoT.

For these four channels, the integral and amplitude is calculated. Up to this point, the only available time information concerning the neutron is the time provided by the online trigger. Since the online trigger is based on the PoT of the last 256 samples, the trigger time is typically located at the end of the waveform. Therefore, the integral for each channel (I_i) is calculated over the 512 samples prior to the online trigger time. The amplitude for each channel (A_i) is the amplitude of the highest peak found within the integration window. Using the average integral over amplitude ratio 'IonA'[1]

$$\text{IonA} = \frac{1}{4}\sum_{i=1}^{4}\frac{I_i}{A_i}, \tag{4.2}$$

an FPNT rejection is performed. The IonA versus amplitude plot for calibration data collected in March 2018 with a neutron source (AmBe) mounted on CROSS is shown in Figure 4.5. It can be seen that a large population exists at high amplitudes. These amplitudes are consistent with crossing muons, the two peaks at low IonA values and with an amplitude of 8000 and 16000 ADC are due to saturation of the analogue to digital converters, a telltale sign of a crossing muon. Triggers in the 16000 ADC peak have saturation on all four fibres whereas the peak at 8000 ADC is due to saturation

[1] 'IonA' is similar to the μ parameter that was used in the analysis of the data collected with the SM1 detector, described in Chapter 3. It was chosen to change the name of this parameter at this point in the thesis in order to maintain uniformity with the notations used within the SoLid collaboration.

of only one direction. This is typically the Y direction since muons travel mostly downwards.

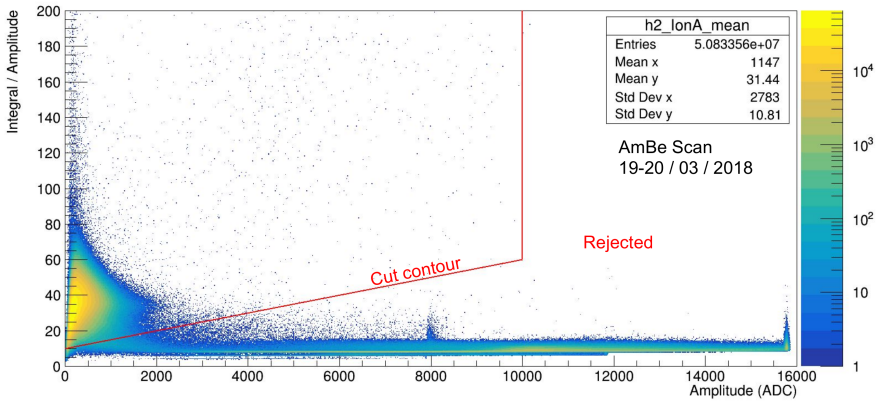

Figure 4.5: The average integral to amplitude ratio (IonA) of the channels of a cube as a function of the mean amplitude of those channels [79]. The clusters at low IonA values and amplitudes of 8000 and 16000 ADC are due to the saturation of the electronics, behaviour consistent with crossing muons. Also shown is the offline selection that is made, all events that fall right of the 'cut contour' line are considered FPNTs.

Signals in cubes with an IonA and amplitude value combination above and left of the empirically optimised line indicated in Figure 4.5 are considered 'true' NS triggers. All others signals are rejected as FPNTs.

4.3.2 NS signal start time determination

As mentioned in the previous paragraph, the time provided by the online neutron trigger is the time at which the PoT reaches a local maximum. This time corresponds to the tail of the NS signal instead of the start. The tail typically consists of a high number of small peaks, whereas the start of the ZnS scintillation consists of only a few large peaks. Due to the long tail of an NS signal, the online trigger time can be up to 12 μs later than the actual start time of the scintillation. An example of this is shown in Figure 4.6. It can be seen that there are approximately 200 samples between the online trigger (green inverted triangle) and the waveform start time (red triangle) for this particular NS signal. Moreover, the online triggers for the four channels in a cube do not take place at the same moment. There is a difference of 50 samples between the earliest and latest online trigger for this signal.

The online neutron trigger time is subject to statistical fluctuations in the number of detected photons and varies between channels. Therefore, it does not serve as a good basis to define coincidences between ES and NS signals required for antineutrino detection. An algorithm to determine the start time of the NS signal using all four channels was developed. The algorithm should work both for NS signals that are isolated like the one shown in Figure 4.6 as well as for NS signals where other nearby signals take place and share light on one or more fibres.

Due to the Phase 1 detector design, NS and ES signals in the same row or column of cubes will share two fibres (four in case of both signals taking place in the same cube). When the ES signal precedes the start of the NS signal by a small number of samples, the ES signal might be mistaken to be part of the NS signal, thus removing a coincidence and assigning a start time to the NS signal that is too early. These

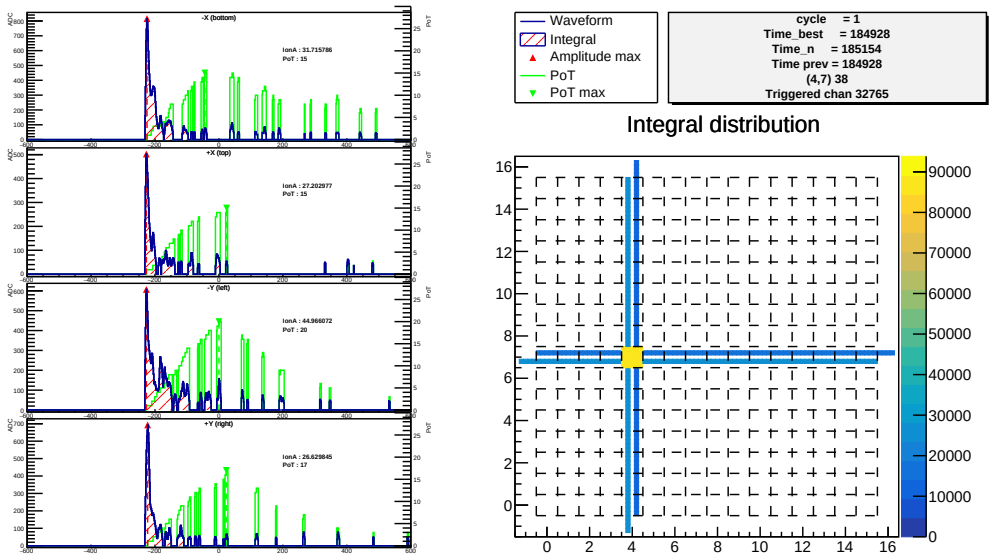

Figure 4.6: Example of a reconstructed neutron in plane 38 of the Phase 1 detector. The four waveforms (blue, left axis) and PoT variables (green, right axis) are shown in the left panels of the figure as a function of time (samples). On the right, a plane map with the fibres that detected the neutron is shown. The fibres are colour coded to the integral detected by each fibre [80].

coincidences are dubbed 'shared'. Due to the two dimensional orthogonal fibre layout of the SoLid detector, shared coincidences are those where the ES cube (X_{ES}, Y_{ES}, Z_{ES}) and the NS cube (X_{NS}, Y_{NS}, Z_{NS}) satisfy the following condition:

$$\text{shared: } Z_{ES} = Z_{NS} \;\&\; (X_{ES} = X_{NS} \;||\; Y_{ES} = Y_{NS})\,. \tag{4.3}$$

All coincidences that are not shared are considered 'exclusive' and fulfil the logical counterpart of Equation 4.3:

$$\text{exclusive: } Z_{ES} \neq Z_{NS} \;||\; (X_{ES} \neq X_{NS} \;\&\; Y_{ES} \neq Y_{NS})\,. \tag{4.4}$$

For exclusive coincidences, the reconstruction of the NS signal start time is more robust.

A simple algorithm to determine the NS signal start time shows the impact of shared coincidences. This simple start time determination works as follows. Assuming a sufficiently high light yield to avoid the timing issues that plagued the SM1 detector (Section 3.3.3), the peak with the maximal amplitude in the four fibres reading out the cube is considered to be the first peak of the NS signal. In each channel, the maximal peak search window was limited to 512 samples before the emulated neutron trigger time[2]. The NS start time is computed as the average time obtained from the highest amplitude peak of the four channels in the cube. To study the algorithm accuracy, the time difference (ΔT) between ES and NS signals is determined by applying the algorithm on a calibration run with an AmBe neutron source. This time difference is shown in Figure 4.7. The ΔT shape for exclusive coincidences is close to the expected shape shown in the left panel of Figure 4.3. The difference in shape between shared and exclusive fibres can be seen clearly. In particular in the first 12.6 μs (512 samples), the ΔT shape of the shared fibre prompt-neutron coincidences is distorted. Beyond this range, the shapes of the two ΔT distributions are similar since any ES signals taking place outside the scan window do not influence the start time reconstruction.

[2]Beyond the search window, there is no difference between shared and exclusive coincidences.

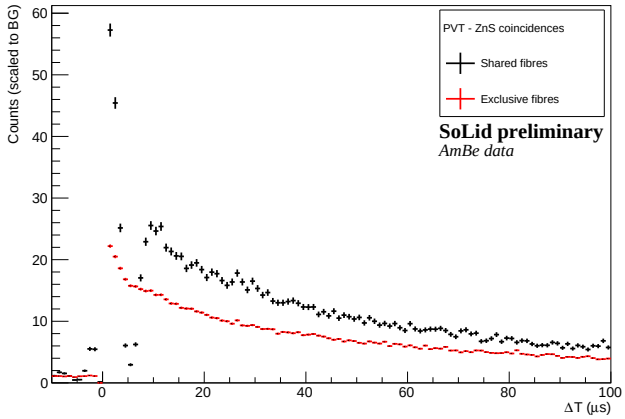

Figure 4.7: ΔT distribution of ES-NS coincidences for AmBe neutron source calibration data using a simple start time algorithm for shared and exclusive fibres.

In order to correct the shape of the ΔT distribution for coincidences with shared fibres, a more elaborate start time reconstruction algorithm is required. First, in order to avoid the mismatched search windows present in the simple method, all search windows are fixed relative to the trigger time of the triggering channel. Second, the start time reconstruction no longer relies on the amplitude of the peaks. Because the light yield improvements made for the Phase 1 detector benefit both ES and NS signals, the amplitude of neutron capture on ^{6}Li remains relatively low; nearly all ES signals preceding an NS signal will have a higher amplitude than the highest amplitude peak of the NS signal. The start time reconstruction therefore relies only on the timing of the individual peaks and their width, where the width of a peak is defined as the time it takes for the waveform to fall back to half the maximal value of the peak. Within a time window of 512 samples ahead of the trigger time, a time sorted list of all peak times (t_i) and peak widths (w_i) on the four channels is created. Next, the peaks are clustered according to the 'minimal gap time' (MGT) parameter. The first cluster is seeded by the first detected peak within the time window. A loop through the remaining peaks adds the considered peak (peak N) to the latest cluster when

$$t_N < t_{N-1} + w_{N-1} + MGT. \tag{4.5}$$

If the condition in Equation 4.5 is not met, a new cluster is created with peak N as seed. The time assigned to a cluster, i.e. the 'cluster time', is the time of the seeding peak of that cluster.

The size of each peak cluster is determined using the so-called 'large cluster size' (LCS) parameter, i.e. the minimum number of peaks a cluster is required to have in order to be considered large. The reconstructed NS start time is the cluster time of the first large cluster in the set of peak clusters formed from the peaks in the four channels. When there is no cluster passing the LCS requirement, the cluster time of the largest cluster is used instead. An example of the first large cluster time (FLCT) NS start time determination is given in Figure 4.8. In this example, all peaks of the NS signal are in a single cluster. The MGT parameter guarantees the peak observed by all four channels is not considered a part of the NS signal waveform.

The NS start time reconstruction algorithm introduces two parameters, MGT and LCS, which were set at a value of respectively 15 samples and 13 peaks after an optimization comparing the relative shapes of the shared and exclusive ΔT distributions.

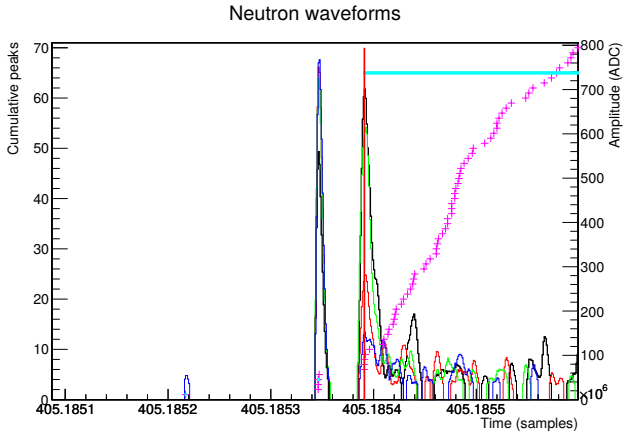

Figure 4.8: Example of the NS start time determination using the algorithm described above. The black, red, blue and green lines are the waveforms, the cumulative number of detected peaks is shown using pink pluses, the clusters are indicated with horizontal cyan lines and the reconstructed NS start time is indicated with a vertical red line. With the simple algorithm used in Figure 4.7, the NS start time would be set at the peaks some 40 samples before the newly reconstructed NS start time.

The shape of the exclusive coincidences is assumed to be correct for all values of both parameters since it is much harder to wrongly reconstruct the NS start time. Indeed, a multi-cube ES signal is required to wrongly reconstruct the ΔT between the ES and NS signals. Additionally, at least one ES cube must share fibres with the NS cube and another ES cube must be exclusive. On top of that, the fibre sharing cube must be within one MGT of the true NS start time (for the simple reconstruction, it is sufficient for the sharing cube to have the highest amplitude and to be within the search window).

In order to check the efficacy of a (MGT, LCS) pair, ΔT distributions are made for both shared and exclusive coincidences, as is shown in the left panel of Figure 4.9 for a non optimal parameter pair corresponding to ($MGT = 5$, $LCS = 5$). The ratio of the shared over the exclusive ΔT distribution is calculated and a function is fitted on both sides of $\Delta T = 0$, each time outside the start time search window. The range corresponding to coincidences where the ES signal takes place after the NS signal is fitted with a 0^{th} order polynomial. On the other side, a first order polynomial is used since a slope is observed over the entire range, as can be seen in the right panel of Figure 4.9. The accuracy of the NS start time for the parameter pair is then evaluated by extrapolating the fitted functions into the search window and calculating the χ^2 for each window. The sum of the χ^2 of both windows is a quality measure of the NS start time algorithm using a specific parameter pair. A scan over (MGT, LCS) pairs, shown in the left panel of Figure 4.10, was performed in order to find the optimal values. The optimal value pair is located at ($MGT = 15$, $LCS = 13$), the ΔT distributions for these parameters are shown in the right panel of Figure 4.10.

4.4 Neutron capture time

The neutron capture time determined from simulation of IBD events guided the decision to set the IBD buffer length at 380 μs. The capture time determined from simulation, $\tau = 63.1 \pm 0.1$ μs, can be verified using two types of events that are known to be rich in neutrons and to some extent mimic the signature of an antineutrino interaction, i.e. an

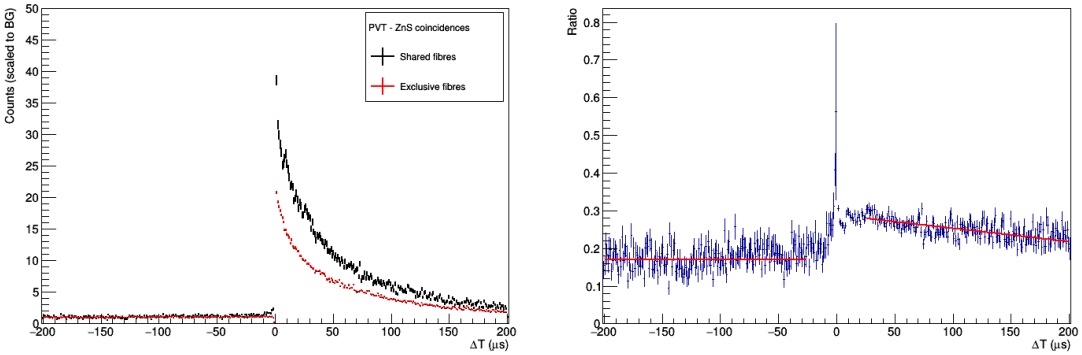

Figure 4.9: FLCT optimization method example ($MGT = 5$ and $LCS = 5$). The left panel shows the equivalent of Figure 4.7. While not fully optimized, it can be seen that the shape of the shared ΔT distribution is much closer to the ideal value than with the simple algorithm shown in Figure 4.7. The right panel shows the ratio of the two unscaled histograms in the left plot as well as the fits outside the search window.

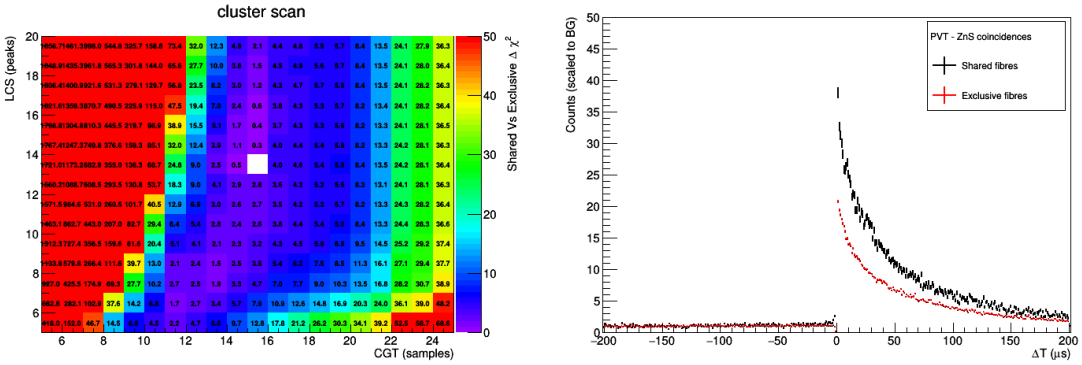

Figure 4.10: Left, a scan performed over (MGT, LCS) pairs in order to determine the optimal parameter values for the FLCT method. Right, the ΔT distributions for shared and exclusive coincidences is shown for the optimal pair.

ES signal followed by the thermalization and capture of neutron on ^{6}Li. The first type makes use of a radioactive source such as ^{252}Cf or AmBe, these are most similar to the actual IBD process. These sources emit neutrons of sufficiently high energy such that elastic neutron - proton scattering produces scintillating protons in the PVT cubes. Indeed, when such a neutron enters the detector, the first elastic scattering processes will quickly take away the available kinetic energy of the neutron, the scintillation light produced by the recoiling protons serves as an ES signal. Once the neutron is fully thermalized, it might get captured on ^{6}Li, producing scintillation in the ZnS(Ag) of the lithium screens. Even though the initial neutron energy is much higher for neutrons produced by these sources, the impact on the capture time is small since the neutron looses its energy exponentially.

Another source of neutrons makes use of cosmic ray muons. Muons crossing the detector have a probability to scatter elastically with a neutron in a nucleus. When enough energy is transferred in the collision, the neutron is freed, thermalizes and is captured again. This process is topologically different from the IBD reaction since the prompt signal is a muon track crossing the detector. The physics process for the neutron capture is however identical: the so-called spallation neutron will thermalize and be captured within a typical time similar to that for neutrons produced in the IBD reaction or radioactive sources.

4.4.1 Neutron capture time from muons

A muon with a sufficiently high energy is a minimally ionizing particle (MIP). A MIP muon crossing a PVT cube deposits 1.8 MeV/cm of visible energy [53]. When crossing the detector, a muon travels through a large number of consecutive cubes, leaving a trail of cubes with a high but track length dependent energy deposit in each cube. This pattern can be recognized by requiring at least 5000 ADC, corresponding to roughly 9.5 MeV, deposited over the entire detector and having at least eight channels on both X and Y that detect data. From these channels, a track can be fitted. These muons are known as 'track muons'. For muons that clip the detector, a track can not be reconstructed. These are recognised by energy deposited in the outer layer of the detector, requiring at least one cube with 6000 ADC in the outer detector layer. These clipping muons are referred to as 'cube muons'.

The coincidence time is determined as the time difference between all reconstructed muons, both track and cube muons, and NS signals that fall within 2 ms from one another. This time difference is shown in the left panel of Figure 4.11. No additional requirements were imposed on either the object nor on the coincidence requirement. The negative side of this histogram, where the NS signal is observed before the muon, gives the rate of accidental combinations. Imposing additional requirements would reduce the amount of accidental combinations, but it would have no influence on the determined capture time. The accidental population extends also to the positive side of the histogram and its rate can be estimated in two ways. The rate can be estimated from an off-time window and subtracted or a constant can be added to the fit in the on-time window.

Clearly visible in the left panel of Figure 4.11 is a large excess at the smallest positive ΔT values. This population is caused by the contamination of muons into the NS sample as discussed in Section 4.2. Since a large fraction of NS signals in this sample are false positives, the region in coincidence with the NS signal start time scan window, 512 samples or 12.7 μs, is excluded from the fit.

The right panel of Figure 4.11 shows a zoomed version of the left panel, including

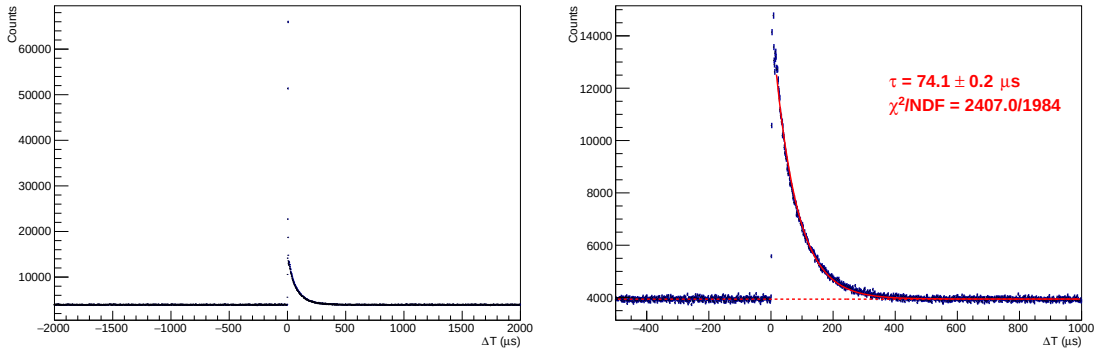

Figure 4.11: Time difference between a reconstructed NS signal and a muon, including both accidental combinations and correlated coincidences. The right panel is a zoomed version of the left panel with a fit to both the accidental (dashed line) and the correlated (full line) coincidences.

an exponential plus constant fit function superimposed. The constant parameter is initialized at the average rate in the negative time window and is subsequently left free to float in the fit of the positive time window. The capture time of muon induced spallation neutrons using a single exponential is determined to be 74.1 ± 0.2 μs. This is not in agreement with the result from the IBD simulation, where 63.1 ± 0.1 μs is obtained by fitting the distribution with a double exponential function. A single exponential function was used in this study since the time range sensitive to the first exponential was excluded due to muon contamination of the NS sample. The discrepancy between the two results is expected, as the capture time is a convolution of the time it takes for the neutron to be thermalised and of the time it takes for a thermal neutron to be captured on a ^{6}Li nucleus. Since neutrons produced in IBD reactions have an inherently low initial energy and muon induced spallation neutrons potentially have a very large initial kinetic energy, the thermalisation component of the muon induced neutron capture time is expected to be longer.

4.4.2 Neutron capture time from an AmBe source

The AmBe source is placed between the first and the second module using CROSS. It is positioned centrally in the XY plane in order to maximise the number of captured neutrons. The NS signal Z distribution after 16.1 s of running with the AmBe source is shown in the left panel of Figure 4.12.

As was shown in the previous section, neutrons generated by muon spallation are captured with a typical capture time of 74.7 ± 0.4 μs. From this, it can be determined that 93% of all muon induced neutrons are captured within 200 μs. In order to determine the capture time purely from the AmBe source, a muon veto of 200 μs is applied, including both track and cube muons; any NS signal observed following less than 200 μs after a track or cube muon is ignored. Other selection or rejection criteria are inspired by a simulation of an AmBe source in the SM1 detector. These criteria are mentioned below [81]. While there are differences between the Phase 1 and the SM1 detector, these will have a minor influence on the result.

The first selection is based on the energy of the ES signal. The energy of the neutrons emitted by the source ranges from 0 to 10.70 MeV, with a mean energy of 4.16 MeV. During an elastic collision with a proton, roughly the same mass as the neutron, on average half of the kinetic energy is transferred to the proton. The resulting neutron energy is roughly halved, with the mean of the remaining kinetic

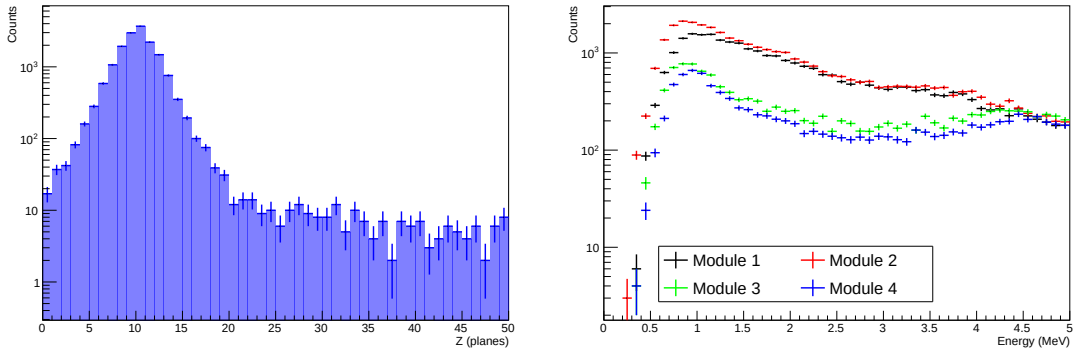

Figure 4.12: The effect of an AmBe source located between planes 10 and 11 on different parts of the Phase 1 detector. In the left panel, the amount of NS signals as a function of plane number is shown, the right panel shows the observed ES spectra for the first four modules at low energies.

energy distribution at roughly 2.08 MeV after one collision. Subsequent collisions will further reduce the mean neutron energy, providing ever less energy to protons.

Since a proton is more highly ionizing than an electron, kinetic energy is converted to visible energy at a lower rate for a proton due to quenching and recombination [5]. Application of the semi-emperical Birks' model to take this effect into account results in the production of scintillation light equivalent with a 0.98 MeV electron for a 2.08 MeV proton. The maximal kinetic energy of 10.70 MeV is similarly converted to 8.15 MeV of visible energy. The energy range is selected by comparing the amplitude of ES signals in the first two modules to the amplitudes of the third and fourth module. From the left panel of Figure 4.12, it can be seen that the first two modules contain the majority of all NS signals and therefore the majority of all high energy proton recoils. The third and fourth modules on the other hand have a relatively flat NS distribution and are therefore expected to be consistent with background. The right panel of Figure 4.12 shows the visible energy of ES signals per module. A clear excess in events can be observed below 4 MeV. As expected from Birks' model, the signal peak is located at roughly 1 MeV. Unfortunately, there is also a higher rate of background events at these low energies. In order to reject the background at low energies, a minimum energy requirement of 1.5 MeV is introduced. The accepted energy range of the ES signal cube is thus between 1.5 and 4 MeV.

The second selection criterion limits the maximum allowed distance between the proton recoil signal and neutron capture. In this case, the simulation of the SM1 detector is less accurate since the increased amount of ^{6}Li in the Phase 1 detector will reduce both the time and distance it takes for a thermal neutron to be captured. However, the effect on the capture distance is minimal since the neutron travels the largest distance while it is not thermal [57]. Ultimately, the only effect of a suboptimal distance selection is either an inefficient selection of 'true' collision-capture coincidences when the $\Delta R = \sqrt{\Delta X^2 + \Delta Y^2 + \Delta Z^2}$ selection is too tight or a relative increase in random coincidences if it is too loose. Therefore, the requirement of $\Delta R < 3$ cubes from the equivalent SM1 detector study is retained [81].

Coincidences between NS and ES signals are determined by considering all cubes with an ES signal up to 500 μs before an NS signal. From this list, the ES cube with the maximum amplitude is selected. The time difference between this cube and the NS signal is used unless this cube is more than three cubes away from the NS signal or the energy of that cube falls outside the $[1.5, 4]$ MeV energy window. In

that case, the NS signal is discarded. Figure 4.13 shows the ΔT distribution of ES-NS time coincident signals. A double exponential and a constant are fitted (full red line). Both exponentials in the fit represent a different capture process. The slower decaying exponential ($\tau = 68.8 \pm 3.6$ μs) represents thermal neutron capture. The fast decaying exponential ($\tau = 12.2 \pm 4.6$ μs) represents epithermal captures, where a non-thermal neutron is captured by a ^{6}Li nucleus.

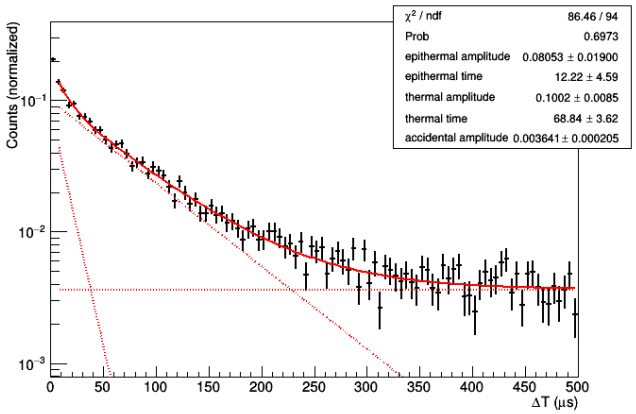

Figure 4.13: Time difference between an NS and an ES signal with an AmBe source placed in the detector. A double exponential with a constant background (solid line) is fitted. The individual exponentials and the constant are displayed as well (dashed lines).

The thermal capture time is the convolution of the time needed for thermalisation and the time a thermal neutron on average needs to be captured on a ^{6}Li nucleus. Since neutrons lose kinetic energy exponentially, the thermalisation fraction is small. It is therefore expected that the thermal capture time of IBD and AmBe neutrons is nearly identical, with the value for AmBe being a bit higher. Comparing the values from the IBD simulation (Figure 4.3), the capture time determined from AmBe data and IBD simulation indeed show this behaviour, respectively 68.8 ± 3.6 μs and 63.1 ± 0.1 μs. The difference between the epithermal capture times (5.7 ± 3.6 μs) and the thermal capture times (3.7 ± 4.6 μs) are consistent.

4.5 Neutron detection efficiency

Similar to the neutron detection efficiency determination for the SM1 detector (Section 3.3), the detection efficiency is split in the capture efficiency and the identification efficiency. The neutron capture efficiency is determined to be 66%, using simulation [61]. No dedicated per cube study similar to the one performed for the SM1 detector [72] has been performed at the time of writing, the quoted figure is the one obtained with the simulation performed during the design process of the Phase 1 detector.

The neutron identification efficiency is determined from a comparison between simulation and calibration data using radioactive sources on the CROSS robot. Figure 4.14 shows the number of neutrons expected and measured after three days of data taking with either an AmBe or a ^{252}Cf source mounted on the CROSS calibration head. By dividing the measured rate by the simulated rate of ^{6}Li captures, neutron identification efficiencies of $73.6 \pm 7.6\%$ and $76.4 \pm 7.0\%$ are obtained for the ^{252}Cf and AmBe sources, respectively. After a fine tuning of the GEANT4 model, the efficiency determined with the AmBe source was determined to be $75.8 \pm 6.8\%$ [82]. These relatively large uncer-

tainties are due to the low amount of statistics available for the planes in the middle of the detector. When only the 32 planes with the highest statistics are taken into account, the uncertainty drops to two percent.

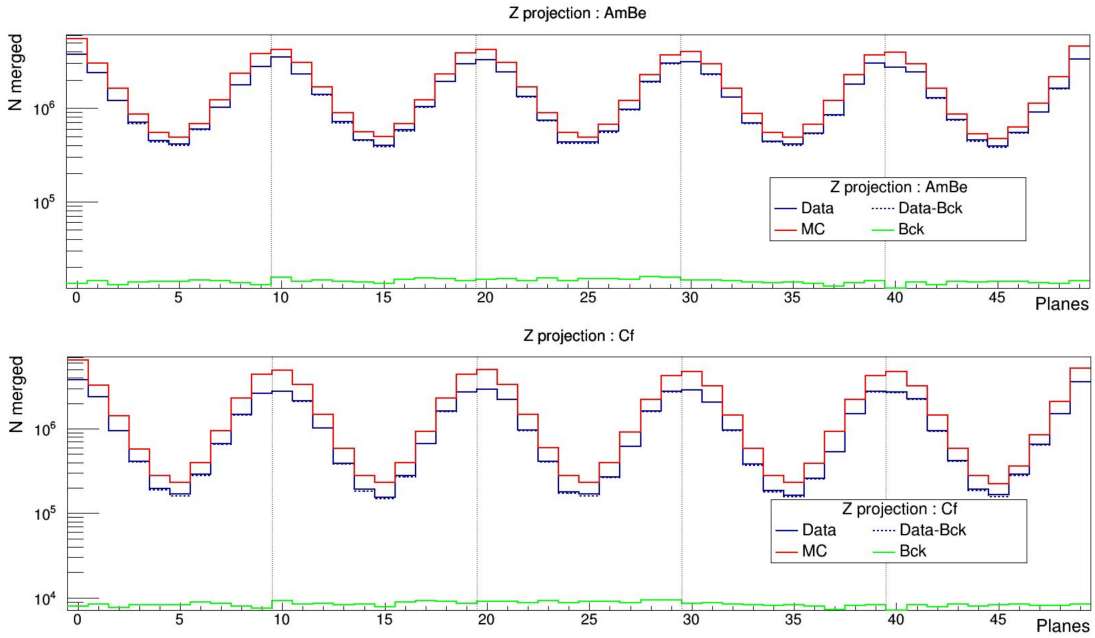

Figure 4.14: Number of neutrons predicted and detected per plane using an AmBe (top) and a ^{252}Cf (bottom) source. Due to the discrete calibration positions (Figure 2.13), the distributions per plane hide a large variation per cube. The background for each plane is estimated from data collected while the source was positioned in a different gap [68].

The difference between the determined AmBe and ^{252}Cf efficiencies can be explained by the very different nature of neutron emission of these two sources. The AmBe neutron source is a compound source existing of mixed ^{241}/!Am oxide and ^{9}Be metal powder. First, ^{241}/!Am decays to ^{237}Np via alpha decay with a half life of 432.2 yr. The alpha particle is then captured by a ^{9}Be nucleus and produces ^{12}C, a free neutron with an average kinetic energy of 4.2 MeV and a 4.4 MeV γ. ^{252}Cf mainly decays via alpha decay (97%), the remaining 3% of decays happen through spontaneous fission. In a fission decay, on average 3.75 neutrons are emitted with an average energy of 2 MeV [83]. The SoLid detectors and algorithms have not been designed to deal with the high neutron multiplicity of a ^{252}Cf source, causing some neutrons from the ^{252}Cf source to be missed.

The difference between the neutron identification efficiencies obtained by CROSS ($76 \pm 2\%$) and CaliPSo ($60.5 \pm 3.3\%$) are due to the suboptimal signal selection in the CaliPSo calibration. Due to the inherent temporary character of CaliPSo and its main goal being the quick identification of construction issues, the trigger settings and reconstruction parameters were never fully optimized. It is worth noting that the neutron identification efficiency of the Phase 1 detector depends on the trigger settings used. The results discussed here are obtained using the trigger settings of December 2017 (first column of Table 4.1). Calibration with the trigger settings used since April 2018 (second column of Table 4.1) yields an improvement of 3 percentage points, up to $79 \pm 3\%$ [82].

The detection efficiency achieved with the Phase 1 detector is a factor 14 larger than the detection efficiency of the SM1 detector, clearly demonstrating the improved

neutron identification capabilities of the redesigned detector. With this neutron capture and neutron identification efficiency, the neutron detection efficiency is about 52%, compared to only 2.8% for the SM1 detector. This almost twenty fold improvement in neutron detection efficiency is consistent with the design goal [84].

4.6 Data quality and run selection

4.6.1 Reactor and detector settings

The source of antineutrinos detected with the SoLid experiment is the BR2 reactor, where the number of neutrinos depends on the thermal power of the reactor. On average six antineutrinos and 200 MeV are emitted per fission, leading to roughly $2 \cdot 10^{17}$ antineutrinos per MW [5]. As listed in Table 2.2, the typical thermal power of the BR2 reactor is 60 MW, the hourly values determined by the BR2 staff are shown in Figure 4.15. The reactor on and reactor off periods are clearly defined. In both datasets used in this thesis, the period starts with the reactor on and ends with the reactor turned off. For the December (May) cycle, the reactor turns of at 9:30 on 12/12/2017 (14:30 on 22/05/2018).

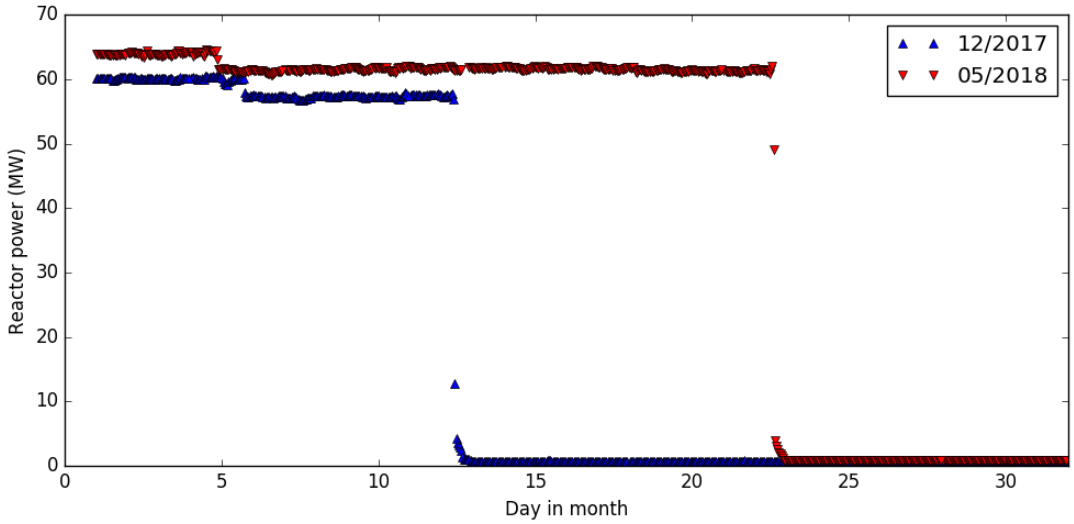

Figure 4.15: The thermal power of the BR2 reactor during December 2017 (blue triangles, pointing up) and May 2018 (red triangles, pointing down).

In order to detect antineutrinos, only those runs that are in good condition can be used. First of all, this requires consistent detector settings or in case of different settings carefully cross calibrated datasets. In order to define datasets with internally consistent detector settings, all parameters of the different active triggers as well as the voltages set on the SiPMs must be consistent. The different trigger settings are listed per run number in Figure 4.16. Those runs that have the desired settings are indicated with a plus. For the Phase 1 detector operation, it was opted to operate all SiPMs at the same over voltage. Until April 2018, all over voltages were set at 1.5 V. Afterwards, the over voltage was increased to 1.8 V. The values of the over voltages are not shown in Figure 4.16.

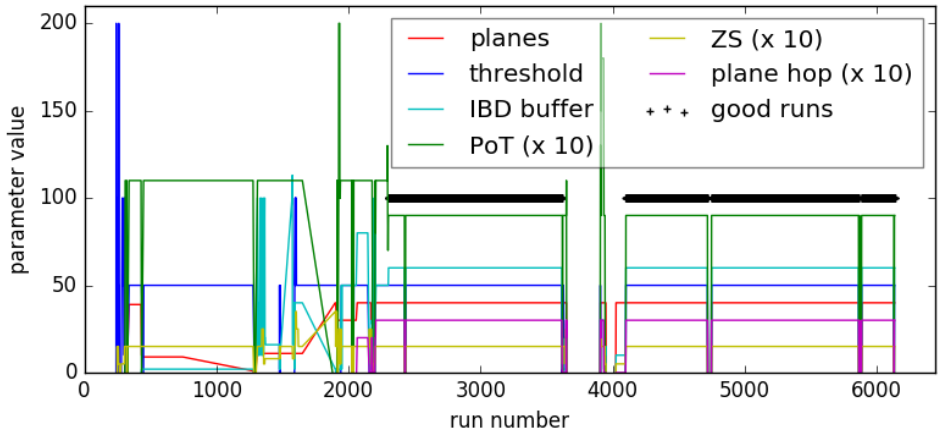

Figure 4.16: Neutron trigger and threshold trigger settings for the data collected in November and December 2017. The commissioning period where settings were being tested is clearly visible for run numbers below 2300. On the third of December 2017, starting from run number 2302, stable data taking began. The gap at run number 4000 is an AmBe calibration campaign on the 13^{th} and 14^{th} of December which was not included in this overview. Data taking ceased on Christmas day due to a leak in the cooling circuit.

4.6.2 Data quality

The runs selected based on the trigger settings provide a first selection of the dataset that can be used for (sterile neutrino) analysis. Secondly, the actual content of these runs should undergo a sanity check to detect any deviating runs that do not show up in the detector settings, e.g. a significant increase in trigger rate due to a single channel or a module that fails to write data to disk. For the December 2017 data, these sanity checks are performed on the FPNT rate, the muon rate and the NS rate. When the May 2018 data became available, collaboration wide reconstruction objects were available. The data sanity checks for the May 2018 data were performed using these objects.

Data quality in December 2017

The FPNT rate is the rate of ES signals the Phase 1 detector is constantly experiencing and is determined from the IBD buffer of FPNTs. From Section 4.2, it is clear that a significant fraction of online neutron triggers do not result in a reconstructed NS signal. These are mainly caused by muons that activate the ZnS(Ag) crystals and pass the neutron trigger PoT requirement. The IBD buffer of these FPNT events is therefore filled with the ES signals the Phase 1 detector is constantly experiencing and provides an unbiased sample. Unlike the threshold applied in the threshold trigger, the energy threshold in the IBD buffer is effectively the ZS threshold.

From the FPNT IBD buffers, an ES signal rate can be determined. Since the probed time of each plane depends on the number of FPNTs, care has to be taken in order to correctly determine the rate observed by the entire detector. Even though about 85% of the neutron triggers are FPNTs in the settings used in December 2017 (see Table 4.1), this results in a limited dataset spanning only 0.4% of the real time in at most seven planes. When an FPNT takes place in the first or last couple of planes, only four, five or six planes are being read out. Additionally, since most FPNTs are caused by passing muons, the last two blocks of each IBD buffer are discarded in order to avoid any contamination.

The NS rate is taken from the neutron triggers that passed the offline reconstruction and the muon rate is determined using muon tagging techniques designed for the SM1 detector [85] with an energy threshold extrapolated to the appropriate values for the Phase 1 detector. The object rates are shown in Figure 4.17 for the December 2017 data.

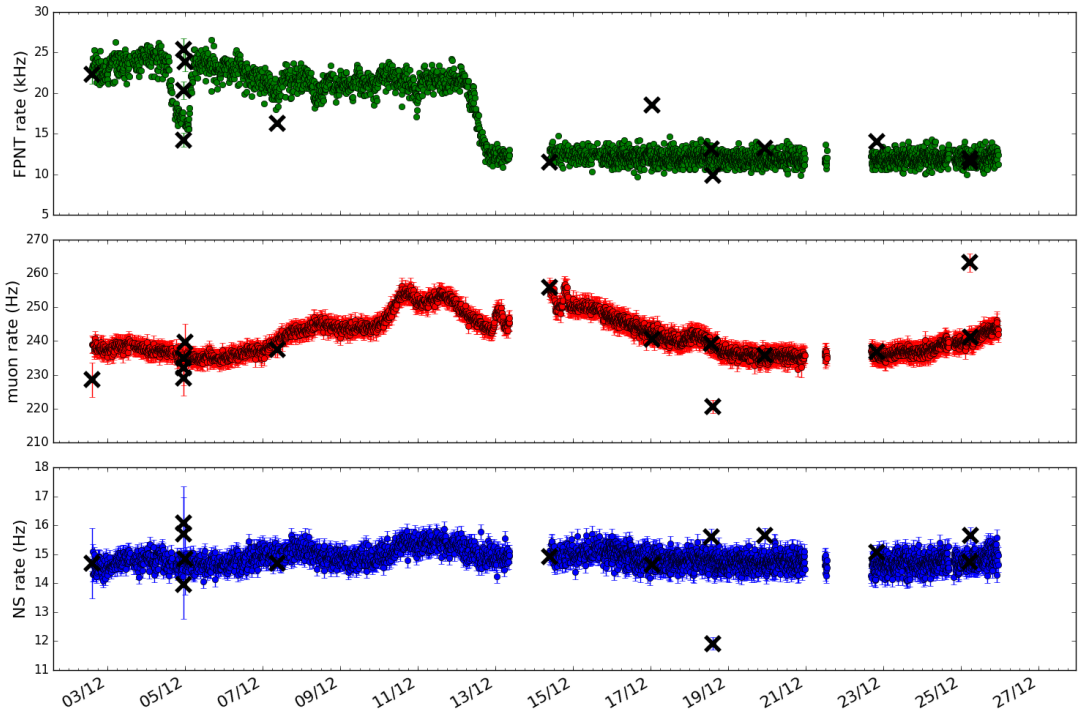

Figure 4.17: FPNT (top), muon (middle) and NS (bottom) rate for all runs in the stable data taking period in December 2017. Runs with rates that do not show consistent behaviour are indicated with a cross (see Table 4.2).

The fluctuations in the top panel of Figure 4.17 are discussed extensively in Section 4.6.3. The fluctuations in the muon rate in the middle panel are anticorrelated to the fluctuations in the atmospheric pressure as will be discussed in more detail in Section 5.2.1. This anticorrelation is expected since a higher atmospheric pressure increases the amount of material a muon from in a cosmic ray shower has to traverse in order to reach the detector. The NS rate is relatively stable over time. However, it is expected to correlate with the reactor power, since this is a source of neutrons and antineutrinos, and anticorrelate with the atmospheric pressure due to atmospheric neutrons and muon induced spallation neutrons (see Sections 5.2.1 and 5.2.2).

A number of runs stand out in Figure 4.17 due to the rate of one or more objects being too far away from the expected values. The expected rate for a run i is determined by performing a linear regression on the ten runs leading up to and following the run under investigation. The difference between the observed (O_i) and expected (X_i) rate is determined. For all runs, the standard deviation of the rate differences for each of the three objects is determined $\left(\sigma^{\mathrm{FPNT}},\ \sigma^{\mu},\ \sigma^{NS}\right)$. The total deviation of a single run (d_i) is then given by

$$d_i = \sqrt{\sum_j \left(\frac{O_i^j - X_i^j}{\sigma^j} \right)^2} \tag{4.6}$$

Run number	Deviation	Status	Cause
2879	4.0	keep	low FPNT rate, consistent with NaI
5979	4.1	keep	slightly higher NS rate
5458	4.3	keep	slightly higher NS rate
4895	4.4	keep	slightly higher NS rate
5193	4.6	discard	high FPNT rate in planes 22, 23, 24, 25, 32
4099	5.4	keep	first file post AmBe, unreliable fit
2584	5.4	discard	10 s
2583	5.5	discard	10 s
2586	8.2	discard	10 s
2302	9.4	discard	10 s
4540	10.0	discard	high FPNT rate in planes 28 to 33
2585	11.9	discard	10 s file
5976	20.6	discard	high μ rate in planes 23, 24, 25, 28
4903	20.9	discard	no μ, no NS in planes 28 to 33
6128	∞	discard	excluded from scan (extreme μ rate), 10 s

Table 4.2: Summary of runs with a poor total deviation in the December 2017 dataset and the cause of the deviation. A number of runs are only ten seconds long, these are indicated with '10 s' in the table and are always discarded.

where j runs over the FPNT, muon and NS objects.

From the 3287 runs under investigation, all those runs with a total deviation of more than four are listed in Table 4.2. These runs were individually inspected and the reason for the deviation is included in the table, as well as the decision to discard or keep the file for further analysis. In total, ten runs with appropriate trigger settings were discarded. This dataset of 3277 runs amounts to 281 hours of reactor on data and 249 hours of reactor off data.

Data quality in May 2018

A data validation study was also performed on the dataset collected during May 2018, the second dataset used in this thesis. Figure 4.18 shows the run time, average SiPM gain, NS rate, muon rate, SEvent rate and threshold trigger rate as a function of the run number. Within the software, an SEvent is the collection of all reconstructed peaks that take place within 100 ns. The SEvent rate is thus a combination of the ES and the NS rate in which the NS rate is possibly counted multiple times due to the long decay constant of ZnS(Ag). More quantities were used in this quality study than in the study performed for the December 2017 data, this is simply due to the development of new reconstruction algorithms. More algorithms and objects were available when the study on the May data was performed. Similarly to the data quality study for the December 2017 data, runs were compared to the ten previous and following runs and the deviation from this expectation was calculated using Eq. 4.6, this time running over six quantities instead of three.

In the May 2018 data, a larger fraction of runs are deemed unfit for physics analysis compared to the December 2017 dataset (1.6% vs. 0.3%). This difference is due to a different approach taken to masking channels between the data collected with four and five modules. In the commissioning data of December 2017 with four modules, all channels that could cause excessive triggering at some times were masked all the time. In the five module 2018 data, only those channels that are erratic all the time

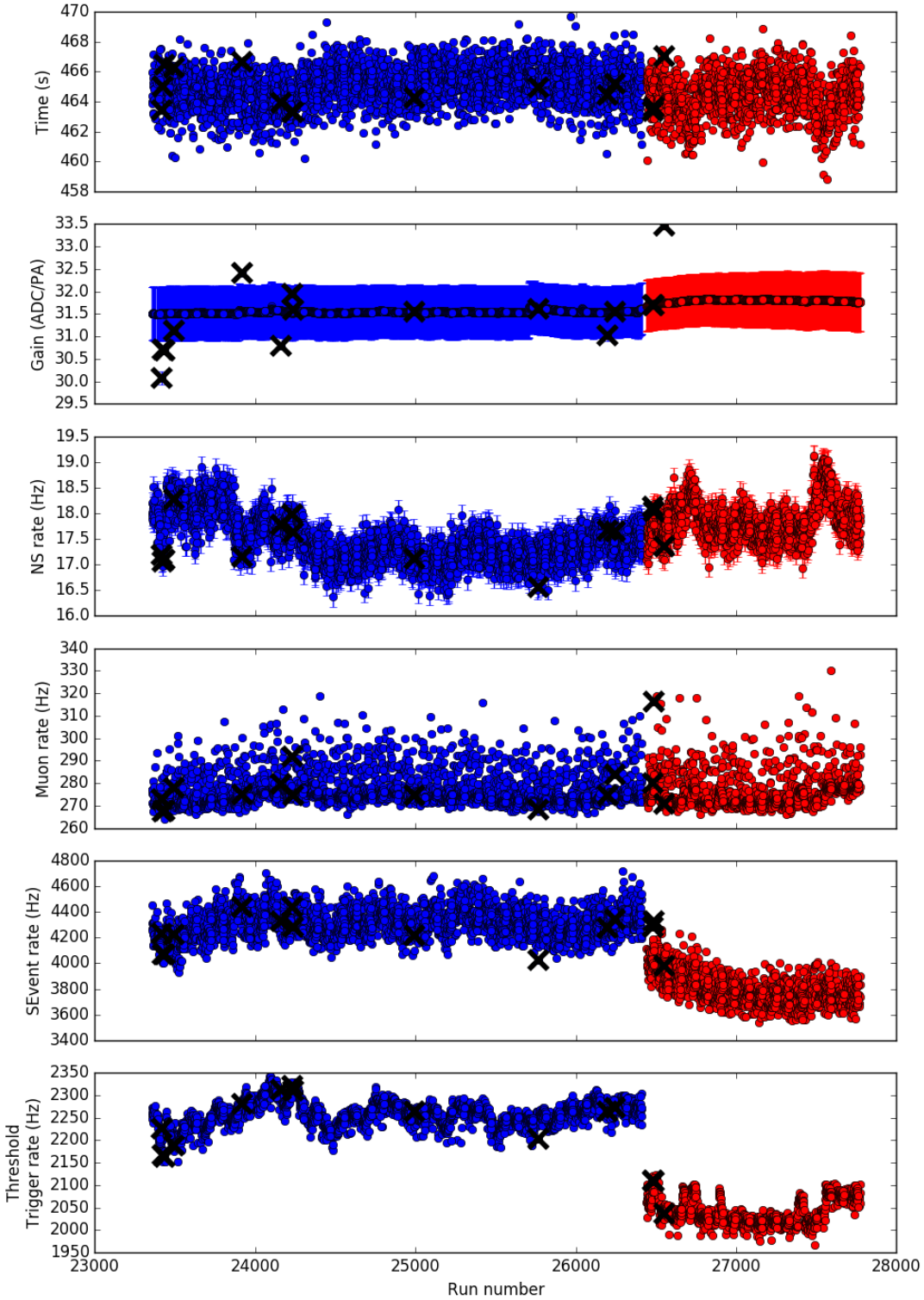

Figure 4.18: Data quality inspection for data taking in May 2018. The runs indicated with a cross are discarded.

are masked. In practice, the number of masked channels in the four common modules between the two different approaches falls from 22 to 16 out of 2560 channels. Due to a faulty ADC chip, 20 more channels are masked in the fifth module. The faulty ADC chip serves channels located on the top half of the second to last plane, leading to no data being collected there. This can be seen in the bottom right panel of Figure 4.23.

For the runs with excessive triggering on one or more of the studied objects, two approaches can be taken. That run can either be completely discarded or an offline masking can be applied to the faulty channel. The first approach rejects good data originating from all other channels but has the advantage of being very simplistic, both for the implementation and for the consequences to any further analysis. The second approach does not waste all good data in that run, only the triggers originating from that channel are discarded. The implementation of an offline mask is relatively straightforward, the effects of a single channel excessively triggering the detector however are not. A single channel dominating the bandwidth for writing data to disk can increase the dead time experienced by the other channels. In order to avoid these complications, the first approach is taken for the studies presented in this thesis.

Up to 11 a.m. on May 22^{nd} 2018, humidity has been an issue for the Phase 1 detector. The cooling of the container made the detector the coldest spot in the containment building. Due to the relatively high temperature of the containment building (typically 25 °C during the day) and the open water surface of the reactor pool, the humidity is constantly high. Up to May 22^{nd}, the relative humidity was close to 80%. Since electricity and water do not combine very well, the high humidity required periodically flushing the container with dry air in order to avoid damaging the SiPMs and electronic boards. Flushing was done by bringing a pressurised tank into the containment building, attaching it to a pipe that leads into the container and gradually letting the dry air flow out of the tank. This process was both logistically challenging and inefficient, as can be seen in Figure 4.19. The episodes of flushing can clearly be seen as the sharp decline followed by the gradual recovery to the pre-flush level of the humidity. On May 22^{nd}, permission was obtained to hook up the container to a pressurised air supply integrated in the BR2 containment building. The air in this system is pressurised and dehumidified by pumps outside the containment building. As a result, the humidity level is relatively stable around 35%. While moisture is removed from the air, airborne radioactive isotopes are not scrubbed, thus potentially introducing the Phase 1 detector to a new background environment. Unfortunately, the connection of the container to the pressurised air system coincides with the moment the reactor turned off (2 p.m. that same day, only three hours later).

4.6.3 FPNT rate fluctuations

Using the FPNT sample, the evolution of the ES signals over time can be studied, as shown in the left panel of Figure 4.20. In this figure, the gamma rate observed by a NaI detector is also shown. This NaI detector is operated by the SoLid collaboration and is placed inside the container (except for the data collected in December 2017 when the NaI detector was placed outside the container). The overall rate is correlated for the two sets of measurements. This is especially visible the moment the reactor was turned off on 12/12/2017 and for the dip in both rates on 4 and 5 December 2017. This dip in the FPNT rate reveals the origin of a large fraction of the ES rate at low energies. Apparently, the SoLid detector is very sensitive to airborne ^{41}Ar. ^{41}Ar is formed when naturally occurring and stable ^{40}Ar (0.9% by volume of the atmosphere [86]) captures a neutron and subsequently decays to ^{41}K via beta decay with a half life of 6576.6 ± 2.3 s.

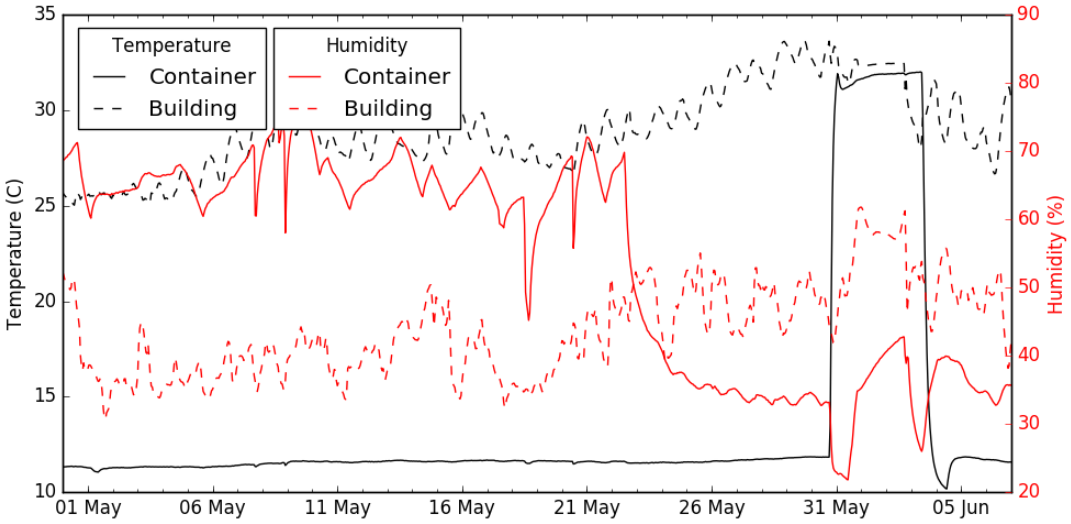

Figure 4.19: Evolution of the temperature (left axis) and humidity (right axis) in the container (solid lines) and in the containment building (dashed lines). The jump in container temperature from May 30^{th} to June 4^{th} is due to a pressure test of the BR2 containment building during which the detector and the container cooling were switched off.

The dominant decay ($99.17 \pm 0.02\%$) is into a $1.29364 \pm 4 \cdot 10^{-5}$ MeV excited state that decays to the ground state via a single photon 100% of the time with a half life of 6.7 ns [87]. When correlating the FPNT rate with the rate observed by the NaI detector after applying an energy threshold, as is shown by the different coloured lines in Figure 4.20, it is clear the correlation drops at roughly 2200 ± 200 ADC. Using the measured gain of the December 2017 data, 25.4 ± 1.4 ADC/PA and the CaliPSo light yield of 87.3 ± 7.2 PA/MeV, this corresponds to about 0.99 ± 0.13 MeV, consistent with the Compton edge of the ^{41}Ar gamma at 1.076 MeV. Additionally, the delayed rate reduction observed by the NaI detector when the reactor is turned off is consistent with the half-life of ^{41}Ar ($\tau_{\mathrm{NaI}} = 2.89 \pm 0.17$ h, $\tau_{\mathrm{Ar}} = 2.64$ h).

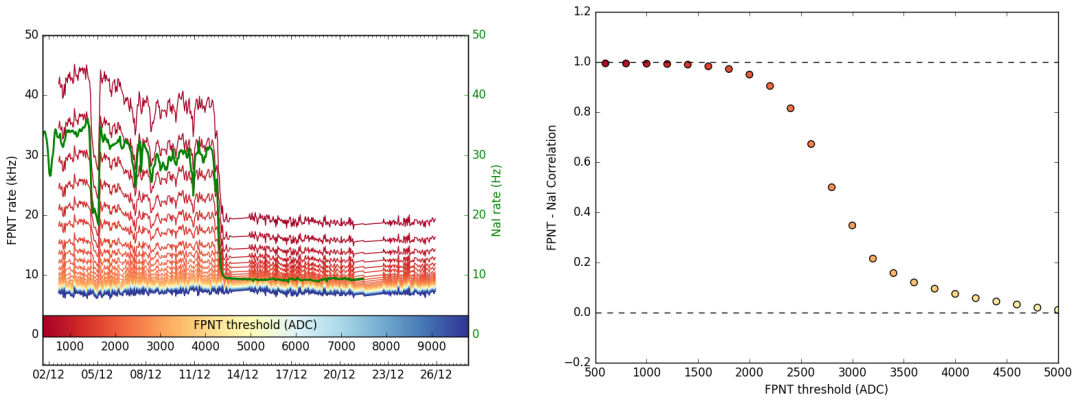

Figure 4.20: The Phase 1 detector accidental rate as a function of amplitude compared with the corresponding NaI measurement (left panel). On the right panel, the corresponding correlations are shown using the same colour coding for the Phase 1 points. In both panels, a rough conversion from ADC to MeV can be done by using 2000 ADC $\approx$ 1 MeV.

When performing the same exercise for the May 2018 data, Figure 4.21 is obtained. Similar fluctuations in the ^{41}Ar rate can be observed in both the December and May

datasets. The correlation between NaI and FPNT is very strong in both cases, with a linear correlation factor off 0.99 for December 2017 and 0.95 for May 2018 at the lowest energy threshold.

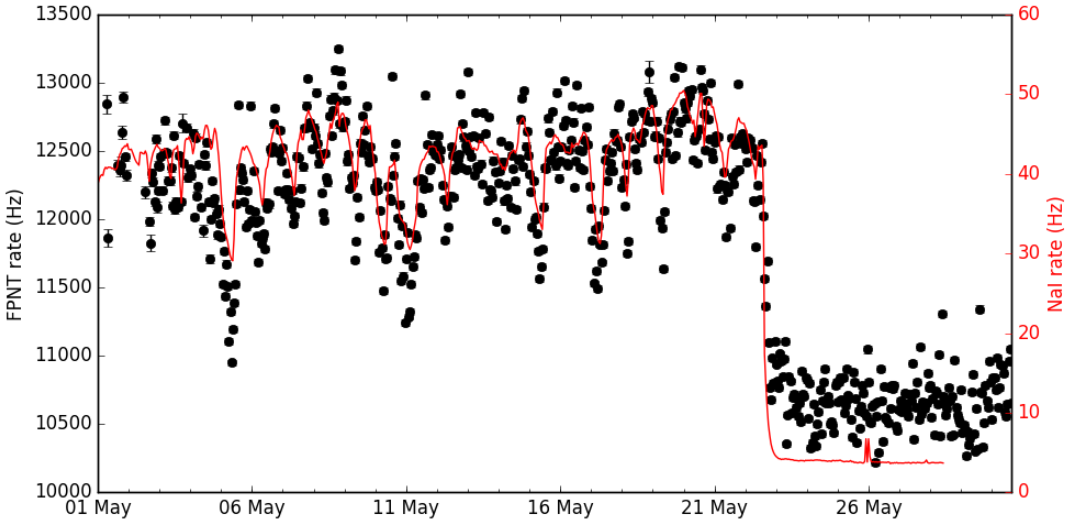

Figure 4.21: FPNT rate evolution during May 2018 (left axis) and the rate evolution of the NaI detector operated by the SoLid collaboration during the same period (right axis). The two measurements are strongly correlated, $\rho = 0.95$.

When the fifth module was installed in January 2018, the NaI detector was moved from its position between the container and the shielding to the inside of the container. Additionally, the voltage over the PMT in the NaI detector was changed after a calibration performed by the BR2 staff. Both of these changes took place in between the two data taking periods. As a result, the NaI rate for the two data taking periods can not be compared. The BR2 staff automatically logs a multitude of environmental parameters, among others the rate of ^{41}Ar, ^{133}Xe and ^{135}Xe using a single monitor placed inside the containment building, i.e. the same volume of air the Phase 1 detector is located in. Since the detector hardly picks up Xe radiation [88], it can be used as an ^{41}Ar rate measurement. The rate evolution observed by this detector is shown in Figure 4.22 and indicates the amount of radiation in the BR2 containment building due to ^{41}Ar is nearly identical for the two data taking periods, as expected.

Comparing hitmaps for data taken when the reactor was turned on and off indicates where most of the ^{41}Ar and other ES signals are located. Projections in the XY, XZ and YZ planes for the difference in rate when the reactor was on and off are shown for December 2017 and May 2018 data in Figure 4.23. The excess at the back of the detector in the December 2017 data is expected since the rear part of the water wall was not yet constructed. The lack of this excess in the May 2018 dataset demonstrates the efficacy of the shielding. Secondly, the total rate and the rate difference between reactor on and reactor off is much lower for data collected in May 2018 than for December 2017 data, also demonstrating the impact of the shielding. Turning on the reactor in May 2018 raised the FPNT rate from 10.7 kHz to 12.3 kHz while in December 2017, the rate raised from 25.8 kHz to 49.4 kHz, despite an additional module being operated in May 2018.

The excess at low X and high Y values can be understood as a geometric effect due to the layout of the BR2 containment building. The ceiling on the third floor of the

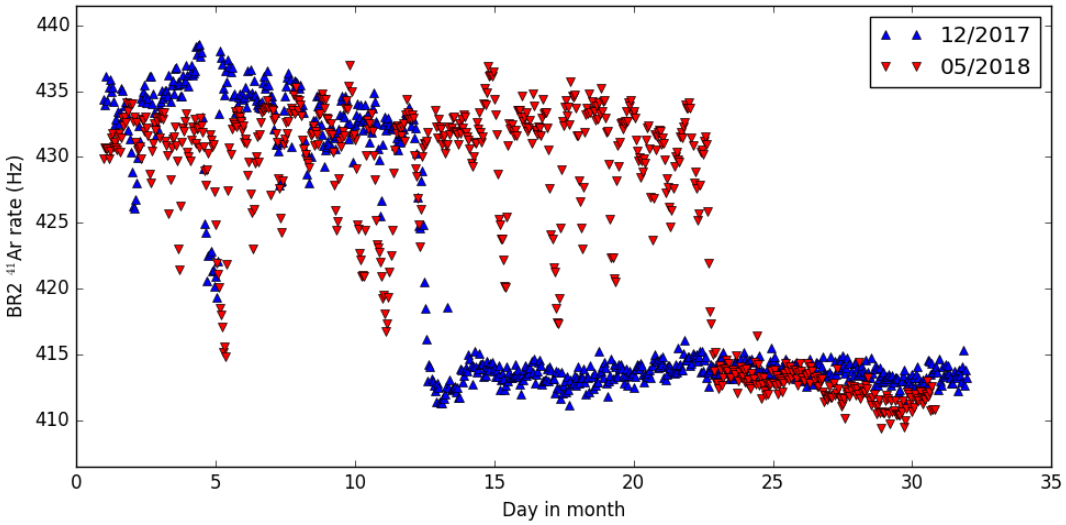

Figure 4.22: Evolution of the ^{41}Ar decay rate in the BR2 containment building measured by a BR2 operated detector. The rate evolution for December 2017 (blue triangles, pointing up) and May 2018 (red triangles, pointing down) are shown. These are the two datasets used in this thesis.

BR2 containment building is limited to roughly one third of the floor, starting from the east side of the reactor wall. On the remaining two thirds of the third floor, the concave containment building roof over 20 meters higher can be seen. From the floor plan in Figure 2.1, it can be seen that this limited ceiling creates a small air volume at the right side of the detector (high X) and a large volume on the left (low X). Additionally, this large air volume is directly connected with the surface of the reactor pool and parts of the cooling circuit. These are the main source of free neutrons and therefore ^{41}Ar. Similarly for Y, the ^{41}Ar comes from the reactor pool and the cooling circuit, both of which are located above the detector (high Y).

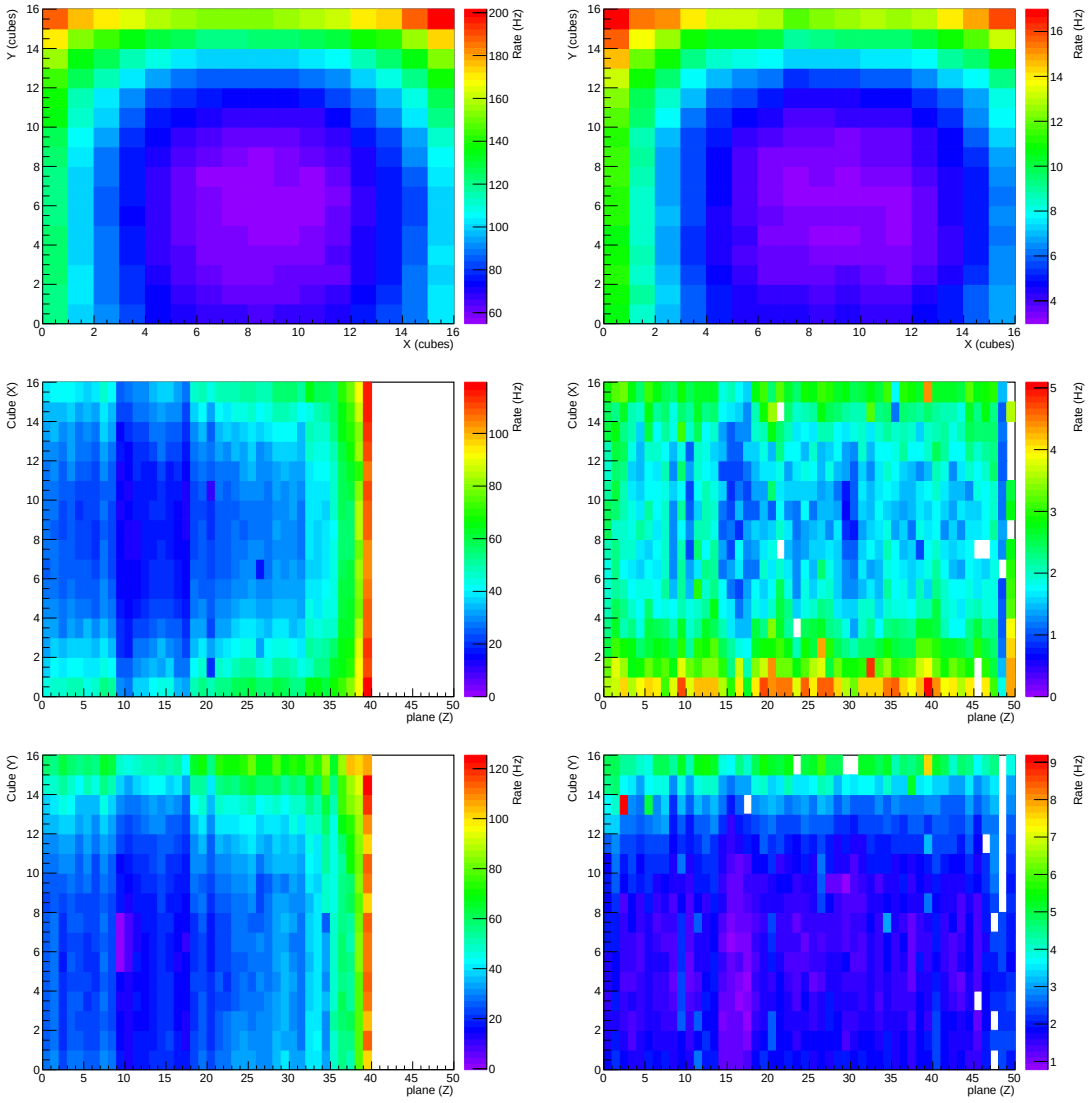

Figure 4.23: Projections of the difference in rate observed by the SoLid experiment when the reactor was on and off for December 2017 (left) and May 2018 (right) data.

Chapter 5

Antineutrino detection with the SoLid Phase 1 detector

As mentioned in Chapter 2, the Phase 1 detector is located on the third floor of SCK•CEN's BR2 containment building. The shielding to the detector is limited to the containment building itself ($\sim$ 10 m.w.e.) and the additional shielding placed around the detector (0.5 m.w.e.). This limited amount of shielding exposes the detector to significant amounts of background mimicking the IBD process. Additionally, the detector is constructed out of material. Inherent to any material is a contamination with radioactivity. Some of the radioactive decay processes also mimic the IBD process. The majority of these correlated backgrounds are characterised in Section 5.2 as well as measures taken to reduce these backgrounds. Section 5.3 motivates the IBD event selection criteria. The agreement between reactor on and reactor off data at high energies is verified, this is discussed in Section 5.4. The observed reactor on excess is described in Section 5.5. This chapter begins with a short description of the expected signature of IBD events using simulations.

5.1 $\bar{\nu}_e$ event topology

As described in Chapter 2, when an electron antineutrino with sufficient energy interacts with a proton in the detector, a positron and a neutron are created. The positron scintillates in the PVT cube where the neutrino interaction took place, depositing an amount of light correlated to the energy of the neutrino. The positron then annihilates when it interacts with an electron, creating two 511 keV gammas. Both the scintillation and annihilation happen as good as instantaneous. The neutron thermalization and capture process typically takes about 70 μs in the Phase 1 detector. During the thermalization process, the neutron undergoes a random walk and may therefore be observed at a certain distance from the corresponding positron signal.

Figure 5.1 shows the expected distributions for the positron energy and for the ΔX, ΔY, ΔZ, ΔR and ΔT distribution for IBD events, where

$$\begin{aligned} \Delta X &= X_{NS} - X_{ES} \\ \Delta Y &= Y_{NS} - Y_{ES} \\ \Delta Z &= Z_{NS} - Z_{ES} \\ \Delta R &= \sqrt{\Delta X^2 + \Delta Y^2 + \Delta Z^2} \\ \Delta T &= t_{NS} - t_{ES}. \end{aligned} \tag{5.1}$$

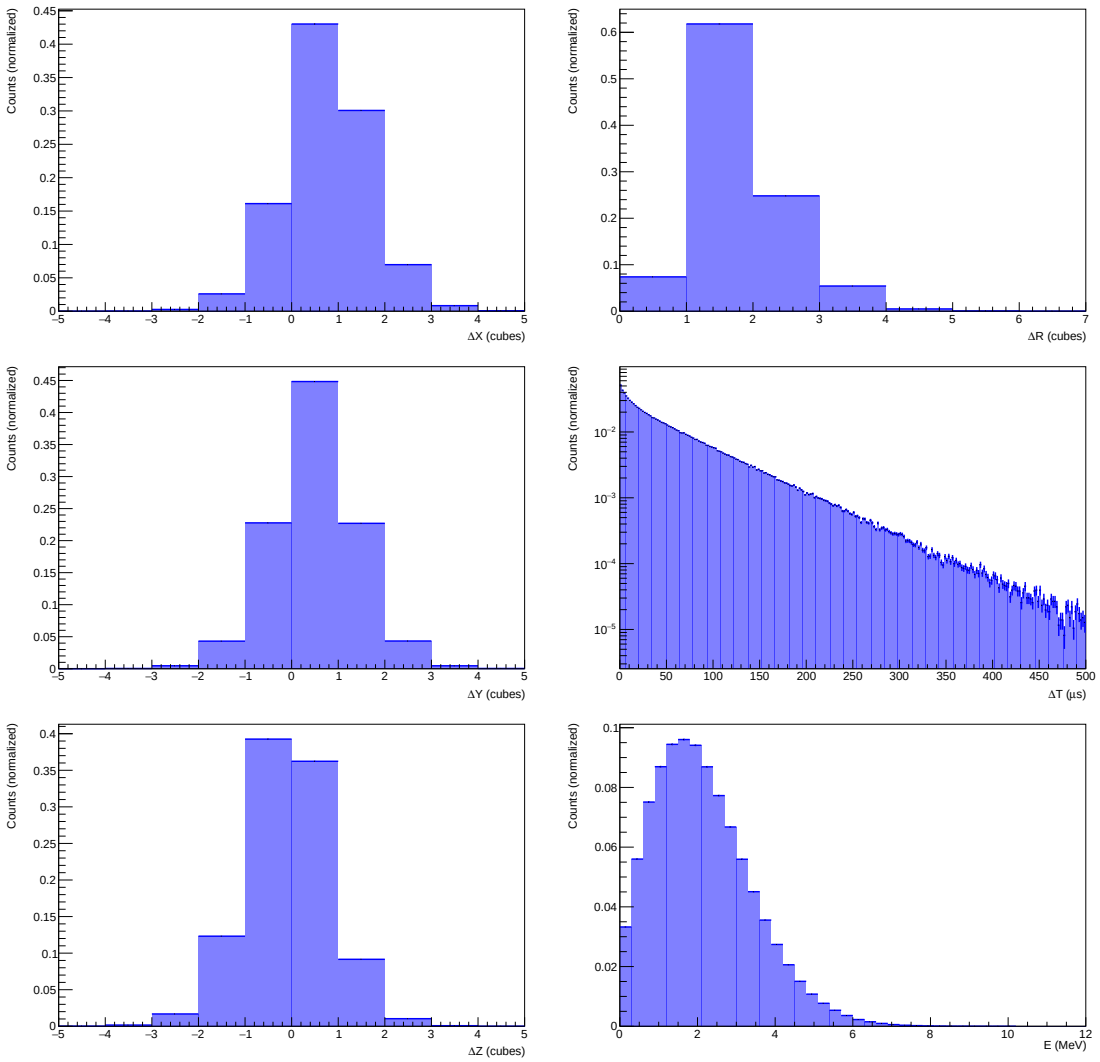

Figure 5.1: GEANT4 simulation of the IBD process. The left column shows the shift from the neutrino interaction cube to the neutron capture cube in X (top), Y (middle) and Z (bottom). The right column depicts the distance ΔR (top) and the time ΔT (middle) between the production and capture of the neutron as well as the energy deposited in PVT by the positron (bottom).

The ΔX, ΔY, ΔZ and ΔR distributions indicate the spatial component of the neutron random walk, the ΔT distribution shows the temporal character. All these distributions are generated using GEANT4 and show the MC truth without simulating the detector response.

The symmetry, or lack thereof, in the ΔX, ΔY and ΔZ distributions shown in Figure 5.1 can be understood from the position of the lithium screens on the PVT cube. Lithium screens are placed on the low Z side and on the high X side of each cube. When taking the lithium screens of the neighbouring cubes into account, all cubes except those in the outer layer have lithium screens on both sides in the X and Z directions, either before or behind two layers of Tyvek, while the Y direction remains open. Since the lithium screen placement is symmetric in the Y direction, the ΔY distribution of IBD events is therefore symmetric as well. A neutron has a certain chance to get captured on a ^{6}Li nucleus when passing trough a lithium screen. The cubes facing the interaction cube on $-X$ and $+Z$ have a much higher capture

probability than the cubes on the $+X$ and $-Z$ sides since a neutron has to make it through a lithium screen without being captured in order to get captured on the $+X$ and $-Z$ cubes. This is illustrated in Figure 5.2.

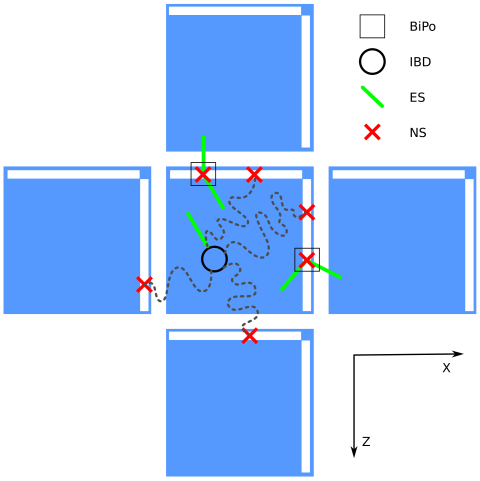

Figure 5.2: Sketch of how some cubes obtain a higher rate than others for IBD and BiPo events. BiPo events are dicussed in Section 5.1.

In the previous paragraphs, the basic distributions used to select IBD candidate events have been mentioned. An observable that was not mentioned is the prompt multiplicity. Occasionally, particularly for higher energies, the positron can exit the interaction cube and enter neighbouring cubes before annihilation. In those cases, multiple cubes sharing faces detect light from the positron. However, even in case of a multi-cube positron, the multiplicity of the prompt ES signal is low. For a 10 MeV positron, which is above the highest energy reasonably expected from an IBD positron, the mean travel distance is only 4.5 cm [55,89], limiting the prompt multiplicity to two or three cubes. Annihilation gammas interact mainly via Compton scattering, scattering mainly in the forward direction, depositing little energy per interaction [57]. Due to the low density and low atomic number of the detector, the interactions are relatively far apart. This combination of gamma interactions that are far apart and low in energy again limits the multiplicity of the prompt signal.

From the combination of reactor calculations, neutrino cross sections and available free protons, 1155.6 IBD interactions per day from ^{235}U are predicted to occur when the reactor runs at a thermal power of 60 MW [90]. When folding in the neutron detection efficiency ($\varepsilon_{det} = \varepsilon_{Li} \times \varepsilon_{ZnS} = 0.66 \times 0.79 = 0.52$, see Section 4.5), this number reduces to roughly 600 IBD interactions per day for which the IBD neutron is captured on a ^{6}Li nucleus and the following ZnS(Ag) scintillation is reconstructed as an NS signal. This corresponds to about 0.065 and 0.034 events per cube per day in respectively the first and last detector plane. Due to the background processes, a 100% efficient IBD selection can not be obtained. The selection efficiency is discussed in Section 5.3 for a preliminary analysis on the first data.

5.2 Correlated backgrounds to neutrino detection

Correlated backgrounds are those events that induce the same signature as a $\bar{\nu}_e$ interacting in the detector. In contrast, accidental backgrounds also mimic the IBD process,

but in those cases, the ES and NS signal have a different origin. The accidental background depends on the initial NS and ES rates as well as on the selection requirements and will be discussed in Section 5.5.1.

An example of a correlated background process is a high energy neutron which undergoes elastic scattering on a proton followed by capture on ^{6}Li. The recoiling proton scintillates in the PVT providing the ES signal and the neutron capture on a ^{6}Li nucleus initiates an NS signal. Two types of cosmic ray induced high energy neutrons are discussed in Sections 5.2.1 and 5.2.2, these are the so-called cosmic backgrounds.

Another type of correlated background comes from the natural contamination of all materials with trace amounts of radioactive thorium and uranium. These elements decay to a stable isotope via a decay chain. In some cases these chains contain a beta decay followed by an alpha decay. When the electron or positron and subsequent alpha particle scintillate in respectively the PVT cube and the lithium screen, the detector registers an IBD like event. This background is discussed in Section 5.2.4.

5.2.1 Cosmic ray muons and spallation neutrons

When a high energy charged particle, a so-called cosmic ray, impinges on the Earth's atmosphere, it will interact with oxygen and nitrogen nuclei. Energy transferred in the collision will heat the nucleus, requiring it to cool down via either neutron evaporation or breaking up. When the nucleus breaks up, an avalanche of particles is created. The combination of several broken up nuclei initiates a so-called cosmic ray air shower. The cosmic ray is typically a proton (86%) or an alpha particle (11%) while the particles created in the cosmic ray air shower are pions (91%) and kaons (9%). These decay into gammas, muons and neutrinos and in case of kaons also into pions. Hard interactions of all air shower particles with atoms in the atmosphere can propagate the avalanche. Of the aforementioned particles, only muons, neutrinos and neutrons make it to ground level [5, 91]. The effect of these so-called atmospheric neutrons will be discussed in Section 5.2.2. This section will discuss the effect of muons on the detector. The expected detection rate of the atmospheric neutrino flux is so small that it can safely be ignored.

Sufficiently high energy muons can make it to ground level while still being MIPs. As mentioned in Section 4.4, these MIP muons deposit 1.8 MeV/cm in PVT and leave a recognisable track in the detector. This track can easily be rejected, but the possible creation of high energy neutrons (spallation neutrons) is the main cause of concern. Spallation neutrons can not only be created inside the detector, but also in the surrounding materials such as the container, detector shielding and the reactor building. A spallation neutron created near the detector can enter the detector, create scintillating protons and be captured on a ^{6}Li nucleus while the muon does not cross the detector. Those events are much harder to identify and subsequently reject. The topology of these events is identical to that of atmospheric neutrons and will thus be discussed in the next section.

The muon veto

In order to reject the first category of events, where both the muon and the neutron appear in the detector, an offline muon veto is introduced. When a muon is detected, all signals in a time window following the muon are ignored. The effect of this veto on the rate of IBD-like events and the induced dead time as a function of the time window length is shown in Figure 5.3. IBD-like events in this case are ES-NS signal pairs that

satisfy a loose coincidence selection based on IBD simulations, detailed in Table 5.1. This selection refers to the signal generated by recoiling protons, it ignores energy and multiplicity requirements since these would be biased by the close proximity of the muon. The IBD event selection is discussed in more detail in Section 5.3.

Variable	**Value range**
ΔT	[0, 100] μs
ΔX, ΔY	[-2, 2] cubes
ΔZ	[-2, 3] cubes
ΔR	] 0, 3] cubes

Table 5.1: Loose ES-NS coincidence requirements to select IBD like background events used in the muon veto optimization [92].

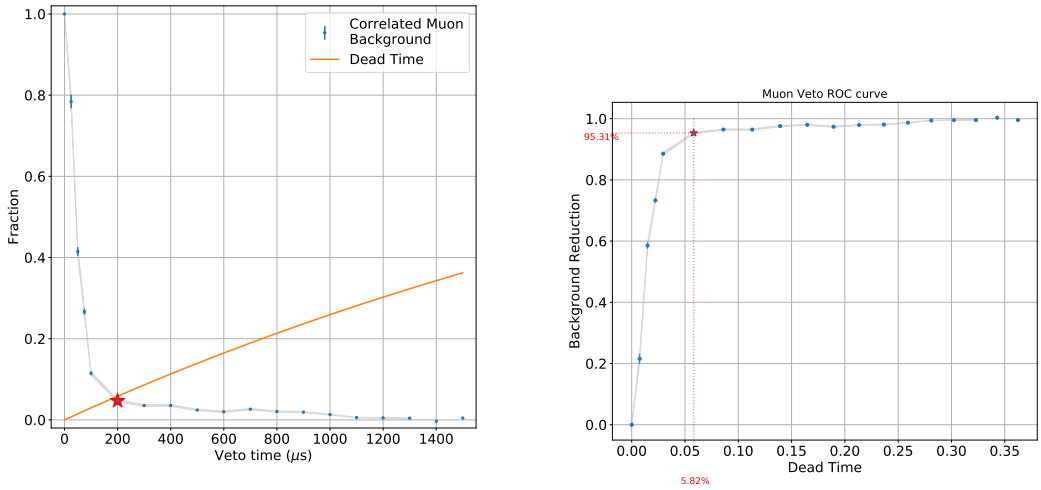

Figure 5.3: The fraction of IBD like events and the induced dead time as a function of muon veto length (left) and the background event reduction as a function of the induced dead time (right). The criteria used to select the IBD like background events can be found in Table 5.1 [92].

As expected from the neutron capture time, the majority of selected events follow an exponential distribution after the detected muon, levelling off to a plateau. While the plateau is caused by IBD-like events uncorrelated to the detected muon, the drop at 1200 μs in the left panel of Figure 5.3 is an offline reconstruction effect. In order to process a data file, a section of data is loaded into RAM until a specified amount of trigger blocks has no signals in it. The default setting for this parameter is 200 blocks or 1.28 ms[1]. The exponential behaviour observed in Figure 5.3 warrants a relatively short muon veto time of 200 μs, reducing the correlated background from spallation neutrons for which a muon is detected by 95% while inducing a dead time of 6%.

Rate of muon induced neutrons

The rate of neutrons originating from muons crossing the detector can be estimated from the ΔT distribution of NS signals following a reconstructed muon, the ΔT distribution in Figure 4.11 is used here. NS signals from neutrons induced by the crossing

[1]When working with source calibration data, this parameter is reduced since 200 empty blocks are almost never reached due to the high source activity.

muons follow the typical exponential capture distribution, uncorrelated (accidental) ES and NS signals show a flat distribution over time. The positive part of the distribution can thus be fitted by an exponential function plus a constant,

$$f(x) = Ae^{-x/B} + C. \tag{5.2}$$

The integral of the exponential function, AB, gives the number of ^{6}Li captured neutrons induced by muons. This number can be divided by the data collecting time to get the rate of muon induced and captured neutrons. A rate of 0.814 ± 0.004 Hz is obtained. After application of the muon veto, this rate is reduced to 0.0407 ± 0.0002 Hz. This rate, which corresponds to 0.27 per cube per day, is roughly an order of magnitude larger than the expected signal rate.

5.2.2 Atmospheric neutrons

As mentioned in the previous section, high energy neutrons are created near the interaction point in cosmic ray air showers. Due to the limited amount of shielding surrounding the SoLid experiment, these neutrons can make it to the detector with sufficiently high energy to create an IBD like event. Geant4 simulation of atmospheric neutron events indicates a tendency for multiple neutron production. The neutron capture multiplicity distribution is shown in Figure 5.4. In cosmic ray air showers where at least one neutron is captured in the detector, on average 1.7 neutrons are captured.

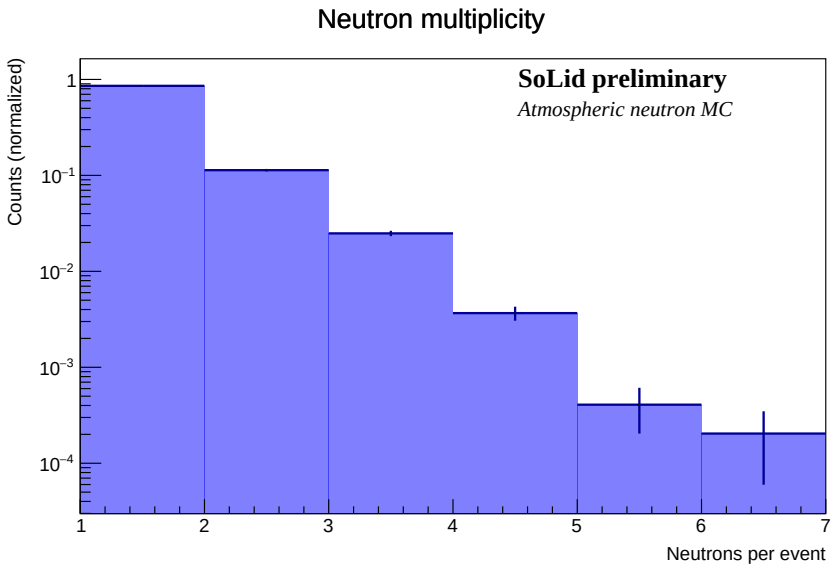

Figure 5.4: Captured neutron multiplicity for simulated atmospheric neutron events.

The neutron multiplicity veto

For $85.7 \pm 0.9\%$ of the atmospheric neutron events, only a single neutron is detected. A neutron multiplicity veto would reject at most the remaining 14.3%, hopefully without significantly reducing the selection efficiency for IBD events for which only a single neutron is expected. Figure 5.5 shows the time between consecutive NS signals detected in the Phase 1 detector. In both the reactor off and reactor on data, a double exponential behaviour is visible. A fit with a double exponential function to both reactor on and off data shows the exponential parameters are fully consistent. The parameter value of the

first short exponential $B = (146 \pm 2) \cdot 10^{-4}$ μs^{-1} is consistent with the inverse neutron capture time determined from AmBe (see Section 4.4), $1/\tau = 1/68.8$ μs resulting in $(145 \pm 8) \cdot 10^{-4}$ μs^{-1}. This behaviour is consistent with neutrons arriving in the detector at the same time. When considering the thermalization and capture process to be a completely random process, the capture time of both neutrons will be drawn at random from an exponential distribution with a characteristic time. The distribution of time differences between two captured neutrons will also follow an exponential distribution with the same characteristic time.

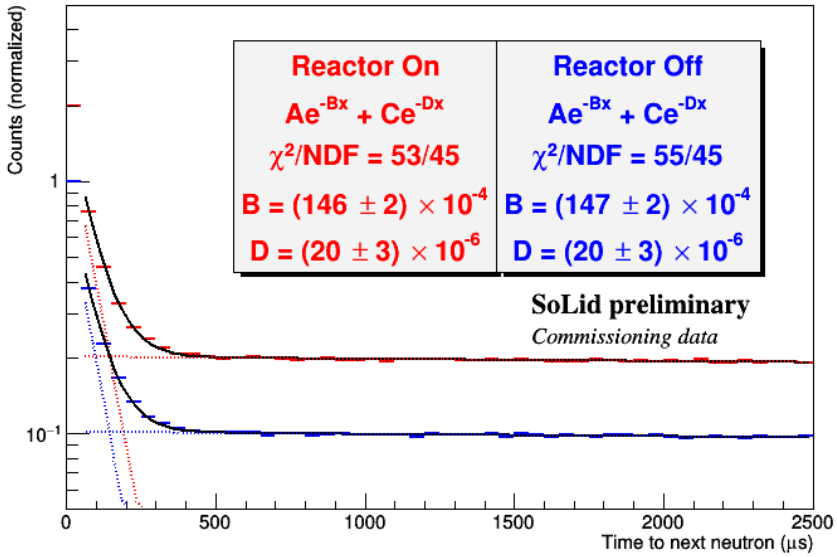

Figure 5.5: Time difference between consecutive NS signals for reactor on (red) and reactor off (blue) commissioning data collected in December 2017. For visualisation, the data is normalized such that the bin content of the first bin of the reactor on (off) data is at 1 (2).

The efficiency of the multiplicity veto can be determined from the fast exponential parameter value. The fraction of surviving high neutron multiplicity (i.e. ≥ 2) atmospheric neutron events as a function of the veto time is shown on the left axis of Figure 5.6. The dead time is calculated as the time between two vetoed NS signals plus the veto time, because all ES signals leading up to the first NS signal are vetoed as well as all ES signals leading up to the later neutrons. It is clear the dead time induced by this veto is minimal, the fraction of rejected NS signals is more relevant. For a veto time of 200 μs, the same value as applied for the muon veto, $2.5 \pm 0.2\%$ of all NS signals are rejected, while rejecting 94.5% of all high multiplicity atmospheric neutron events. From integration of the individual exponential functions, it can be determined that roughly 80% of the rejected neutrons come from the fast exponential, i.e. belong to atmospheric neutron events. The real cost of this veto is therefore at most 0.6% of NS signals from different sources.

The second exponential fitted in Figure 5.5, with parameter $D = (20 \pm 3) \cdot 10^{-6}$ μs^{-1}, corresponds to an arrival rate of uncorrelated NS signals of 20 ± 3 Hz in the detector. This is roughly consistent (1.7σ) with the NS signal rate of 14.8 ± 0.2 Hz measured during the data quality control study of the same data (Section 4.6.2, Figure 4.17).

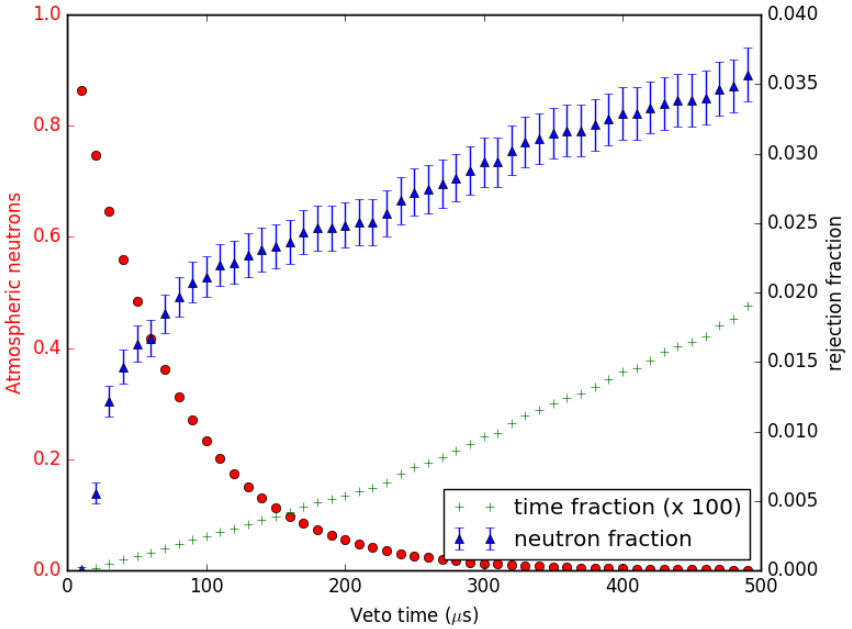

Figure 5.6: The fraction of high multiplicity atmospheric neutrons surviving the veto (red circles, left axis), the rejected NS signal fraction (blue triangles, right axis) and the dead time expressed as the fraction of running time vetoed with respect to the total running time (green pluses, right axis) as a function of the neutron multiplicity veto length.

Atmospheric neutron rate

Similarly to the way the rate of spallation neutrons was determined, the rate of atmospheric neutrons can be determined from the integral of the short exponential in Figure 5.5. Combined with the data taking time, this gives a rate of 7.25 ± 0.18 mHz for atmospheric neutrons with at least two neutrons. Taking into account atmospheric neutrons with only a detected single neutron, the atmospheric neutron rate becomes 0.051 ± 0.01 Hz. This corresponds to 0.34 ± 0.09 counts per cube per day, an order of magnitude above the expected signal rate. The proposed neutron multiplicity veto, effective on only 14.3% of this sample, therefore removes a background that is twice the expected signal rate in the last planes of the detector, while rejecting at most 0.6% of the NS signals from a different source.

5.2.3 Correlation of cosmic backgrounds with the atmospheric pressure

The high energy neutrons reaching the detector without accompanying muon or neutron are not rejected by the two vetoes discussed in the previous sections. A significant fraction of these neutrons will be rejected via prompt multiplicity and energy selection requirements discussed in Section 5.3. The remaining fraction of high energy neutron events has to be quantified and taken into account when calculating the signal rate. Since both sources of neutrons originate from cosmic rays impinging on the Earth's atmosphere, the environmental parameters influence the rate. Taking these into account allows determination of a correct signal rate.

Motivation for matching pressure datasets

Both the muon rate, and therefore the spallation neutron rate, and the atmospheric neutron rate show an anticorrelation with the atmospheric pressure. An increased atmospheric pressure increases the density of the air column through which these particles have to propagate. As a result, the attenuation of these particles is larger due to an increased number of interactions. Figure 5.7 shows the neutron and muon rates as a function of pressure, for data collected by respectively the Oulu Cosmic Ray Station [93] and by Georgia State University [94]. For neutrons, the increase in attenuation is much stronger than for muons. The fractional change in rate as a function of pressure can for both muons and neutrons be expressed as

$$\frac{\Delta j}{j} = -\alpha \Delta P \tag{5.3}$$

where j is either the observed muon or neutron rate. For neutrons, the pressure coefficient α can be approximated as $9.6 \cdot 10^{-3}$ mm^{-1}Hg. For muons the pressure coefficient is smaller: $\alpha \approx 2.15 \cdot 10^{-3}$ mm^{-1}Hg [95]. The difference in amplitude can also be seen in Figure 5.7.

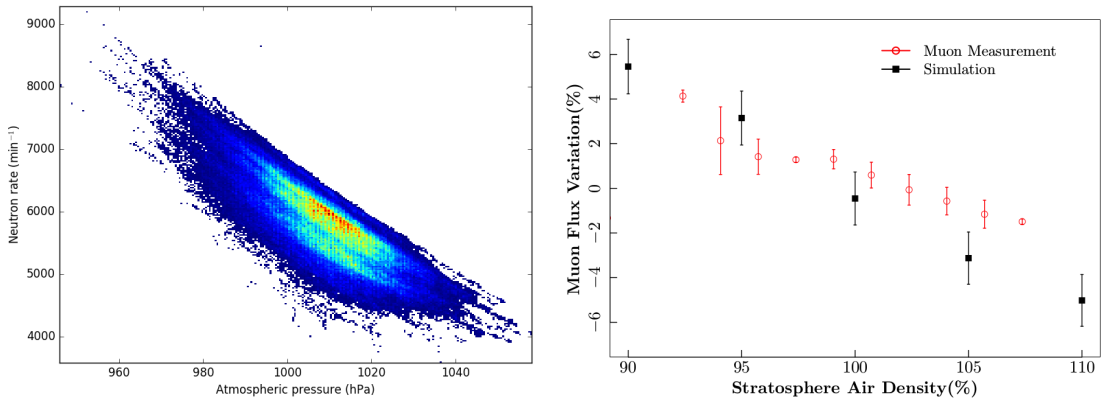

Figure 5.7: Neutron (left) and muon (right) rate as a function of atmospheric pressure. The neutron rate shows hourly rates between 1965 and 2015 [93]. The width of the distribution is explained by the 11 year solar cycle. The muon rate shows the daily variation between 2011 and 2013 at Georgia State University as a function of the atmospheric density, which is parametrised as $\rho = \frac{P}{0.2869(T+273.15)}$ with P the pressure in kPa and T temperature in °C [94].

These trends are also observed in the Phase 1 SoLid detector. Since there is no source of muons other than cosmic rays, one can simply use the reconstructed track rate to demonstrate the correlation with the pressure. This is shown in Figure 5.8 for the commissioning data taken in December 2017. The data points are shown with a different colour for the reactor on and reactor off periods. The trends are consistent between these two sets. This shows the muon rate is not correlated with the status of the reactor, as is expected.

Correlating the neutron rate to the atmospheric pressure requires the neutron rate to be split according to the source. The strong anticorrelation observed in the Oulu Cosmic Ray Station is only there for neutrons originating from high up in the atmosphere. Other sources will show a weaker correlation (spallation neutrons) or no correlation at all (neutrons originating from the reactor and from IBD processes). Lastly, radioactive alpha decays taking place in the lithium screens contribute to the NS signals used to identify neutrons with the SoLid detectors (see Section 5.2.4). In order to disentangle

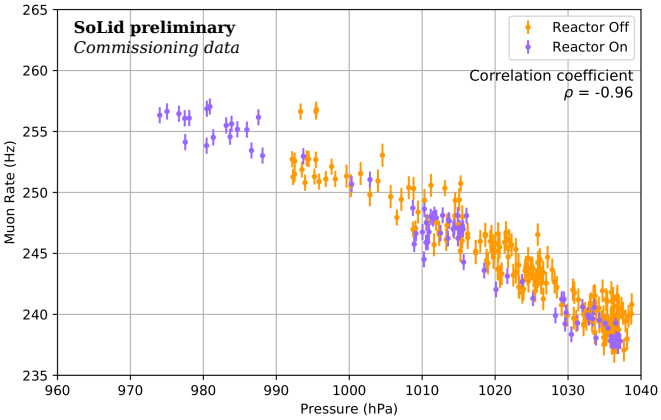

Figure 5.8: Correlation between the atmospheric pressure measured outside the BR2 containment building and the muon rate observed by the Phase 1 detector.

these sources, the atmospheric neutron multiplicity shown in Figure 5.4 can be used. Figure 5.9 shows the amplitude of both exponentials in the double exponential fit as a function of pressure. The data was split in blocks of four hours to obtain sufficient statistics per point in order to allow a double exponential fit while keeping the pressure variations minimal. For these fits, the parameters of both exponentials were fixed to the values obtained from a fit to the entire dataset but the amplitudes, which correspond to the high-multiplicity and single neutron event rates, were left free.

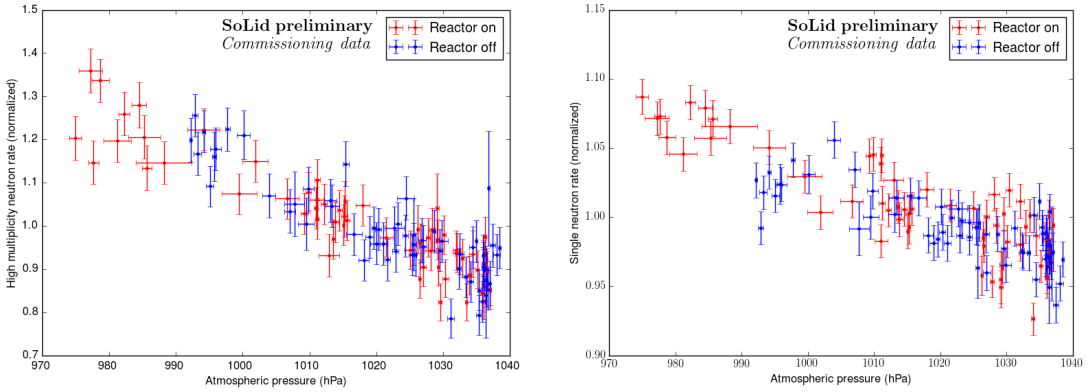

Figure 5.9: Correlation between the high multiplicity neutron event rate and the atmospheric pressure (left) and between the single neutron event rate and the atmospheric pressure (right). The high multiplicity neutron rate is dominated by atmospheric neutrons whereas the single neutron event rate also contains contributions from spallation neutrons and other uncorrelated events. For both figures, the rates are normalized to the average value of the entire dataset, i.e. reactor on and reactor off combined.

A fit with a linear function $y = A + Bx$ to the points in Figure 5.9 for the reactor on, the reactor off and combined datasets yields consistent results within the uncertainties for the high-multiplicity events, as is shown in Table 5.2. For the single neutron events, a small excess exists for reactor on, suggesting the presence of reactor induced effects. This could be explained by the fact that only NS signal arrival times are being considered for this study. At least a part of this excess is due to neutrino interactions and there is also the possibility of neutrons coming directly from the reactor being detected since the rear water wall was not constructed during this data taking period.

Dataset		Amplitude	Slope (hPa^{-1})
High-multiplicity neutron events	Reactor On	7.34 ± 0.37	$(-6.23 \pm 0.36) \cdot 10^{-3}$
	Reactor Off	7.88 ± 0.51	$(-6.74 \pm 0.50) \cdot 10^{-3}$
	Both	7.48 ± 0.30	$(-6.36 \pm 0.29) \cdot 10^{-3}$
Oulu neutrons		8.434 ± 0.007	$(-7.371 \pm 0.007) \cdot 10^{-3}$
Single neutron events	Reactor On	2.75 ± 0.14	$(-1.72 \pm 0.14) \cdot 10^{-3}$
	Reactor Off	2.29 ± 0.14	$(-1.27 \pm 0.14) \cdot 10^{-3}$
	Both	2.61 ± 0.10	$(-1.58 \pm 0.10) \cdot 10^{-3}$
Phase 1 muons		2.31 ± 0.02	$(-1.28 \pm 0.02) \cdot 10^{-3}$

Table 5.2: Parameters of the fits with a linear function $y = A + Bx$ to the neutron or muon rate as a function of atmospheric pressure. In this table, 'Amplitude' corresponds to A and 'Slope' to B. All datasets are normalized so the average value of all data in each dataset equals one.

Performing the same fit on the normalized neutron rate as a function of pressure measured at the Oulu Cosmic Ray Station results in a similar result as those measured for the high-multiplicity slopes, this is shown in Table 5.2. The slightly steeper slope for the data collected in Oulu can be understood from the higher latitude (67° 22′ N vs 51° 11′ N) and altitude (180 m vs 27 m above sea level) of the detectors [96].

Techniques to obtain pressure matched datasets

In the above paragraphs, it was made clear that a pressure dependent component exists for the cosmic background experienced by the SoLid Phase 1 detector. While the vast majority of the high multiplicity neutrons is removed by the neutron multiplicity veto, a strong pressure dependent component still exists for single neutrons. Creating a dataset with an equal pressure distribution for reactor on and reactor off does not remove this background but it does make it equal for both the reactor on and reactor off datasets.

The pressure for each run is determined from the timestamp. Since a run is at most ten minutes long, it is reasonable to assume the pressure remains constant throughout the run. The pressure at the start of a run can therefore be used for the entire run. A histogram of the pressure of all runs is then made for both the reactor on and the reactor off datasets, this is shown in Figure 5.10 for the commissioning data collected in December 2017 and the data of May 2018. In the next step, runs are selected for each pressure bin until the minimum of the reactor on and reactor off time is reached in each bin. This method is named pressure restriction. The selected dataset is indicated in Figure 5.10 with the filled blue area. The total amount of data available in each set is given in the legend. It is clear this method is very expensive when it comes to selecting data, particularly over short periods of time. From the $13.3 \cdot 10^5$ s in the commissioning data, only $7.2 \cdot 10^5$ s are used in order to obtain a reactor on and off dataset that has identical cosmic backgrounds. When using a larger dataset, a larger fraction of the data will be available when using this method since the environmental pressure fluctuates in a rather limited range. The left panel of Figure 5.7 shows that over the course of 50 years, the pressure remains within the $[950, 1050]$ hPa range with the vast majority of the data points between 1000 and 1020 hPa. While the data in the left panel of Figure 5.7 concerns Oulu, Finland, pressure measurements from the past eleven years in Mol confirm this range.

In order to maximise the data fraction used in these limited datasets, the reactor off data can be scaled. In the left panel of Figure 5.10, there is much more reactor

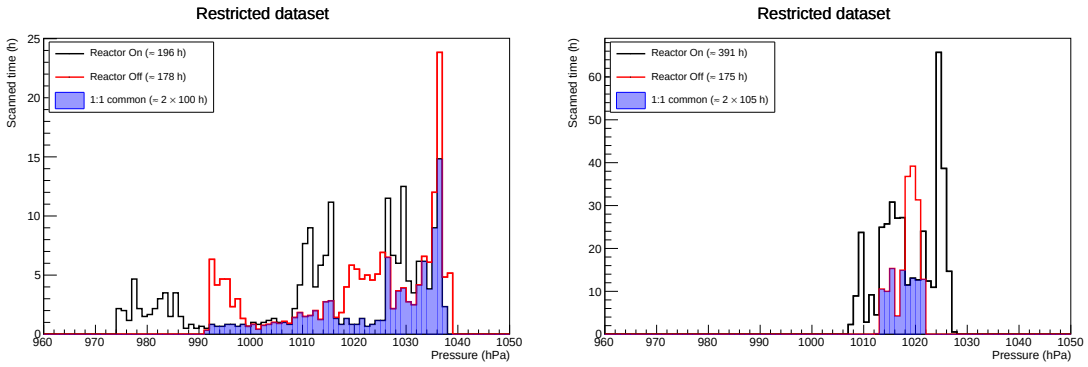

Figure 5.10: Data available per pressure bin in the December 2017 commissioning data (left) and in the May 2018 data (right). In each histogram, the reactor on (black) and reactor off (red) datasets are shown. The amount of data that is common in each pressure bin is indicated with the blue shaded area. For each case, the total amount of data available is indicated in the legend.

off data than reactor on data between 990 and 1000 hPa. In that case, the reactor off data can be scaled down to match the pressure data of the reactor on data. This will reduce the statistical uncertainty on the reactor off prediction compared to the pressure matching method. Similarly, there is much more reactor on data at 1010 and 1015 hPa than reactor off data in the commissioning dataset. For these runs, five minutes of reactor off data can be used for e.g. 20 minutes, this however comes at the cost of an increased statistical uncertainty for the reactor off dataset. In order to avoid blowing up the statistical uncertainties, a cap of two was introduced to the scaling factor, i.e. two hours of reactor off data can be used to compare against at most four hours of reactor on data. This second method of creating identical pressure profiles is named pressure scaling.

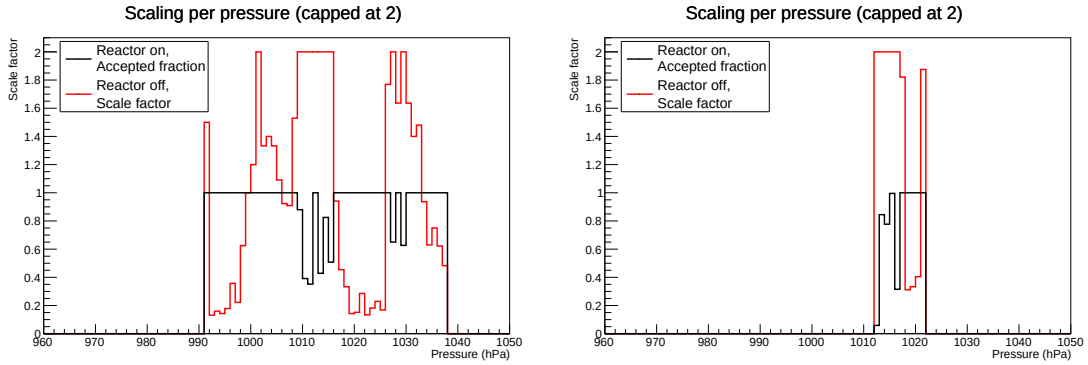

Figure 5.11: Run scale factors used to maximise the available data with identical pressure profiles for December 2017 commissioning data (left) and the May 2018 data (right). For reactor off data, each event is given a weight depending on the atmospheric pressure. For reactor on data, the value represents the fraction of runs used.

The reactor on data should not be scaled in this way since a scaling of the reactor on dataset would not only scale the cosmic background but also potential backgrounds originating from the reactor as well as the IBD events in the data, making IBD rate calculations much harder. In Figure 5.11, the scaling factors per pressure bin are shown for reactor off. For reactor on, Figure 5.11 indicates the fraction of runs at a specific pressure. Bins where the used fraction is not one had less than half the amount of reactor off data available for comparison.

Application of the pressure scaling method boosts the fraction of used reactor on data from 26.5% and 51.0% for pressure matching to 42.6% and 67.9% for pressure scaling, respectively for the December 2017 and May 2018 data. The limiting factors are different for the December and May data. In May 2018, the reactor on fraction that is used is limited by the low amount of reactor off data, which is less than half of the reactor on data. For the commissioning data, the limiting factor is due to the large variations in pressure, hence the weather is to blame. A review of the atmospheric pressure variations in the last eleven years shows that the largest pressure variations in a single month were observed in December 2017.

5.2.4 The BiPo background

Uranium and thorium naturally occur in the environment, with respectively 2.7 and 10.5 mg/kg in the Earth's crust [97]. Both these elements have long decay chains that lead to lead (Pb) or bismuth (Bi), as is shown in Figure 5.12. The unavoidable contamination of the detector materials with these elements and the structures surrounding it follow the natural abundance of the isotopes. On Earth, uranium is composed of 99.27% ^{238}U, 0.72% ^{235}U, $5 \cdot 10^{-5}$ ^{234}U and trace amounts of ^{233}U and ^{236}U. Similarly, thorium is composed of 99.98% ^{232}Th, 0.02% ^{230}Th and trace amounts of ^{227}Th, ^{228}Th, ^{229}Th and ^{231}Th. These abundances combined with the prevalence of both elements in the environment dictates the occurrence of all decays in the decay chains.

When an alpha decaying isotope is located in the lithium screen, it will eject an energetic alpha particle into the ZnS(Ag) micro crystals upon decay. The resulting signal will be very similar to that of neutron capture on ^{6}Li which produces an alpha and tritium particle sharing 4.78 MeV of kinetic energy. If such an alpha decay is preceded by a beta decay, the electron or positron can readily escape the lithium screen and scintillate in a PVT cube, producing an ES signal. A beta-alpha sequence of an isotope in a lithium screen therefore produces the ES-NS coincidence expected from an IBD reaction, albeit with a non-neutron induced NS signal. The half life of the alpha decaying isotope determines the characteristic time of the ES-NS coincidence. For a decay sequence to enter the IBD event selection at a non-negligible rate, the half life of the alpha decaying isotope has to be similar to the neutron capture time. From the 20 beta-alpha decay sequences present in Figure 5.12, only ^{214}Bi to ^{214}Po to ^{210}Pb (BiPo) in the uranium series is relevant (164.3 μs). In all other beta-alpha decays, the half life of the alpha decaying isotope is either too short (^{212}Bi to ^{212}Po to ^{208}Pb, 299 ns half life) or too long (all other combinations, half lives between 1.8 ms and $245.5 \cdot 10^3$ yr) to be a significant background to IBD events. The ^{212}BiPo background can be easily rejected by a minimum ΔT requirement. With a characteristic time of 0.431 μs, every added microsecond reduces the contribution by roughly a decade. A minimum requirement of 5 μs reduces this background to $9 \cdot 10^{-4}$% of the original. The longer decays do not contribute to the correlated background, they do however contribute to the accidental background.

Apart from the ^{238}U contamination of the lithium screen itself, contamination of the BR2 containment building is a source of correlated background as well. Concrete, a mixture of water, cement and filler, is the main building material of the BR2 containment building. Both water and filler have a relatively low concentration of uranium and thorium. However, cement has a ^{226}Ra activity between 37 and 64 Bq/kg [99]. Two types of concrete are used in the construction of the BR2 containment building: 'ordinary' concrete for the structural parts such as walls, ceilings and floors and 'heavy' barite concrete for the reactor vessel. In barite concrete, the sand and gravel filler is

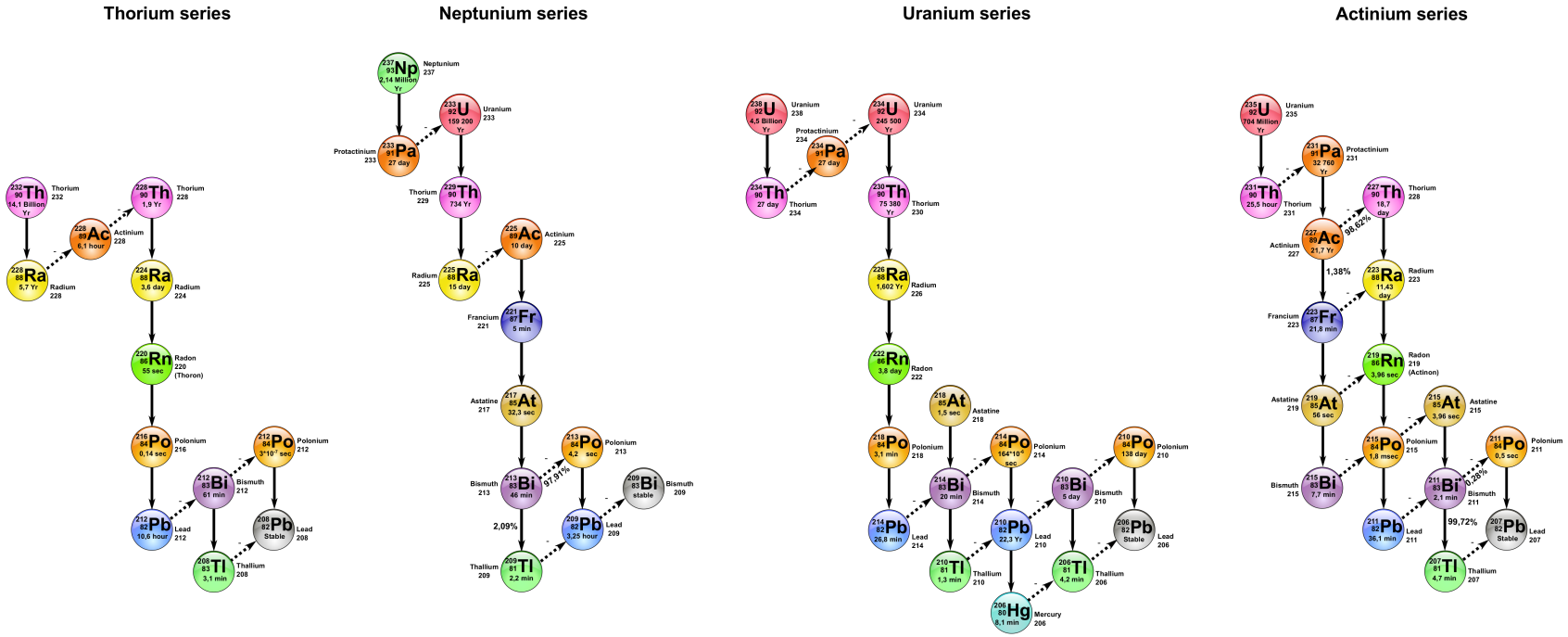

Figure 5.12: The four decay chains with for each element the half life [98]. The decays straight down (full line) are alpha decays, the decays indicated right and up (dashed line) are beta minus decays.

partially or completely replaced by ground barite ($BaSO_4$), giving it a higher atomic number and a higher density (3.5 g/cm^3 instead of 2.3 g/cm^3). It therefore has stronger attenuation of high energy gammas than ordinary concrete. Due to the chemical similarity of barium and radium, radium is readily adsorbed into $BaSO_4$ crystals, resulting in relatively high concentrations of radium (typically between 9.2 and 15 Bq/kg but concentration could be up to 1 kBq/kg) [100]. The large amount of concrete concerned, over 5000 ton, creates a vast and virtually everlasting supply of radium [101].

Luckily, most of the concrete is located far enough from the detector to avoid additional background contributions directly from the concrete. Only gaseous isotopes in the decay chains in Figure 5.12 can induce backgrounds from the concrete. From all the elements in Figure 5.12, only radon (Rn) is gaseous. It can collect in small cavities and seep out of microscopic cracks in the concrete, resulting in variations of the radon concentration in the BR2 building and hence in the air surrounding the detector. Indeed, a correlation exists between the ^{222}Rn rate and the observed NS rate in the Phase 1 detector, as shown in Figure 5.13. A delay is observed between variations in the ^{222}Rn rate and the NS rate. This is expected, as radon has to decay to polonium before it contributes to the correlated background. The observed delay, roughly two hours, is however longer than the anticipated 50 minutes from the decay of ^{218}Po (3.1 minutes), ^{214}Pb (26.8 minutes) and ^{212}Bi (19.9 minutes). This longer than expected delay is likely due to the limited airflow from the containment building into the container.

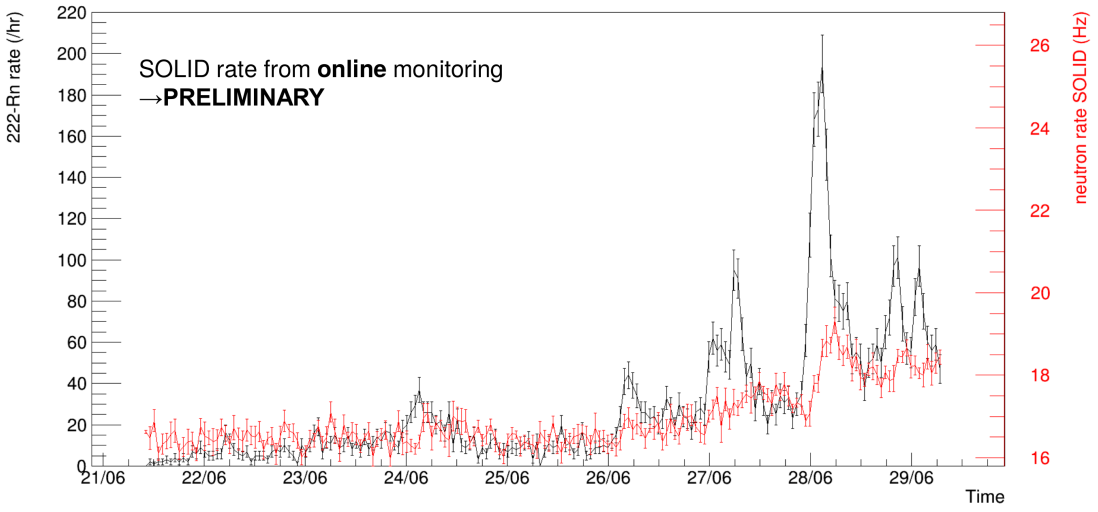

Figure 5.13: Evolution of the ^{222}Rn activity outside the water wall and the observed Phase 1 NS rate over time [102].

The BiPo event topology and energy spectrum

The Q-value of the ^{214}Bi decay is 3.270 MeV, resulting in an electron energy spectrum overlapping with the positron energy spectrum of IBD reactions. An approximation of the beta energy spectrum of ^{214}Bi is shown in Figure 5.14, clearly showing the overlap of the beta energy spectrum with the peak of the IBD energy spectrum. The β^- energy spectrum is calculated from

$$N\left(T_e\right) = \frac{C}{c^5}\left(T_e^2 + 2T_e m_e c^2\right)^{1/2}\left(Q - T_e\right)^2\left(T_e + m_e c^2\right) \tag{5.4}$$

for each decay level. In Equation 5.4, C is a normalization factor, T_e is the electron kinetic energy and Q the Q-value of the decay under consideration. This spectrum is only approximate since Coulomb attraction between the emitted electron and the nucleus has not been taken into account. Adding this would shift the spectrum to lower energies [103]. The IBD energy spectrum is obtained from GEANT4 simulations, it is the same spectrum as is shown in Figure 5.1. Although the comparison is not fully fair, the overlapping ^{235}U IBD and ^{214}Bi β^- energy spectra illustrate that the correlated background due to BiPo will be hard to reject.

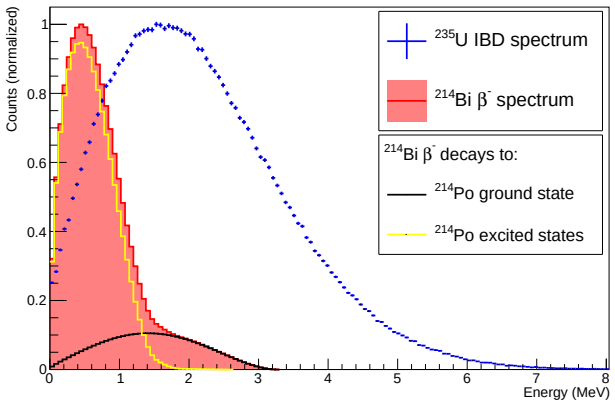

Figure 5.14: Comparison of the electron energy spectrum in ^{214}Bi beta decay (red, filled) to the positron energy spectrum from IBD interactions originating from ^{235}U (blue). Also shown are the contribution from decays to the ground state of ^{214}Po (black) and to excited states (yellow). Coulomb attraction was ignored while obtaining the electron spectrum, taking this into account would shift the entire spectrum to lower energies [103, 104].

Two categories can be distinguished in the BiPo background: decays to the ground state (19.1%) and decays to excited states (80.9%), respectively indicated in black and yellow in Figure 5.14. For beta decays to the ground state, all energy is distributed between the emitted electron and neutrino. These therefore have a fairly straightforward topology. There are however also 65 excited states of ^{214}Po to which ^{214}Bi can decay. These excited states are extremely short lived, the remaining energy is radiated away almost instantaneously, decaying to the ground state via one or more gammas. In decays to excited states, the electron and the neutrino combined take at most 2.66 MeV of the 3.27 MeV. The remaining energy is carried away by photons with energies up to 3.18 MeV, resulting in a more complicated topology.

For BiPo decays where ^{214}Bi decays to the ground state, the ES signal is contained in a single cube since the range of a 3 MeV electron in PVT is only 0.7 cm [89]. Since the electron is emitted from the lithium screen, it will scintillate in one of the two cubes facing the screen. The electron is emitted isotropically, the ES signal will therefore be detected in the same cube as the NS signal in 50% of cases or in the cube at $X+1$ or $Z-1$ with respect to the NS cube in 25% of cases each. 50% of this background can thus be rejected by requiring that no ES signal is detected in the cube with the NS signal. This can be implemented by requiring $\Delta R > 0$. From the ΔR panel of Figure 5.1 (top right), it can be seen this cut comes at a cost of rejecting 6.36 ± 0.03% of all IBD signals.

Requiring that also no signal is observed in the two cubes facing the lithium screens of the cube with the NS signal to reject the remaining 50% of the ground state BiPo decays would reject a larger fraction of IBD events. While the starting point for BiPo

and IBD events is different, the resulting distributions are similar. For an IBD, when the positron scintillates in the PVT, the neutron starts its thermalization process. As mentioned before, four of the six sides of the cube have a lithium screen, either before or behind two layers of Tyvek. This leads to increased capture fractions of IBD neutrons in the cubes located at $-X$ and $+Z$ with respect to the interaction cube. Similarly for BiPo, the electron is emitted from the $+X$ or $-Z$ face of the cube. The electron will therefore either scintillate in the cube itself or in the cubes on the $+X$ and $-Z$ sides of the NS signal, both processes are sketched in Figure 5.2. From Figure 5.21, it is clear that the ΔX and ΔZ distributions of IBD and BiPo processes have a similar asymmetry. It is therefore not feasible to reject all candidate events that have an ES signal in these two cubes. Unless these BiPo events can be rejected in some other way (see Chapter 6), they will be part of the event selection, driving down the signal to background ratio.

As mentioned, most ^{214}Bi decays are into excited states of ^{214}Po, resulting in gammas that are emitted alongside the electron. These gammas are not contained to the three cubes in which the electron can deposit its energy. The lowest Q-value of beta decays into excited states is only 0.09 MeV, the electron emitted by decays to this level will simply not be detected. The ES signal of much of the excited state decays is thus dominated by the gammas emitted in the ^{214}Po de-excitation. Additionally, not all decays from excited states to the ground state are allowed, some decays therefore take place via intermediate states. This leads to multiple gammas, on average 1.34, being emitted in a single decay as good as simultaneous (the longest living excited state has a half life of 99 ps). In addition, each gamma can undergo Compton scattering multiple times. Both these characteristics increase the number of cubes with an ES signal in the detector, increasing the ES signal multiplicity.

BiPo rate

A pure sample of BiPo events can be obtained using reactor off data. The selection requirements are listed in Table 5.3. The ΔT requirement has to be set as broad as possible due to the long ^{214}Po half life (164.3 μs). It is limited on the high side by the length of the IBD buffer while the low ΔT constraint has been placed before the neutron start time determination laid out in Section 4.3.2 became available. The ΔR requirement and the upper energy bound are motivated by the discussion in the previous paragraphs. The lower energy bound is effectively the detection threshold due to parameter settings in the reconstruction algorithm (see Section 5.3).

Variable	**Value range**
ΔT	[18, 380] μs
ΔR	0 cubes
Energy	[0.6, 3] MeV

Table 5.3: Selection criteria to obtain a pure sample of BiPo events [105].

Fitting an exponential function to the ΔT spectrum, shown in Figure 5.15, indeed shows decay constants consistent with the one expected from the ^{214}Po half life ($\tau = t_{1/2}/ln(2) = 237.1$ μs). From the low value for the reduced χ^2, it can be concluded this is indeed a pure BiPo sample. If contributions from neutron capture or accidental coincidences were present, this would show itself in deviation from this single exponential behaviour and hence increase the χ^2 value. The high purity of this sample can be understood from the very narrow energy and ΔR requirements. Cosmic backgrounds

typically have higher energies and larger ΔR values, as will be shown in Section 5.3. Accidental backgrounds are limited due to the restrictive $\Delta R = 0$ requirement. Both panels of Figure 5.15 have a good χ^2, while only in the right panel the reactor is off. This indicates that even though the ^{41}Ar energy window is within the selection (Section 4.6.3), the contribution from accidental backgrounds is very small.

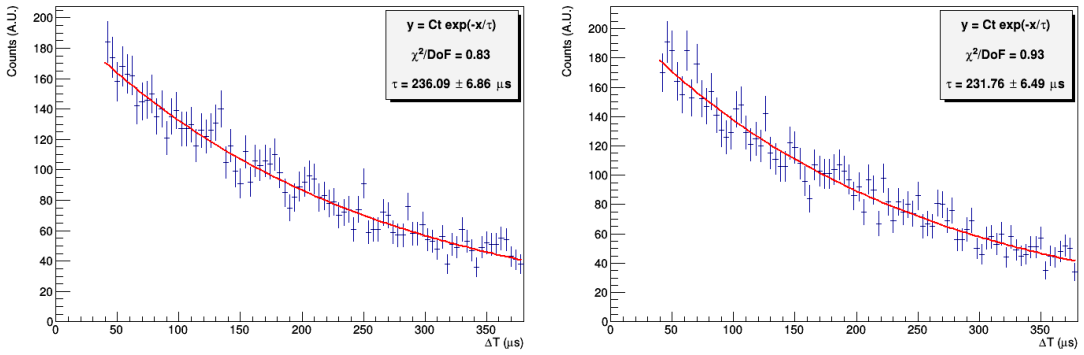

Figure 5.15: ΔT distribution of ES-NS coincidences collected over six hours during December 3^{rd} 2017 (left) and December 15^{th} (right), selected using the criteria listed in Table 5.3. An exponential is fitted to the distribution, the slope $\tau = 236.1 \pm 6.9$ (231.8 ± 6.5) μs is consistent with the ^{214}Po half life: $\tau = t_{1/2}/ln(2) = 164.3/ln(2)$ μs $= 237.1$ μs for reactor on (off).

This selection shows some variation over time as can be expected from the ^{222}Rn emissions but generally hovers around 6 events per day per cube for inner cubes with new lithium screens and 1 event per day per cube for cubes in the outer layer that were equipped with old lithium screens (see Section 2.2.4). Simulation (GEANT4 + ROSim) of BiPo events shows this selection is $10.5 \pm 0.1\%$ efficient, resulting in an actual BiPo rate of 10 and 60 events per day per cube respectively for cubes with old and new lithium screens [105]. Including the rate and cube variations, the BiPo rate per cube is between three and four orders of magnitude higher than the expected IBD rate. BiPo is therefore the main background to the experiment before application of any selection requirements.

5.3 Selection of IBD events

In the previous section, a description of the correlated backgrounds and a strategy to reject them has been given. In this section, the criteria to select IBD events will be discussed in more detail. A comparison between signal and background simulations is performed in order to motivate the selection criteria. Before making this comparison, additional information on the simulation is provided.

On the simulated data

Detector simulation typically happens in two steps: the particle interactions are simulated first, the detector response to these interactions are simulated next. Of these two steps, the first step is computationally the most expensive while the second step (ROSim) is most prone to change, e.g. when detector settings such as the over voltage or IBD buffer length are changed. The first step provides a list of energy depositions, the ROSim takes that list and translates them in waveforms to mimic what is observed in data. This translation involves parameters such as the amount of light produced in the lithium screen upon neutron capture, the fraction of light that makes it into the

PVT cube, the fraction entering in each WLS fibre, the attenuation in the WLS fibre, the fraction that is detected by each SiPM and the conversion of detected photons into a waveform. Finally, the various triggers have to be applied on these waveforms before the output can be written to disk so the simulation files can be processed by the same analysis software used for data files. While not computationally intensive, this second step depends on a lot of parameters. All of which have to be tuned in order to have an accurate description of the detector output.

Unfortunately, at the time of the analysis, a bug in the ROSim created a very long energy tail in simulated events, e.g. BiPo events had an ES signal tail up to 20 MeV despite having an endpoint energy of 3.2 MeV. As a result, it was decided not to use the ROSim for this thesis. In order to still compare the simulation to the data, a script that replicates the cube reconstruction algorithm described in Section 4.1, including the 'wrongly' reconstructed cubes, was written. While this script is accurate in the way it reconstructs cubes, it does not take statistical fluctuations due to the ROSim parameters described earlier into account. It is therefore only a crude approximation of a full ROSim. While the energy of individual ES signals in these files is not realistic due to the lack of smearing, one would expect the same average energy. This approach is roughly validated by comparing the energy spectrum of the highest energy ES signal for the BiPo selection described in Section 5.2.4. As can be seen in Figure 5.16, the agreement between data and the GEANT4 simulation with the cube reconstruction emulation is reasonable. The location of cubes, ΔT and the ES cluster size are not influenced by this lack of smearing.

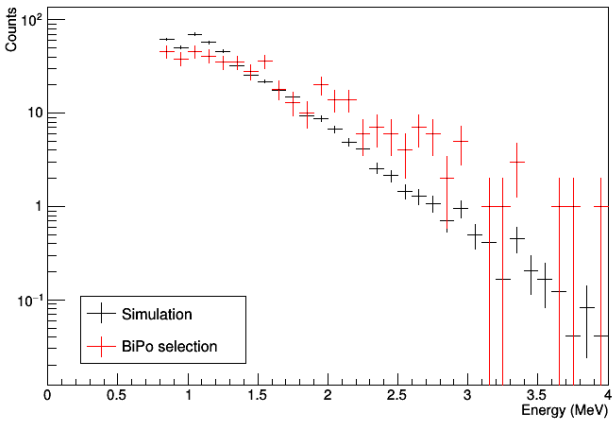

Figure 5.16: Comparison of the energy spectrum of data and cube reconstruction emulated GEANT4 simulation for a BiPo selection. For this comparison, smearing was added.

5.3.1 Selection procedure and initial selection criteria

IBD candidates are ES-NS coincidences, with the NS signal as starting point. As a first step, for each NS event, all ES cubes within the plane hop and within in a time window preceding the NS signal are listed. The maximal distance between any two of the reconstructed ES cubes is calculated. If this distance is larger than a specified value, the NS signal is rejected. Additionally, all reconstructed ES cubes have to take place within four samples (100 ns) in order to exclude random coincidences. The ES cube with the highest reconstructed energy is chosen as the corresponding ES signal. If that cube is outside the selected energy or space window, the NS signal is discarded.

The remaining ES-NS coincidences are considered IBD candidates. From these coincidences, all distributions shown in Figure 5.1 can be extracted and compared to the same distributions obtained from simulation in order to determine the fraction of each topology in the selection. For the reactor off data, there are no IBD events present, while for the reactor on data, there should be. Comparison between the selected reactor on and reactor off events indicates the purity of the selection. The difference between the ΔT, energy and spatial distributions for reactor on and reactor off events should align with the corresponding distributions expected from simulated IBD events.

Initial minimum and maximum values for the selection parameters can be established from the previously discussed vetoes and trigger settings. Even though the energy window within the IBD buffer is bound by the ZS threshold on the low side and the 14 bits of the ADC chip on the high side, a more restricted initial selection has to be made. To reconstruct an ES cube, a threshold of 200 ADC is applied in the peak finder and a peak in all four channels is required. When taking into account the average light yield and gain and assuming a Poison distribution for the number of detected photons, the initial lower bound on the energy is chosen as 0.8 MeV. Figure 5.17 motivates this decision since the trigger reaches an efficiency of 99% at this energy. While this efficiency is reached at a lower energy for the data collected in May 2018 due to different trigger settings, also shown in Figure 5.17, this initial lower energy value is maintained in both datasets[2]. In order to minimize the accidental background, the lower energy is increased to 2 MeV. This completely rejects the radiation from ^{41}Ar, which has a Compton edge at 1.08 MeV. For the upper energy bound, the light yield, the gain and the non-zero pedestal value determine the energy corresponding with 16384 ADC, the upper limit of the 14 bit ADC chip. For the over voltages applied in December 2017, this corresponds to 28.5 MeV. The higher over voltage in May 2018 reduces this value to 20 MeV. In order to be consistent between both datasets, the initial energy window is taken as 2 MeV $< E <$ 20 MeV.

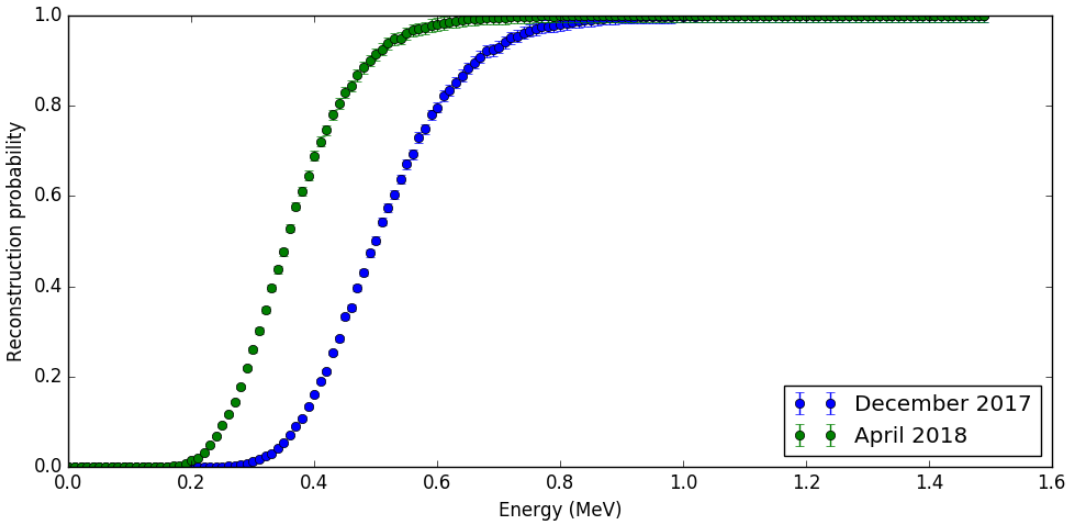

Figure 5.17: ES cube reconstruction efficiency as a function of energy. The energy of the 99% point is determined by a combination of the requirement to have a 200 ADC peak in all four channels and the applied over voltage. The over voltage applied on the SiPMs is different in the two datasets, influencing both the gain and the light yield.

[2]No calibration was performed for the detector settings used in May at the time of writing. Light yields were extrapolated based on muon energy depositions.

Also the initial ΔT window is more narrow than what is permitted by the length of the IBD buffer, which has a capacity of 380 μs. The introduced muon and neutron multiplicity veto only scans up to 200 μs prior to the NS signal. Since one obviously does not want a muon or a second neutron within the ES-NS coincidence search window, ΔT is limited to 200 μs.

The spatial restrictions are limited by the plane size for ΔX and ΔY to $[-16, 16]$ and by the plane hop parameter for ΔZ to $[-3, 3]$. For ΔZ, an optimization in terms of signal efficiency versus data volume has been performed in order to reach $\Delta Z \in [-3, 3]$. Since the data volume of the IBD buffer is dominated by random coincidences, the data volume optimization can be interpreted as signal efficiency versus random coincidences. While the orientation of random coincidences is not necessarily 100% isotropic, it is to first order. One can therefore restrict both ΔX, ΔY and ΔZ to $[-3, 3]$ as initial spatial selection criteria. The left column of Figure 5.1 shows these distributions, confirming $[-3, 3]$ is not too strict as initial selection criteria. Since ΔR is a combination of the three Cartesian coordinates, it is limited to $3\sqrt{3} = 5.2$ cubes by the initial restrictions on ΔX, ΔY and ΔZ mentioned above.

5.3.2 Motivation of the IBD selection criteria

Requirements on the energy range

From Figure 5.1, it can be seen the energy distribution of the positron emitted in the IBD process has a peak at 1.65 MeV and an end point at roughly 10 MeV. It is however expected to observe only one IBD with 10 MeV deposited by the positron in 19.2 years of taking data. In fact, 99.4% of all IBD positrons deposit less than 6 MeV of visible energy in the PVT cubes [90]. The energy distributions of spallation and atmospheric prompt neutrons have a long tail towards high energies. The BiPo background is located at low energies. These four distributions are shown in Figure 5.18. In order to reach an acceptable level of BiPo events, at least 99.9% of this background has to be rejected. Such a high rejection is achieved easiest via an energy cut, although it comes at a high cost to the signal detection efficiency. The surviving fraction of events after application of a lower energy threshold is shown for signal and the correlated backgrounds in Figure 5.19.

All curves in Figures 5.18 and 5.19 were produced using MC truth information with emulated cube reconstruction and combination algorithms, no smearing in the energy response and gain variations were taken into account. In particular for low light yield cubes, fluctuations will lead to events being reconstructed as having a lower or higher energy, resulting in a tail to higher energies due to the falling spectra. While selecting an energy of 3 MeV as lower limit reduces the simulated BiPo background by $99.995 \pm 0.040\%$, energy smearing will lead to a non-zero contribution above this threshold. Considering the average CaliPSo light yield for the first four modules, 86.3 ± 6.5 PA/MeV, a 2.5 MeV deposit has a 0.2% probability to be reconstructed as a 3 MeV deposit or higher when assuming the light is split equally over the four fibres and the number of photons detected can be sampled from a Poison distribution. For 2.6, 2.7 and 2.8 MeV, this number rises to 1.3, 4.9 and 14.0% respectively. Taking these probabilities into account reduces the cut efficiency by almost a factor ten, to 99.965% rejection. Making a similar calculation for the signal efficiency increases the selection efficiency from $23.78 \pm 0.03\%$ to 25.14%. The far less steep spectra of atmospheric and spallation neutrons are affected less by taking the light yield spread into account, with rejection efficiencies moving respectively from $54.3 \pm 1.7\%$ and $53.0 \pm 1.5\%$ to 54.0%

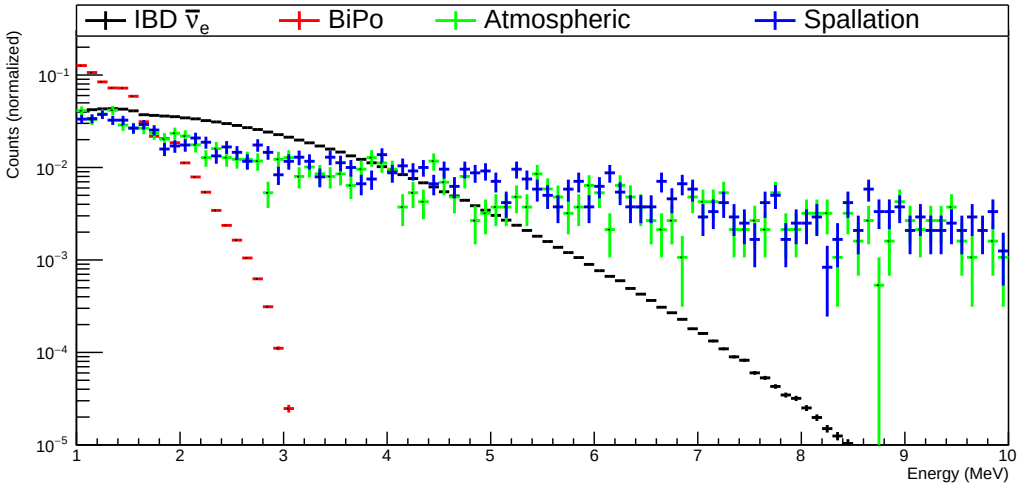

Figure 5.18: Energy distribution of signal and the correlated backgrounds. Errors are statistical only, no ROSim was used although the cube reconstruction discussed in Section 4.1 was emulated on the MC truth.

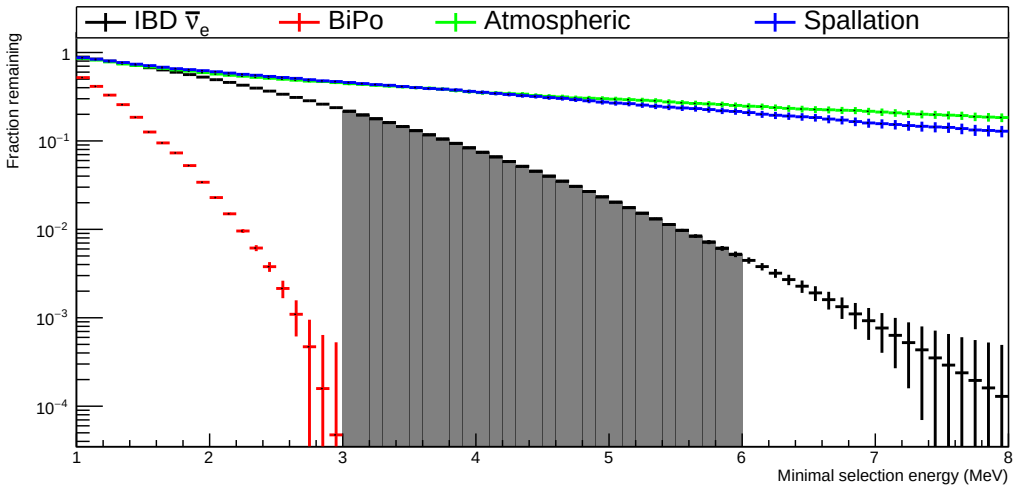

Figure 5.19: The surviving fraction of events for signal and correlated backgrounds after the application of a lower energy threshold. The selected energy range, 3 to 6 MeV, is indicated for signal (gray shaded area).

and 52.4%.

On the high energy side, the energy distribution of the cosmic correlated background is decreasing very slowly. The much faster reduction of the expected signal allows placing an upper energy limit that keeps most of the remaining signal while rejecting a significant fraction of the cosmic backgrounds. Placing the upper energy limit at 6 MeV reduces the signal selection efficiency by $0.52 \pm 0.04\%$ of the original sample while the atmospheric and spallation neutron backgrounds are reduced by $25.2 \pm 2.0\%$ and $21.6 \pm 1.8\%$ respectively. Applying the light yield smearing results in a total signal selection efficiency of 24.5% and a background reduction of 99.965% for BiPo, 79.36% for atmospheric neutrons and 74.14% for spallation neutrons.

Inspection of the ΔT distribution in a reactor off sample requiring the energy of the highest ES energy cube to be between 3 and 6 MeV, shown in Figure 5.20, indeed shows contributions from both BiPo and neutron capture events. While the contribution of BiPo events is no longer dominant, a rate of 0.10 ± 0.02 events per cube per day is still observed. This is a reduction of roughly 99.98% with respect to the rate obtained in Section 5.2, i.e. close to the value predicted from simulation.

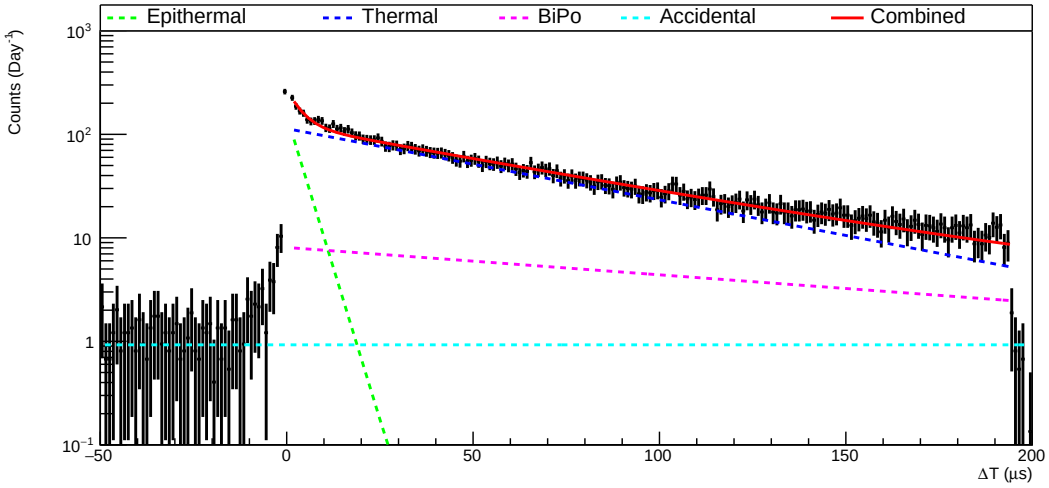

Figure 5.20: ΔT distribution of the events selected by the energy requirement in a reactor off sample. A fit with a constant and three exponentials is performed in order to determine the contributions from accidental coincidences, epithermal and thermal neutron captures and from BiPo events. The slopes of the three exponentials were fixed to the IBD capture times and the ^{214}Po half life to determine the rate of each process.

Spatial requirements

ΔX, ΔY and ΔZ (and ΔR) are inherently correlated since all three (four) are a different aspect of the same property, the relative position of the ES and NS signals. Figure 5.21 shows the spatial distributions for IBD signal and the correlated backgrounds. The distributions for atmospheric neutrons events are the broadest of the four distributions in each of the three dimensions. Therefore, the following requirement are applied on ΔX, ΔY and ΔZ respectively: the highest energy ES cube must be within $[-2, 2]$, $[-2, 2]$ and $[-2, 3]$.

Since these distributions are strongly correlated, the backgrounds are reduced by respectively $24.8 \pm 4.5\%$, $6.1 \pm 3.7\%$ and $11.7 \pm 7.8\%$ for atmospheric and spallation neutrons and BiPo. Identically for the signal, $94.46 \pm 0.09\%$ is kept by the selection.

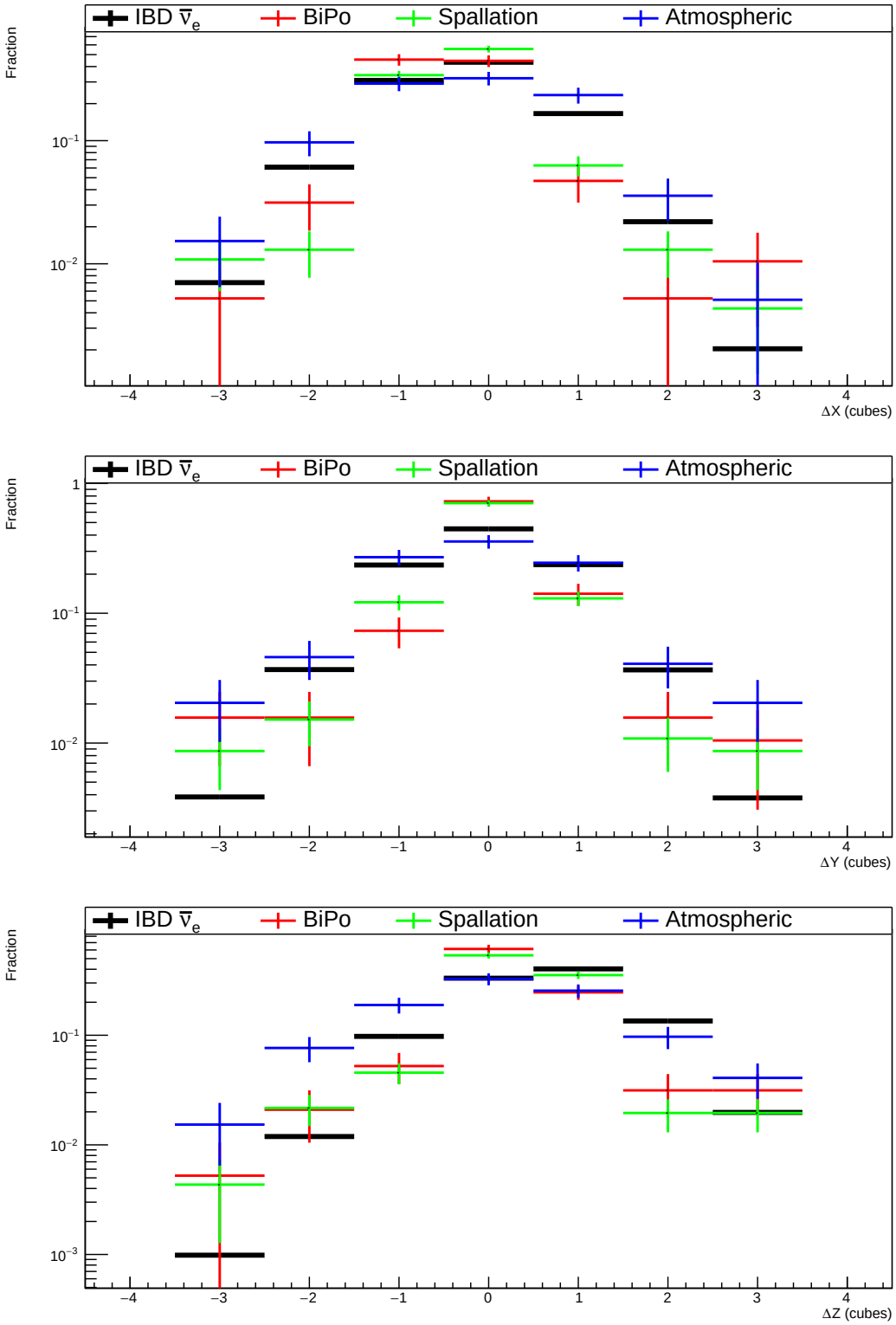

Figure 5.21: ΔX, ΔY and ΔZ distributions for IBD and correlated backgrounds events.

The larger uncertainty on the BiPo simulation is due to the high BiPo rejection fraction of the energy selection. From the initial 20 million simulated events, a mere 300 have a reconstructed energy over 3 MeV and the highest energy ES cube within the $7 \times 7 \times 7$ cube box selected as initial ΔXYZ.

As it was opted to include the $\Delta Z + 3$ bin in the selection, it does not make sense to make the maximal accepted value for the ΔR less than three. The combined simulated background for $\Delta Z + 3$ after the previous selections is 21 events. Additionally, the rejection of the four outer most cubes of the $\Delta Z \pm 2$ plane $\left(\Delta R = \sqrt{12}\right)$ is also being decided via this parameter. For these four cubes as well, as good as no simulated events are registered. Due to the restrictions on ΔX and ΔY, the $\Delta Z + 3$ cubes lie on a 5×5 cube square, combining 1.95% of al so far surviving IBD coincidences. From these 1.95% of events, 1.46% lie within the inner 3×3 cube square of which 0.43% on the corners of the inner square. The eight cubes on the corners of the $\Delta Z \pm 2$ plane are expected to combine to only 0.37% of IBD events. In order to limit the accidental background, it is therefore opted to allow a maximal ΔR of $\sqrt{11}$, selecting the entire inner square of $\Delta Z + 3$ and rejecting the eight outer cubes of $\Delta Z \pm 2$.

Requirements on the ES cluster size

Up to this point, clusters of ES cubes, each of which has an energy of minimally 2 MeV[3], with a maximal internal distance of $\sqrt{2}$ (cubes minimally sharing an edge) have been used. This requirement is based on the possibility of a positron moving from one cube to another via an intermediate cube, crossing close to the edge. Figure 5.22 shows this is a reasonable selection requirement. In order to gain signal selection efficiency, one could consider relaxing the requirements on the maximal distance to two, which would increases the selection efficiency by 17.64 ± 0.02%. However, this also increase the BiPo, atmospheric and spallation neutron backgrounds by (4.6 ± 1.4) %), (13.2 ± 1.0) %) and (14.6 ± 1.8) % respectively. The maximal internal distance is therefore kept at $\sqrt{2}$.

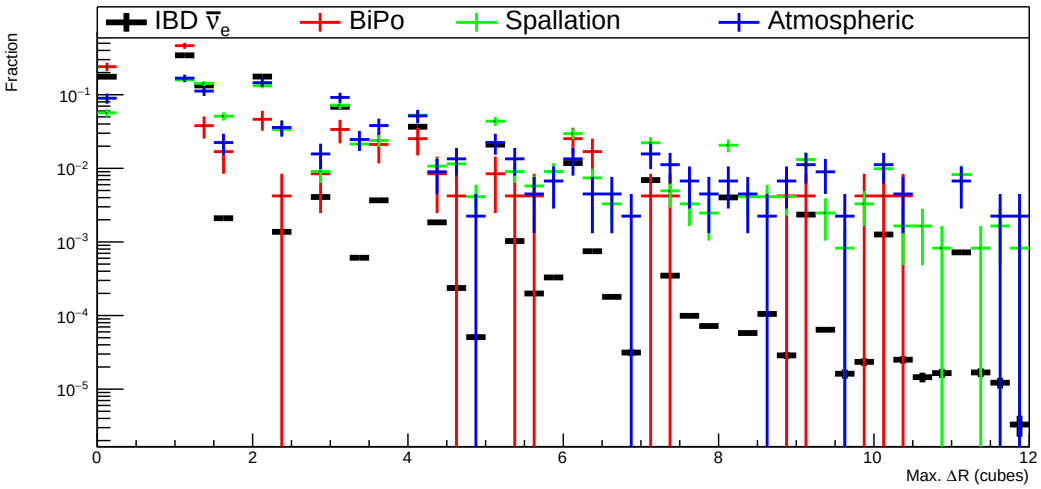

Figure 5.22: Distribution of the maximal distance between all reconstructed ES cubes with energy above 2 MeV produced in association with an NS signal. The bins 0 (same cube), 1 (touching face), 1.25 (touching edge) and 1.5 (touching corner) are populated by only one topology, bins from 2 onwards can have multiple topologies in them.

[3]There might be double counting of energy for cubes in the same plane and with the same X or Y.

Figure 5.22 also shows the very different topology high energy neutrons have. A single high energy neutron can transfer enough energy to protons in several cubes so that multiple of these cubes pass the 2 MeV energy threshold for an ES cube to be considered in this IBD analysis. These ES cubes can be quite far apart, sometimes having more than ten cubes in between them. This can be seen from the average maximum internal distance values, these are 1.62 and 1.63 for simulated IBD and BiPo events and 3.0 and 3.1 for atmospheric and spallation neutron events.

Requirements on ΔT

As with the distance parameters, increasing the accepted ΔT window for ES-NS coincidences will increase the amount of random coincidences. In addition, it will also increase the fraction of BiPo events in the selection due to the longer half life of ^{214}Po compared to the neutron capture time. On the low side, the ΔT selection is put at 5 μs in order to avoid any possible contamination from ^{212}BiPo events. This minimum requirement also removes possible remaining issues with the neutron start time reconstruction. On the high ΔT side, the capture time of spallation and atmospheric neutrons is slightly longer than for IBD neutrons (see Section 4.4). This effect is however minimal compared to the typical time constant for BiPo events. Reducing the maximum ΔT by half, i.e. to 100 μs, will select 78% of the remaining IBDs events and reject 65.6% of the remaining BiPo events.

Combining the minimum and maximum requirements (5 μs $< \Delta T <$ 100 μs) selects 71.0 ± 0.1% of all IBD events within the IBD buffer while rejecting 67.7% of the remaining BiPo events. The BiPo rejection rate is determined from the ^{214}Po half life since insufficient simulated events remained within the selection to provide an accurate value. For the cosmic backgrounds, the efficiency of the ΔT selection is assumed to be identical to the one determined for IBD events since here as well, insufficient simulated events remain within these datasets.

5.3.3 Overview of the selection requirements

The previous section listed all quantities on which an ES-NS coincidence is judged as well as the range that was selected for these quantities and the effect this selection has on the signal and correlated background populations. In this section, an overview of all these selection parameters is given. Ultimately, the selection efficiency of the combined criteria is given. All of the efficiencies are shown in Table 5.4.

Parameter	IBD	BiPo	Atmospheric neutrons	Spallation neutrons
	100	100	100	100
Energy	22.91 ± 0.01	$(1.82 \pm 0.08) \cdot 10^{-3}$	17.18 ± 0.48	10.83 ± 0.41
ΔXYZ	22.29 ± 0.01	$(1.46 \pm 0.08) \cdot 10^{-3}$	14.89 ± 0.45	7.47 ± 0.34
ΔR	20.28 ± 0.01	$(1.33 \pm 0.07) \cdot 10^{-3}$	12.38 ± 0.40	6.76 ± 0.32
Cluster size	17.27 ± 0.01	$(1.21 \pm 0.07) \cdot 10^{-3}$	7.09 ± 0.30	3.96 ± 0.24
ΔT	12.25 ± 0.01	$(0.39 \pm 0.02) \cdot 10^{-3}$	5.03 ± 0.21	2.81 ± 0.17

Table 5.4: Overview of the signal and background cumulative selection efficiency after application of each parameter requirement. All values given are expressed in percent of the original sample. The finel selection efficiency predicted by the simulation is listed in the last (ΔT)

The total selection efficiency for IBD events is about 12.3%, while the original BiPo

background is reduced by more than three orders of magnitude. When the neutron capture efficiency and the NS identification efficiency are taken into account (Section 4.5), the IBD selection efficiency reduces to 6.4%. In order to reach the design goal of 30%, a fivefold increase in IBD selection efficiency is required. The energy cut is both most efficient at rejecting BiPo and most damaging to the signal selection. Additionally, this high energy threshold also makes a part of the L/E range unavailable, further damaging the capabilities of the experiment. It is clear that in order to reach the design goal, the energy selection will have to be relaxed. In order to deal with the increased BiPo background that comes with a lower energy threshold, new selection requirements will have to be introduced. A few suggestions are given in Chapter 6.

5.4 Reactor on and off event rate at high energies

As mentioned in Section 5.3, the IBD positron deposits less than 6 MeV of visible energy in the PVT cube in 99.4% of all IBD events. At high energies, e.g. prompt energy above 8 MeV, it is therefore expected for the reactor status to have no influence on the rates and distributions of selected ES-NS coincidences. Differences in environmental parameters such as the atmospheric pressure do however maintain their influence in this high energy regime. Figure 5.23 shows the ES-NS coincidence rate during December 2017 for high energies. Other than moving the accepted energy window from 3 MeV $< E <$ 6 MeV to 8 MeV $< E <$ 20 MeV, the selection criteria applied are the same as those mentioned in Section 5.3. The anticorrelation between the high energy background rate and the atmospheric pressure ($\rho = -0.95$) can clearly be seen in Figure 5.23. Due to the inverted pressure axis, the rate and pressure move in the same direction. The accidental background, see Section 5.5.1, is determined from an identical sized off-time window following the NS signal ($-105\ \mu\text{s} < \Delta T < -10\ \mu\text{s}$).

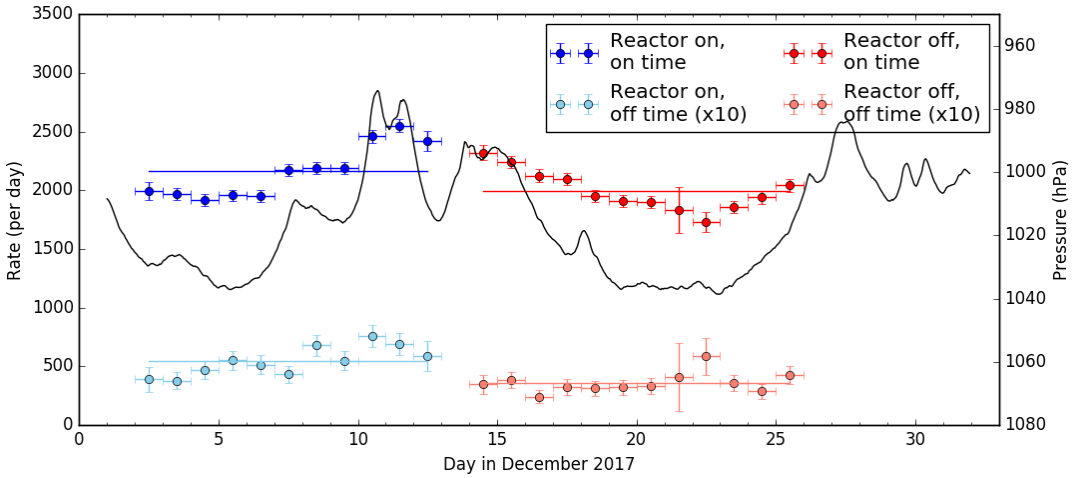

Figure 5.23: ES-NS coincidence rate per day at high energies in the December 2017 data. The accidental background rate is multiplied by a factor 10 for visualisation.

The observed event rate during the reactor on period is higher than for reactor off, as is expected due to the lower average atmospheric pressure when the reactor was on. When calculating the rate using the pressure equivalent datasets introduced in Section 5.2, the reactor on and reactor off periods are consistent within one standard deviation. This is shown in Table 5.5. The 2.5 σ significance of the reactor on excess

in the 'reference' dataset, i.e. without considering pressure variations, indicates the necessity to take these variations in the atmospheric pressure into account.

	Reactor On Day^{-1}	**Reactor Off** Day^{-1}
Restricted	713 ± 9	722 ± 9
Scaled	713 ± 8	723 ± 8
Reference	757 ± 7	733 ± 7

Table 5.5: ES-NS coincidence rate per day after subtracting the accidental background for the December reactor on and reactor off datasets at high energy.

5.5 Observation of IBD events

The event selection explained in Section 5.3 is aimed at minimizing the amount of correlated background that enters the selection while maximizing the number of IBD events. The ES-NS event rate per day obtained for both datasets after applying these event selection requirements is shown in Figure 5.24. Contamination from cosmic background events can clearly be seen by the anticorrelation between the atmospheric pressure and the event rate, especially in the December 2017 data. This anticorrelation can also be seen in the accidental rate.

5.5.1 Accidental background

The accidental background is determined using an off-time window ($-105\ \mu\text{s} < \Delta T < -10\ \mu\text{s}$) with reference to the reconstructed NS signals. All selection criteria remain the same other than the shifted time window and the fact that the muon veto is not applied. In the off-time window, the coincidence is made between ES signals following NS signals, the opposite order of what is expected for spallation neutrons. Since the goal of the muon veto is to reject spallation neutrons, the muon veto is not needed. If a muon were to enter the time and space window in which coincidences are made, it would be rejected by both the energy and ES cluster size requirements. The off-time window is not only mirrored, it is also shifted away from the NS signal so the tail of the NS signal does not enter the accidental window.

One is in principle not limited to a single off-time window. Using multiple off-time windows would reduce the statistical uncertainty on the accidental background rate. Thanks to the segmentation of the SoLid detector, one could also consider off-position windows. In this thesis, a single off-time window is used directly following the NS signal.

An average rate of 55.4 ± 2.6 (34.2 ± 2.1) events per day is observed for reactor on (off) in December 2017 before applying pressure matching. For the data collected in May 2018, the observed rates in both the on-time and off-time window are lower than those observed in December 2017, as is expected from the completion of the shielding. For reactor on (off) in May 2018, the observed accidental rate is 33.5 ± 1.4 (14.5 ± 1.4) per day. The accidental rate follows the combined prevalence of ES and NS signals, it is therefore also subject to the anticorrelation between the atmospheric pressure and cosmic background. The neutrons of the cosmic background lead to an increased NS rate and therefore an increased accidental rate. The much larger excess for reactor on in accidental coincidences in May 2018 compared to December 2017 is unexpected.

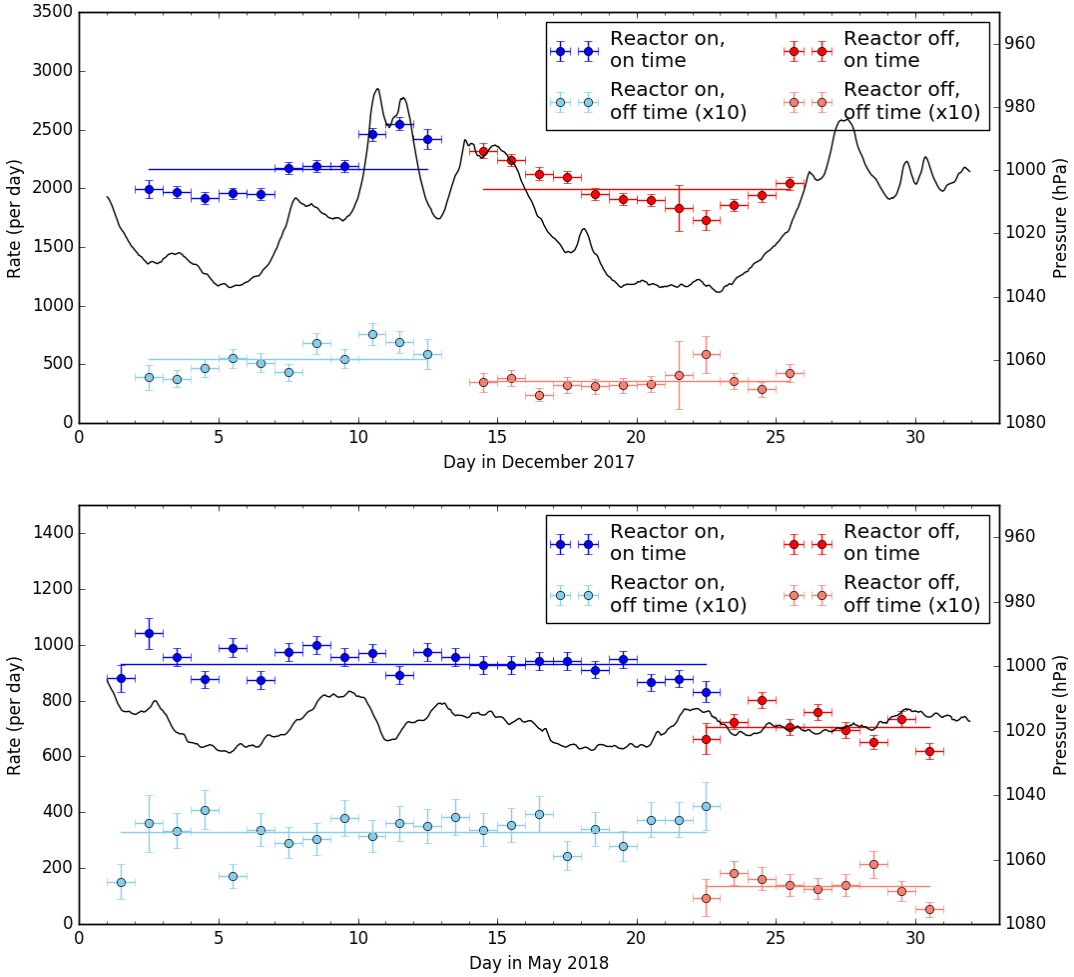

Figure 5.24: Observed rate per day of ES-NS coincidences passing the IBD event selection for the December 2017 (top) and May 2018 (bottom) datasets. The environmental pressure (black line) is indicated on the right axis using an inverted scale to better show the anticorrelation with the event rate. The range of the right axis is the same for both panels. The accidental background is for both datasets multiplied by ten for visualisation.

The spatial distributions as well as the ΔT and ES cube energy distributions are shown in Figure 5.25 for both December 2017 and May 2018 and for reactor on and reactor off. Since different processes are at the basis of the ES and NS signal for accidental backgrounds, the spatial distribution are not the well contained distributions caused by a single underlying process, such as the IBD distributions shown in the left column of Figure 5.1. Instead, the equivalent distributions are broad and to first order consistent with random combinations. In Figure 5.25, the expected spatial distributions are indicated with a pink line. These are obtained by making all possible ES-NS cube combinations that satisfy the spatial selection criteria. The normalization is chosen for aesthetic reasons. The ΔT distribution is expected to be flat since the ES and NS signal bear no relation. The ES energy and the ES cluster size distributions of the accidental background are expected to follow the equivalent ES distributions in absence of an NS signal, i.e. the distributions observed in the FPNT sample.

Once the accidental background is determined using an off-time window, it is subtracted from the on-time window. Special care is taken for the ΔT distribution. Since the number of accidental coincidences is limited and these few events are spread over a large number of bins in case of ΔT, this can induce statistical fluctuations. The ΔT distribution is different from the other distributions since the expected distribution is perfectly known, i.e. a constant. The accidental background subtraction for the ΔT distribution is therefore calculated as the average rate per bin observed over the entire off-time window. This average value is subsequently subtracted.

5.5.2 Correlated background and reactor on excess

While the pressure variations in December 2017 make it hard to see in Figure 5.24, the observed event rate for reactor on is slightly higher than the rate observed when the reactor was turned off. Table 5.6 shows the total event rate per day for reactor on and off, after subtracting the accidental background. The event rate is shown for the full dataset, i.e. without applying pressure matching ('Reference'), as well as for the 'Restricted' and 'Scaled' datasets, for which the pressure variations are taken into account according to the matching techniques described in Section 5.2.3.

	Reactor On Day^{-1}	**Reactor Off** Day^{-1}	**Reactor On Excess** Day^{-1}	σ	**Expected** Day^{-1}
December					
Restricted	2051 ± 22	1991 ± 22	60 ± 31	1.9	∼ 59
Scaled	2052 ± 19	1994 ± 19	59 ± 27	2.2	
Reference	2157 ± 16	2022 ± 16			
May					
Restricted	961 ± 15	734 ± 13	227 ± 20	11.5	∼ 76
Scaled	942 ± 12	735 ± 10	207 ± 15	13.4	
Reference	932 ± 10	724 ± 10			

Table 5.6: Overview of the rate of ES-NS coincidences per day after subtracting the accidental background for reactor on and reactor off datasets in different pressure correction schemes. For the event rates of the reactor on excess obtained with the pressure matched data, the statistical significance is indicated as well.

Despite the small size of the reactor on excess for the December 2017 data with respect to either the reactor on or off selection, Table 5.6 shows the excess is significant[4].

[4]It should be noted that no systematic uncertainties have been considered. Including these would

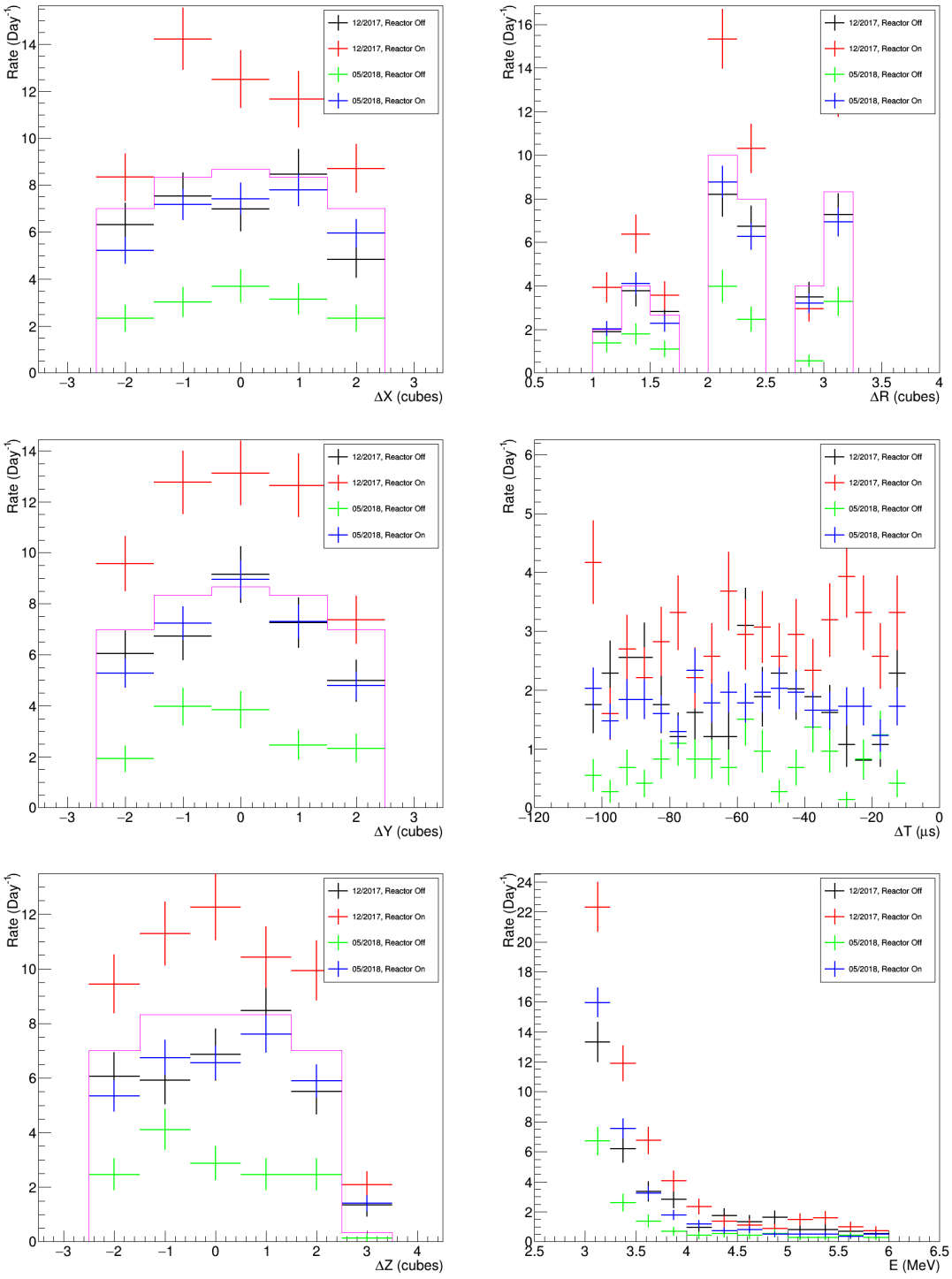

Figure 5.25: Accidental background distributions for both the reactor on and reactor off periods in December 2017 and May 2018. For the spatial distributions, the shape of the expected distributions is shown with a thin pink line.

The reactor on excess is more obvious in the May 2018 data as can be seen in the lower panel of Figure 5.24. The ES-NS coincidence rates for the may 2018 data are included in Table 5.6 as well. The two pressure equivalent datasets are fully consistent. The uncertainty on the scaled dataset is somewhat smaller due to the larger amount of data used in the scaled dataset compared to the restricted dataset.

Due to the lower average pressure during the reactor on data taking period in December 2017, a large excess is observed in the 'Reference' dataset. When applying the pressure matching techniques, these pressure variations are eliminated. With the pressure matched datasets, an excess remains in both the December 2017 and the May 2018 data. Figures 5.26 and 5.27 show the ΔX, ΔY, ΔZ, ΔR, ΔT and energy distributions for reactor on and reactor off pressure matched datasets after accidental background subtraction, collected respectively in December 2017 and May 2018.

When taking into account the selection requirements (Table 5.4) and the reactor power (Figure 4.15), 59 (76) of the 502 (603) expected number of events per day remain in the December (May) dataset if a perfect energy reconstruction is assumed. Due to the smearing in the energy reconstruction and the falling energy spectrum at the lower threshold (Figure 5.19), this number can be expected to be somewhat higher. For the December 2017 data, the observed reactor on excess is consistent with the IBD rate predicted from simulation. For the May 2018 data, the observed reactor on excess is roughly three times larger than the prediction from simulation. The increased rate due to energy smearing can not account for this factor three. The explanation of this excess should therefore be found elsewhere.

While the pressure matched samples balance the cosmic correlated background, they do however not take variations in the amount of BiPo events into account. As mentioned in Section 4.6.2, the background environment changed between the reactor on and reactor off periods in May 2018 due to the introduction of continuously flushing the detector with dry air. Even without changing the background environment, the BiPo rate can undergo large fluctuations over time, as is shown in Figure 5.13 for the last week of June 2018. The radon detector used for the measurement in June 2018 was not present during December 2017 and May 2018. The BiPo rate evolution is therefore estimated using the data from the Phase 1 detector. Selecting ES-NS coincidences according to the BiPo selection laid out in Table 5.3 allows tracking the evolution of the BiPo rate. This evolution is shown in Figure 5.28 for both December 2017 and May 2018. The jump in the BiPo rate when the continuous flushing is started stands out. However, in order to explain the excess of reactor on events in the May 2018 data, a dramatic drop in the BiPo rate would be required. As is indicated in Table 5.4, only a very small fraction of the BiPo events are selected. A second remarkable feature in Figure 5.28 is the higher rate of BiPo events in the December 2017 data, despite having one less module.

The December 2017 reactor on excess

Fitting the six simulated distributions of Figure 5.1 after they underwent the cube reconstruction emulation and the selection criteria of Section 5.3 to the reactor on excess observed in the 'Restricted' dataset shown in Figure 5.26 results in a best fit value of 56 ± 17 events per day, albeit with a relatively poor chi square of 83 for 48 degrees of freedom. This is shown in Figure 5.29. When the BiPo simulation is included as well, the best fit value becomes 88 ± 26 IBD events and -32 ± 26 BiPo events per

most likely change this.

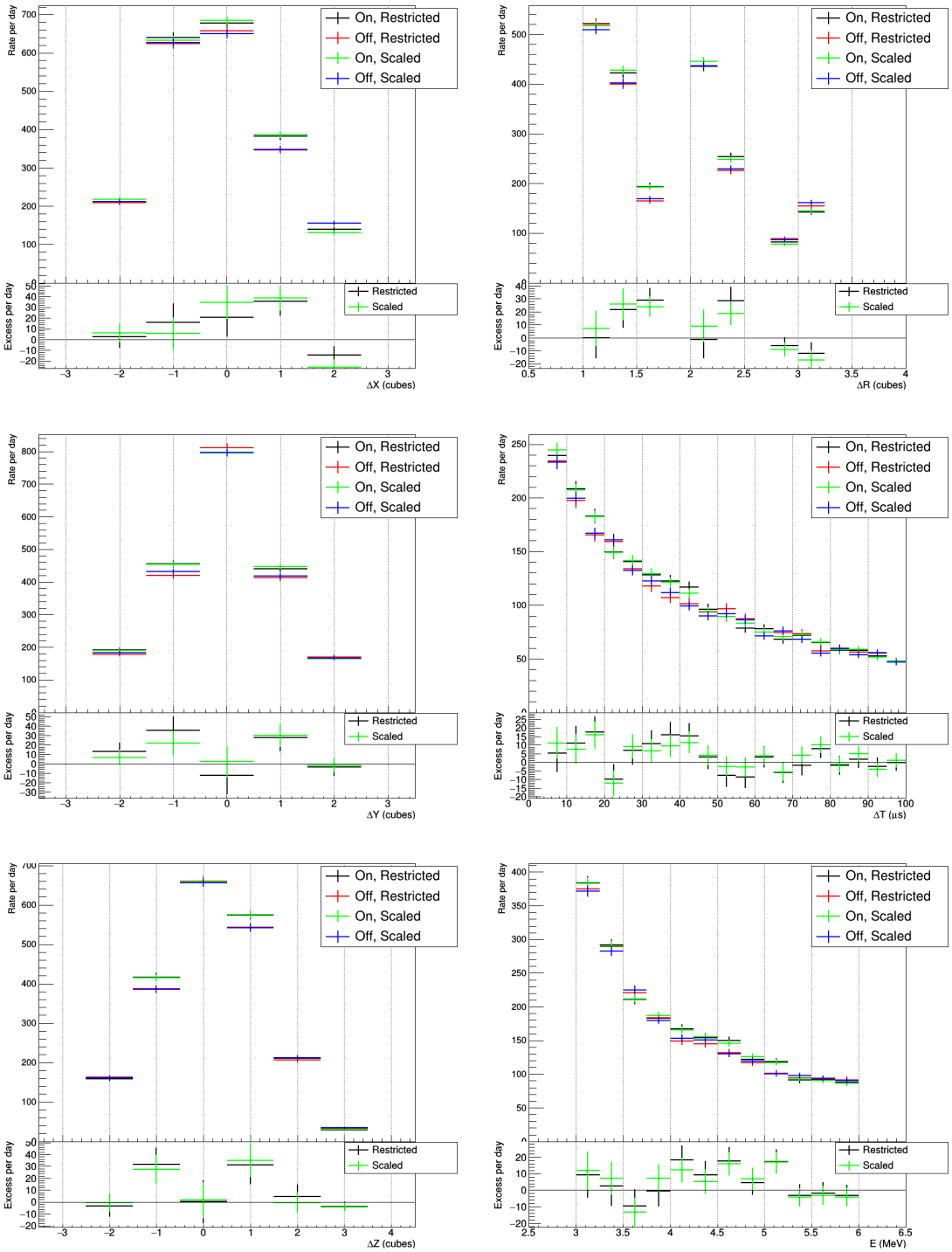

Figure 5.26: Comparison of the spatial, temporal and energy distribution of reactor on and reactor off data after accidental background subtraction for the December 2017 dataset. The comparison is made for the restricted and scaled pressure matching methods.

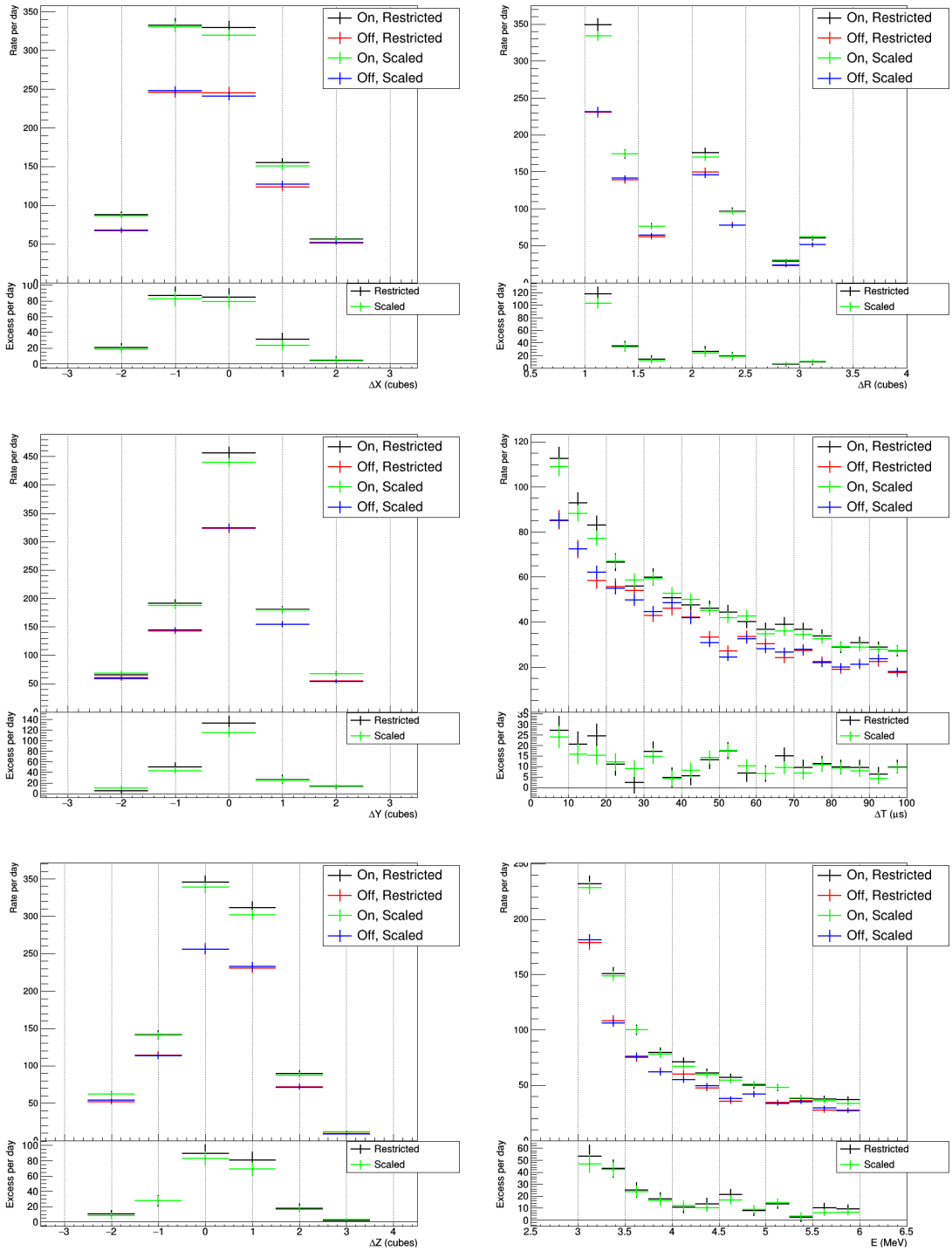

Figure 5.27: Comparison of the spatial, temporal and energy distribution of reactor on and reactor off data after accidental background subtraction for the May 2018 dataset. The comparison is made for the restricted and scaled pressure matching methods.

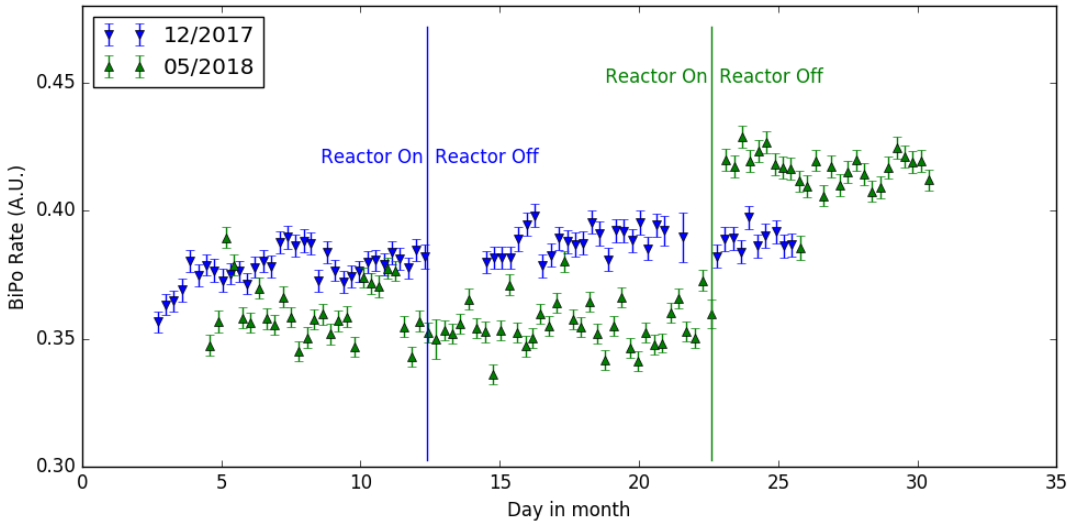

Figure 5.28: Evolution of the BiPo rate determined from data using the selection criteria listed in Table 5.3. The BiPo rate for December 2017 (blue triangles pointing down) and May 2018 (green triangles pointing up) is shown.

day for an equally poor chi square of 79 for 47 degrees of freedom. The fitted negative BiPo rate is expected from the small increase in the BiPo rate shown in Figure 5.28 for reactor off with respect to reactor on. The sum of the fitted IBD and BiPo distributions is included in Figure 5.29. Both these fitted values and the rates listed in Table 5.6 for December 2017 are consistent with the expectation of 59 events per day based on the simulation and the applied selection criteria.

The May 2018 reactor on excess

Repeating this exercise for the excess in the May 2018 data returns a rate of 204 ± 11 events per day with a χ^2 of 516 for 48 degrees of freedom. As with the rate determination from counting the number of events in the reactor on and off selection, the rate determined by the fit is a factor three larger than the expected rate. Additionally, the bad χ^2 value indicates a severe mismatch between the shapes of the expected and the observed distributions. Including the BiPo simulation ($\chi^2 = 471$) reduces the IBD rate to 129 ± 17 events per day and sets the reactor on BiPo excess rate at 86 ± 17, the opposite sign of what is expected from the jump in the BiPo rate when the reactor turns off, shown in Figure 5.28.

Comparing the bottom right panel of Figure 5.27 to the expected IBD energy spectrum suggests an issue with the energy threshold of either the reactor on or reactor off sample. The majority of events in the excess are expected at low energies since the IBD energy spectrum is falling, whereas only 0.617 ± 0.004 events per day are expected in the highest energy bin. In contrast, 9.2 ± 3.8 events per day are observed in that energy bin. This is a factor 17 larger than expected, indicating a mismatch in the energy spectrum since the global mismatch is 'only' a factor three.

A correction factor of 1.1 was applied to the light yield to take into account the increased SiPM over voltage between December 2017 and May 2018. This correction factor was based on the comparison of a single run for December 2017 and a single run for May 2018 [77]. Performing a scan of the light yield of all runs in the May 2018 data, shown in Figure 5.30, indicates a single correction factor is insufficient. For

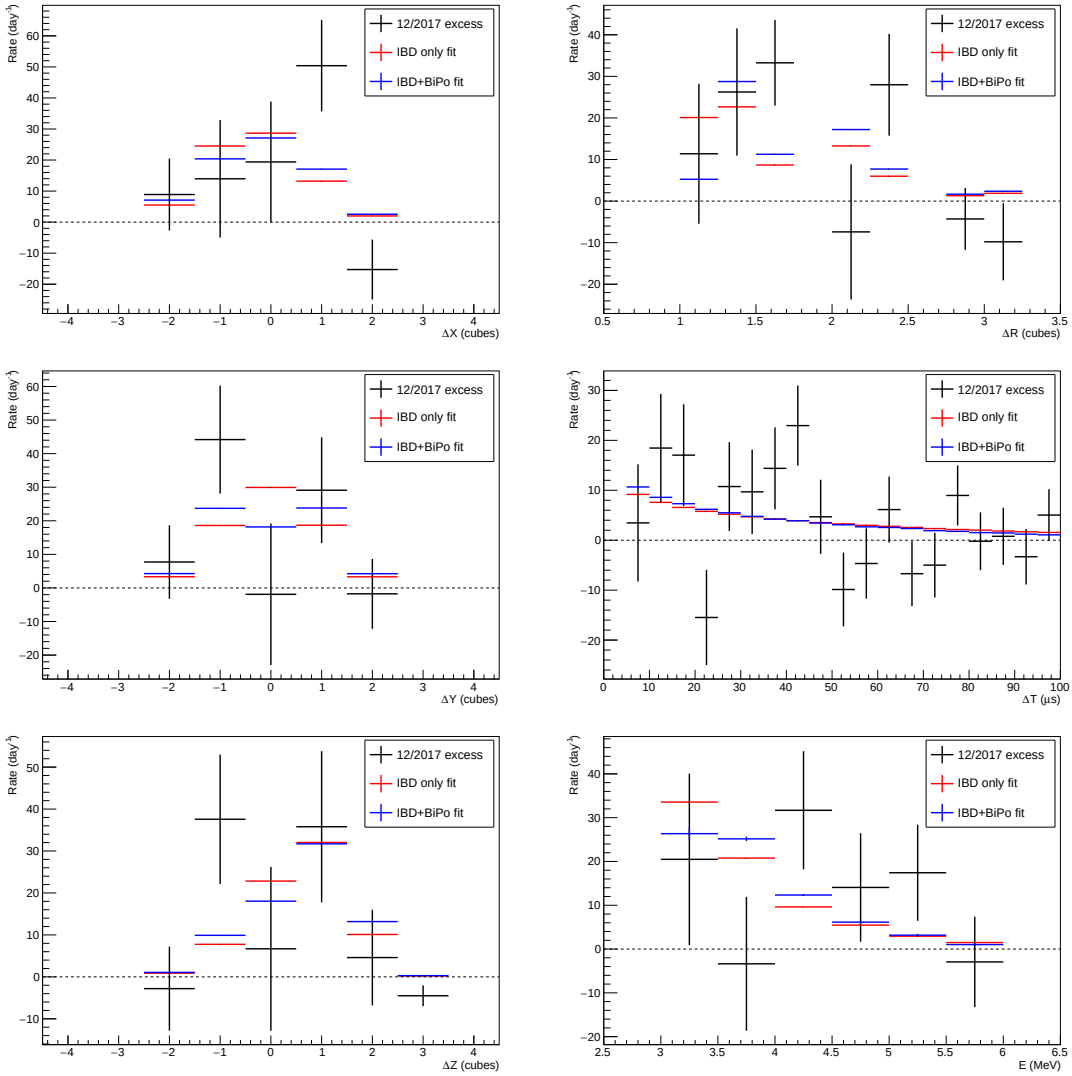

Figure 5.29: Comparison of the December 2017 pressure matched (restricted) reactor on excess to simulation of IBD and BiPo events. The normalization of the simulation distributions is obtained by fitting the distributions to the excess both for IBD only and for IBD + BiPo.

completeness, the light yield of the data collected in December 2017 and the calibration data mentioned in Section 4.1.2 are shown as well.

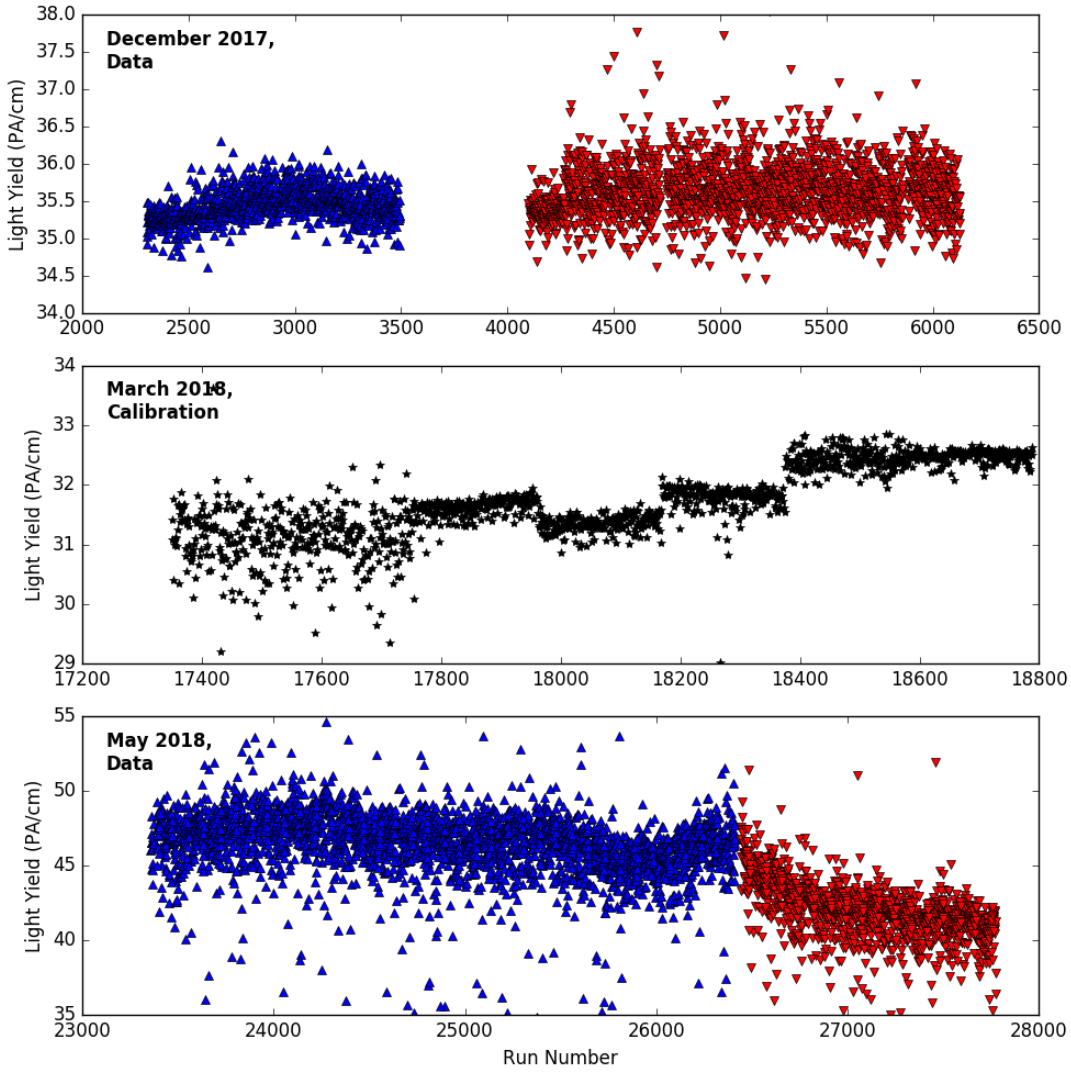

Figure 5.30: Light yield evolution for the December 2017 data (top), the March 2018 calibration (middle) and the May 2018 data (bottom). Reactor on (off) runs are indicated in blue (red) triangles pointing up (down), calibration runs are indicated with black stars.

The light yields shown in Figure 5.30 are determined from the energy deposited in the detector by crossing muons, this calibration method is explained in Appendix 6.2.4. Briefly, muon tracks are fitted and the amount of light per cm track is determined per channel. With a perfectly consistent light yield, this would lead to a Landau distribution. Due to inefficiencies, this Landau distribution is smeared by a Gaussian distribution. The light yield (in ADC/cm) is determined by fitting a Gaussian function to the peak range. Conversion from ADC to PA is performed per channel on a per run basis for the December 2017 and May 2018 data. The gain of the March 2018 files is determined from a dedicated run at the start of the calibration campaign. Constraints on dead time and statistics were introduced to guarantee a reasonable fit. Due to the ^{22}Na source placed in the detector, the surrounding planes experienced a large amount of dead time. The steps in the middle plot indicate when the source was moved to a

different gap, this is further explained in Appendix 6.2.4 as well. The broadening of the distribution at run 4264 is due to the reduction in statistics since the time per run was halved from 600 to 300 seconds. Similarly, at run 17755 the time per run is doubled from 120 to 240 seconds. The time per run in May 2018 is always set at 480 seconds.

Comparison of the bottom panel of Figure 5.30 to Figure 4.18 shows the SEvent rate has a similar trend except for the drop due to the reactor background disappearing. The same drop can also be seen in the container humidity line of Figure 4.19. Figure 5.31 combines the humidity and the light yield measured using muons in one figure, a clear correlation (linear correlation $\rho = 0.96$) can be observed.

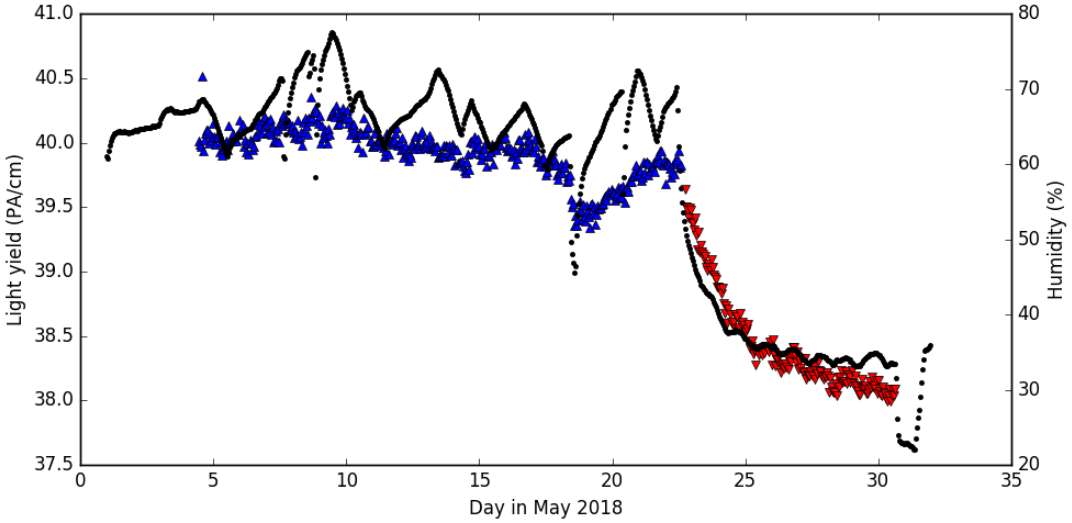

Figure 5.31: Evolution of the light yield (read and blue triangles, left axis) and humidity in the container (black points, right axis) during April 2018. The split between reactor on and reactor off is again made using respectively blue and red triangles pointing up and down.

A first hypothesis is that the light yield varies due to the amount of light that enters and remains in the WLS fibres. If the refractive index of air increases, the critical angle for total internal reflection reduces as well. This reduced angle allows more photons to escape, leaving less photons to be detected by the SiPMs. The humidity dependence of the refractive index of air can however not explain this effect. The refractive index of air can be approximated as

$$n_{air} = 1 + 7.86 \cdot 10^{-3} \frac{P}{273 + T} - 1.5 \cdot 10^{-11} \left(T^2 + 160\right) H_R \tag{5.5}$$

where P is the pressure in hPa, T de temperature in °C and H_R the relative humidity in % [106]. Filling in the container temperature (10 °C) results in

$$n_{air} = 1 + 2.77 \cdot 10^{-5} P - 3.9 \cdot 10^{-9} H_R. \tag{5.6}$$

Even though the refractive index moves in the correct direction to limit the amount of total internal reflection in the WLS, the magnitude of the effect due to humidity changes is much smaller than the effect of pressure changes. In contrast to the May 2018 data, the light yield of December 2017 is very stable while the pressure was varying dramatically. This hypothesis is therefore rejected.

A second hypothesis is that the humidity has an effect on the electronics, thus in-

fluencing the light yield. Evidence for this is the increase in gain[5] when the pressurised air is connected, as can be seen in the second panel of Figure 4.18. Hamamatsu advises to store SiPMs at a relative humidity no higher than 60% but does not mention conditions for operation [63]. There seem to be no investigations into the effect of high humidity on the characteristics of SiPMs, most studies explicitly mention working in a low humidity environment. High humidity may lead to leakage currents [57], which would explain the gain increase when the humidity decreases.

Regardless of the origin of the reduced light yield in the reactor off period, it effectively corresponds to a gradual increase of the trigger threshold, explaining the large excess observed in the May 2018 data. The BiPo rate evolution shown in Figure 5.28 shows neither this gradual behaviour nor the decrease expected from an increased threshold. Instead, the BiPo rate in the selection increases suddenly by almost 30%, despite the higher threshold.

The May 2018 data with modified calibration

Taking into account the changes in light yield can be done by introducing a time dependent energy scale factor instead of the global scale factor of 1.1 applied in the previous sections. The new time dependent scale factors are determined as the ratio of the light yield in an hour, as shown in Figure 5.31, and the global light yield of the December data, 34.4 ± 5.3 ADC/cm. An overview of the correction factor per hour is shown in Figure 5.32.

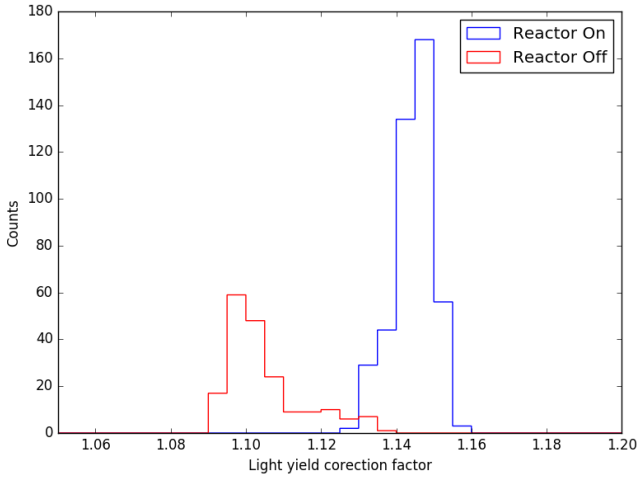

Figure 5.32: Hourly light yield correction factors for the May 2018 data with respect to the December 2017 data.

When the correction factors in Figure 5.32 are applied, a deficit of -42 ± 17 events per day is observed in the restricted dataset. For the scaled dataset, the deficit is -47 ± 14 events per day. Given the fitted BiPo rate of -23 ± 20 events from the small increase in the BiPo rate observed when the reactor was turned off in December 2017, this deficit is not entirely unexpected due to the size of the increase for May 2018.

When the IBD and BiPo distributions are fitted to the data, it is expected from simulation to observe 76 events per day. In order to reach the -42 or -47 events observed in the restricted and scaled datasets respectively, a BiPo rate of -118 or -123 events per

[5]The ADC/cm evolution has the same features as the PA/cm evolution, the change in gain is therefore insufficient to explain the reduction in light yield expressed in PA/cm.

day is required. Performing the IBD+BiPo fit on the restricted and the scaled datasets returns (IBD events per day, BiPo events per day) points (-41, 5) and (-45, 0) with χ^2 values of 57 and 97 for 47 degrees of freedom, not at all what is expected.

Despite the good and reasonable reduced χ^2 values of the best fit points for the restricted and scaled pressure matched datasets, these are incompatible with the information obtained from the reactor status and the BiPo rate evolution. It is therefore concluded that the combined effects of the increased over voltage on the SiPMs with respect to the December 2017 data, the changing light yield as measured by crossing muons during the data taking period, the unwanted change in gain and the introduction of a new background environment due to the continuous flushing when the reactor turned off prevent the observation of a signal consistent with antineutrino observation with the current analysis techniques.

Chapter 6

Outlook

The ultimate goal of the SoLid experiment is to resolve the reactor antineutrino anomaly and to measure the positron energy spectrum for ^{235}U. In order to actually probe the sterile neutrino hypothesis, sufficient statistical power has to be collected to compare predictions to measurements as was laid out in Chapter 2. The neutrino events have to be binned in energy and length bins in order to make this comparison. The prediction can either be calculated based on reactor settings or it can be data driven. Given that the entire premise of the experiment, namely the reactor antineutrino anomaly, is based on a discrepancy between prediction and measurements, this second approach is worth being investigated. Preliminary studies into this so-called flux free analysis have been done and are promising [107].

In Chapter 5, the backgrounds and the IBD signal selection were discussed and applied on two sets of data collected in December 2017 and May 2018 in order to demonstrate the capability of the SoLid experiment to detect IBD events. However, due to a variety of cuts required to reduce the overwhelming background, the signal selection efficiency is poor. Despite the poor selection efficiency, the signal to background ratio is low. From Section 2.3.3, in particular the two panels in Figure 2.18, it is clear a vast improvement to the IBD selection efficiency combined with a significant further reduction of the background is needed in order to reach the goal of resolving the reactor antineutrino anomaly within a reasonable time scale.

As a result of the low statistics, low selection efficiency and low signal to background ratio, an oscillation analysis has not yet been performed. Moreover, the discussion in Section 5.5.2 shows that the reactor on excess is not yet fully understood. Section 6.1 discusses how the understanding can be improved. Section 6.2 lists a number of improvements that could be made to the selection and reconstruction of IBD events in order to make an oscillation analysis possible, other than collecting more data. Section 6.1 discusses how the existing reactor on excess can be understood better.

6.1 Understanding the reactor on excess

While the reactor on excess in December 2017 is statistically significant, this is most likely only true because no systematic uncertainties were included. This section lists a number of actions that should be taken in order to better understand the excess. For May 2018, no conclusions could be drawn. The items listed here will help to understand the collected data but are beyond the scope of this thesis.

6.1.1 Data comparison to full ROSim

The comparison of data to simulation, both to determine the selection requirements in Section 5.3 and to fit the reactor on excess in Section 5.5.2, did not make use of the full ROSim. Instead, an algorithm that mimics the cube reconstruction algorithm but forgoes all statistical effects or inefficiencies in the readout system was employed. The effect of using the full ROSim on the selection requirements will most likely be small for the spatial distributions since these parameters are discrete. The ES energy and time distributions are not, larger differences might occur here. For the fit of the reactor on excess, using the better modelled distributions for IBD and BiPo events should improve the χ^2 value of the fits.

6.1.2 Detailed detector calibration

All ADC to energy conversions in this thesis were based on a detector calibration performed in March 2018. Between the December 2017 data and this calibration the fifth detector module was installed and some electronic boards were swapped. Between the March 2018 and May 2018, the over voltage on the SiPMs was changed from 1.5 V to 1.8 V. These changes make the calibration not quit fit for either dataset, as shown by the light yield obtained with crossing muons (Figure 5.30).

A new calibration was performed at the end of August, the first preliminary results of which indicate the correction factor between 1.5 V and 1.8 V over voltage should be around 1.19 instead of the previously established 1.1 [108]. A full calibration of the detector in the exact same conditions as those during data taking would help the understanding of the reactor on excess. Unfortunately, mimicking the effect of the start of the automated flushing will most likely not be possible.

Completing the muon calibration would provide a constant monitoring tool for the detector. Alternative strategies for constantly monitoring the energy response of the detector are making use of the ^{41}Ar Compton edge when the reactor is on and the tail of the BiPo energy spectrum, both when the reactor is on and off. While the BiPo background was daunting for the selection of IBD events, it is too low in statistics to perform a real calibration [109]. The same is true for the ^{41}Ar Compton edge, but both can be used as a global monitoring tool.

6.1.3 Inclusion of systematic uncertainties

So far, no systematic uncertainties have been considered in the analysis. These would include, but are not limited to:

- Energy reconstruction. There is not only an uncertainty due to the Poissonian nature of counting a number of photons, there is also a systematic uncertainty due to the collection efficiencies which vary from fibre to fibre and from cube to cube. A detailed detector calibration would help to reduce these uncertainties.

- Selection efficiency. The selection efficiency is obtained from simulation and is therefore sensitive to the uncertainties therein.

- Background modelling. In particular for the cosmic neutron backgrounds due to the many parameters involved in neutron transport and capture.

- Pressure matching. So far, it was assumed the pressure remains constant throughout a run lasting up to ten minutes. For ten (five) minute runs, at least one run

per day can be expected to have a 0.3 hPa (0.2 hPa) pressure difference, as is shown in Figure 6.1. For both five and ten minute runs, differences close to or over 1 hPa have been observed. The fractional change of the atmospheric neutron background is almost 1% for a pressure bin that is 1 hPa wide [95].

- Expected IBD rate. As mentioned in Section 1.3.3, predicting the antineutrino rate from a nuclear reactor is notoriously difficult. An uncertainty of up to 5% on the reactor power can be present [110]. This systematic uncertainty cancels when the flux free method is applied to perform the oscillation analysis.
- All other values in Table 2.2 come with an uncertainty as well, in particular the point of closest approach and the proton density.

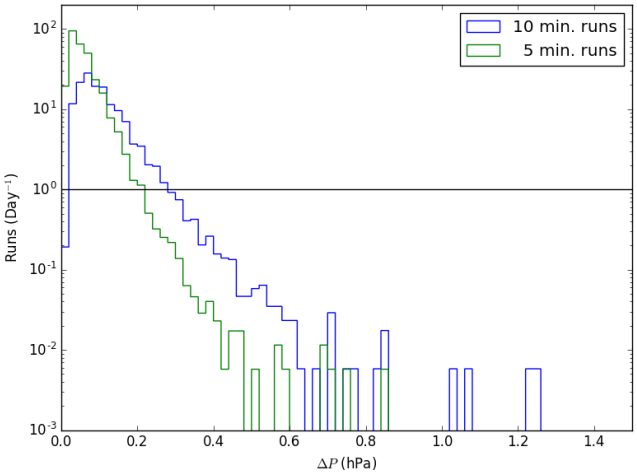

Figure 6.1: Maximal pressure difference observed within five and ten minute runs normalized to the number of runs per day. The horizontal line indicates one run per day.

6.2 Improving the selection efficiency

6.2.1 Enhanced energy reconstruction

In this thesis, the first version of the ES cube reconstruction was used. As mentioned in Section 4.1, reconstructing all possible cubes has a number of drawbacks. Matches between uncorrelated events are being made and the energy of positrons that deposit signal in multiple cubes is poorly reconstructed. Workarounds such as the asymmetry requirement and selecting the highest energy ES cube have been introduced to deal with these shortcomings. A second version of the ES cube reconstruction based on a maximum likelihood using the expectation maximisation algorithm ML-EM is currently under development [111]. This algorithm is also used for medical imaging, e.g. for PET scans. Using this algorithm, the ambiguities of the first algorithm should be lifted. Initial tests on ROSim IBD MC, as shown in Figure 6.2, are very promising [112].

An improved energy resolution is not only helpful for the oscillation study and the determination of the energy spectrum, it can also make the IBD selection more efficient. Backgrounds such as BiPo and ^{41}Ar have a limited energy range, an improved energy reconstruction allows for a tighter selection. Removing the wrongly reconstructed ES cubes avoids smearing of the ES cube multiplicity and the ES cluster size. This in turns allows for better discrimination between signal and background.

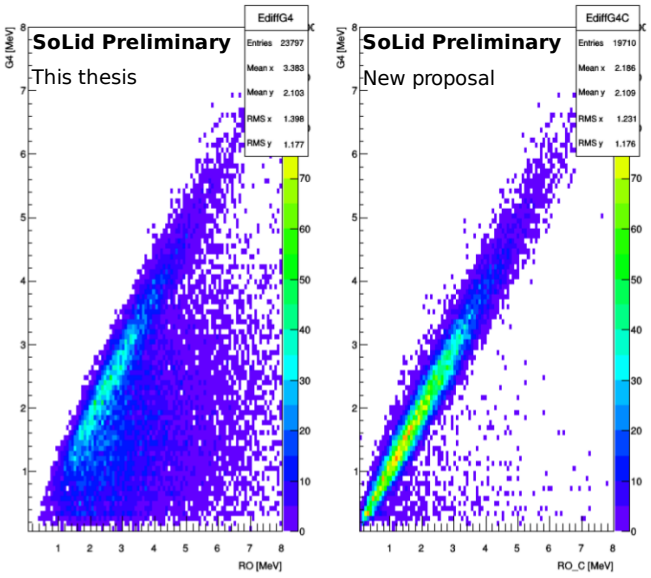

Figure 6.2: Side by side comparison of the ES energy reconstruction used in this thesis (left) and the new iterative reconstruction (right). In both panels, the MC truth is on the Y-axis and the reconstructed energy on the X-axis [112].

6.2.2 Machine learning for selection and classification

The IBD selection procedure so far made use of one dimensional cuts optimized by eye. This procedure mostly ignores correlations between the different variables on which a selection is made. In contrast, machine learning is ideal to optimize the selection requirements since it can take correlations between parameters into account and construct discrimination variables based on multiple observables (e.g. ΔR).

Additionally, a classifying neural net trained on ROSim data of signal and the various backgrounds can learn to identify an ES-NS coincidence not only as signal or background but also as what type of background this coincidence likely is. For each event, a probability-like score is provided for it to belong to a certain class of events, e.g. IBD, BiPo, atmospheric or spallation neutrons.

Accidental background rejection

Primary to increasing the signal selection efficiency is reducing the energy threshold. Next to increasing the BiPo selection (see next section), this also increases the accidental background. When the selection threshold falls below 1.076 MeV, ^{41}Ar enters the accidental background. The Double Chooz collaboration has successfully used machine learning to reduce the accidental background by an order of magnitude by applying machine learning techniques in the hydrogen capture analysis [113].

Data driven background samples

Setting the selection requirements by eye or by the output of a neural net both rely heavily on simulated samples of signal and background. The effectiveness of the selection is therefore limited by the quality of the simulation. In particular the neutron thermalization process is hard to simulate due to the many interactions a neutron undergoes before it is in thermal equilibrium with the surrounding material. Making use

of the known anticorrelation of atmospheric neutrons and atmospheric pressure, machine learning can be used to find a class of events for which the rate moves opposite to the pressure evolution.

Similarly, the rate of BiPo events follows the rate of ^{222}Rn decays, albeit with a slight delay due to intermediate radioactive decays. Using the same machine learning method as the one proposed to obtain a sample of atmospheric neutron events, a pure and more complete BiPo sample can be obtained. Using these two background samples obtained from data will allow for better IBD selection criteria.

This data driven approach of creating background samples can potentially reduce systematic uncertainties due to background modelling. In particular neutron transportation is a non-trivial task.

6.2.3 Alpha-neutron discrimination

The BiPo background is a correlated background due to the alpha emission into a neutron screen being reconstructed as an NS signal. Even though in both Po decay and neutron capture a lot of energy is deposited in the thin neutron screen (respectively 7.83 MeV and 4.78 MeV), the deposition from an alpha decay comes from a single alpha particle while the energy deposit from neutron capture originates from an alpha and a tritium particle. Due to the single charge of a tritium particle, its range is much larger than an alpha particle of the same energy. Since tritium is lighter than an alpha particle, it also receives more energy due to conservation of momentum. The NS signals from alpha decays therefore have a much more concentrated energy deposition, leading to more quenching and recombination of excited levels. This leads to a shorter peak for the alpha decay NS than for the more stretched out neutron borne NS signal. Figure 6.3 shows the comparison of a neutron enhanced sample using an AmBe source, a BiPo enhanced selection and an 'all signal' selection (labelled as 'Physics') [114]. The NS signals satisfying the BiPo selection criteria are indeed located at lower values compared to the NS signals from the AmBe source. The higher energy of the ^{212}Po decay may also contribute to this difference.

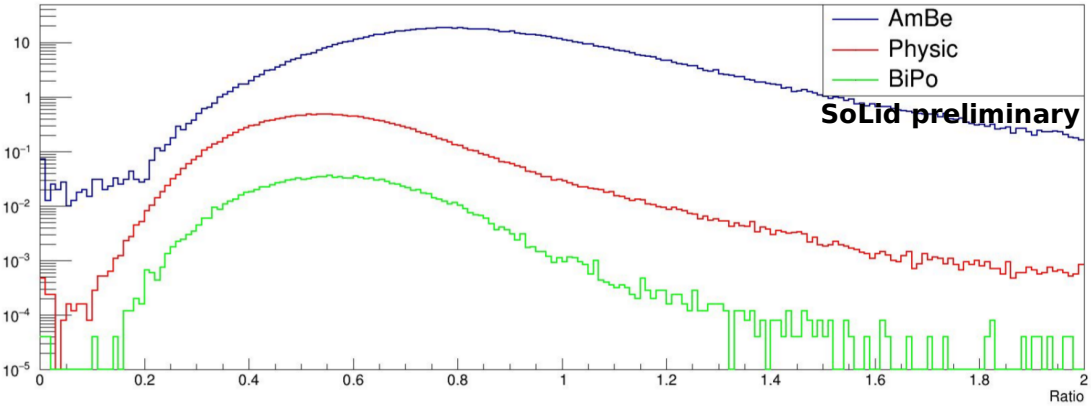

Figure 6.3: Ratio of the early over late part of NS waveforms in reactor off data and in a neutron enhanced dataset [114].

As can be seen from the similar shape of the 'Physics' and BiPo samples, the 'Physics' sample consists mainly of alpha induced NS events. Using this variable would allow rejecting a fraction of the BiPo background at a smaller cost to the IBD signal than the energy cut that is applied in this thesis. For example a selection that rejects

all signals with a ratio less than 0.6 would reject ten percent of neutrons while rejecting half of the alphas. In the 'Physics' sample, this leads to a reduction of 40% of all NS signals [107].

6.2.4 Position reconstruction within a cube

A preliminary study to locate the NS signal to a specific lithium screen and a location on that screen had some success, achieving a location precision of about 1 cm [115]. The location is determined from the amount of light collected by each of the four fibres in the cube. A different location distribution between BiPo decay and IBD signal might exist: BiPo from airborne ^{222}Rn has to reach the detector via the air and might be centred on the fibre grooves. IBD neutrons on the other hand originate from the center of a cube.

While no study has been performed into localizing the ES signal within a cube, it is likely the technique to localize NS signals would also work for ES signals. This would allow further separation of BiPo and IBD signals. Due to the very limited range of the alpha particle emitted in ^{214}Po decay, the BiPo decay has to take place on the surface of lithium screen. This limits the location of the ^{214}Bi decay electron to the X and Z faces of the cubes. In contrast, the IBD positron is emitted from the interaction location, which is expected to be distributed homogeneously throughout the cube. This difference is sketched in Figure 5.2.

Summary

Measurements of the neutrino flux coming from nuclear reactors consistently have a deficit with respect to predictions, this is the so-called reactor antineutrino anomaly. This anomaly combined with several other observed deficits within the field of neutrino physics resulted in the theoretical prediction of the 'sterile neutrino'. The sterile neutrino does not interact with matter and is not included in the Standard Model of particle physics, the mathematical framework that describes interactions between elementary particles with a very high precision.

The effect of such a sterile neutrino would manifest itself via oscillations of 'active flavours', those neutrinos that are incorporated within the Standard Model, into a sterile state. The oscillation probability, given by the properties of the sterile neutrino and the energy and travel distance of the active neutrino before interaction, results in a wave-like pattern subtracted from the neutrino detection rate in absence of oscillations into sterile neutrinos. The period and the amplitude of this pattern are determined respectively by the mass difference and the mixing angle between the sterile and active neutrinos.

In order to resolve the reactor antineutrino anomaly, the SoLid collaboration designed a novel detector technique consisting of a large number of scintillating cubes and deployed it next to SCK•CEN's BR2 reactor. When an antineutrino interacts with a proton in such a cube, the neutrino and the proton become a positron and a neutron. The positron scintillates immediately, providing the location and the energy of the antineutrino. From these two values, the wave-like pattern created by sterile neutrinos can be reconstructed. The neutron first has to thermalize before it is detected, leading to a delay with respect to the positron signal. Due to background processes originating from the reactor and the environment, the coincidence between the positron and neutron has to be observed in order detect antineutrinos.

This thesis provides details on the commissioning and operation of two generations of antineutrino detectors operated by the SoLid experiment over the last four years. For the first detector, the identification of neutron signals as well as the neutron detection efficiency are discussed. For the second detector, a first analysis of data collected during December 2017 and May 2018 is presented. This involves characterisation of the various background processes and creating an event selection in order to minimize the contamination of signal with background. The analysis demonstrates the capability of the experiment as an antineutrino detector. In order to reach the design goals of the experiment in terms of sensitivity, it is concluded that a number of improvements are necessary.

Samenvatting

Metingen van de neutrino flux afkomstig van kernreactoren zijn consistent lager dan de voorspelling, dit is de zogenoemde reactor anti-neutrino anomalie. Samen met andere anomalieën binnen de neutrino fysica heeft deze anomalie geleid tot de theoretische voorspelling van het 'steriel neutrino'. Het steriel neutrino interageert niet met materie en is niet opgenomen in het Standaard Model van de deeltjesfysica, het wiskundig kader dat de interacties tussen de elementaire deeltjes erg goed beschrijft.

Het steriel neutrino zou zichzelf kenbaar maken via oscillaties van 'actieve' naar steriele neutrinos, actieve neutrinos zijn de neutrinos die wel deel uitmaken van het Standaard Model. De kans tot oscilleren hangt af van de eigenschappen van het steriel neutrino, de energie van het gedetecteerde neutrino en de afstand die het heeft afgelegd voor het gedetecteerd werd. De oscillatie naar steriele neutrinos leidt tot een golf vormige reductie van de verwachte flux in afwezigheid van oscillaties. De periode en amplitude van dit patroon hangen respectievelijk af van het massa verschil en van de menghoek tussen het steriele en de actieve neutrinos

Om de reactor anti-neutrino anomalie te ontrafelen heeft de SoLid collaboratie een nieuw type neutrino detector ontworpen bestaande uit scintillerende kubusjes, deze detector werd naast de BR2 reactor in het SCK•CEN geplaatst. Wanneer een anti-neutrino interageert met een proton in een dergelijk kubusje worden het het neutrino en het proton omgezet in een positron en een neutron. Het positron geeft meteen scintilatie licht af, hieruit kan de positie en de energie van het neutrino bepaald worden. Voor het neutron gedetecteerd kan worden moet het eerst voldoende kinetische energie verliezen, hierdoor ontstaat een tijdsverschil tussen de detectie van het positron en het neutron. Aangezien de reactor en de omgeving allerlei achtergronden veroorzaken is het samengaan van het positron en het neutron noodzakelijk om een anti-neutrino te herkennen.

In deze thesis worden details gegeven over de ingebruikname en de exploitatie van twee generaties anti-neutrino detectoren gebouwd door de SoLid collaboratie in de afgelopen vier jaar. Voor de eerste detector wordt de identificatie van neutronen en de neutron detectie efficiëntie besproken. Voor de tweede detector wordt een eerste analyse van data genomen tijdens december 2017 en mei 2018 gepresenteerd. Deze bevat een bespreking van de verschillende achtergronden en het opstellen van selectie voorwaarden om de besmetting van anti-neutrino signalen met achtergrond processen te minimaliseren. Deze analyse toont het potentieel van het experiment als anti-neutrino detector aan. Er wordt geconcludeerd dat verbeteringen in de analyse noodzakelijk zijn om de vooropgestelde gevoeligheid te behalen.

Appendix A

Muon calibration

The muon calibration procedure mentioned in Section 5.5.2 is introduced in reference [116]. Since the muon calibration is referenced heavily in that section, the calibration method is included within this thesis.

The muon calibration uses the 'track' selection also used in Section 4.4.1, an SEvent is considered a 'track muon' when:

- at least eight X and eight Y channels exceed the 200 ADC peak finder threshold
- the sum of all channels exceeds 5000 ADC

For the muon calibration, additional requirements on these tracks are introduced:

- the mean X and Y positions must be within five planes of one another
- the peaks that make up the track must be spread over multiple planes

In these cases, two dimensional straight lines are fitted to the XZ and YZ data. From these two fits, the track length per cube and per row or column is determined. When the track length in a cube is the same as the track length in a row or column, the corresponding peaks are used for the calibration. Since the muon inclination spectrum follows a $cos^2\theta$ distribution around the zenith angle, this condition dramatically reduces the statistics on vertical channels since only muons with an inclination θ of more than 45° are selected for these channels. This restriction is introduced so that in a later stage, a calibration per cube can be performed. For a calibration per channel, this requirement is not strictly necessary. It not only limits the available statistics, it also limits the maximum available track length to $\sqrt{75}$ cm. If a muon were allowed to go through two cubes, the maximal available track length increases to $\sqrt{150}$ cm and the minimal deviation from zenith reduces to 26.6°.

When a muon satisfies the conditions above and a channel pair is selected, the amplitude of the peak on both channels is divided by the track length and the ADC/cm value is added to a histogram for each channel. In a ten minute run, this leads to $1.16 \cdot 10^6$ channel calibration points spread over 2538 channels or 0.77 calibration points per channel per second. As mentioned in Section 5.5.2, the light yield of a channel is determined by fitting a Gaussian to the ADC/cm histogram. This is shown in Figure 6.4 for the four channels that serve the cube $X = 12$, $Y = 12$, $Z = 12$ using a run covering ten minutes of taking data. While a Gaussian is not an accurate shape, it captures the position of the peak of the distribution in a consistent way[1].

[1] Comparison of only a Gaussian to the accurate Gaussian convoluted with a Landau distribution shows the same trends as those shown in Figures 5.32 and 5.31.

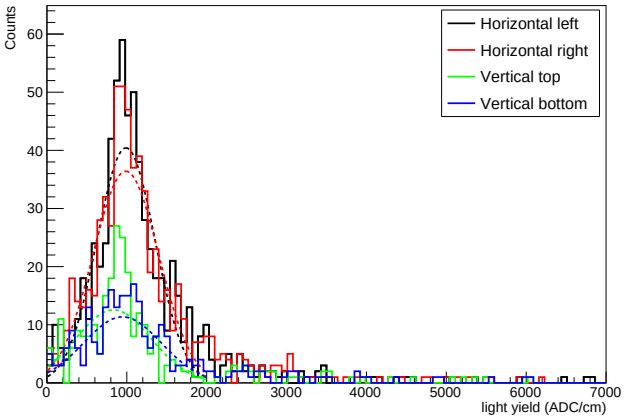

Figure 6.4: Light yield per cm determined from muons in run 3456 (Reactor On, December 2017) for the channels serving cube $(X, Y, Z) = (12, 12, 12)$.

Once the light yield for a channel is obtained in ADC/cm using a Gaussian fit, it is converted to PA/cm via the gain of that specific channel. The light yield for the entire detector is then determined as the average of all channels. The light yield per channel is shown in Figure 6.5, as well as the average values per module and for the entire detector.

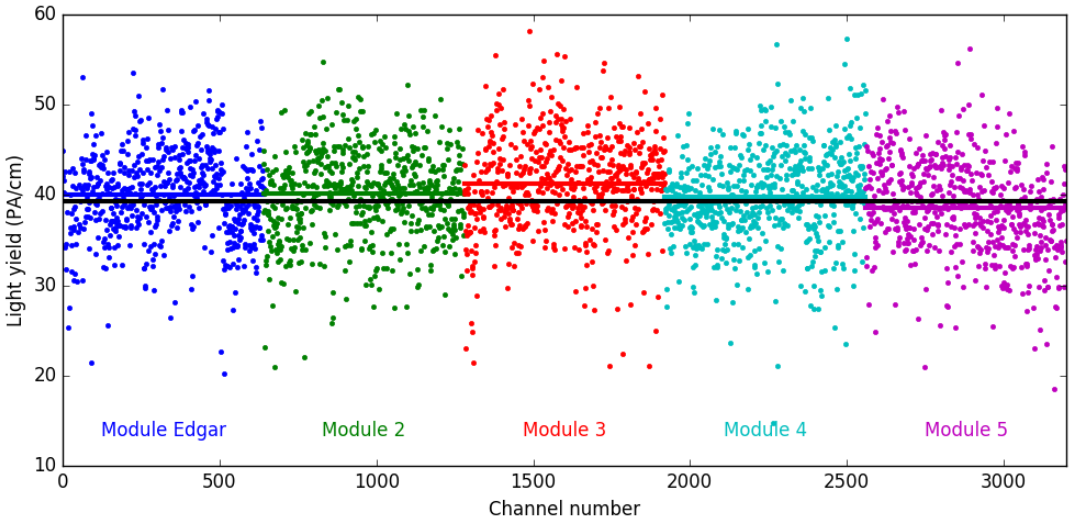

Figure 6.5: The Light yield per channel (points) determined from ten runs during the May 2018 reactor on period (runs 23450 to 23459, 4651 s of data). The average value of each module and of the whole detector are indicated with lines

This calibration per channel does not take attenuation into account. Attenuation in the WLS fibres is relatively small, the attenuation length is 112 ± 11 cm [66]. The WLS fibres are 80 cm long but due to the double readout, a SiPM is at most 40 cm away. Since the single cube requirement is in place, attenuation could be taken into account. This however requires much higher statistics since the light yield has to be determined for every channel in every cube, resulting in 51200 light yield determinations instead of the current 3200.

The small differences per module shown in Figure 6.5 explain the steps observed

in Figure 5.30. Due to the large dead time induced by the source, the channels in the planes near the source are excluded from the light yield determination. These planes are taken out of the pool from which the average is calculated, leading to shifts when the source is moved and a different set of planes is used to calculate the average light yield of the detector.

Bibliography

[1] Nobelprize.org. The Nobel Prize in Physics 1979. `http://www.nobelprize.org/nobel_prizes/physics/laureates/1979/`. accessed on 04/11/2017.

[2] M. Thomson. *Modern particle physics*. Cambridge University Press, New York, 2013.

[3] Nobelprize.org. The Nobel Prize in Physics 2013. `https://www.nobelprize.org/nobel_prizes/physics/laureates/2013/`. accessed on 04/11/2017.

[4] A. W. P. Poon et al. Neutrino observations from the Sudbury Neutrino Observatory. *AIP Conf. Proc.*, 610:218–230, 2002. [,218(2001)].

[5] C. Patrignani et al. Review of Particle Physics. *Chin. Phys.*, C40(10):100001, 2016.

[6] Q. R. Ahmad et al. Direct evidence for neutrino flavor transformation from neutral current interactions in the Sudbury Neutrino Observatory. *Phys. Rev. Lett.*, 89:011301, 2002.

[7] Nobelprize.org. The Nobel Prize in Physics 2002. `http://www.nobelprize.org/nobel_prizes/physics/laureates/2002/`. accessed on 06/11/2017.

[8] Nobelprize.org. The Nobel Prize in Physics 2015. `http://www.nobelprize.org/nobel_prizes/physics/laureates/2015/`. accessed on 06/11/2017.

[9] A. Einstein. Does the inertia of a body depend upon its energy-content. *Annalen der Physik*, 323(113):639–641, March 1905.

[10] I. Esteban, M. C. Gonzalez-Garcia, M. Maltoni, I. Martinez-Soler, and T. Schwetz. Updated fit to three neutrino mixing: exploring the accelerator-reactor complementarity. *JHEP*, 01:087, 2017.

[11] K. N. Abazajian et al. Light Sterile Neutrinos: A White Paper. arXiv:1204.5379, April 2012.

[12] R. B. Patterson. Prospects for Measurement of the Neutrino Mass Hierarchy. *Ann. Rev. Nucl. Part. Sci.*, 65:177–192, 2015.

[13] S. Mertens. Direct Neutrino Mass Experiments. *J. Phys. Conf. Ser.*, 718(2):022013, 2016.

[14] C. Weinheimer and K. Zuber. Neutrino Masses. *Annalen Phys.*, 525(8-9):565–575, 2013.

[15] C. Hartnack, J. Jaenicke, L. Sehn, H. Stöcker, and J. Aichelin. Kaon production at subthreshold energies. *Nuclear Physics A*, 580(4):643 – 677, 1994.

[16] C. Athanassopoulos et al. The Liquid scintillator neutrino detector and LAMPF neutrino source. *Nucl. Instrum. Meth.*, A388:149–172, 1997.

[17] G. B. Mills. Neutrino oscillation results from LSND. *Nucl. Phys. Proc. Suppl.*, 91:198–202, 2001. [,198(2001)].

[18] A. A. Aguilar-Arevalo et al. Observation of a Significant Excess of Electron-Like Events in the MiniBooNE Short-Baseline Neutrino Experiment. 2018.

[19] C. Giunti and M. Laveder. Statistical Significance of the Gallium Anomaly. *Phys. Rev.*, C83:065504, 2011.

[20] J. N. Abdurashitov et al. Measurement of the response of a Ga solar neutrino experiment to neutrinos from an Ar-37 source. *Phys. Rev.*, C73:045805, 2006.

[21] F. Kaether, W. Hampel, G. Heusser, J. Kiko, and T. Kirsten. Reanalysis of the GALLEX solar neutrino flux and source experiments. *Phys. Lett.*, B685:47–54, 2010.

[22] Internation Atomic Energy Agency. Average number of neutrons emitted per fission. `https://www-nds.iaea.org/sgnucdat/a6.htm`. accessed on 04/11/2017.

[23] M. Cribier. Reactor monitoring with neutrinos. *Nucl. Phys. Proc. Suppl.*, 221:57–61, 2011.

[24] Th. A. Mueller et al. Improved Predictions of Reactor Antineutrino Spectra. *Phys. Rev.*, C83:054615, 2011.

[25] F. Von Feilitzsch, A. A. Hahn, and K. Schreckenbach. Experimental beta spectra from neutron fission products and their correlated anti-neutrino spectra. *Phys. Lett.*, 118B:162–166, 1982.

[26] K. Schreckenbach, G. Colvin, W. Gelletly, and F. Von Feilitzsch. Determination of the anti-neutrino spectrum from ^{235}U thermal neutron fission products up to 9.5 MeV. *Phys. Lett.*, 160B:325–330, 1985.

[27] A. A. Hahn, K. Schreckenbach, G. Colvin, B. Krusche, W. Gelletly, and F. Von Feilitzsch. Anti-neutrino Spectra From ^{241}Pu and ^{239}Pu Thermal Neutron Fission Products. *Phys. Lett.*, B218:365–368, 1989.

[28] G. Mention, M. Fechner, Th. Lasserre, Th. A. Mueller, D. Lhuillier, M. Cribier, and A. Letourneau. The Reactor Antineutrino Anomaly. *Phys. Rev.*, D83:073006, 2011.

[29] S. Gariazzo, C. Giunti, M. Laveder, and Y. F. Li. Updated Global 3+1 Analysis of Short-BaseLine Neutrino Oscillations. *JHEP*, 06:135, 2017.

[30] M. Dentler, Á. Hernández-Cabezudo, J. Kopp, M. Maltoni, and T. Schwetz. Sterile neutrinos or flux uncertainties? - Status of the reactor anti-neutrino anomaly. *JHEP*, 11:099, 2017.

[31] F. P. An et al. Evolution of the Reactor Antineutrino Flux and Spectrum at Daya Bay. *Phys. Rev. Lett.*, 118(25):251801, 2017.

[32] J. H. Choi et al. Observation of Energy and Baseline Dependent Reactor Antineutrino Disappearance in the RENO Experiment. *Phys. Rev. Lett.*, 116(21):211801, 2016.

[33] G. Mention, M. Vivier, J. Gaffiot, T. Lasserre, A. Letourneau, and T. Materna. Reactor antineutrino shoulder explained by energy scale nonlinearities? *Physics Letters B*, 773(Supplement C):307 – 312, 2017.

[34] J. I. Crespo-Anadń. Double Chooz: Latest results. *Nucl. Part. Phys. Proc.*, 265-266:99–104, 2015.

[35] F. P. An et al. New Measurement of Antineutrino Oscillation with the Full Detector Configuration at Daya Bay. *Phys. Rev. Lett.*, 115(11):111802, 2015.

[36] S. Schael et al. Precision electroweak measurements on the Z resonance. *Phys. Rept.*, 427:257–454, 2006.

[37] M. Dentler, Á. Hernández-Cabezudo, J. Kopp, P. Machado, M. Maltoni, I. Martinez-Soler, and T. Schwetz. Updated Global Analysis of Neutrino Oscillations in the Presence of eV-Scale Sterile Neutrinos. *JHEP*, 08:010, 2018.

[38] C. Giunti and E. M. Zavanin. Appearance - disappearance relation in $3 + N_s$ short-baseline neutrino oscillations. *Mod. Phys. Lett.*, A31(01):1650003, 2015.

[39] M. Durero et al. The 144 Ce source for SOX. *Journal of Physics: Conference Series*, 675(1):012032, 2016.

[40] The National Institute for Nuclear Physics (INFN). SOX - Short distance Oscillations with boreXino. `http://home.infn.it/en/sox-ingl`. accessed on 03/08/2018.

[41] I. Alekseev et al. DANSS: Detector of the reactor AntiNeutrino based on Solid Scintillator. *JINST*, 11(11):P11011, 2016.

[42] Y. J. Ko et al. Sterile Neutrino Search at the NEOS Experiment. *Phys. Rev. Lett.*, 118(12):121802, 2017.

[43] J. Ashenfelter et al. The PROSPECT Physics Program. *J. Phys.*, G43(11):113001, 2016.

[44] L. Manzanillas. STEREO: Search for sterile neutrinos at the ILL. *PoS*, NOW2016:033, 2017.

[45] A. P. Serebrov et al. The first observation of effect of oscillation in Neutrino-4 experiment on search for sterile neutrino. 2018.

[46] I. Alekseev et al. Search for sterile neutrinos at the DANSS experiment. 2018.

[47] J. Ashenfelter et al. First search for short-baseline neutrino oscillations at HFIR with PROSPECT. 2018.

[48] H. Almazán et al. Sterile neutrino exclusion from the STEREO experiment with 66 days of reactor-on data. 2018.

[49] G. Boireau et al. Online Monitoring of the Osiris Reactor with the Nucifer Neutrino Detector. *Phys. Rev.*, D93(11):112006, 2016.

[50] N. S. Bowden, K. M. Heeger, P. Huber, C. Mariani, and R. B. Vogelaar. Applied Antineutrino Physics 2015 – Conference Summary. 2016.

[51] C. Lane et al. A new type of Neutrino Detector for Sterile Neutrino Search at Nuclear Reactors and Nuclear Nonproliferation Applications. arXiv:1501.0693, 2015.

[52] SCK•CEN. BR2, Research reactor with multiple aplications. `https://www.sckcen.be/-/media/Files/Public/Publications/BR2_brochure/BR2_brochure_ENG_WEB.pdf`. accessed on 13/12/2017.

[53] Y. Abreu et al. Performance of a full scale prototype detector at the BR2 reactor for the SoLid experiment. *JINST*, 13(05):P05005, 2018.

[54] Y. Abreu et al. A novel segmented-scintillator antineutrino detector. *JINST*, 12(04):P04024, 2017.

[55] Eljen Technology. GENERAL PURPOSE PLASTIC SCINTILLATOR EJ-200, EJ-204, EJ-208, EJ-212. `http://www.eljentechnology.com/images/products/data_sheets/EJ-200_EJ-204_EJ-208_EJ-212.pdf`. accessed on 13/12/2017.

[56] Scintacor. Neutron Screens. `https://scintacor.com/wp-content/uploads/2015/09/Datasheet-Neutron-Screens-High-Res.pdf`. accessed on 13/12/2017.

[57] Glenn F Knoll. *Radiation detection and measurement; 4th ed.* Wiley, New York, NY, 2010.

[58] P. Vogel and John F. Beacom. Angular distribution of neutron inverse beta decay, $\bar{\nu}_e + p \to n + e^+$. *Phys. Rev.*, D60:053003, 1999.

[59] I. Piñera. Systematics study of ZnS(Li) parameters in SM1 with G4 simulation. *SoLid DocDB 56-v1*, November 2015.

[60] V. F. Sears. Neutron scattering lengths and cross sections. *Neutron News*, 3(3):26–37, 1992.

[61] I. Piñera. Including extra layers of ZnS(Li) - extra slides. *SoLid DocDB 54-v1*, October 2015.

[62] Saint-Gobain Ceramics & Plastics, Inc. Organic Scintillation Materials and Assemblies. `https://www.crystals.saint-gobain.com/sites/imdf.crystals.com/files/documents/sgc-organics-plastic-scintillators_0.pdf`. accessed on 28/12/2017.

[63] Hamamatsu Photonics K.K., Solid State Division. MPPC (multi-pixel photon counter) S12572-025, -050, -100 C/P. `https://seltokphotonics.com/upload/iblock/79d/79dd6b2f84b2cacddf2716a8f04ce21e.pdf`. accessed on 28/12/2017.

[64] DuPont de Nemours (Luxembourg) S.ár.l. DuPont™ Tyvek® Graphics - Typical Properties of Tyvek® style 10. `hhttp://www2.dupont.com/Tyvek_Graphics/en_US/assets/downloads/Typical_properties_UK_10%20styles.pdf`. accessed on 05/04/2018.

[65] S. Agostinelli et al. GEANT4: A Simulation toolkit. *Nucl. Instrum. Meth.*, A506:250–303, 2003.

[66] Y. Abreu et al. Optimisation of the scintillation light collection and uniformity for the SoLid experiment. *JINST*, 13(09):P09005, 2018.

[67] A. Vacheret et al. Characterization and Simulation of the Response of Multi Pixel Photon Counters to Low Light Levels. *Nucl. Instrum. Meth.*, A656(1):69–83, 2011.

[68] V. Pestel. NS calibration: Quick analysis of the first neutron CROSS scans. *SoLid DocDB 1005-v1*, March 2018.

[69] G. L. Fogli, E. Lisi, A. Marrone, D. Montanino, and A. Palazzo. Getting the most from the statistical analysis of solar neutrino oscillations. *Phys. Rev.*, D66:053010, 2002.

[70] S. Kalvecha, M. Fallot, L. Giot. Recent efforts for the BR2 reactor simulation and anti-neutrino spectrum @ SCK-CEN & SUBATECH. *SoLid DocDB 252-v1*, May 2016.

[71] P. Vichoudis, S. Baron, V. Bobillier, S. Haas, M. Hansen, M. Joos, and F. Vasey. The gigabit link interface board (glib), a flexible system for the evaluation and use of gbt-based optical links. *Journal of Instrumentation*, 5(11):C11007, 2010.

[72] Y. Abreu, S. Ihantola, L. N. Kalousis, I. Piñera, D. M. Saunders, S. Vercaemer. SoLid Technical Note - Neutron detection efficiency in SM1. *SoLid DocDB 856-v2*, April 2016.

[73] Mikhail Danilov. Sensitivity of the DANSS detector to short range neutrino oscillations. *PoS*, EPS-HEP2013:493, 2013. [Nucl. Part. Phys. Proc.273-275,1055(2016)].

[74] J. Ashenfelter et al. PROSPECT - A Precision Reactor Oscillation and Spectrum Experiment at Short Baselines. In *Proceedings, 2013 Community Summer Study on the Future of U.S. Particle Physics: Snowmass on the Mississippi (CSS2013): Minneapolis, MN, USA, July 29-August 6, 2013*, 2013.

[75] V.B. Mikhailik, S. Henry, M. Horn, H. Kraus, A. Lynch, and M. Pipe. Investigation of luminescence and scintillation properties of a ZnS-Ag/6LiF scintillator in the 7-295 K temperature range. *Journal of Luminescence*, 134(Supplement C):63 – 66, 2013.

[76] D. Boursette. Cube reconstruction study. *SoLid DocDB 946-v1*, February 2018.

[77] S. Vercaemer. First look at May 2018 data. *SoLid DocDB 1103-v1*, June 2018.

[78] Y. Abreu on behalf of the MC group. MC Group Status and Plans. *SoLid DocDB 1012-v1*, March 2018.

[79] V. Pestel on behalf of the nuclear signal group. Neutron reconstruction : Current Saffron implementations. *SoLid DocDB 1007-v1*, March 2018.

[80] V. Pestel. Preliminary neutron WF catalog : AmBe data. Private communication, April 2018.

[81] Y. Abreu and I. Piñera. Neutron capture time evaluation in SM1 with AmBe calibration source: Data & MC simulation. *SoLid DocDB 621-v1*, January 2016.

[82] V. Pestel. NS calibration. *SoLid DocDB 1060-v1*, May 2018.

[83] United States Nuclear Regulation Commission. Neutron sources. `https://www.nrc.gov/docs/ML1122/ML11229A704.pdf`, October 2010.

[84] S. Vercaemer. Neutron detection in the SoLid experiment. In *Proceedings, 2016 IEEE Nuclear Science Symposium and Medical Imaging Conference: NSS/MIC 2016: Strasbourg, France*, page 8069691, 2016.

[85] L. Kalousis. Muons and after muon events in SM1. *SoLid DocDB 692-v2*, February 2016.

[86] National Oceanic and Atmospheric Administration - Earth System Research Laboratory - Global Monitoring Division. Basics of the Carbon Cycle and the Greenhouse Effect. `https://www.esrl.noaa.gov/gmd/ccgg/basics.html`. accessed on 22/01/2018.

[87] V. Chisté and M. M. Bé on behalf of Laboratoire National Henri Bequerel. Table de Radionucléides $^{41}_{14}\mathrm{Ar}_{23}$. `http://www.nucleide.org/DDEP_WG/Nuclides/Ar-41_tables.pdf`. accessed on 22/01/2018.

[88] S. Vercaemer. Determination of the accidental amplitude spectrum. *SoLid DocDB 1002-v1*, March 2018.

[89] National Institute for Standards and Technology - Physical Measurement Laboratory. ESTAR, stopping power and range tables for electrons. `https://physics.nist.gov/PhysRefData/Star/Text/ESTAR.html`. accessed on 28/07/2018.

[90] L. N. Kalousis and S. Vercaemer. SoLid sensitivity contours. *SoLid DocDB 784-v1*, January 2017.

[91] D. H. Perkins. *Particle Astrophysics, Second Edition.* Oxford Master Series in Physics. OUP Oxford, 2008.

[92] G. Vandierendonck. Muon Veto Optimization and After Muon Events. *SoLid DocDB 1116-v1*, June 2018.

[93] Sodankyla Geophysical Observatory. Oulu neutron monitor. `http://cosmicrays.oulu.fi/`. accessed on 23/08/2018.

[94] M. Dayananda, X. Zhang, C. Butler, and X. He. Understanding the effect of atmospheric density on the cosmic ray flux variations at the earth surface. arXiv:1303.7191.

[95] P. K. F. Grieder. *Cosmic rays at earth: Researcher's reference, manual and data book*. Elsevier, Amsterdam, 2001.

[96] A. Chilingarian, T. Karapetyan, and B. Mailyan. Calculation of the barometric coefficients for the particle detectors belonging to the world-wide networks at the start of the 24^{th} solar activity cycle. In *31st International Cosmic Ray Conference (ICRC 2009) Lodz, Poland, July 7-15, 2009*, pages 3291–3295, 06 2009.

[97] R. Salminen. *Geochemical Atlas of Europe*. EuroGeoSurveys, Brussels, 2005.

[98] J. Helebrant. Radioactive series. `http://www.clker.com/clipart-90240.html`. accessed on 30/06/2018, modified by P. Vercaemer.

[99] R. Trevisi, S. Risica, M. D'Alessandro, D. Paradiso, and C. Nuccetelli. Natural radioactivity in building materials in the european union: a database and an estimate of radiological significance. *Journal of Environmental Radioactivity*, 105:11 – 20, 2012.

[100] Internation Atomic Energy Agency. *The Environmental Behaviour of Radium: Revised Edition*. Number 476 in Technical Reports Series. Internation Atomic Energy Agency, 2014.

[101] I. Piñera. BR2 building geometry & model for SoLid Geant4 simulations. *SoLid DocDB 714-v2*, April 2017.

[102] L. Ghys. Correlation Rn rate and NS signal rate in SOLID. *SoLid DocDB 1025-v2*, July 2018.

[103] K. S. Krane. *Introductory nuclear physics*. Wiley, New York, NY, 1988.

[104] S.-C. Wu. Nuclear data sheets for a = 214. *Nuclear Data Sheets*, 110(3):681 – 748, 2009.

[105] L. Simard. BiPo rates. *SoLid DocDB 1047-v1*, May 2018.

[106] National Institute for Standards and Technology. Engineering Metrology Toolbox: Refractive Index of Air Calculator. `https://emtoolbox.nist.gov/wavelength/EquationB1.asp`.

[107] S. Vercaemer. Updates from the Final Fit group. *SoLid DocDB 829-v3*, September 2017.

[108] D. Henaff, B. Viaud and L. Manzanillas. August calibration campaign status. *SoLid DocDB 1145-v1*, August 2018.

[109] L. Simard. Try to test the energy scale with ^{214}Bi β^- end-point : comparison of December 2017 and May 2018 data sets. *SoLid DocDB 1131-v1*, July 2018.

[110] J. van Muiden. Determination of the accuracy and precision of BR2 thermal power. *SoLid DocDB 256-v1*, May 2016.

[111] A. Dempster, N. Laird, and D. B. Rubin. Maximum likelihood from incomplete data via the em algorithm. *Journal of the Royal Statistical Society. Series B (Methodological)*, 39:1–38, 01 1977.

[112] H. Chanal. Yet Another Cube Reconstruction Proposal. *SoLid DocDB 1120-v1*, May 2018.

[113] Y. Abe et al. Measurement of θ_{13} in Double Chooz using neutron captures on hydrogen with novel background rejection techniques. *JHEP*, 01:163, 2016.

[114] V. Pestel. NS signals update. *SoLid DocDB 1068-v1*, May 2018.

[115] K. Graves, A. Vacheret *et al.* NS signal position reconstruction in SoLid cubes. *SoLid DocDB 1035-v1*, April 2018.

[116] C. Moortgat. First look at muon calibration. *SoLid DocDB 982-v1*, March 2018.

List of abbreviations

ADC	analogue to digital converter
APD	avalanche photo diode
CaliPSo	calibration plane for SoLid
CC	charged current interaction
CROSS	calibration on site SoLid
DaR	decay at rest
DCR	dark count rate
DiF	decay in flight
ES	electromagnetic scintillation
FLCT	first large cluster time
FoM	figure of merit
FPGA	field programmable gate array
FPNT	false positive neutron trigger
GLIB	gigabit link interface board
HDPE	high density polyethylene
IBD	inverse beta decay
LCS	large cluster size
LH	left handed
MGT	minimal gap time
MIP	minimally ionizing particle
NC	neutral current interaction
NEMENIX	neutrino measurement non income experiment
NS	nuclear scintillation
PA	pixel avalanche
PCB	printed circuit board
PId	particle identification
PMT	photomultiplier tube
PoT	peaks over threshold
PVT	polyvinyl toluene
RAA	reactor antineutrino anomaly
RH	right handed
SiPM	silicon photomultiplier
SM	Standard Model of particle physics
SM1	SoLid module 1
WLS	wavelength shifting
ZS	zero suppression

Author's contributions

This thesis provides an overview of the work I performed over four years. During this time two detectors were installed, commissioned and operated by the collaboration. I contributed extensively to all these tasks for both detectors, by physically assembling the detector cubes and planes in the particle physics laboratory in Ghent and building the shielding when installing the detectors next to the BR2 reactor. I provided first measurements on critical parameters and by performed data quality shifts (remote and on location).

For the SM1 detector, the author provided the gain determination and the neutron identification algorithms and contributed to the determination of the neutron detection efficiency. All these results are published in

Performance of a full scale prototype detector at the BR2 reactor for the SoLid experiment, JINST 13 (2018), P05005

and were presented in international conferences, the proceedings of which are published:

Neutron detection in the SoLid experiment, IEEE NSS/MIC 2016, p8069691
and
Neutron identification in the SoLid experiment, PoS EPS-HEP2015 083

My research, in particular results on the neutron identification and the neutron detection efficiency, led to the redesign of the detector and the implementation of a new trigger system. The results of this redesign led to the following publications:

The SoLid antineutrino detector's readout system, JINST 12 (2017), C02012
and
Optimisation of the scintillation light collection and uniformity for the SoLid experiment, accepted by JINST

to which I contributed indirectly.

For the Phase 1 detector, I detected an inaccuracy in the neutron timing and provided the start time determination algorithm. Similarly, I first observed a large rate of ES signals, contributing to the accidental background and traced it back to ^{41}Ar decays. Also the strong correlation between the atmospheric pressure and the correlated cosmic background was first observed by me. To correct for this dependence, I developed two techniques that allow the comparison of data collected during different periods, in particular for the comparison of reactor on data to reactor off data. Using these methods on two very different datasets, commissioning data from December 2017 and physics data from May 2018, I observed a reactor on excess in both. I presented these results in the 2018 International Conference for High Energy Physics is Seoul, South Korea.

Acknowledgements

To all the great people...

First and foremost, I'd like to thank my parents. This would literally not have been possible without you. I can not thank you enough for all the support you gave me throughout the years. Not only prior to my PhD but also during these last four years. I also have to thank my sisters for being there, I wasn't always the most pleasant person (when stressed). Thank you Mom. Thank you Dad. Thank you Maud. Thank you Suzan. I can not leave out my home town friends for many fun off days and evenings to clear my mind, in particular my life long friend Jasper and his amazing girlfriend Ozanette.

I thank the members of the jury for taking the time to go through my thesis manuscript and provide helpful comments to improve it. I also much appreciate the discussion we had during the private defence. I can't forget my promotors, Petra and Nick. While technically members of the jury, they deserve a special mentioning. Thank you for giving me the opportunity to start this adventure four years ago. Of course I also appreciate all the discussions we've had during my PhD to improve my research and the many iterations of thesis drafts that returned with more remarks on them then there would actually fit in the margins. This was key to the quality of my work.

The nice people of the SoLid collaboration deserve a word of thanks as well, you have been my (remote) colleagues over the past four years. We constructed and operated antineutrino detectors together, I had a great time doing so. Two people I have to mention explicitly are Céline and Delphine, we had a nice and productive collaboration in the proto analysis group.

I must thank all the people who have made my PhD fun, who have made me enjoy coming to the office every morning. All lunch and coffee breaks with colleagues, past and present, at both the VUB and in Antwerp, are deeply appreciated. A list, in no particular order: Doug[1], Emil, Dom, Petra (again), Quentin, Shimaa, Isis (thanks again for the lovely cover design), Lieselotte[1], Isabelle, Kevin, Yarne, Kirill, Dennis, Leonidas, Sara, Alex, Hans, Merijn, Tom, Wim, Maja, Ibrahin and Yamiel. A special thanks goes to the staff of both institutes who keep them running. This is the IT department and the secretaries, thank you Sarah and Marleen.

[1]You made me a tea snob, I still mostly drink coffee though.